



Universität Hamburg

DER FORSCHUNG | DER LEHRE | DER BILDUNG

Synthesis of  $\text{ZrO}_2/\text{YSZ}-\text{Al}_2\text{O}_3$  composite and  
 $\text{ZrO}_2/\text{YSZ}@-\text{SiO}_2$  core@shell microparticles for  
high-temperature photonic applications

Synthese von  $\text{ZrO}_2/\text{YSZ}-\text{Al}_2\text{O}_3$  Komposit- und  $\text{ZrO}_2/\text{YSZ}@-\text{SiO}_2$   
Kern@Schale-Mikropartikeln für photonische  
Hochtemperaturanwendungen

DISSERTATION

zur Erlangung des Grades  
„Doktor der Naturwissenschaften“  
(Dr. rer. nat.)

vorgelegt von  
**Maik Finsel**

Institut für Physikalische Chemie  
Universität Hamburg

**2019**

Gutachter der Dissertation:

Dr. Tobias Vossmeier  
Prof. Dr. Alf Mews

Gutachter der Disputation:

Prof. Dr. Horst Weller  
JProf. Dr. Simone Mascotto  
Prof. Dr. Gabriel Bester

Datum der Disputation:

27. September 2019

# Publications

Maik Finsel, Maria Hemme, Sebastian Döring, Jil Rüter, Gregor T. Dahl, Tobias Krekeler, Andreas Kornowski, Martin Ritter, Horst Weller, and Tobias Vossmeier. Synthesis and thermal stability of  $\text{ZrO}_2@\text{SiO}_2$  core-shell submicron particles. In: Royal Society of Chemistry (RSC) Advances 9 (2019), pp. 26902-26914. doi: 10.1039/C9RA05078G.

Hendrik Schlicke, Svenja Kunze, Maik Finsel, Elisabeth W. Leib, Clemens J. Schröter, Malte Blankenburg, Heshmat Noei, and Tobias Vossmeier. Tuning the Elasticity of Cross-Linked Gold Nanoparticle Assemblies. In: The Journal of Physical Chemistry C 123.31 (2019), pp. 19165-19174. doi: 10.1021/acs.jpcc.9b03553

Jan Schwenger, Stefan Romeis, Patrick Herre, Tadahiro Yokosawa, Maik Finsel, Elisabeth W. Leib, Horst Weller, Tobias Vossmeier, Erdmann Spiecker, and Wolfgang Peukert. Pressure induced local phase transformation in nanocrystalline tetragonal zirconia microparticles. In: Scripta Materialia 163 (2019), pp. 86-90. doi: 10.1016/j.scriptamat.2018.12.035.

Alexey Petrov, Hauke Lehmann, Maik Finsel, Christian Klinke, Horst Weller, and Tobias Vossmeier. Synthesis and Characterization of Monodisperse Metallo-dielectric  $\text{SiO}_2@\text{Pt}@\text{SiO}_2$  Core-Shell-Shell Particles. In: Langmuir 32.3 (2016), pp. 848-857. doi: 10.1021/acs.langmuir.5b03631.



# Contents

<b>Publications</b>	<b>i</b>
<b>Abbreviations</b>	<b>vii</b>
<b>1 Zusammenfassung</b>	<b>1</b>
<b>2 Abstract</b>	<b>5</b>
<b>3 Introduction</b>	<b>9</b>
<b>4 Theory</b>	<b>15</b>
4.1 Photonic structures . . . . .	15
4.1.1 Photonic crystals . . . . .	17
4.1.2 Photonic glasses . . . . .	20
4.2 Zirconia . . . . .	21
4.2.1 Crystalline phases . . . . .	22
4.2.2 Grain growth and sintering . . . . .	25
4.2.3 Phase stabilization and grain growth inhibition . . . . .	27
4.3 Zirconia particles . . . . .	31
4.3.1 Synthetic approaches . . . . .	31
4.3.2 High-temperature behavior . . . . .	36
4.3.3 Doping . . . . .	37
4.4 Core@shell structures . . . . .	38
4.4.1 Types . . . . .	39
4.4.2 Synthesis . . . . .	39
<b>5 Objectives</b>	<b>45</b>

<b>6</b>	<b>Results and Discussion</b>	<b>49</b>
6.1	ZrO <sub>2</sub> -Al <sub>2</sub> O <sub>3</sub> and YSZ-Al <sub>2</sub> O <sub>3</sub> composite microparticles . . . . .	49
6.1.1	Synthesis and calcination of ZrO <sub>2</sub> and YSZ microparticles . . . . .	49
	Assembly of ZrO <sub>2</sub> and YSZ microparticles to photonic glasses . . . . .	52
6.1.2	Atomic layer deposition of alumina on ZrO <sub>2</sub> microparticles . . . . .	53
	<i>Ex situ</i> heating experiments . . . . .	54
6.1.3	Post-synthetic modification of ZrO <sub>2</sub> microparticles with alumina . . . . .	58
	<i>Ex situ</i> heating experiments . . . . .	58
6.1.4	Atomic layer deposition and post-synthetic modification of YSZ microparticles with alumina . . . . .	60
6.1.5	EDX-mapping . . . . .	65
6.1.6	Optical properties . . . . .	67
6.2	ZrO <sub>2</sub> @SiO <sub>2</sub> and YSZ@SiO <sub>2</sub> core@shell submicron particles . . . . .	70
6.2.1	Synthesis of ZrO <sub>2</sub> @SiO <sub>2</sub> core@shell submicron particles . . . . .	70
6.2.2	Thermal stability . . . . .	76
	Shape stability . . . . .	76
	Phase stability and grain growth . . . . .	77
	EDX-mapping . . . . .	83
6.2.3	Optical properties . . . . .	87
6.3	Sub-projects . . . . .	92
6.3.1	Mechanical properties . . . . .	92
6.3.2	YSZ microparticles as absorber/emitter for TPVs . . . . .	95
<b>7</b>	<b>Outlook</b>	<b>99</b>
<b>8</b>	<b>Experimental Section</b>	<b>103</b>
8.1	Materials . . . . .	103
8.2	Methods . . . . .	105
8.2.1	Assembly of photonic glasses . . . . .	110
8.2.2	Deposition of a YSZ microparticle monolayer . . . . .	111
8.2.3	Atomic layer deposition of alumina . . . . .	112
8.2.4	Microcompression of zirconia microparticles . . . . .	113
8.3	Thermal loading . . . . .	113
	<b>Bibliography</b>	<b>137</b>

<b>Appendix</b>	<b>139</b>
Supplementary Material . . . . .	139
Safety . . . . .	145
Danksagung . . . . .	159
Curriculum Vitae . . . . .	162
Conferences . . . . .	163
<b>Eidesstattliche Erklärung</b>	<b>167</b>



# Abbreviations

<b>1D</b>	one-dimensional
<b>2D</b>	two-dimensional
<b>3D</b>	three-dimensional
<b>a</b>	amorphous
<b>Al<sub>2</sub>O<sub>3</sub></b>	alumina
<b>ALD</b>	atomic layer deposition
<b>APTES</b>	3-aminopropyltriethoxysilane
<b>as-fab.</b>	as-fabricated
<b>b</b>	instrumental broadening
<b>c</b>	cubic
<b>CTAB</b>	cetyltrimethylammonium bromide
<b>d</b>	period of the motif (PC), average plane to plane distance (PG)
<b>D</b>	diameter
<b>D<sub>b</sub></b>	atomic diffusivity
<b>FWHM</b>	full width at half maximum
<b>δ<sub>b</sub></b>	grain boundary thickness
<b>demin.</b>	demineralized
<b>ESB</b>	energy selective backscattered
<b>EDX</b>	energy-dispersive X-ray spectroscopy
<b>FD</b>	force-deformation
<b>FE</b>	finite element
<b>FEM</b>	finite element method
<b>FG</b>	functional group
<b>FIB</b>	focused ion beam
<b>HAADF-STEM</b>	high angle annular dark-field scanning transmission electron microscopy
<b>HPC</b>	hydroxypropyl cellulose
<b>IR</b>	infrared

<b>k</b>	Boltzmann constant
<b><i>K</i></b>	dimensionless shape factor
<b><i>L</i></b>	crystallite size
<b><math>\lambda</math></b>	wavelength of radiation
<b><math>\lambda_e</math></b>	reflection edge at long wavelengths of a photonic structure
<b><math>n_{\text{eff}}</math></b>	effective refractive index
<b>NIR</b>	near infrared
<b>NNN</b>	next nearest neighbor
<b>m</b>	monoclinic
<b><i>M</i></b>	grain mobility
<b>MAO</b>	methylalumoxane
<b>MIR</b>	mid infrared
<b>MPTMS</b>	3-mercaptopropyl(trimethoxy)silane
<b><math>\Omega</math></b>	atomic volume
<b>PC</b>	photonic crystal
<b>PEG</b>	polyethylene glycol
<b>PES</b>	polyethersulfone
<b>PG</b>	photonic glass
<b>PMMA</b>	polymethyl methacrylate
<b>PS</b>	polystyrene
<b>PSM</b>	post-synthetic modification
<b>PTFE</b>	polytetrafluorethylene
<b>PVP</b>	polyvinylpyrrolidone
<b>RI</b>	refractive index
<b>SAED</b>	selected area electron diffraction
<b>SC</b>	structural color
<b>SEM</b>	scanning electron microscopy
<b>SiO<sub>2</sub></b>	silica
<b>t</b>	tetragonal
<b>t'</b>	tetragonal prime
<b><i>T</i></b>	temperature
<b><math>\theta_0</math></b>	Bragg angle
<b>TBC</b>	thermal barrier coating
<b>TEM</b>	transmission electron microscopy
<b>TEOS</b>	tetraethyl orthosilicate
<b>TGO</b>	thermally grown oxide

<b>THF</b>	tetrahydrofuran
<b>TiO<sub>2</sub></b>	titania
<b>TMA</b>	trimethylaluminum
<b>TPV</b>	thermophotovoltaic
<b>UV</b>	ultraviolet
<b>vis</b>	visible
<b><i>w</i></b>	full width at half maximum
<b>XPS</b>	X-ray photoelectron spectroscopy
<b>XRD</b>	X-ray diffraction
<b>YAG</b>	yttrium aluminum garnet
<b>YSZ</b>	yttria-stabilized zirconia
<b>ZrO<sub>2</sub></b>	zirconium dioxide, zirconia



# 1 Zusammenfassung

In den letzten Jahren ist das Interesse an Zirkonia-basierten Submikro- und Mikropartikeln und deren potenziellen Hochtemperaturanwendungen, z.B. in der Katalyse, Thermophotovoltaik (TPV), Strukturfarben (SC) und Wärmedämmschichten (TBC), gewachsen.

Für TBCs, die z.B. in Gasturbinen-Triebwerken für Flugzeuge Verwendung finden, werden bevorzugt Keramiken wie Y-stabilisiertes Zirkonia (YSZ) aufgrund ihrer niedrigen Wärmeleitfähigkeit eingesetzt. Hierbei wird das Ziel verfolgt, die darunter liegende Superlegierung thermisch zu isolieren. Die TBC ist hierbei extremen Belastungen mit Temperaturen bis zu 1400 °C und Drücken bis zu 10 bar ausgesetzt. Ein großes Problem von TBC-Systemen ist die Sauerstoffdiffusion durch die YSZ-Beschichtung aufgrund von Sauerstofffehlstellen, was zur Korrosion der Turbinenschaufel und schließlich zum Materialversagen führen kann. Neben der thermischen Stabilität und der Korrosionsbeständigkeit muss die TBC auch eine mechanische Robustheit aufweisen, um Materialbrüche zu vermeiden.

Zirkonia- und YSZ-Mikropartikel würden mehrere dieser Anforderungen für eine verbesserte TBC-Anwendung erfüllen, da sie hochtemperaturstabil und mechanisch robust sind. Darüber hinaus kann eine breitbandige Reflektivität im IR-Bereich (Wärmestrahlung) durch die Assemblierung zu photonischen Gläsern erreicht werden, indem die Partikeldurchmesser im Mikrometerbereich liegen. Zur Darstellung der  $\text{ZrO}_2$ - und YSZ-Mikropartikel ( $D = 2\text{-}3 \mu\text{m}$ ) wurde in dieser Arbeit ein modifiziertes Sol-Gel-Verfahren eingesetzt. Anschließend wurden die erhaltenen Mikropartikel nass-chemisch mit Alumina modifiziert, bevor eine Assemblierung zu photonischen Gläsern erfolgte. Des Weiteren wurden photonische Gläser aus unbehandelten  $\text{ZrO}_2$ - und YSZ-Mikropartikeln hergestellt und anschließend mit Alumina durch Atomlagenabscheidung (ALD) beschichtet, mit dem Ziel die Sauerstoffdiffusion zu reduzieren.

## 1 Zusammenfassung

Die  $\text{ZrO}_2$ - und YSZ-Kerne sowie die  $\text{ZrO}_2\text{-Al}_2\text{O}_3$  und  $\text{YSZ-Al}_2\text{O}_3$ -Kompositpartikel wurden bei Temperaturen zwischen 800 und 1500 °C kalziniert, um die thermische Stabilität zu untersuchen. Nach der Wärmebehandlung wurden die Partikel mittels SEM, Querschnitts-EDX-Mapping, XRD und IR-Reflektionsmessungen charakterisiert. Für Alumina-beschichtete  $\text{ZrO}_2\text{-Al}_2\text{O}_3$  und  $\text{YSZ-Al}_2\text{O}_3$ -Kompositpartikel konnte keine signifikante Verbesserung der thermischen Stabilität im Vergleich zu den unbeschichteten Kernen festgestellt werden. Eine post-synthetische Modifikation von  $\text{ZrO}_2$ -Mikropartikeln mit Alumina in einer Sol-Gel-Synthese führte hingegen zum Erhalt der tetragonalen Phase bis 1000 °C, während die unbehandelten  $\text{ZrO}_2$ -Kerne bereits vollständig in die monokline Phase umgewandelt waren. Des Weiteren konnte das Kornwachstum bis 1500 °C gehemmt werden, wodurch wesentlich kleinere Korngrößen im Vergleich zu den Kernen erhalten wurden. Weitere Analyse der optischen Eigenschaften ergab, dass die intensive Breitbandreflexion im IR-Bereich auch nach Hochtemperaturen bis zu 1500 °C nahezu erhalten blieb. Für Alumina-modifizierte YSZ-Mikropartikel konnten hingegen keine signifikanten zusätzlichen Stabilisierungseffekte bei dem t→m Phasenübergang und dem Kornwachstum gegenüber den unbehandelten YSZ-Kernen nachgewiesen werden. Mögliche Erklärungen für die verbesserte Hochtemperaturbeständigkeit der  $\text{ZrO}_2\text{-Al}_2\text{O}_3$ -Kompositpartikel aus der post-synthetischen Modifikation sind Al-Einlagerungen in den Zirkonia-Kernen während der Synthese und Al-Segregation zu den Korngrenzen bei thermischer Behandlung.

Eine Reduzierung der Zirkonia-Mikropartikelgröße auf einen Durchmesser im Submikrometerbereich führt zu optischen Eigenschaften im sichtbaren Bereich, da der Partikeldurchmesser im Bereich der Wellenlänge des sichtbaren Lichts liegt. Somit sind Zirkonia-Submikropartikel mit einem hohen Brechungsindex ein interessantes Material für Strukturfarben und könnten somit als Alternative zu Pigment-basierten Farben dienen, die teilweise immer noch giftige Stoffe enthalten. Um hochtemperaturstabile Strukturfarben zu erhalten, werden monodisperse Zirkonia-Submikropartikel mit einer glatten Oberfläche und einer Schale aus einem Material mit starkem Brechungsindexkontrast zum Kern benötigt. Außerdem ist ein einfaches Syntheseverfahren ohne die Verwendung von organischen Liganden als Haftvermittler zwischen dem Kern und der Schale wünschenswert, um Hochtemperaturanwendungen zu ermöglichen. Daher wurden Zirkonia- (durchschnittlicher Durchmesser nach der Kalzinierung: ~270 nm) und YSZ-Submikropartikel (durchschnittlicher Durchmesser nach dem Kalzinieren: ~117 nm) unter Verwendung

einer Sol-Gel-Methode synthetisiert. Für die Verschalung wurde Silika als Prototyp verwendet, da das Verfahren nach Stöber bereits etabliert ist und Silika einen starken Brechungsindexkontrast zum Zirkonia-Kern darstellt. Die Silika-Verschaltung von Zirkonia-Partikeln stellt jedoch eine herausfordernde Aufgabe dar, da in früheren Studien organische Haftvermittler verwendet werden mussten, welche für potentielle Hochtemperaturanwendungen ein Problem darstellen können. Aus diesem Grund wurden  $\text{ZrO}_2@\text{SiO}_2$  Kern@Schale-Partikel unter Verwendung einer verbesserten Syntheseroute synthetisiert, bei der eine kontrollierte Abscheidung von homogenen Silika-Schalen (10 bis 60 nm) auf vorkalzinierte Zirkonia- und YSZ-Kerne ohne den Einsatz zusätzlicher organischer Haftvermittler möglich ist.

Um die thermische Stabilität von  $\text{ZrO}_2$ - und YSZ-Kernen sowie  $\text{ZrO}_2@\text{SiO}_2$  und  $\text{YSZ}@\text{SiO}_2$  Kern@Schale-Partikeln zu untersuchen, wurden diese bei 450 bis 1200 °C kalziniert. Nach der Wärmebehandlung wurden die Partikel mittels SEM, TEM, STEM, Querschnitts-EDX-Mapping und XRD charakterisiert. Hierbei führten ein signifikantes Kornwachstum und die  $t \rightarrow m$  Phasentransformation von  $\text{ZrO}_2$ -Kernen bei 600 °C zu einer Zerstörung der sphärischen Partikelgestalt nach weiterem Heizen auf 800 °C. Im Gegensatz dazu ergab die Silika-Verschaltung von  $\text{ZrO}_2$ -Submikropartikeln ein deutlich gehemmtes Kornwachstum und der  $t \rightarrow m$  Phasenübergang wurde erst nach dem Heizen auf 1000 °C beobachtet, wobei die Partikelform, mit einer glatten Silika-Schale, stabil blieb. Folglich sind  $\text{ZrO}_2@\text{SiO}_2$  Kern@Schale-Partikel für Hochtemperaturanwendungen bis 1000 °C geeignet. In dieser Arbeit werden verschiedene Mechanismen, wie z.B. die räumliche Einschränkung von Zirkonia-Kristalliten durch die Silika-Schale, gehemmter Massentransport,  $\text{SiO}_2$  als Sauerstoffdiffusionsbarriere und Si-Dotierung, zur Erklärung der deutlich verbesserten Stabilität der  $\text{ZrO}_2@\text{SiO}_2$  Kern@Schale-Partikel diskutiert.

Darüber hinaus wurden die optischen Eigenschaften von photonischen Gläsern aus  $\text{YSZ}@\text{SiO}_2$ -Partikeln mit Silika-Schalendicken zwischen 10 und 50 nm untersucht. Zu diesem Zweck wurde die Reflektivität vor und nach der Wärmebehandlung bis 1000 °C gemessen. Hierbei konnte die Position und Steigung der Reflektionskante im sichtbaren Bereich durch Variation der Silika-Schalendicke verändert werden, welches zu einer blauen Strukturfarbe führte.

Als Teilprojekt wurden zudem die mechanischen Eigenschaften von  $\text{ZrO}_2$ -Mikropartikeln ( $D \sim 2.5 \mu\text{m}$  nach der Synthese) mittels Mikrokompressionsexperimenten untersucht. Hierbei wurde eine Druck-induzierte  $t \rightarrow m$  Phasenumwandlung in Ab-

## 1 Zusammenfassung

hängigkeit von der lokalen Kristallitorientierung und der verwendeten Scherspannung beobachtet. Darüber hinaus wurde die Sol-Gel-Synthese von YSZ-Mikropartikeln für potentielle TBC-Anwendungen modifiziert, um YSZ-Mikropartikel mit einem Durchmesser von nur  $D \sim 1 \mu\text{m}$  nach dem Kalzinieren für eine potentielle Anwendung als Absorber/Emitter-Material in TPV-Systemen zu erhalten. Zu diesem Zweck wurde eine Monolage aus YSZ-Mikropartikeln auf einem W/HfO<sub>2</sub>-Substrat abgeschieden, um die optischen Eigenschaften zu untersuchen. Dabei konnte eine Hochtemperaturbeständigkeit des TPV-Systems bis 1400 °C (6 h unter Vakuum) nachgewiesen werden, wobei die gewünschten optischen Eigenschaften erhalten blieben.

## 2 Abstract

In recent years, there has been an increasing interest in zirconia-based submicron and microparticles and their potential high-temperature applications, e.g., in catalysis, thermophotovoltaics (TPV), structural colors (SC), and thermal barrier coatings (TBC).

For TBCs, e.g., in gas-turbine engines operated in aircrafts, low-thermal conductivity ceramics such as Y-stabilized zirconia (YSZ) are used to provide thermal insulation of the underlying superalloy. Here, the TBC is exposed to extreme conditions with temperatures up to 1400 °C and pressures up to 10 bar. One of the main obstacles of the TBC system is the oxygen diffusion through the YSZ top-coat due to oxygen vacancies, which leads to corrosion and failure of the turbine blade. Besides thermal stability and corrosion resistance, the TBC also needs to exhibit mechanical robustness to resist material fracture.

Zirconia and YSZ microparticles would meet several requirements for improved TBC application, as they are high-temperature stable and mechanically robust. Furthermore, a broadband reflectivity in the IR range (thermal radiation) can be obtained by assembly to photonic glasses due to the particle diameter in the micrometer range. Therefore,  $\text{ZrO}_2$  and YSZ microparticles (2-3  $\mu\text{m}$ ) were synthesized using a modified sol-gel method. Afterwards, alumina was introduced by wet-chemical modification of these microparticles before assembly to photonic glasses. Furthermore, a photonic glass made out of bare  $\text{ZrO}_2$  and YSZ microparticles was coated with alumina by atomic layer deposition (ALD) to reduce oxygen diffusion.

To study the thermal stability of bare  $\text{ZrO}_2$  cores, bare YSZ cores,  $\text{ZrO}_2\text{-Al}_3\text{O}_2$  composite particles, and  $\text{YSZ-Al}_3\text{O}_2$  composite particles they were calcined at 800 to 1500 °C. After heat treatments, the particles were characterized by SEM, cross-sectional EDX mapping, XRD, and IR-reflection measurements. For alumina-coated  $\text{ZrO}_2\text{-Al}_2\text{O}_3$  and  $\text{YSZ-Al}_3\text{O}_2$  particles, no difference in thermal stability

could be noticed, i.e. stabilization of the tetragonal phase and inhibition of grain growth, compared to bare core particles. In striking contrast, post-synthetic modification of  $\text{ZrO}_2$  microparticles by alumina in a sol-gel synthesis yielded preserved tetragonal phase fractions at 1000 °C, while bare  $\text{ZrO}_2$  particles completely transitioned to the monoclinic phase. Furthermore, grain growth could be inhibited up to 1500 °C leading to remarkably reduced grain sizes compared to bare  $\text{ZrO}_2$  cores. Further analysis of the optical properties revealed that the intensive broadband reflection in the IR range was nearly preserved even after high-temperatures up to 1500 °C. For alumina-modified YSZ microparticles, the t→m phase transition and grain growth did not show any significant additional stabilization effects compared to bare YSZ cores. Possible explanations for the improved high-temperature stability of  $\text{ZrO}_2\text{-Al}_3\text{O}_2$  composite particles from post-synthetic modification are Al diffusion into the zirconia cores during synthesis and Al segregation to the grain boundaries upon thermal loading.

Reducing the zirconia microparticle size to diameters in the submicrometer range leads to optical properties in the visible range as the particle diameter then is comparable to the wavelength of light. Thus, zirconia submicron particles with a high refractive index are an interesting material for structural coloration as an alternative to pigment-based colors, which sometimes still contain toxic materials. For high-temperature stable structural colors, well-defined monodisperse zirconia submicron particles with smooth surfaces and a shell material with a strong refractive index contrast would meet these requirements. Furthermore, a straightforward synthesis method without the use of organic ligands as adhesive layer between the core and the shell is desirable to enable high-temperature photonic applications.

Therefore, zirconia (average diameter after calcination:  $\sim 270$  nm) and YSZ (average diameter after calcination:  $\sim 117$  nm) submicron particles were synthesized using a modified sol-gel method. For encapsulation, silica was considered as prototype material due to the well-known encapsulation process by the Stöber method and a strong refractive index contrast. However, silica encapsulation of zirconia particles seems to be challenging as previous studies used organic coupling agents, which may preclude high-temperature applications. Therefore,  $\text{ZrO}_2\text{@SiO}_2$  core@shell particles were synthesized using an improved seeded growth protocol, which enables the well-controlled deposition of homogeneous silica shells (10 to 60 nm) onto pre-calcined zirconia and YSZ cores without using additional organic coupling agents.

To study the thermal stability of bare  $\text{ZrO}_2$  cores, bare YSZ cores,  $\text{ZrO}_2@SiO_2$  and  $\text{YSZ}@SiO_2$  core@shell particles, they were calcined at 450 to 1200 °C. After heat treatments, the particles were characterized by SEM, TEM, STEM, cross-sectional EDX mapping, and XRD. Here, significant grain coarsening and the t→m transformation at 600 °C of bare  $\text{ZrO}_2$  particles destroyed the spheroidal particle shape after further heating to 800 °C. In striking contrast, silica-encapsulation of  $\text{ZrO}_2$  submicron particles significantly inhibited grain growth and the t→m transition progressed considerably only after heating to 1000 °C, whereupon the particle shape, with a smooth silica shell, remained stable. Thus,  $\text{ZrO}_2@SiO_2$  core@shell particles are suited for high-temperature applications up to ~1000 °C. Different mechanisms such as spatial confinement of the zirconia crystallites due to the silica shell, inhibited mass transport,  $SiO_2$  as oxygen diffusion barrier, and Si-doping are considered to explain the markedly enhanced stability of  $\text{ZrO}_2@SiO_2$  core@shell particles.

Moreover, the optical properties of photonic glasses made of  $\text{YSZ}@SiO_2$  particles with different silica shell thicknesses between 10 and 50 nm were investigated. For this purpose, the reflectivity was measured before and after heat treatments up to 1200 °C. Here, the position and steepness of the reflection edge in the visible range could be tuned by varying the silica shell thickness yielding a blue coloration.

As sub-projects, the mechanical properties of  $\text{ZrO}_2$  microparticles ( $D \sim 2.5 \mu\text{m}$  as-synthesized) were investigated by microcompression experiments. Here, a pressure-induced t→m phase transformation dependent on the local crystallite orientation and the applied shear stress was observed. Furthermore, the sol-gel synthesis of YSZ microparticles for potential TBC application was modified to yield YSZ microparticles with a diameter of only  $D \sim 1 \mu\text{m}$  after calcination for potential application as absorber/emitter in TPVs. For this purpose, a YSZ monolayer on a W/ $HfO_2$  substrate was deposited to investigate the optical properties. Here, high-temperature stability of the TPV system up to 1400 °C (6 h under vacuum) was demonstrated, whereby the desired optical properties were preserved.



### 3 Introduction

Over the last decades, zirconia ( $\text{ZrO}_2$ ) micro- and submicron particles have gained substantial attention due to their outstanding properties such as chemical inertness, thermal[1–3] and mechanical stability,[4, 5] high refractive index,[6, 7] and low thermal conductivity.[1, 2] These ceramic particles are promising materials for a wide range of scientific studies and potential applications such as fuel cells,[8] sensors,[9, 10] catalysis,[11] high performance liquid chromatography,[12] absorber/emitter in thermophotovoltaics (TPV),[13, 14] and ceramic abutments in medicine.[15–18]

However, previous studies mostly focused on zirconia particles as building blocks for high-temperature applications, including thermal barrier coatings (TBC)[1–3, 19–21] and structural colors (SC).[6, 22–25] For TBC operation, zirconia microparticles in a disordered assembly (photonic glass) with particle diameters of 2–3  $\mu\text{m}$ , narrow size distributions, and spherical shape are needed to achieve high reflectivity in the infrared (IR) range. Much of the current literature on TBCs pay particular attention to yttria-stabilized zirconia (YSZ) as yttrium-doping decreases the grain growth. As stabilization mechanisms, the solute-drag effect and lattice distortion due to oxygen vacancies are proposed, which therefore stabilize the preferable tetragonal crystal phase.[26, 27] Recently, our group showed that the optimum Y content of YSZ particles is 8–10 wt%.[1] Matsumoto *et al.*[28] demonstrated that the addition of small amounts of lanthania to zirconia coatings suppresses sintering during deposition and thereby contributes to a reduction in the thermal conductivity. Furthermore, Leib *et al.*[3] proposed a co-doping process with 5% Y and either 1% La or 1% Gd, which yields  $D \sim 2 \mu\text{m}$  extremely stable particles even after heating to 1200 °C. These co-doped zirconia particles exhibit smaller grain sizes than undoped or Y-doped zirconia particles and the tetragonal phase was stabilized until 1500 °C.

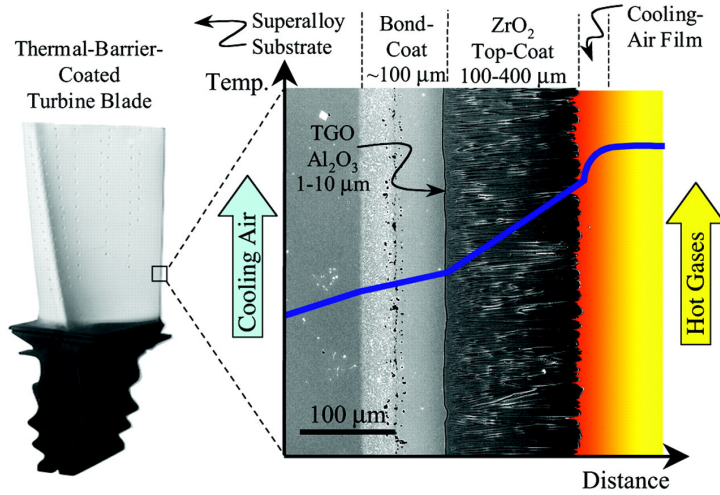


**Figure 3.1** – Cross-sectional scanning electron micrograph of an electron-beam physical-vapor deposited TBC (top-coat), superimposed onto a schematic diagram showing the temperature reduction provided by the TBC. The turbine blade contains internal hollow channels for air-cooling, whereas the outside hot-section surface is thermal barrier-coated, setting up a temperature gradient (blue line) across the TBC. From [29]. Reprinted with permission from AAAS.

For the desirable application as TBC, the superalloy substrate in gas-turbine engines needs to be protected against oxidation as shown in Fig. 3.1. Therefore, the nickel- or cobalt-based structural superalloy contains as many as 5 to 12 additional elements that are added for enhancement of high-temperature stability.[29] Furthermore, the bond-coat between the substrate and the ceramic top-coat is an oxidation-resistant metallic layer, where a thermally grown oxide (TGO) forms as  $\alpha$ -Al<sub>2</sub>O<sub>3</sub> (see Fig. 3.1), which protects the underlying superalloy against oxidation due to its very low oxygen ionic diffusivity. In contrast, the YSZ top-coat provides thermal insulation, but is oxygen transparent due to its high number of vacancies in the oxygen crystal sub-lattice.

Hence, the main challenge faced by many researchers is to improve prevention of superalloy oxidation in TBCs. Ren *et al.*[26] showed that a thin Al<sub>2</sub>O<sub>3</sub>/YAG (alumina-yttrium aluminum garnet) layer as bond-coat exhibits superior properties to resist oxidation of the underlying alloy and improves the spallation resistance up to 1000 °C. Their recent findings suggest that these beneficial effects should be mainly attributed to the sealing effect of  $\alpha$ -Al<sub>2</sub>O<sub>3</sub> and reduced thermal stress due to the use of nano/micro composites with increased porosity. Data from oxidation resistance studies by Keyvani *et al.*[30] support this hypothesis as an alumina overlay

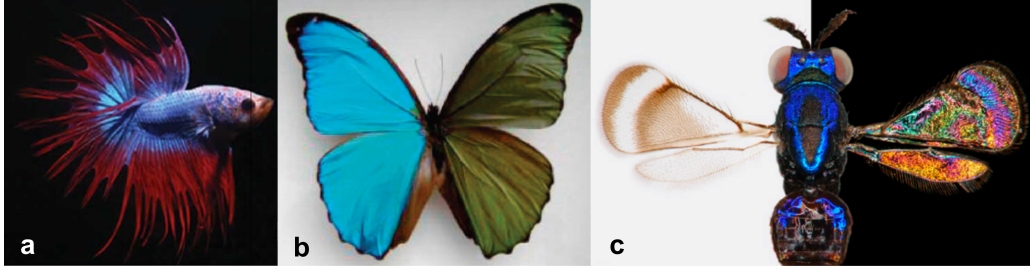


**Figure 3.2** – Structural coloration in nature. Siamese fighting fish (*Betta splendens*) (a), (adapted from reference[31]) a butterfly (*Morpho menelaus*) with blue and green wings (b), (adapted from reference[32]) and an insect (*Closterocerus coffeellae*) with different colored wings (c). Adapted from reference.[33] Different coloration of the wings in (c) arises from the light reflecting white background compared to light absorbing black background. The color impressions originate from periodic microstructures.

on YSZ increased the oxidation resistance of the TBC by preventing infiltration of oxygen through the YSZ layer.

Thus, the first part of this dissertation examines the impact of  $\text{Al}_2\text{O}_3$ -encapsulation by post-synthetic modification and ALD on the temperature stability of  $\text{ZrO}_2$  and YSZ microparticles for potential application as TBC.

Besides reflection in the infrared region, photonic glasses of zirconia submicron particles could also be used to achieve reflection in the visible range as it is needed for structural colors. In nature, many plants and animals use periodic dielectric structures to obtain bright colors in the visible wavelength range. Fig. 3.2 shows three exemplary photographs from structural coloration in nature. Here, the coloration of a Siamese fighting fish (*Betta splendens*, a), a blue butterfly (*Morpho menelaus*, b), and an insect (*Closterocerus coffeellae*, c) originates from periodic microstructures.

As known from nature for different types of periodic structures, the reflection band is proportional to the size of the periodic microstructure. In the case of spherical particles it is proportional to its particle size. Thus, a decrease in particle diameter from the micrometer to the submicrometer range is needed for a reflection in the visible range.[6] Furthermore, structural colors as an alternative to commercial pigment-based colors, which sometimes still contain toxic materials (such as cadmium-based pigments[34]), need a specific refractive index distribution.[35, 36]

### 3 Introduction

Core@shell particles with different refractive indices meet this requirement as they represent a novel class of functional materials with numerous prospective applications apart from structural coloration.[6, 24, 37] They are also well-suited for applications, such as catalysis,[38–44] high performance liquid chromatography,[45–47] as well as biomedical diagnosis and therapy.[43, 44, 48–52] Additionally, they are highly promising candidates for the development of advanced optical materials, which are needed, e.g., for thermophotovoltaic (TPV) systems[13, 53] and photonic displays.[54] Among the broad variety of core@shell particles studied to date, especially those consisting of ceramic materials are very robust and suitable for applications in hostile chemical environments or at elevated processing and operating temperatures.

Inorganic cores such as zirconia submicron particles encapsulated by silica shells are probably one of the most widely studied types of core@shell particles. Silica coatings can be grown on various inorganic materials, including metals,[52, 55] semiconductors,[49] and high band gap metal oxides.[7, 56, 57] Usually, the Stöber method[58] is adapted to grow silica shells with well-controlled thicknesses. In general, silica encapsulation decreases the particles' initial polydispersity and surface roughness. Furthermore, silica is optically transparent and has good mechanical, chemical, and thermal stability. Using well-established silane coupling chemistry, the silica shells can easily be functionalized and bioconjugated, as already shown, e.g., for fluorescent nanodiamonds and magnetic nanoparticles.[48, 49] In other examples, gold nanoparticles have been coated with silica shells of varying thicknesses to tune the optical properties of thin films assembled from these particles.[59] Further, photonic display pixels have been fabricated using silica encapsulated iron oxide nanoparticles.[60]

The sol-gel synthesis of  $\text{ZrO}_2@\text{SiO}_2$  core@shell nanoparticles has been reported in previous works by Bai *et al.*[56] and Yang *et al.*[7] They proposed applications of these particles for the self-assembly-based fabrication of functional optical devices and coatings with adjustable refractive indices. In another study, zirconia nanoparticles were silica coated to enable their surface functionalization via silane coupling chemistry.[61] The modified zirconia particles were then used to provide quartz fiber reinforced composites with radiopacity. However, the thermal stability of such  $\text{ZrO}_2@\text{SiO}_2$  core@shell particles has not been explored so far.

When heated to several hundred degree centigrade, sol-gel derived zirconia submicron particles shrink significantly and transition, first, from the amorphous into the metastable tetragonal (t) phase and, later, into the stable monoclinic (m) phase.[1, 62, 63] These transformations are associated with significant grain coarsening and the t→m transition is accompanied by a 5% volume increase of formed crystallites.[64] As a result, submicron zirconia particles disintegrate after calcining at 850 °C.[1] However, since earlier studies have shown an improved phase stability in sol-gel derived ZrO<sub>2</sub>-SiO<sub>2</sub> mixed oxides,[65, 66] it is conceivable that silica encapsulation may significantly improve the thermal stability of zirconia submicron particles.

Thus, the objective in the second part of the present study was to characterize the thermal stability of ZrO<sub>2</sub>@SiO<sub>2</sub> core@shell submicron particles. This study also offers some important insights into the link between the core@shell structure of YSZ@SiO<sub>2</sub> particles and the appearance of the reflection band in the visible range yielding structural coloration.

Among potential TBC and SC applications, ZrO<sub>2</sub> and YSZ microparticles are promising materials as high-temperature stable absorber/emitter in TPV systems. The requirements for effective TPV systems are high absorption/emission at short wavelengths (1–2 μm) and low absorption/emission at longer wavelengths (> 2 μm). Previous research by Dyachenko *et al.*[14] showed that a monolayer of ZrO<sub>2</sub> submicron particles on a tungsten substrate exhibits the desired optical properties even after temperature treatment up to 1000 °C. Nevertheless, higher temperatures destroyed the tungsten substrate due to chemical reactions with the underlying silicon substrate.

Thus, the objective of a sub-project in the present study was to synthesize YSZ microparticles with the desired average particle diameter of  $D \sim 1 \mu\text{m}$  after calcination for potential application as absorber/emitter in TPVs. Furthermore, the optical properties of YSZ monolayers on improved tungsten substrates after heat treatment up to 1400 °C (6 h, vacuum) were investigated.



# 4 Theory

## 4.1 Photonic structures

In recent years, there has been an increasing interest in the optical properties of natural materials and on synthetic approaches to mimic these optical properties or to modify them.[31, 33, 67–71] These so called photonic structures are the optical analog to semiconductor materials.

In the case of photonic structures, periodicity in dielectric constants leads to forbidden frequencies of incident photons, which is called photonic band gap.[72] Photons with such energies cannot propagate through the material due to Bragg scattering from differences in refractive indices. The spectral range of the photonic band gap thereby is determined by the refractive index of the different media and the length scale of the motif. Therefore, the size of the motif directly determines the wavelength range of the photonic band gap. Consequently, photonic structures with a dielectric variation in the micrometer range would cause a photonic band gap in the infrared (IR) range, while submicron dielectric arrangements yield a band gap in the visible range.[6]

Using photons (light) as information carrier has several advantages compared to electrons. Light can travel much faster in a dielectric material compared to electrons in a semiconductor. Furthermore, photons can carry a larger amount of information per second and do not strongly interact with each other as electrons do. As a result, the energy loss is reduced.[72] Photonic structures are already essential for a wide range of technologies such as telecommunications in industry, laser engineering, high-speed computing, and spectroscopy.[73] A growing body of the literature recognizes the importance and potential of these structures for new technological developments. Here, the aim is to design new structures, which interact with light waves over a desired range of frequencies by perfectly reflecting

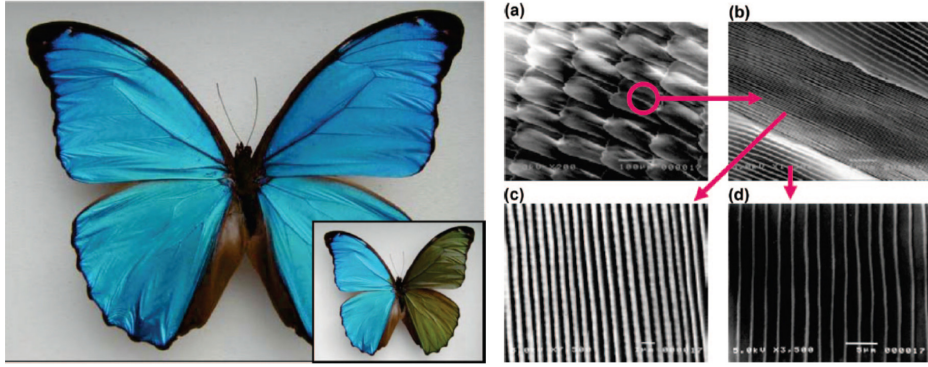


**Figure 4.1** – Photograph of a *Morpho menelaus* butterfly (left). Inset, the right wing of the butterfly is wetted with ethanol. The change in the refractive index induces the color change from blue to green. SEM images of the wing (right): low magnification (a), high magnification (b), ground scales (c), and cover scales (d). Figure and caption adapted from reference.[32]

them, or allowing them to propagate only in certain directions, or confining them within a specified volume.[73]

Periodic dielectric structures are inspired by nature, where large amounts of plants and animals with photonic structures in the visible wavelength range are known for a long time.[71] One of the most well-known species is the *Morpho menelaus* butterfly (see Fig. 4.1). Its blue color originates from the diffraction of light and interference effects due to the presence of microstructures on its wings.[32] Filling the air holes in the right wing with ethanol leads to a green color impression due to the change of the refractive index as shown in Figure 4.1 (left, inset). The periodic microstructures in the butterfly wings mainly consist of chitin. SEM images of different magnifications can be found in Figure 4.1 (right). There are numerous other examples in nature such as beetles, moths, sea mice, and various bird species.[68, 70, 74]

These remarkable properties and their high potential for optical applications have gained great interest of the scientific community, aiming for a more profound understanding of these structures. For this purpose, two different types of photonic structures need to be differentiated, i.e., ordered (photonic crystal, PC) and disordered (photonic glass, PG) structures as schematically shown in Figure 4.2. Both arrangements can be produced in a direct or indirect manner. The optical properties of the various photonic structures are quite different. In the case of a photonic crystal, narrow and angle-dependent reflectivity can be achieved, while photonic

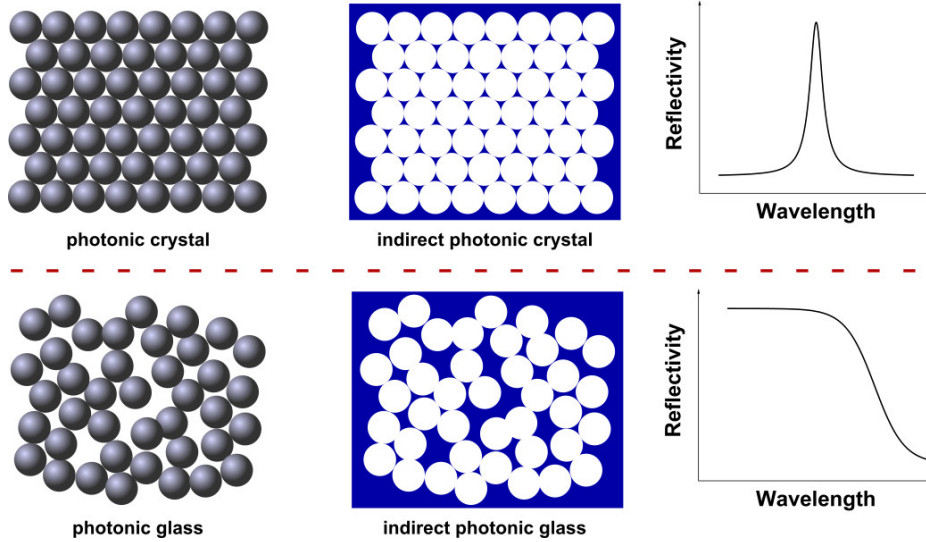


**Figure 4.2** – Schematic drawings of a photonic crystal, a photonic glass, their indirect analogs, and optical properties. The photonic crystal shows a narrow and angle-dependent reflectivity, while the photonic glass exhibits an angle-independent broadband reflection.

glasses yield angle-independent broadband reflection. Further details will be discussed in the following sections.

#### 4.1.1 Photonic crystals

Photonic crystals are characterized by a periodic arrangement of dielectric structures, consisting of at least one high refractive and one low refractive index material. This construction of a low-loss periodic dielectric medium allows optical control and manipulation of light. Thus, preventing light with certain frequencies from propagating in certain directions can be achieved by PCs with specific photonic band gaps. These frequencies are tuneable in a wide range as they only depend on the dimensions of the photonic structure and the refractive constants.[73] To calculate the wavelength of the predicted (right) reflection edge at longer wavelengths, the Fresnel equation is used as an approximation:[75]

$$\lambda_e = 2 \cdot n_{\text{eff}} \cdot d \quad (4.1)$$

## 4 Theory

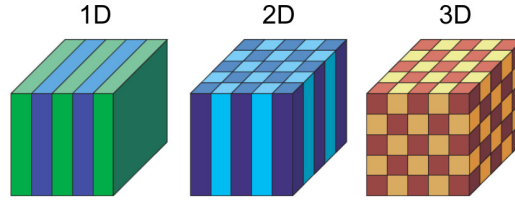


**Figure 4.3** – Examples of one-(1D, left), two-(2D, middle), and three-dimensional (3D, right) photonic crystals. Different colors represent materials with different refractive indices. Each photonic crystal has a periodicity of the dielectric material in  $x$ -dimensions ( $x$ D). Figure and caption adapted from reference.[73]

Here,  $\lambda_e$  is the approximated wavelength of right reflection edge,  $n_{\text{eff}}$  is the effective refractive index, and  $d$  is the period of the motif (distance between neighboring repeating units).[75] In general, the Fresnel equation describes the behavior of light waves, which move through the interface between two media with different refractive indices.

The simplest one-dimensional (1D) PC is a stacked multilayer film consisting of two materials with different dielectric constants as shown in Figure 4.3 (left). Various studies analyzed the optical properties of multilayer films such as that conducted by Lord Rayleigh (1917), who published a photonic structure called Bragg-mirror as one of the first studies.[76] In this 1D case, a plane incident light wave propagates through the dielectric material and is thereby reflected and refracted multiple times at each interface. Here, traveling waves can experience constructive or destructive interference by creating a standing wave of frequencies fulfilling the Bragg-condition. In this energy regime, which is called the photonic band gap, electromagnetic waves cannot propagate through the PC. As a result, the 1D photonic crystal acts as a perfect reflector for the corresponding wavelength range.

For alternating materials of low and high refractive index in two or three dimensions, two-dimensional (2D) or three-dimensional (3D) photonic crystals are obtained as shown in Figure 4.3. In the 2D case, the PC is periodic along the  $x$ - and  $y$ -axes and homogeneous along the  $z$ -axes. Unlike the multilayer 1D film, this 2D PC can prevent light from propagation in any direction within the  $xy$ -plane. 3D photonic crystals have the potential to achieve a complete photonic band gap by preventing light propagation for a specific range of frequencies for all three dimensions.[73]

Besides theoretical predictions and simulations of different photonic crystal structures, fabrication of such 3D structures remains the major challenge. The literature on production methods has highlighted several techniques to control surface roughness, lattice constants in all three dimensions, size distribution, etc.[54, 72, 73, 77–79] The fabrication strategies include both top-down and bottom-up approaches. Top-down methods such as lithography are time-consuming and require costly devices. In addition, they have limitations on the fabrication of 3D PCs especially in the visible and near infrared (NIR) range.[54]

More recent attention has focused on self-assembly processes of colloids as bottom-up approaches. As colloids, nano- and microparticles are used, which are suspended in a gas or liquid phase. Much of the current literature on materials for fabrication of PCs pays particular attention to inorganic materials as these high refractive index materials provide a better photonic band gap performance, while creating higher scattering rates at the same time.[78] Here, colloidal systems, which consist of nano- and micro-sized particles suspended in a liquid or a gas, are investigated by many research groups. There are numerous approaches to assemble such particles. Previous research has established self-assembly methods such as simple sedimentation,[78] Langmuir-Blodgett method,[80] evaporation-assisted deposition,[81] and direct assembly techniques.[82] In the case of sedimentation, electric[83] and magnetic[84] effects play a key role.

For a complete photonic band gap, inverse/indirect photonic crystals with high porosity and therefore, high refractive index contrast are needed.[85] It has been demonstrated that indirect photonic structures can be fabricated by deposition of a direct photonic crystal with template particles such as silica or polymer spheres, which will be removed by chemical etching or burnout after infiltration with the desired material.[78] The infiltration can be achieved by wet chemistry methods comprising chemical bath deposition, electrodeposition, and dry methods like chemical vapor deposition. Furthermore, infiltration with a nanoparticle suspension or injection of a molten substance are also conceivable. The obtained indirect PCs may find application in sensors, super-refractive devices, and as templates to grow spherical particles in their pore networks.[78]

### 4.1.2 Photonic glasses

In contrast to photonic crystals, which are highly ordered and periodic structures, photonic glasses are disordered (randomly packed) structures (see Fig. 4.2). Photonic crystals reveal a short- and long-range order yielding iridescent color impressions.[31, 77] Hence, PCs show varying colors depending on the viewing and illumination angle due to their photonic band gap. On the contrary, most PGs only exhibit a short-range order yielding non-iridescent color impressions and broadband reflections, which are independent of the viewing angle.[54, 86]

The construct of photonic glasses was first articulated by Garcia *et al.*[87] and popularized in his study, where two different growth methods of PGs have been explained. First, PGs were obtained by using colloidal charge interactions (sphere-sphere repulsive potential) of monodisperse polystyrene (PS) spheres yielding very thick and randomly packed samples. Second, an alloy colloidal crystal was obtained from a suspension of PS and polymethyl methacrylate (PMMA) spheres. Afterwards, the PS spheres were selectively etched by dissolving them in cyclohexane to deposit a disordered film. Further investigations demonstrated that the formation of PGs from colloidal suspensions of PS spheres ( $D = 1.2 \mu\text{m}$ ) can be controlled by changing the electrolyte concentration.[88] The higher the electrolyte concentration, the larger the formed particle clusters, which influence the optical properties of the obtained PGs.

Disordered PGs have various promising optical properties such as coherent backscattering enhancement (of laser[89] and visible light[90]), Anderson localization of light[91–95], and random lasing.[96] Anderson localization describes the absence of electron wave diffusion in a disordered medium.[91, 92] Overall, the disordered nature of photonic glasses yields a high diffuse reflection over a broad wavelength range.[21] To calculate the predicted broadband reflection wavelength range, the Fresnel equation is also used as an approximation (already described for photonic crystals, see Section 4.1.1). In contrast to PCs, PGs exhibit a broadband reflection starting from the calculated right reflection edge to shorter wavelengths due to multiple scattering. In the case of PGs, the parameter  $d$  from Fresnel equation does not represent the period of the motif as PGs are disordered structures. Here,  $d$  is the average straight plane to plane distance, if the imagined planes lie on the centers of the neighboring particles from the PG.

Equivalently to PCs, direct and indirect/inverse PGs can be produced.[87, 88] A recent study by do Rosário *et al.*[97] involved a colloidal and single-step deposition of yttria-stabilized (YSZ)-inverse photonic glasses. Therefore, heterocoagulation of negatively charged PS spheres and positively charged YSZ nanoparticles was performed. Afterwards, the PS spheres were burned out leaving behind a disordered inverse PG of a YSZ network. As a result, broadband reflection of  $\sim 70\%$  in the wavelength range of 0.4–2.2  $\mu\text{m}$  and high-temperature stability up to 1200  $^{\circ}\text{C}$  were achieved.

PGs made from monodisperse ceramic spheres are highly interesting materials for application as broadband visible reflectors, structural colors (SC), and thermal barrier coatings (TBC). More recent attention has focused on the application of PGs from  $\text{ZrO}_2$ [21] and YSZ[2] microparticles as high-temperature stable TBCs with broadband reflection in the wavelength range from 1–5  $\mu\text{m}$ . Furthermore, lots of previous research into PGs has focused on structural colors. Takeoka *et al.*[98] and Harun-Ur-Rashid[23] demonstrated that colloidal amorphous arrays show desirable optical properties such as angle-independent color. Moreover, it has been shown that structural colors can be achieved by self-assembly of colloidal polymer nanoparticles[99] and by using artificial 3D macroporous  $\text{SiO}_2$  and  $\text{TiO}_2$  structures[67] or by deposition of a dielectric multilayer on top of a silica microsphere base layer.[100] Besides, Shang *et al.*[6] pointed out by theoretical predictions and numerical simulations that PGs from core@shell particles (diameter: 100–300 nm) with a non-monotonous refractive index distribution are promising candidates for structural coloration.

## 4.2 Zirconia

Zirconium dioxide ( $\text{ZrO}_2$ , zirconia) has emerged as one of the most powerful ceramics for industrial processes. Traditionally,  $\text{ZrO}_2$  and  $\text{ZrO}_2$ -containing materials have been used for foundry sands and flours, refractory ceramics and abrasives.[101] Due to its outstanding properties such as chemical inertness and high oxygen conduction[1]  $\text{ZrO}_2$  ceramics are also used in fuel cells,[8, 102] catalysts,[11, 103, 104] and sensors.[9, 10] Furthermore, it has a high thermal[1] and mechanical stability,[4, 5] which opens up a wide range of technologies such as high-performance liquid chromatography[12] and high-temperature applications, including

## 4 Theory

absorber/emitter in thermophotovoltaics[13] and TBCs.[1–3, 19, 20] Recently, researchers have shown an increased interest in  $\text{ZrO}_2$  as structural colors[6, 22, 23] and jewelry as zirconia offers excellent optical properties due to its high refractive index.

This section will address the properties of zirconia ceramics with regard to high-temperature applications, whereby the martensitic tetragonal-to-monoclinic (t→m) phase transformation and the accompanying volume expansion of ~5% are the limiting factors for the high-temperature stability of undoped  $\text{ZrO}_2$  ceramics.[64, 105]

### 4.2.1 Crystalline phases

Bulk zirconia crystallizes in three different polymorphs as shown in Fig. 4.4. At room temperature and ambient pressure, the monoclinic (space group:  $P2_1/c$ , Fig. 4.4(c)) structure is the thermodynamically stable structure of zirconia, which is a distortion of the parent cubic fluorite structure.[106] Upon heating, zirconia transforms to the high-temperature stable tetragonal ( $P4_2/nmc$ , Fig. 4.4(b)) phase at ~1200 °C, before transition to the cubic ( $Fm\bar{3}m$ , Fig. 4.4(a)) structure at temperatures >2370 °C (melting point: ~2750 °C).[64, 105] The cubic structure consists of an alternate stacking of full and empty cubes, with  $\text{O}^{2-}$  anions (Fig. 4.4(c, blue)) at each corner and a  $\text{Zr}^{4+}$  cation (Fig. 4.4(c, red)) in the middle of each cube.[106] The cations are surrounded by eight anions (at each corner of the cube), while the anions are surrounded by four cations. Anion sublattice distortion of the cubic phase leads to the tetragonal phase, whereby further distortion creates the monoclinic phase with a reduced cation coordination number of seven.[106]

Of particular concern is the martensitic t→m phase transformation upon cooling below ~950 °C, which is diffusionless in nature and accompanied by a volume expansion of ~5% and a shear strain of 10–16%.[64, 105, 107] Leading to a catastrophic material failure upon cooling, this is a major drawback of undoped bulk zirconia. To overcome this, stabilizers such as Y can be added to zirconia as it will be discussed in Section 4.2.3.

In striking contrast to bulk zirconia, nano- and microsized zirconia, e.g., sol-gel fabricated, crystallize in the tetragonal phase at first upon heating. The tetragonal phase is only high-temperature stable for fine-grained zirconia and transforms

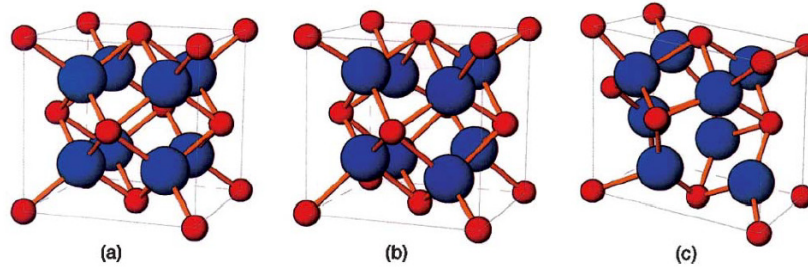


**Figure 4.4** – Schematic representation of the three polymorphs of  $\text{ZrO}_2$  with  $\text{Zr}^{4+}$  cations (red) and  $\text{O}^{2-}$  anions (blue): cubic (space group:  $Fm\bar{3}m$ , a), tetragonal ( $P4_2/nmc$ , b), and monoclinic ( $P2_1/c$ , c). Figure adopted and caption adapted from reference.[106]

into monoclinic phase during cooling.[106] There are likely two main reasons for this difference in crystallization behavior between bulk and nanophase zirconia. First, the initial transition to the tetragonal phase is attributed to the local coordination environment and short-range order in the amorphous phase that is more similar to the tetragonal than the monoclinic polymorph.[63, 101, 108–111] Thus, the initial crystallization yields the tetragonal phase. The thermodynamically stable monoclinic phase is formed only after heating to higher temperatures. Second, high-temperature oxide melt solution calorimetry confirmed the hypothesis that fine-grained monoclinic  $\text{ZrO}_2$  has the largest surface enthalpy and amorphous zirconia the smallest, as shown in Fig. 4.5.[112, 113]

The most interesting feature in the graphs in Fig. 4.5 is that there are crossovers between the excess enthalpies of the three zirconia polymorphs with increasing surface area (a) and increasing particles size (b). Overall, these results indicate that the amorphous phase of nanosized zirconia is energetically preferred for grain sizes  $<10$  nm, before transitioning to the tetragonal phase and finally transformation to the monoclinic phase for grain sizes  $>50$  nm (see Fig. 4.5, b).

A much debated question in the literature is the critical grain size, at which nanophase zirconia transforms from the tetragonal to the monoclinic phase.[63, 101, 106, 114] Investigations such as those conducted by Navrotsky *et al.*[106] and Shukla *et al.*[63] have shown that the  $t \rightarrow m$  transformation occurs at grain sizes around  $\sim 40$  nm. On the contrary, Chraska *et al.*[101] observed that zirconia particles undergo a phase transformation when the grain size is in the order of only  $\sim 18$  nm. Differences in the observed critical grain sizes can be explained by considering the nature of the  $\text{ZrO}_2$  particles. For isolated particles, the crossover of

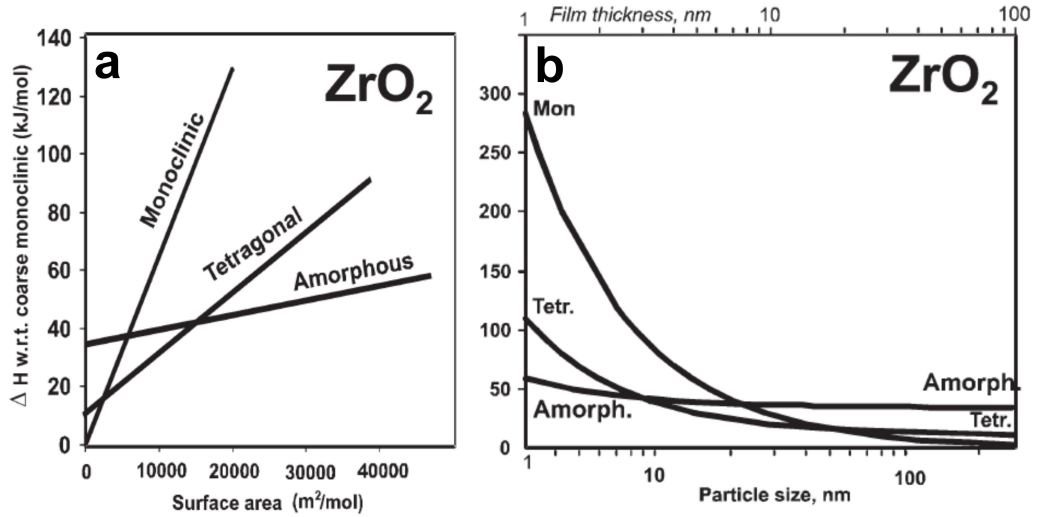


**Figure 4.5** – Excess enthalpy crossovers for amorphous, tetragonal, and monoclinic zirconia. Excess enthalpy of nanophase zirconia plotted versus surface area (a). Excess enthalpy of nanophase zirconia plotted versus particle size (logarithmic scale, b). Figure and caption adapted from reference.[106]

the surface energies between the tetragonal and monoclinic phase exists around  $\sim 10$  nm.[63] For agglomerated zirconia particles, the critical nanosize for the  $t \rightarrow m$  transformation increases due to decreased free surface energy.

A major challenge faced by many researchers is the distinction between the tetragonal and the cubic phase as both have similar cell parameters (see Tab. 4.1).

**Table 4.1** – Polymorphs of  $\text{ZrO}_2$  from the Joint Committee on Powder Diffraction File (JCPDF) Database. [111]

JCPDF no.	phase	space group	$a$ ( $\text{\AA}$ )	$b$ ( $\text{\AA}$ )	$c$ ( $\text{\AA}$ )	$\beta$ (deg)
37-1484	monoclinic	$P2_1/a$	5.3129	5.2125	5.1471	99.218
42-1164	tetragonal	$P4_2/nmc$	3.64		5.27	90
49-1642	cubic	$Fm\bar{3}m$	5.1280			90

Previous research by Srivastava *et al.* found that the cubic phase just exhibits single peaks which show a characteristic splitting in the tetragonal phase, such as (002)(200), (113)(311), (004)(400), and (006)(600) reflexes.[109] For example, Garvie *et al.*[115] used this splitting at high-angle reflexes to differentiate between tetragonal and cubic phase. Furthermore, Miller *et al.*[116, 117] reported a relation

between the tetragonal to cubic ratio and the Y content in YSZ. With increasing Y content, the dominant phase changes from monoclinic to tetragonal and finally to cubic phase, whereby the (400) region was investigated. Similar results were found by Leib *et al.*[2], where the tetragonal phase of zirconia was stabilized by Y contents  $< 10$  wt%, before the cubic phase was formed at higher Y contents. Here, the authors proposed an optimum Y content of 8–10 wt% as the cubic phase at higher Y contents showed increased grain growth compared to the tetragonal phase, which will be discussed in the following section.

#### 4.2.2 Grain growth and sintering

Grain growth and sintering behavior are key aspects for defining the properties of ceramic materials. The grain boundaries control the mechanical properties, including fracture strength, toughness, plastic deformation, and high-temperature stability.[118] Moreover, grain boundary movement influences also the electrical properties, e.g., conductivity and other processes, such as sintering, grain growth, and phase transformations. Therefore, the understanding and control of grain boundary segregation emerge as a powerful platform to optimize the properties of ceramic materials.

Many grain boundary phenomena found in metals can be directly transferred to nonmetals such as ceramics. In both cases, grain boundaries have an interfacial energy and tension, which determine their mobility.[118] Their flexibility in turn can be influenced by impurities from dopants or vacancies. Grain boundaries make a considerable impact on ceramic material properties, because diffusion is often more rapid along grain boundaries. Furthermore, deformation occurs by grain boundary sliding, segregation of solutes occurs at grain boundaries, and grain boundaries act as sinks for lattice imperfections.[118]

A ceramic oxide contains cations and anions, whereby an electrostatic potential forms at the grain boundaries, which strongly depends on impurities and temperature.[118] In the specific case of  $\text{ZrO}_2$ , a higher concentration of positively charged  $\text{O}^{2-}$  vacancies is found at the grain boundary due to a lower anion vacancy formation energy compared to cations.[119] Consequently,  $\text{Zr}^{4+}$  vacancies form in close proximity to the grain boundary maintaining the neutral character of the bulk material. As a result, the zirconia grain boundaries are positively charged surrounded by a negatively space-charge cloud.

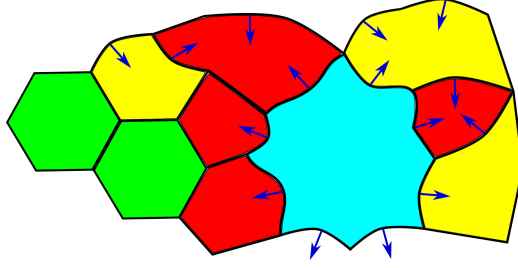


**Figure 4.6** – Schematic 2D illustration of different-shaped grains in a ceramic material. Grains with only  $120^\circ$  angles, which neither grow nor shrink (green), shrinking grains with less than six adjacent grains (red, convex grain boundaries), growing grains with more than six adjacent grains (blue, concave grain boundaries), and grains with both convex and concave grain boundaries (yellow).

The main driving force for grain growth in ceramic materials is the reduction of grain boundary energy.[120] Therefore, some grains grow and some grains shrink as shown in Fig. 4.6. At this grain growth process, the number of grains shrinks, while the average grain size increases.[119, 120] There are different types of grains: Equal grain boundary energies lead to grains with one or more  $120^\circ$  angles (green for only  $120^\circ$  grain boundaries), where no grain boundary movement will occur. Grains with less than six adjacent grains exhibit convex grain boundaries (red), which shrink. Grains with more than six adjacent grains exhibit concave grain boundaries (blue), which grow, and grains with both convex and concave grain boundaries (yellow).

At a grain boundary, individual atoms from the shrinking grains have to change their orientation by jumping across the grain boundary to the growing grain.[119] This atomic diffusivity ( $D_b$ ) in the grain boundary is the limiting factor for grain mobility ( $M$ ), which is described in the following equation:[121]

$$M = \frac{D_b \Omega}{kT \delta_b} \quad (4.2)$$

Here,  $\Omega$  is the atomic volume,  $k$  is the Boltzmann constant,  $T$  is the temperature, and  $\delta_b$  is the grain boundary thickness.[121] As  $D_b$  can be expressed by an Arrhenius term, it is strongly dependent on the temperature. Therefore, the grain boundary mobility ( $M$ ) increases with increasing temperature. Growing grain sizes and expanding porosity of ceramic materials due to sintering processes at higher temperatures lead to a destabilization of the material structure as shown

by Schwenger *et al.*[5] for  $\text{ZrO}_2$  microparticles in microcompression experiments. This inverse relationship between the mechanical properties (yield stress) and grain size of a ceramic material is known as the Hall-Petch effect.[122]

Crystallite sizes (grain sizes) can be determined from XRD data using the Scherrer equation (see Eq. 4.3).[123] The full width  $w$  at half maximum (FWHM) can be obtained by fitting Lorentzians to the peaks of the X-ray diffractograms. For this purpose, usually the (101) reflex of the tetragonal phase and the (-111) reflex of the monoclinic phase are used. In the case of mixed phases, Lorentzians are fitted to both reflexes and additionally to the monoclinic (111) reflex.

$$L = \frac{K\lambda}{(w - b)\cos\theta_0} \frac{180^\circ}{\pi} \quad (4.3)$$

In Eq. 4.3,  $L$  is the crystallite size,  $K$  the dimensionless shape factor ( $K \approx 1$  for spherical grains),  $\lambda$  is the wavelength of the radiation ( $\text{Cu-K}\alpha = 0.154 \text{ nm}$  for our XRD equipment),  $w$  is the measured FWHM (in degree),  $b$  is the instrumental broadening (needs to be determined for each instrument,  $b = 0.06^\circ$  for our XRD equipment), and  $\theta_0$  is the Bragg angle.[123]

The next section of this dissertation discusses the stabilization of the tetragonal phase and grain growth inhibition of zirconia by introducing lower-valence dopants.

### 4.2.3 Phase stabilization and grain growth inhibition

The main disadvantage of pure zirconia is the diffusionless martensitic t→m phase transformation which is accompanied by a volume expansion (see Section 4.2.1). Furthermore, progressive grain growth limits the use of undoped zirconia in high-temperature applications (see Section 4.2.2). To overcome these obstacles, doping of  $\text{ZrO}_2$  with different aliovalent cations has gained a broad attention in the literature.

In general, the addition of lower-valence oxides such as  $\text{CaO}$ ,  $\text{MgO}$ , or  $\text{Y}_2\text{O}_3$  stabilizes the more symmetric tetragonal and cubic phases compared to monoclinic phase, whereby an increasing dopant concentration leads first to a tetragonal prime phase ( $t'$ ) and than to a cubic form.[124] The stabilization effects and amounts of

## 4 Theory

dopants differ among each other. Hwang and Chen[125] concluded in their extensive study that divalent and trivalent stabilizers in tetragonal zirconia segregate to the grain boundaries regardless of the ionic size and solubility due to the positively charged grain boundaries (compare Section 4.2.2). Furthermore, they suggested that grain boundary mobility is mainly controlled by the space charge segregation of di- and trivalent solutes and also by lattice diffusivities of the solutes. In their study, they investigated grain growth kinetics and grain boundary segregation of tetragonal zirconia containing 12 mol% CeO<sub>2</sub> and 1 mol% oxides of di- to pentavalent cationic dopants as depicted in Tab. 4.2.

**Table 4.2** – Ionic radii of different di- to pentavalent dopants[126] and grain sizes of tetragonal zirconia containing 12 mol% CeO<sub>2</sub> and 1 mol% oxides of di- to pentavalent cationic dopants. Adapt from references.[125, 126]

Dopant	Ca <sup>2+</sup>	Mg <sup>2+</sup>	Y <sup>3+</sup>	Yb <sup>3+</sup>	In <sup>3+</sup>	Sc <sup>3+</sup>	Ce <sup>4+</sup>	Ti <sup>4+</sup>	Ta <sup>5+</sup>	Nb <sup>5+</sup>
Ionic radius (pm)	112	89	102	99	92	87	97	74	74	74
Grain size (μm)	1.04	1.56	1.75	1.86	2.15	2.36	2.93	3.03	3.20	3.29

There are two main conclusions arising from the data in Tab. 4.2. First, solutes of lower valence are correlated with smaller grain sizes. Second, within the same valence, dopants of a larger ionic radius are also correlated with smaller grain sizes.[125]

One of the most common crystalline phase stabilizers for ZrO<sub>2</sub> is yttria (Y<sub>2</sub>O<sub>3</sub>). Yttria-stabilized zirconia has numerous commercial applications such as high-temperature stable TBCs.[29, 127, 128] Yttria has a large solid solubility range in zirconia and can be used to stabilize the tetragonal phase of (Y<sub>2</sub>O<sub>3</sub>)<sub>x</sub>(ZrO<sub>2</sub>)<sub>1-x</sub> over the composition range of 0.02 < x < 0.09 and the cubic phase in range of 0.04 < x < 0.4.[129] The reason for tetragonal or cubic phase stabilization is the exchange of some Zr<sup>4+</sup> ions by Y<sup>3+</sup> ions, which leads to a distortion or a crystal relaxation, respectively, as shown in Fig. 4.7.[124] Here, an oxygen vacancy (white) is in the center of a fluorite lattice, which forces the neighboring Zr<sup>4+</sup> ions (black) to shift away from the O<sup>2-</sup> vacancy along the ⟨111⟩ directions. The O<sup>2-</sup> ions move simultaneously towards the O<sup>2-</sup> vacancy along the ⟨100⟩ directions. Due to differ-

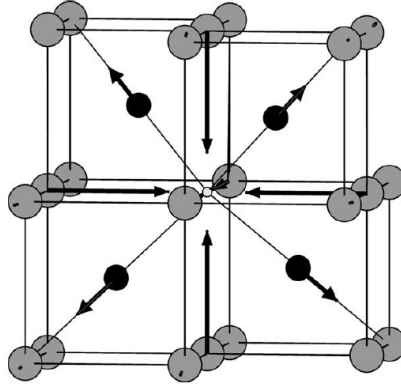


**Figure 4.7** – Crystal relaxation/distortion of  $Zr^{4+}$  ions (black) and  $O^{2-}$  ions (grey) in a fluorite lattice of YSZ in neighborhood of an oxygen vacancy (center, white). Figure adopted and caption adapted from reference.[124]

ent valence, oxygen vacancies ( $O^{2-}$ ) form, whereby every two Y atoms create one  $O^{2-}$  vacancy.[124] According to Li *et al.*,[130] the  $Y^{3+}$  ions have a composition-independent eight-fold coordination in both tetragonal and cubic phase. Therefore, dopants are on average the next nearest neighbors (NNN) to the  $O^{2-}$  vacancy.[124] As a consequence, the average coordination number of  $Zr^{4+}$  ions is reduced from eight towards seven.

Furthermore, it has been shown in the literature that yttria doping of zirconia leads to decreased grain growth by the solute drag effect[27] and thereby forming Y-rich phases at the grain boundaries and Y-lean areas inside the grains. The grain growth inhibition is more pronounced for the tetragonal compared to the cubic phase as the number of oxygen vacancies is higher in the cubic phase. A larger amount of yttria in the cubic system yields an increased mass transport and enhanced grain growth.

To date, several studies have also investigated the influence of an alumina doping (also discussed as shell material in Section 4.4) on phase stability and grain growth inhibition of zirconia. For example, Srdic *et al.*[131] found that grain growth is effectively suppressed by the addition of 3-30 mol% alumina to nanosized powders of zirconia from chemical vapor deposition. In this study, dense or mesoporous (depending on alumina content) zirconia ceramics of small and narrowly distributed grains and pore sizes in the nanometer scale were obtained by using pressureless vacuum sintering at a temperature of 1000 °C (1h). Furthermore, Nazeri and Qadri[132] deposited thin  $ZrO_2-Al_2O_3$  films (7% Al) on different substrates by

## 4 Theory

sol-gel processing. The deposited films were amorphous and crystallized in the cubic phase during annealing at 600 °C (1 h). The observed grain growth inhibition was attributed to constraint effects of alumina on zirconia grains, which yielded peeling-free films without spallation failure. Previous studies by Allemann *et al.*[133] have also demonstrated that Al segregates in zirconia during the sintering processes forming precipitations at the grain boundaries which efficiently suppress grain growth. In that study, it was identified that small alumina concentrations increase grain growth in zirconia, while considerable amounts are needed for grain growth inhibition.

As silica encapsulation of zirconia spheres is also one objective of this dissertation (see Section 4.4), Si-doping should be considered. In the literature, the possibility of Si-doping in zirconia has been discussed controversially. On the one hand, Kajihara *et al.*[134] investigated the superelastic flow in 5 wt% silica-doped tetragonal zirconia and determined that the matter transport across grain boundaries was suppressed by the SiO<sub>2</sub> phase and thereby grain growth was inhibited. Ikuhara *et al.*[135] noticed a similar behavior of superplastic Si-doped tetragonal zirconia. Here, grain growth and mass transport in zirconia were inhibited by dissolved Si ions in the tetragonal zirconia lattice near the grain boundaries and by Si segregation across the grain boundaries. On the other hand, Guo *et al.*[136] did not observe any silicon grain boundary segregation in 8 mol% YSZ, but they found that silica forms vitreous pockets of glassy phase at the triple grain junctions, whereby the grain boundary blocking effect from this Si phase is negligible. Moreover, Gremillard *et al.*[137] investigated the effects of small silica additions on the microstructures and mechanical properties of 3 mol% YSZ. By analysis of 0 to 2.5 wt% silica-doped YSZ via TEM, SEM, and XRD, silica was also found at triple grain junctions, but neither at grain boundaries nor in the lattice. Allemann *et al.*[133], who also investigated Al-doped zirconia (see above), proposed that small amounts of silica decrease the grain growth, probably by forming ZrSiO<sub>4</sub>, while large amounts do the opposite.

The next section of this work discusses the synthetic approaches of spherical nano- and microsized zirconia particles and the state of knowledge concerning sintering, grain growth, and doping.

## 4.3 Zirconia particles

Over the last decades, zirconia micro- and submicron particles have gained substantial attention due to their outstanding mechanical, thermal, and optical properties, which make them promising materials for a wide range of potential applications as specified in Section 3. Different methods have been proposed in the literature to synthesize monodisperse, spherical zirconia micro- and submicron particles. For example, using alkoxides in sol-gel synthesis or polymer-induced aggregation of colloids and aerosol-gel syntheses in low temperature flames. In the sol-gel synthesis, zirconia particles of different sizes can be obtained by the controlled reaction of water, zirconium precursors and stabilizers.

The following sections will give an overview of different strategies to synthesize zirconia particles, their high-temperature stability, and their modifications by doping. As there is a growing body of the literature regarding zirconia particle synthesis, the focus will be on methods, which are relevant to this dissertation.

### 4.3.1 Synthetic approaches

There are numerous methods available for synthesizing zirconia micro- and submicron particles or nanoparticles. Fegley and Barringer[138] were the first to report a sol-gel method to produce monodisperse  $\text{TiO}_2$ ,  $\text{SiO}_2$ ,  $\text{ZrO}_2$ , and  $\text{ZrO}_2\text{-Al}_2\text{O}_3$  powders by controlled alkoxide hydrolysis reactions. One year later, they improved their size distributions and particle shapes yielding 0.2  $\mu\text{m}$  monodisperse (standard deviations: 17–26%) spheroidal  $\text{ZrO}_2$  and YSZ particles.[139] In previous studies by our group, a sol-gel method to produce undoped  $\text{ZrO}_2$  and YSZ particles in the size range of 0.8 to 4.2  $\mu\text{m}$  by using fatty acids as stabilizers was reported.[1] For the purpose of the desired particle sizes in this dissertation, the work was based on a modification of the general method of Widoniak *et al.*[62] for particles with diameters in the submicron range and on comprehensive studies of Yan *et al.*[140] for larger particles in the micrometer range, which were both the basis for the aforementioned studies by Leib *et al.*[1]

Earlier works[62] used alkali halide salts, which lead to ionic impurities after calcination and an affected crystallization behavior, whereas fatty acids as stabilizers

#### 4 Theory

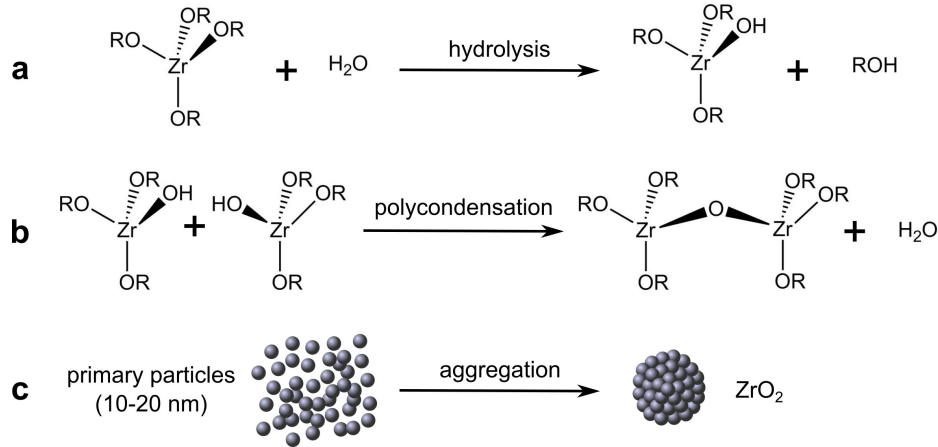


**Figure 4.8** – Sol-gel synthesis of zirconia ( $\text{ZrO}_2$ ) particles. First, the zirconium alkoxide precursor  $\text{Zr}(\text{OR})_4$  with R as propyl or butyl, respectively, gets hydrolysed by water (a). Second, polycondensation of two partially hydrolyzed zirconium alkoxides occurs (b). Finally, small primary particles (10–20 nm) aggregate to zirconia submicron or microparticles depending on the synthesis conditions (c).

can easily be removed by heat treatment. Moreover, previous research has established that the polymer hydroxypropylcellulose (HPC) could be used in sol-gel processes as stabilizer for powder and nanoparticle synthesis, which was already shown in numerous publications for example for  $\text{TiO}_2$ [141] and  $\text{ZrO}_2$ [142] powders or ZnS nanoparticles.[143] In these studies, HPC seems to favor the stabilization of relatively small particles.[144]

The literature of zirconia microparticles has highlighted several growth mechanisms, but it is generally accepted that the zirconia alkoxide precursor first hydrolyses and polycondensates (see Fig. 4.8(a,b)), before it forms small primary particles in the size range of 10 to 20 nm. These primary particles tend to aggregate to form the final zirconia particles (c). In contrast, Lerot *et al.*[145] suggested a LaMer-type formation mechanism, where nuclei grow individually to their final size without any further delayed nucleation. Studies by Ogihara *et al.*[146] supported these findings as they showed that the rate-determining step of surface nucleation in zirconia particle growth was polynuclear-layer growth. This means that each layer is formed by merging of surface nuclei on zirconia particles.

Lerot *et al.*[145] established a new sol-gel method to produce monodisperse spherical zirconia particles in the size range of 0.1 to 2.5  $\mu\text{m}$  by using various long-chain carboxylic acids as stabilizers. As a general rule, they postulated that the particle

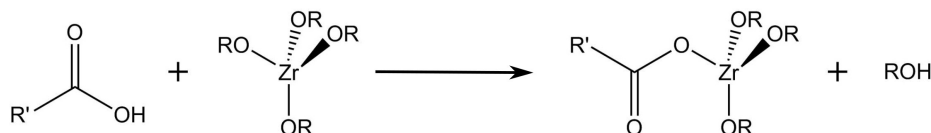


**Figure 4.9** – Reaction of carboxylic acid stabilizer with zirconium alkoxide to form a zirconium carboxy-alkoxide derivate. R denotes a propyl or butyl chain, while R' stands for the alkyl chain of the carboxylic acid.

size is proportional to the induction time. The induction time is the period between the reaction start by addition of water and the formation of zirconia primary particles. The induction time shortens with, e.g., increasing amount of water, shorter chained solvents, etc. Increasing the carboxylic chain length (from C<sub>6</sub> to C<sub>18</sub>) also led to a reduced induction time as expected, but Lerot *et al.*[145] observed surprisingly larger particles which argues against the LaMer model. On the contrary, Leib *et al.* observed decreasing induction times and particle sizes ( $\sim 1.4$  to  $\sim 0.8$   $\mu\text{m}$ ) for zirconia microparticles derived from sol-gel synthesis by increasing the carboxylic chain length from C<sub>14</sub> to C<sub>28</sub>. [1]

To give a possible explanation for this observation, the role of carboxylic acids in the sol-gel synthesis of zirconia particles needs to be clarified. First, carboxylic acids react with the zirconium alkoxide to a zirconium carboxy-alkoxide derivate as shown in Fig. 4.9. These metal carboxylates are known to form micelles with their polar groups pointing to the center. As a consequence, water molecules are incorporated into the cores of the micelles, where a localized hydrolysis and condensation generates nanosized primary particles. Due to micellar structures, aggregation of the primary particles is favored compared to LaMer growth as the superficial charges, which usually prevent aggregation, are diluted due to the presence of oxygenated groups (carboxylate, alkoxyate, or zirconate). Furthermore, Lerot *et al.*[145] concluded from experimental data that the solubility of carboxylic acids increases with the length of the alkyl group of the alcoholic solvent. This observation leads to less micellar structures and hence a decreased hydrolysis rate and small number of nuclei resulting in larger particles.

Studies such as that conducted by Van Cantfort *et al.*[147] have shown that the growth of zirconia particles in a sol-gel synthesis by using fatty acids as stabilizers is a competition between individual LaMer growth and aggregation, especially in the early stages of micelle formation. A comparison of the two growth mechanisms is presented schematically in Fig. 4.10.

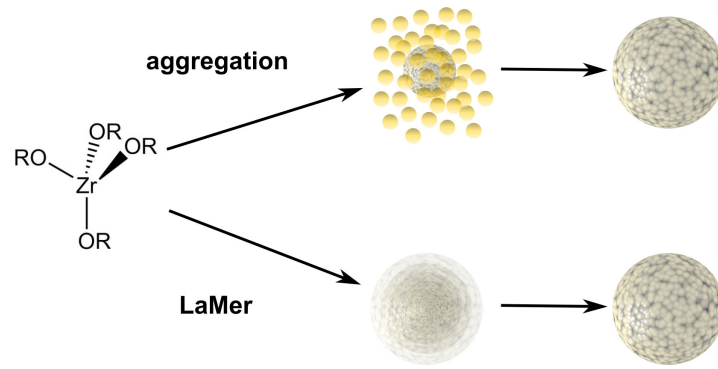


**Figure 4.10** – Comparison of the growth of zirconia particles from sol-gel synthesis by individual growth following the LaMer type mechanism and by aggregation of primary particles. In the synthesis of zirconia particles both compete with each other with regard to reaction conditions and particle size.

Similarly, it has been demonstrated by Park *et al.*[148] that the formation of monodispersed colloids depends on the final particle size. The LaMer mechanism which includes diffusional growth of individual particles (see Fig. 4.10), works well for nanoparticles ( $< 100$  nm), where a broad size distribution is obtained. For larger particles, this growth model fails to describe the collected experimental data, where polycrystalline particles were characterized which consist of small crystalline subunits. These subunits have the same size ( $\sim 10$  nm) as the initially formed primary particles, which suggest an aggregation of primary particles in the growth process of particles with a diameter  $> 100$  nm.

In all studies reviewed here, growth of zirconia particles is recognized as a mixture of LaMer growth and aggregation of primary particles, which strongly depends on particle sizes and various reaction parameters. Therefore, Fig. 4.11 provides an overview of the influence by different reaction parameters on zirconia particle sizes with regard to the synthesis of small submicron particles ( $0.1\text{--}0.4\ \mu\text{m}$ ) compared to large microparticles ( $2\text{--}5\ \mu\text{m}$ ).

Besides the above mentioned reaction parameters (fatty acid length and concentration, water content, and solvents), additionally the precursor nature and concentration, dopants, stirring time, and aging time play a key role in the sol-gel synthesis of zirconia particles. Leib *et al.*[1] investigated in an extensive study the thermal stability of different sized  $\text{ZrO}_2$  particles (diameters:  $\sim 0.86\ \mu\text{m}$ ,  $\sim 2.8\ \mu\text{m}$ , and  $\sim 4.2\ \mu\text{m}$  as-synthesized) by using different zirconia precursors and solvents. The smaller particles were obtained by using zirconium *n*-propoxide as precursor

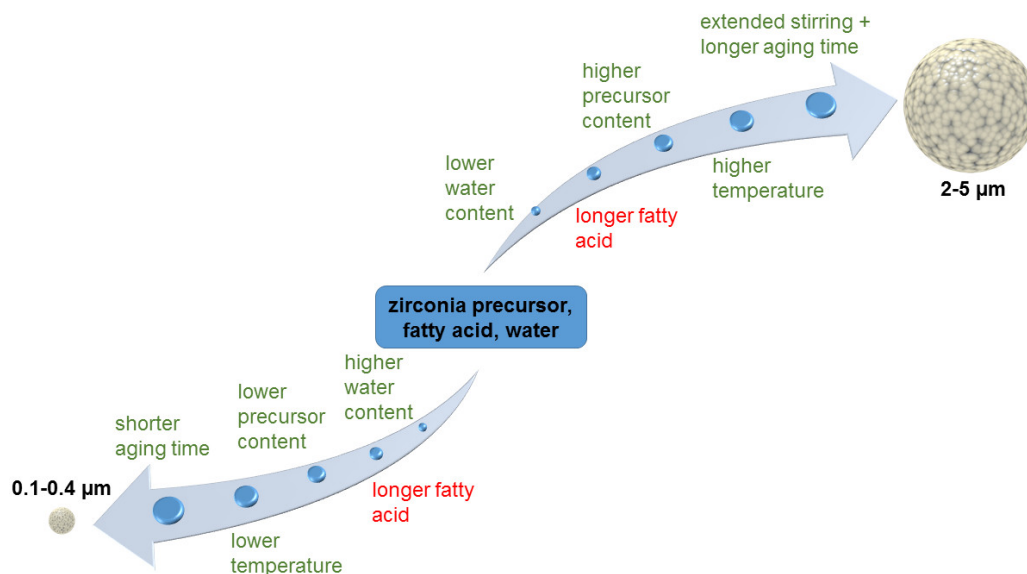


**Figure 4.11** – Overview of the influence by various reaction parameters on zirconia particle sol-gel synthesis with regard to their size. As the growth mechanisms change for different particle sizes, some parameters are not consistent (highlighted in red) for synthesis of small (0.1–0.4 μm) and large (2–5 μm) particles.

and ethanol as solvent, which yields higher hydrolysis rates. For larger particles, they used zirconium *n*-butoxide and butanol. Furthermore, it seems logical that an increased amount of zirconia precursor leads to increased particle sizes, if the other reaction conditions remain the same. Based on the results and conclusions from their first study, Leib *et al.*[2] investigated the applicability of YSZ microparticles (4–18 mol%) for high-temperature photonics. Here, the induction times were faster compared to previously reported undoped zirconia particles. The faster hydrolysis rates can be explained by the higher reactivity of the yttria precursor (yttrium *iso*-propoxide) compared to the zirconia precursor (zirconium *n*-propoxide). Yttrium *iso*-propoxide has only three ligands instead of four and a higher electronegativity which makes it more susceptible to nucleophilic attacks.[2] Furthermore, a relationship between the aging period and final particle size exists. The shorter the aging time (and the lower the temperature), the smaller the zirconia particles, whereby it was found that a gentle rotation of the reaction vessel prevents a secondary nucleation.[140] To increase the zirconia particle size even further, an extended stirring period (2 to 12 min) after the induction and a rotational aging at higher temperatures can be implemented.

### 4.3.2 High-temperature behavior

Sol-gel derived as-synthesized zirconia particles are amorphous and first crystallize in the metastable tetragonal phase before transformation to the monoclinic phase upon thermal treatment at higher temperatures.[62, 63, 109] The initial transition to the tetragonal phase is attributed to the local coordination environment and short-range order in the amorphous phase that is more similar to the tetragonal rather than the monoclinic polymorph.[63, 101, 108–111] Thus, the initial crystallization yields the tetragonal phase. The thermodynamically stable monoclinic phase is formed only after heating to higher temperatures. As this t→m transition is associated with a volume expansion of ~5% [64] it leads to stress-induced structural destabilization of the particles (details can be found in Section 4.2.1).

A number of studies have begun to examine the high-temperature stability of zirconia particles. In a comprehensive study conducted by Leib *et al.*[1] it was shown that zirconia submicron and microparticles from sol-gel synthesis transformed from the amorphous phase to the tetragonal phase at 250–450 °C and to the monoclinic phase after thermal treatment at 450–650 °C, depending on synthesis conditions and particle size. Furthermore, they observed a mass loss of up to 40% and a volume loss of up to 75% upon heating to 450 °C. By comparing three different particle sizes (0.86, 2.8, and 4.2 μm in diameter), an enhanced temperature stability of larger microparticles compared to smaller submicron particles was observed. The martensitic phase transformation of zirconia has been a controversial and much disputed subject within the scientific community. In an *in situ* high-temperature X-ray study, Srinivasan *et al.*[149] determined that the t→m transformation occurs upon cooling below 300 °C. They suggested that at 800 °C surface defects are generated, which absorb oxygen on cooling initiating the t→m transition. By covering the zirconia surface with sulfate anions, the transition could be suppressed. In contrast, more recent *in situ* studies observed the t→m transformation in both heating and cooling of zirconia.[1, 150]

The grain size and growth of zirconia particles are also important parameters as they dictate the mechanical and optical properties (see Section 4.2.2). At large grain sizes compared to particle dimensions, the particles are first destabilized before total disintegration. Shukla and Seal[63] pointed out that the tetragonal structure is more stable for isolated zirconia nanocrystals with sizes up to 10 nm

as it provides lower surface energy than the monoclinic phase. For larger isolated nanocrystals the volume free energy becomes the dominating parameter and forces the transition to the monoclinic phase. Thus, isolated tetragonal zirconia nanocrystals grow until they reach a size of  $\sim 10$  nm before they transition to the monoclinic phase. However, in contrast to isolated nanocrystals, the surface energy of tetragonal crystallites in aggregated structures of zirconia nanocrystals is significantly lower. Furthermore, due to the spatial confinement of the crystallites within aggregated structures the hydrostatic strain energy has to be taken into consideration.[64] As the martensitic tetragonal-to-monoclinic phase transition is associated with a  $\sim 5\%$ [64] volume increase, the resulting strain energy makes this transformation less favorable. Taking into account these contributions, Shukla and Seal[63] calculated a critical tetragonal grain size of  $\sim 41$  nm in aggregated zirconia particles.

A further possibility to stabilize the tetragonal phase and to reduce grain growth of zirconia particles is thermal treatment under inert gas. Livage *et al.*[110] reported that tetragonal zirconia is much more stable when heated in an oxygen-free atmosphere than under air. Srinivasan *et al.*[109] also observed that the phase transition was accomplished more readily under air than under inert gas. They proposed that chemisorption of oxygen at surface defects (oxygen vacancies) upon cooling below  $300^\circ\text{C}$  initiates the  $t \rightarrow m$  transition. Similarly, Collins and Bowman[151] suggested that elimination of oxygen vacancies by incorporation of oxygen from the atmosphere facilitates the transition to the monoclinic phase. Furthermore, it has been demonstrated by Penner *et al.*[152] that in inert atmospheres, the persisting structural defectivity leads to a high stability of tetragonal  $\text{ZrO}_2$  up to  $1000^\circ\text{C}$ .

### 4.3.3 Doping

As already discussed in general for zirconia in Section 4.2.3, the addition of lower-valence oxides such as  $\text{Y}_2\text{O}_3$  stabilizes the more symmetric tetragonal and cubic phases compared to the monoclinic phase. In the literature, there was a significant positive correlation between decreased grain growth, tetragonal or rather cubic phase stabilization, and Y dopant content. Here, an optimum Y content of 8–10% was determined for tetragonal or rather cubic phase stabilization in zirconia microparticles.[2] Furthermore, a new sol-gel process for doping zirconia microparticles with La or Gd and a combination of either with Y were demonstrated.[3]

## 4 Theory

The most striking result was that La and Gd alone have a strong grain growth attenuating effect, whereby the martensitic phase transformation from tetragonal to monoclinic phase could not be suppressed. In contrast to this finding, co-doping with La or Gd and Y led not only to grain growth inhibition but also to phase stabilization.

There are various alternative dopants apart from Y, La, and Gd which are promising candidates to increase the high-temperature stability of zirconia, as explained in Section 4.2.3. Most preparative approaches for doping spherical zirconia particles used one-step methods such as sol-gel or hydrothermal synthesis to produce zirconia doped with mixed oxides such as yttria[2, 153, 154] and ceria[11] or co-doped with ceria-yttria,[155] to name just a few. In contrast to concurrent synthesis of zirconia particles and doping, there is no information about possibilities and effects of post-synthetic modification (PSM) of zirconia microparticles with different dopants to the best of my knowledge. Hence, the properties of the initial bare zirconia particles can be precisely altered by PSM depending on the desired application and its requirements as shown in this dissertation. The major advantage is the reduction of synthetic procedures, which is particularly interesting for potential applications and their industrial processing. For nanocrystals, the literature has highlighted the cation exchange technique to alter the properties of crystalline materials. Here, insertion and exchange of atoms controls both properties and composition as shown for interconversion between CdS, Cu<sub>2</sub>S, and PbS nanocrystals.[156] Additionally, zirconia core particles can be encapsulated by ceramic materials such as alumina and silica in order to modify their optical properties (e.g., for SC application) or to enhance their thermal stability (e.g., for TBC application). These so called core@shell structures will be the topic of the following section.

### 4.4 Core@shell structures

Core@shell structures have gained considerable attention and enabled new research opportunities in almost all areas of science and engineering, including medicine, catalysis, biotechnology, chemistry, optics, electronics, energy storage, etc.[57] During the past 30 years, much more information has become available on the combination and arrangement of existing materials to core@shell structures. Here, different desirable properties of two or more materials can be combined in one new material.

In the late 1980s, Spanhel *et al.*[157] were the first to report such heterostructures, more precisely CdS-Ag<sub>2</sub>S particles, whereby the terminology core@shell was accepted some years later.[158]

Srdic *et al.*[57] classified the different intentions of researchers to fabricate core@shell structures into three categories: First, the combination of two materials to combine two properties within one structure as it was demonstrated for iron oxide nanoparticles covered with a silica-silver-titania multishell.[159] Here, the magnetic properties from the core could be combined with the luminescent optical properties from the silica shell. Second, core@shell particles can be synthesized to yield a specific design or geometry. For example, Zhang *et al.*[42] developed a SiO<sub>2</sub>@Au/N-doped TiO<sub>2</sub> photocatalyst, where the low cost silica as the core material is the carrier for a thin shell of the expensive active material. Third, the combination of two or more materials could cause an entirely new property as known for ceramic core@shell materials, where the interaction between a ferromagnetic core and a ferroelectric shell leads to the magnetoelectric effect.[160–163]

### 4.4.1 Types

Core@shell particles are typically spherical shaped, whereby mainly three types can be distinguished (Fig. 4.12).[57] Core@shell particles with dense or porous cores (a). Here, the core material can also be off-centered yielding so called yolk-shell particles.[41, 164] Furthermore, some core materials are removable by calcination or etching forming hollow particles.[165] Besides the variation of the core structure, dense cores with continuous dense or porous shells are found (b). Moreover, discontinuous/particulate shells are known. Additionally, there are more complex shell systems described in the literature such as core@shell@shell particles,[53] cores with composite shells, and cores with multilayered shell systems (c).

### 4.4.2 Synthesis

There are numerous gas phase processes and liquid phase techniques to synthesize core@shell particles with a defined composition, core size, shell thickness, size distribution, density, and morphology.[57] Gas phase processes are mostly based on reaction/decomposition of flowing gases, whereby a complete coverage of the core surface and desirable shell thicknesses are obtained. For the synthesis based on

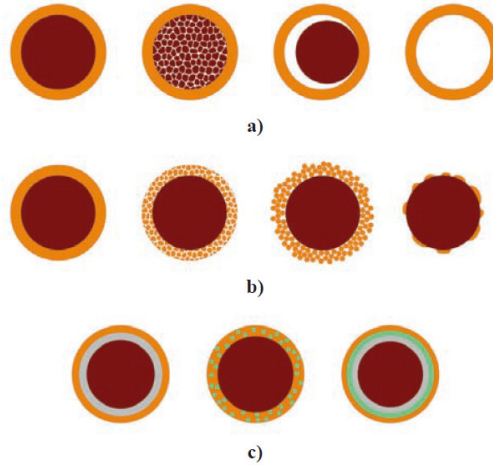


**Figure 4.12** – Schematic illustration of core@shell particles with different types of: cores (a), shells (b), and complex core@shell structures (c). Figure adopted and caption adapted from reference.[57]

reaction/decomposition of flowing gases, usually two reactors are needed. In the first chamber, the desired nanoparticles are formed for example by vapor phase reactions.[166] Afterwards, the obtained core particles are exposed to a gaseous shell precursor. Here, the shell is formed by different mechanisms such as chemical vapor deposition.[166] Furthermore, spray pyrolysis is used to synthesize core@shell particles. Here, in contrast to reaction/decomposition of flowing gases, a mixture of very fine precursor droplets with a carrier gas (flowing aerosol) is applied.[57] The experimental design is similar as one reactor with two reacting zones or two sequential reactors are needed. In principle, the solvent of the precursor droplets evaporates, which leads to precipitation of the core material. Subsequently, the cores are coated by evaporation and precipitation of the selected shell material.

Previous research has also established gas phase reactions, where no precursor gas or aerosol is utilized. One example is the surface oxidation of silicon nanoparticles by oxygen exposure yielding  $\text{Si@SiO}_2$  core@shell particles.[57] Furthermore, obtaining core@shell structures by a low-pressure flame synthesis is also reported in the literature.[167] Here, the addition of a precursor/Ar mixture to premixed  $\text{H}_2/\text{O}_2/\text{Ar}$  flames led to the formation of  $\text{Fe}_2\text{O}_3@\text{SiO}_2$  core@shell nanoparticles.

A considerable amount of the literature has been published on the encapsulation of spherical particles by atomic layer deposition (ALD).[168–171] These studies used different techniques of ALD to obtain a conformal coating of individual particles

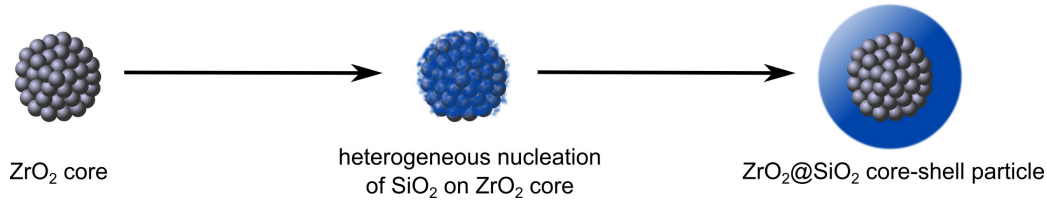


**Figure 4.13** – Schematic illustration of the wet-chemical  $\text{ZrO}_2@SiO_2$  core@shell particle synthesis. First, heterogeneous nucleation of  $\text{SiO}_2$ -seeds on the zirconia surface occurs. Second, growth of a dense silica shell by bridging the gaps of the  $\text{SiO}_2$ -seeds.

such as fluidized bed reactor[170] or rotary reactor.[168] For ALD on particles, which are assembled on a substrate, contact points between adjacent particles and at the particle-substrate interface remain uncovered as shown by Weber *et al.*[169] for Pt shell growth on Pd nanoparticles deposited on  $\text{Al}_2\text{O}_3$  substrates.

Besides gas phase processes, liquid phase (wet-chemical) approaches are used to synthesize various core@shell structures. Srdic *et al.*[57] differentiated between four types of wet-chemical shell growth: chemical deposition on core particles, chemical deposition on functionalized core particles, assembly of preformed nanoparticles by electrostatic interactions, and assembly of preformed nanoparticles onto functionalized core particles. The wet-chemical deposition of a desired shell material on core particles is the most favored method as the shell grows directly on the core without further steps or treatment. However, this type of growth is often difficult to perform due to the hydrophobic nature of the core surface, inadequate surface charges, incompatibility, etc.[57] The direct wet-chemical deposition yields amorphous or crystalline shells due to a heterogeneous nucleation of the solid shell phase as shown in Fig. 4.13 for the growth of silica shells on zirconia core particles.

Here,  $\text{SiO}_2$ -seeds emerge on the zirconia surface, before the gaps of this island-like structure are filled with silica to form a continuous shell, which is called seeded-growth. One of the main obstacles of the direct chemical deposition method is that the large surface to volume ratios or the absence of surface charges leads to an agglomeration of the core particles. In this case, it is necessary to shift the zeta potential to larger absolute values by surface modification to prevent agglomeration.[57] Introducing citric acid on the particle's surface is one possibility to create surface charges, which was already shown for  $\text{Fe}_2\text{O}_3$ [172] and  $\text{ZrO}_2$  particles.[7] For silica encapsulation of zirconia particles, tetraethyl orthosilicate (TEOS) is used as silica precursor. First, silicate groups will attach to the OH-groups on the zirconia

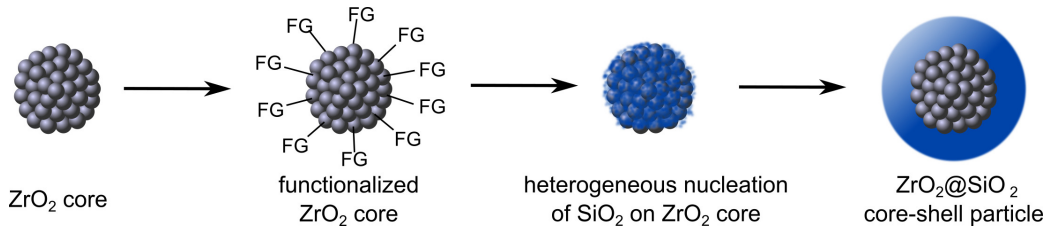


**Figure 4.14** – Schematic illustration of the wet-chemical  $\text{ZrO}_2@SiO_2$  core@shell particle synthesis by using functional groups (FG) on the zirconia core surface. First, the zirconia cores are modified with a specific functional group. Second, heterogeneous nucleation of  $SiO_2$ -seeds on the functionalized zirconia surface occurs, before growth of a dense silica shell by bridging the gaps of the  $SiO_2$ -seeds starts.

surface, before additional layers can be obtained by hydrolysis and polycondensation of TEOS in close proximity to the first silica layer.[57] Furthermore, the silica shell thickness can be accurately controlled in the nanometer regime by changing the concentration of ammonia (catalyst) or TEOS.

Besides seeded-growth of silica, the layer-by-layer technique is used as a multistep deposition of thick shells as shown in the literature for alumina shells on  $BaTiO_3$  and  $ZrO_2$  cores.[173] For this purpose, the core particles ( $D = 70\text{--}140$  nm) were dried and suspended in methylalumoxane (MAO), which anchors to the particle's surface by covalent Al-O bonds. After removal of MAO by washing steps, the particles were exposed to air, whereby the MAO layer on the particle surface oxidized to  $Al_2O_3$ . Characterization by ICP-OES and TEM revealed an alumina shell thickness of up to  $\sim 10$  nm depending on the number of deposition cycles. As the XRD patterns of bare  $BaTiO_3/ZrO_2$  core particles are very similar to the alumina-coated nanoparticles, the authors conclude that the alumina phase is amorphous and only few Al ions might be incorporated into the lattice of the core particles.[173]

As already mentioned above, the direct coating of a homogeneous shell is often challenging or even not possible.[57] Therefore, a convenient strategy is to modify the core particles with functional groups (FGs) prior to the encapsulation process as exemplarily shown for  $ZrO_2@SiO_2$  core@shell particles in Fig. 4.14. Jin *et al.*[174] reported on a sol-gel method for the synthesis of  $SiO_2@Al_2O_3$  core@shell particles by using different surfactants such as polyethylene glycol (PEG) and polyvinylpyrrolidone (PVP) for dispersing and coating the silica core particles with up to 90 nm alumina shell. In a more complex approach, Wang and Tseng[165] demonstrated a novel technique for synthesizing nanoshell hollow alumina particles

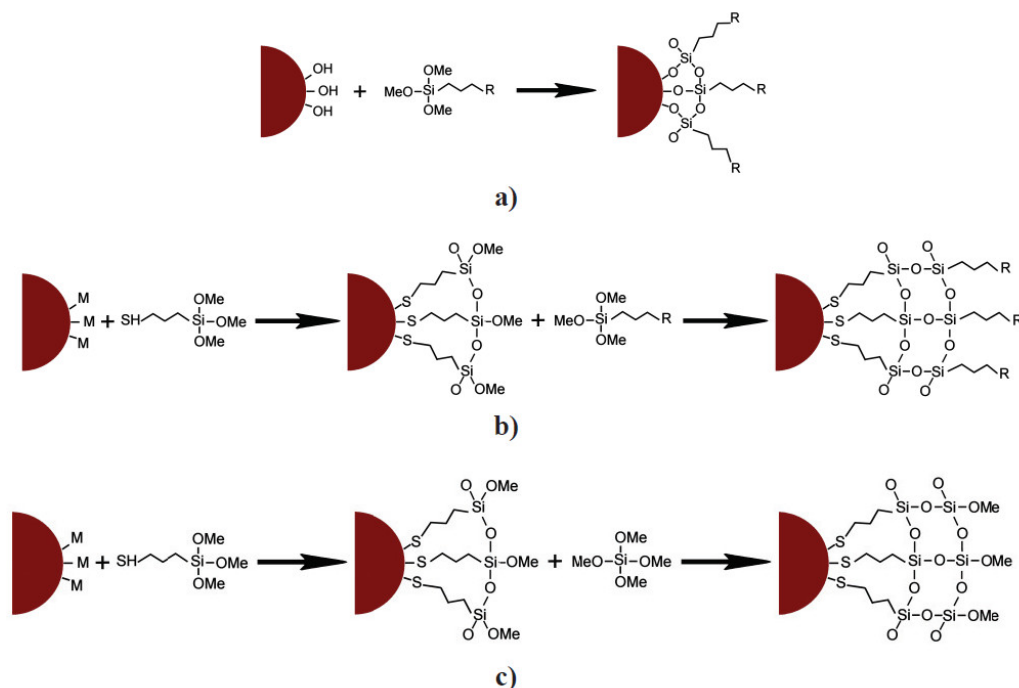


**Figure 4.15** – Three different strategies for functionalization of core particles prior to encapsulation: reaction of core surface hydroxyl-groups with OMe-groups of silane coupling agent (a), chemisorption of thiol-functionalized silane on core surface followed by hydrolysis and condensation of another silica species to introduce a new surface functionality (b), and attachment of tetraalkyl silicate for direct silica shell growth (c). Figure adopted from reference.[57]

by using nonporous PS beads cross-linked with divinyl benzene. After successful alumina encapsulation with a 20–40 nm shell, the polymeric template was removed by thermal pyrolysis to form hollow spheres.

For the encapsulation of hydrophilic core particles with silica by the Stöber method, three different types can be distinguished (see Fig. 4.15).[57] First, the core surface hydroxyl-groups can react with -OMe groups ( $-\text{OCH}_3$  or  $-\text{OC}_2\text{H}_5$ ) of a silane coupling agent to introduce a new surface functionalization (a). Second, chemisorption of thiol-functionalized silane on the core's surface occurs, followed by surface modification with an appropriate ligand via hydrolysis and condensation with another silica species (b). Third, the silica shell formation could be directly initiated by the attachment of a tetraalkyl silicate on the surface of the core (c).

As the selection of the best suitable FG is very important for a successful encapsulation, much of the available literature on surface modification of core par-

#### 4 Theory

ticles considers various functional groups such as cetyltrimethylammonium bromide (CTAB),[175] 3-aminopropyltriethoxysilane (APTES),[176] and 3-mercaptopropyl(trimethoxy)silane (MPTMS).[177] Furthermore, an alternative strategy for synthesis of core@shell particles is the use of preformed nanoparticles as shell material which exhibit the opposite surface charge of the core material.[57] Here, a very uniform shell structure can be obtained as the charged surfaces of the core and the shell materials prevent homonucleation.

## 5 Objectives

The aim of this study is to explore the synthesis and thermal stability of ceramic  $\text{ZrO}_2/\text{YSZ}-\text{Al}_2\text{O}_3$  composite microparticles and  $\text{ZrO}_2/\text{YSZ}@-\text{SiO}_2$  core@shell sub-micron particles in consideration of desirable applications such as thermal barrier coatings and structural colors, respectively. Figure 5.1 provides an illustration of the strategy and procedure to obtain these particle systems.

First, spherical and monodisperse  $\text{ZrO}_2$  and YSZ core particles need to be produced in the micron and submicron range by sol-gel synthesis. Second, these particles have to be calcined at specific temperatures (400–600 °C) to decompose organic residues from synthesis and to complete particle shrinkage (due to mass and volume losses). Afterwards, the  $\text{ZrO}_2$  and YSZ microparticles should be modified with alumina by a wet-chemical procedure and assembled to photonic glasses. For comparison with different alumina modification techniques, photonic glasses made of bare  $\text{ZrO}_2$  and YSZ microparticles should be coated with alumina by ALD. Finally, the obtained  $\text{ZrO}_2-\text{Al}_2\text{O}_3$  and  $\text{YSZ}-\text{Al}_2\text{O}_3$  composite particles should be heat-treated up to 1500 °C as the desirable TBC application requires high-temperature stability.

With the alumina encapsulation, improvement of the high-temperature stability of zirconia microparticles due to blocking of oxygen diffusion and spatial confinement of the crystallites may be possible. Also alumina doping could contribute to phase stability and inhibition of grain growth. For this purpose, complementary characterization methods such as SEM, TEM, XRD, IR reflection measurements, cross-sectional TEM (lamella from FIB technique), and analysis by HAADF-STEM in combination with EDX mappings were used to evaluate their high-temperature stability.

For application as structural colorants, smaller  $\text{ZrO}_2$  and YSZ submicron particles (calcined) need to be encapsulated by a sol-gel synthesis with low refractive silica and deposited to photonic glasses as shown in Figure 5.1. Subsequently, the

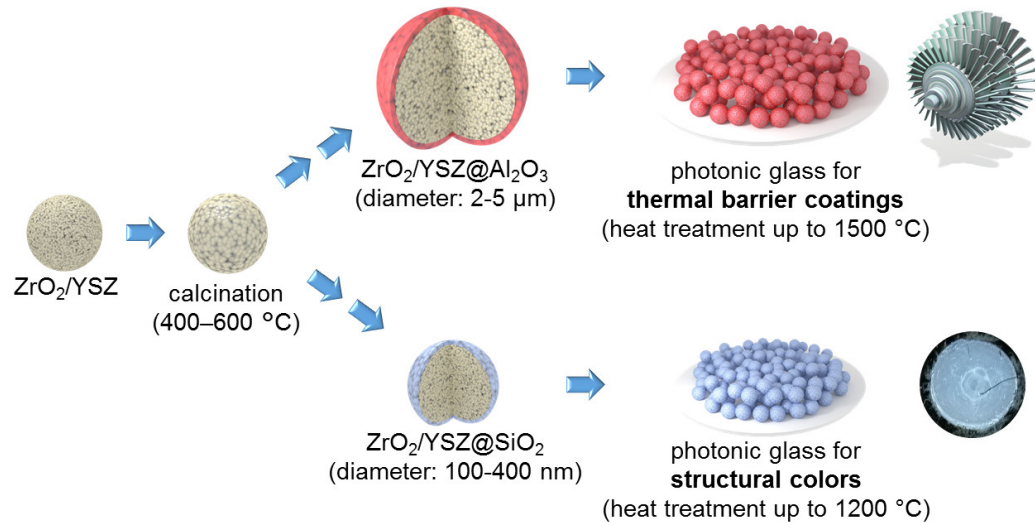


**Figure 5.1** – Illustration of the objectives of this study. Synthesis of ZrO<sub>2</sub>/YSZ micro- (2–5 μm) and submicron (100–400 nm) particles, calcination (400–600 °C), deposition of alumina (Al<sub>2</sub>O<sub>3</sub>) on zirconia microparticles, encapsulation of zirconia submicron particles with silica (SiO<sub>2</sub>), deposition of photonic glasses for both particle systems and heat treatment up to 1200 °C and 1500 °C, respectively. ZrO<sub>2</sub>/YSZ@Al<sub>2</sub>O<sub>3</sub> composite microparticles are promising for application as thermal barrier coating, while ZrO<sub>2</sub>/YSZ@SiO<sub>2</sub> core@shell submicron particles are desirable for structural colors.

obtained ZrO<sub>2</sub>@SiO<sub>2</sub> and YSZ@SiO<sub>2</sub> core@shell particles should be heat-treated up to 1200 °C to examine the suitability for high-temperature stable structural colorants.

The silica shell is not only required for a non-monotonous refractive index distribution but also for crystalline phase stabilization and inhibition of grain growth due to blocking of oxygen diffusion and spatial confinement of the crystallites similarly as it is expected for alumina deposition. Besides, silica doping needs to be considered as literature reveals tetragonal phase stabilization and inhibition of grain growth by SiO<sub>2</sub>-doping of tetragonal zirconia polycrystals.[134, 135] For this purpose, complementary characterization methods were used to evaluate the high-temperature stability.

This dissertation seeks to explain and discuss different mechanisms, which could contribute to an improved high-temperature stability for both, ZrO<sub>2</sub>/YSZ–Al<sub>2</sub>O<sub>3</sub> composite microparticles and ZrO<sub>2</sub>/YSZ@SiO<sub>2</sub> core@shell submicron particles.

As sub-projects, the mechanical properties of  $\text{ZrO}_2$  microparticles should be determined by microcompression experiments to evaluate the structural degradation and phase transformation at high pressures. Furthermore, the high-temperature stability and optical properties of previously designed TPV systems with zirconia submicron particles ( $D \sim 600$  nm after calcination) deposited on tungsten substrates should be improved. For this purpose, YSZ microparticles ( $D \sim 1$   $\mu\text{m}$  after calcination) with a narrow size distribution need to be synthesized and assembled to form a monolayer on a W/ $\text{HfO}_2$  substrate.



## 6 Results and Discussion

### 6.1 $\text{ZrO}_2\text{-Al}_2\text{O}_3$ and $\text{YSZ-Al}_2\text{O}_3$ composite microparticles

Partially, results of the following section were elaborated in collaboration with Jil Rüter[178] who did her master thesis during the time of my PhD-project. The topic and work plan were prepared by me and I supervised the data evaluation and modifications of procedures. Furthermore, I synthesized and provided all three core particles (Zr-1, Zr-2, YSZ-1), which are discussed in this dissertation. Moreover, I added the comparison to undoped zirconia particles after atomic layer deposition (ALD) of alumina to the ALD data for yttria-stabilized zirconia (YSZ) cores. During the master project of Jil Rüter, the successful encapsulation of zirconia cores to  $\text{ZrO}_2\text{-Al}_2\text{O}_3$  and  $\text{YSZ-Al}_2\text{O}_3$  core@shell structures, respectively, could not be confirmed, although the high-temperature stability of alumina-treated  $\text{ZrO}_2$  cores was clearly improved. Thus, I further investigated the obtained  $\text{ZrO}_2\text{-Al}_2\text{O}_3$  composite structure to clarify the mechanisms of increased thermal stability and assigned it to post-synthetic alumina modification (PSM) in this dissertation.

#### 6.1.1 Synthesis and calcination of $\text{ZrO}_2$ and YSZ microparticles

Different methods have been proposed in the literature to synthesize monodisperse, spherical zirconia microparticles. For example, using alkoxides in sol-gel syntheses[1] or polymer-induced aggregation of colloids[179] and aerosol synthesis in low temperature flames[180] were reported. In the sol-gel synthesis, zirconia microparticles of different sizes can be obtained by the controlled reaction of water, zirconium precursors, and the presence of stabilizing agents (see Section 4.3 for details).

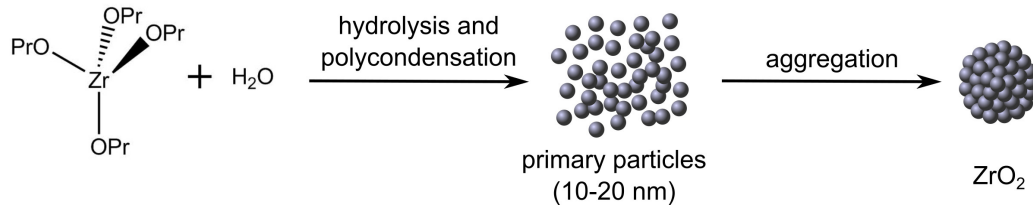


**Figure 6.1** – Sol-gel synthesis of zirconia (ZrO<sub>2</sub>) particles. First, zirconium(IV) *n*-propoxide is hydrolysed by water and polycondensated by forming primary particles (10–20 nm). Second, the zirconia primary particles aggregate to zirconia microparticles.

In previous studies by our group,[1, 2] sol-gel methods for the fabrication of undoped and YSZ particles in the size range of 0.4 to 4.2  $\mu\text{m}$  were reported. In these investigations, fatty acids were used as stabilizers. These studies are based on the general method of Widoniak *et al.*[62] for the synthesis of zirconia submicron particles with diameters between 0.4 and 0.8  $\mu\text{m}$  and on the comprehensive work of Yan *et al.*[140] on preparative methods to obtain zirconia microparticles of up to 4  $\mu\text{m}$  in diameter. This part of my dissertation focuses on undoped zirconia and YSZ microparticles for potential applications as thermal barrier coatings (TBC).

In the present study, a modified sol-gel method for the synthesis of ZrO<sub>2</sub> and YSZ microparticles was used, which is based on investigations by Yan *et al.*[140] and previous works of Leib *et al.*[1, 2] Here, zirconium(IV) *n*-propoxide functions as zirconia precursor, which is hydrolyzed by water (Fig. 6.1). Afterwards, the hydrolyzed zirconia precursor species forms primary particles by polycondensation. Then, these primary particles aggregate yielding zirconia microparticles. The growing microparticles are stabilized by eicosanoic acid during the reaction (see Section 8 for experimental details and Section 4.3 for information about the particle growth mechanisms).

In order to achieve high-temperature stability for potential application as TBC, Y-doping of ZrO<sub>2</sub> microparticles was considered. Therefore, a previously published synthesis method for YSZ microparticles of Leib *et al.*[2] was applied to increase the thermal stability by attenuating grain growth and phase transformations at high temperatures. As the optimum Y content was determined to be 8–10 mol%, YSZ microparticles with 9.5 mol% Y were synthesized in a similar particle size range as the undoped zirconia particles in this work to exclude particle size effects when analyzing and comparing the high-temperature stability. Therefore, yttrium

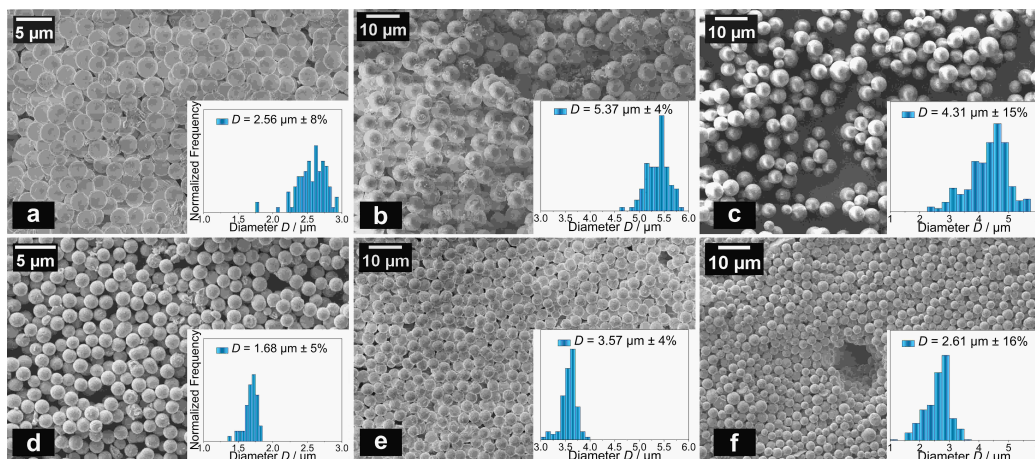


**Figure 6.2** – SEM images and sizing statistics of as-synthesized (dried at 80 °C for 4 h)  $ZrO_2/YSZ$  batches Zr-1 (a), Zr-2 (b), and YSZ-1 (c). SEM images and sizing statistics of calcined (600 °C, 3 h)  $ZrO_2/YSZ$  batches Zr-1 (d), Zr-2 (e), and YSZ-1 (f). Average particle diameters and standard deviations were determined using *ImageJ* software by counting at least 100 particles.

was introduced in the sol-gel synthesis from Fig. 6.1 as yttrium(III) *i*-propoxide (see Section 8 for details).

Figure 6.2 provides an overview of scanning electron microscopy (SEM) images and sizing statistics of two undoped (Zr-1 (a,d), Zr-2 (b,e)) and one YSZ (YSZ-1 (c,f)) batches, which were used as core materials in this section. The first batch Zr-1 (a) had an initial particle diameter of  $2.56 \mu\text{m} \pm 8\%$ , while the second batch Zr-2 (b) yielded larger particles of  $5.37 \mu\text{m} \pm 4\%$  as-synthesized. These batches were used for wet-chemical PSM of the zirconia cores with alumina by sol-gel synthesis using aluminum chloride or aluminum *i*-propoxide as Al precursors (Zr-1-PSM), for atomic layer deposition (ALD) of alumina on zirconia cores (Zr-2-ALD), and as reference (Zr-1 and Zr-2). The Y-doped batch YSZ-1 (c) had a diameter of  $4.31 \mu\text{m} \pm 15\%$  as-synthesized and was used for ALD (YSZ-1-ALD), wet-chemical modification by alumina (YSZ-1-PSM), and as reference (YSZ-1).

After successful synthesis, both undoped and YSZ microparticles exhibited smooth particle surfaces, which are polar in nature due to non-condensed hydroxide groups. To separate the microparticles from remaining primary particles (10–20 nm), the particle suspensions were centrifuged several times with different solvents as explained in detail in Section 8. Furthermore, residual agglomerates were removed by sonication and sedimentation, respectively.

## 6 Results and Discussion

Before modification with alumina to form composite particles, the undoped and YSZ microparticles were dried at 80 °C for 4 h and then calcined at 600 °C for 3 h before alumina deposition. During the calcination process, the particles transform from an amorphous structure to the metastable tetragonal phase (discussed later in detail at Figures 6.6, 6.9, and 6.12). This behavior is well known for sol-gel derived amorphous zirconia (see Section 4.2.1 for details).[62, 63, 109] During calcination, the particles undergo a volume and mass loss. On the one hand, the microparticles loose residual water during drying, on the other hand, organic residues from the fatty acid stabilizer or precursor decompose during calcination.[1] In the sintering process, zirconia cores solidify as the porosity decreased.

SEM images and sizing statistics of the calcined undoped (Zr-1 (d) and Zr-2 (e)) and YSZ microparticles (YSZ-1 (f)) are presented in Figure 6.2. Calcined (600 °C, 3 h) zirconia microparticles Zr-1 exhibit an average particle diameter of  $1.68 \mu\text{m} \pm 5\%$  (volume loss:  $\sim 72\%$ ), Zr-2 of  $3.57 \mu\text{m} \pm 4\%$  (volume loss:  $\sim 71\%$ ), and the YSZ-1 particles showed a volume loss of  $\sim 78\%$  yielding a particle diameter of  $2.61 \mu\text{m} \pm 16\%$  after calcination. An overview of the sizing statistics for all three particle samples used in this section is shown in Tab. 6.1. Experimental details can be found in Section 8.

**Table 6.1** – Sizing statistics of as-synthesized (dried at 80 °C for 4 h) and calcined (600 °C, 3 h) undoped (Zr-1, Zr-2) and YSZ (YSZ-1) microparticle batches used for ALD, PSM, and as reference in this section.

Batch	Particle diameter before calcination ( $\mu\text{m}$ )	Standard deviation (%)	Particle diameter after calcination ( $\mu\text{m}$ )	Standard deviation (%)	used for
Zr-1	2.56	8	1.68	5	PSM
Zr-2	5.37	4	3.57	4	ALD
YSZ-1	4.31	15	2.61	16	ALD, PSM

### Assembly of $\text{ZrO}_2$ and YSZ microparticles to photonic glasses

Turning the focus on the proposed application of zirconia and YSZ microparticles as TBC, photonic glasses needed to be assembled. Therefore, both particle

systems were deposited on sapphire substrates as photonic glasses with a  $\sim 10\ \mu\text{m}$  layer thickness. The deposition process is explained in detail in Section 8 and SEM images for determination of the layer thickness are available in the appendix (Fig. 8.4). For the purpose of obtaining photonic glasses, the ethanol particle suspension ( $1\ \text{g}\cdot\text{L}^{-1}$ ) was combined with a mixture of ethanol and toluene (4:1) in a modified drop-cast method on sapphire substrates by using a polytetrafluorethylen (PTFE) template. Zirconia particles can be well suspended in ethanol, but it has a high vapor pressure leading to rapid evaporation and an inhomogeneous deposition. Furthermore, ethanol has a high contact angle to PTFE due to opposite polarity. To overcome this problem, toluene was additionally used to reduce the contact angle and to decrease the evaporation rate yielding uniform photonic glasses on sapphire substrates. The obtained photonic glasses were investigated by SEM to determine agglomeration, homogeneity, and impurities. An overview photograph (a) and exemplary SEM images (b-d) of photonic glasses on sapphire substrates from Zr-2 and YSZ-1 microparticles can be found in the appendix, Fig. 8.6.

### 6.1.2 Atomic layer deposition of alumina on $ZrO_2$ microparticles

In order to identify the influence of alumina on the temperature stability of zirconia microparticles, photonic glasses from undoped zirconia microparticles (after calcination) were coated with a  $\sim 47\ \text{nm}$  amorphous  $Al_2O_3$  layer by ALD as shown in Fig. 6.3 (Zr-2-ALD). The obtained alumina layer thickness was determined by investigation of the refractive index of a reference silicon sample from the reactor chamber (see appendix, Fig. 8.7). After alumina ALD, contact points between the zirconia microparticles still remain unchanged as the ALD process only coats alumina on free surfaces of the photonic glass. Such contact points exhibit the negative aspect that inter-particle oxygen diffusion and mass transport can still occur in addition to intra-particle oxygen diffusion due to oxygen vacancies in zirconia.[29] Nevertheless, an alumina layer on zirconia microparticles will protect the underlying bond-coat and superalloy substrate against oxidation in a potential TBC application. Here, the alumina-coated TBC top-coat represents an effective oxygen diffusion barrier. Besides, alumina should have a positive effect on zirconia integrity, grain growth, and phase stability, which will be evaluated and discussed later in this section. For the purpose of layer thickness measurements and analysis of the inner-particle and the alumina film structure, the comparable alumina-coated YSZ microparticles were exemplary characterized by cross-sectional

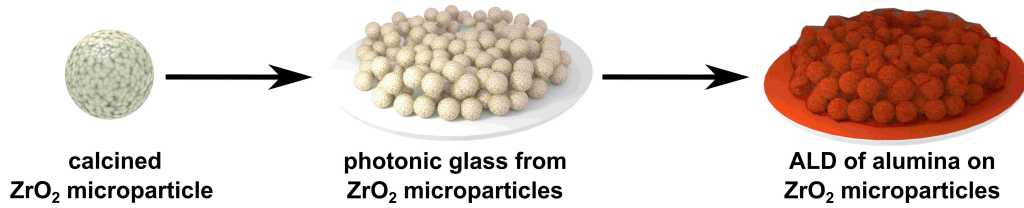


**Figure 6.3** – Preparation process of photonic glasses from ZrO<sub>2</sub> microparticles coated with alumina via ALD. First, photonic glasses from calcined (600 °C, 3 h) bare zirconia microparticles were deposited on sapphire substrates as explained in Section 8.2.1. Second, the obtained photonic glasses were covered with a ~47 nm amorphous Al<sub>2</sub>O<sub>3</sub> layer by ALD.

transmission electron microscopy (TEM) and SEM from focused ion beam (FIB) preparation as described in Section 6.1.4 and shown in Fig. 6.10.

### ***Ex situ* heating experiments**

To compare the differences in particle integrity, grain growth, and phase stability, *ex situ* heating experiments with alumina-coated ZrO<sub>2</sub> microparticles (Zr-2-ALD) were performed. Bare ZrO<sub>2</sub> cores (Zr-2) served as reference.

To begin this process, the photonic glasses on sapphire substrates were heated up to 800, 1000, 1100, 1300, and 1500 °C for 3 h as explained in detail in Section 8.3. Afterwards, the assemblies were investigated by SEM to evaluate the surface quality and integrity of the particles. As second method, XRD was used to identify the crystalline phases and phase transformations. Finally, the average grain sizes up to ~80 nm were calculated from XRD data by using the Scherrer equation. For larger grain sizes, SEM, cross-sectional SEM, and TEM characterization were used. The limitation in crystallite size analysis by the Scherrer equation is due to instrumental broadening of the XRD equipment used. Furthermore, the determined crystallite sizes from the Scherrer equation may be smaller than the visible grain sizes from SEM characterization as single grains can have more than one crystalline domain with different orientations.

Turning first the experimental evidence on undoped zirconia microparticles, their temperature stability before and after an ALD of alumina was investigated. Figure 6.4 shows SEM images of bare undoped (Zr-2) and alumina-coated (~47 nm) zirconia microparticles (Zr-2-ALD) after heat treatments at temperatures between 1100 and 1500 °C for 3 h. Closer inspection reveals that both undoped zirconia and

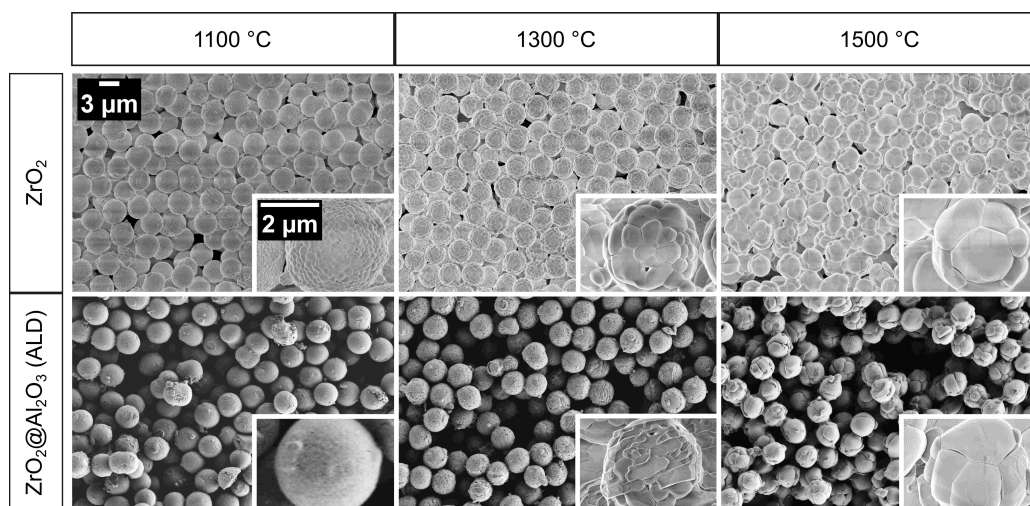


**Figure 6.4** – SEM images of bare  $ZrO_2$  (Zr-2) and  $ZrO_2-Al_2O_3$  microparticles (Zr-2-ALD) from ALD after temperature treatment at 1100, 1300, and 1500 °C for 3 h (heating rate:  $5\text{ °C}\cdot\text{min}^{-1}$ ). SEM images with higher magnification (insets) reveal no significant differences in grain growth as the alumina coat delaminates from 1300 °C on.

alumina-coated zirconia microparticles show grain growth due to increasing temperature in a similar range. In the case of  $ZrO_2-Al_2O_3$  microparticles after ALD, the zirconia grains remain covered by alumina when annealed at temperatures up to 1100 °C. After annealing at 1300 °C or higher, alumina becomes porous and separates from zirconia cores leaving behind unprotected zirconia cores as clearly visible in Fig. 6.5. Here, SEM images were obtained by using an ESB detector for better contrast between the different elements. Interestingly, three different states of alumina delamination can be observed after heat treatment at 1300 °C (b). On the one hand, fully covered zirconia microparticles can be found, on the other hand, zirconia microparticles without any alumina coat were also detected. Furthermore, an intermediate state with partial alumina coverage and also visible zirconia grains was noticed. In accordance with the present results, previous studies by Furlan *et al.*[181] found that inverse opals from ALD of alumina on polystyrene (PS) spheres showed a similar behavior after PS burn-out and sintering at 1300 °C for 1 h. In their study, alumina shells first formed cracks before widening of these openings yielded island-like structures after 8 h temperature treatment at 1300 °C (compare Fig. 6.5(b)). At higher temperatures, alumina forms vermicular structures.[181–185] These filter-like structures can be found as one of three intermediate states after 1300 °C (see Fig. 6.5(b)), but they are absent at higher temperatures. In

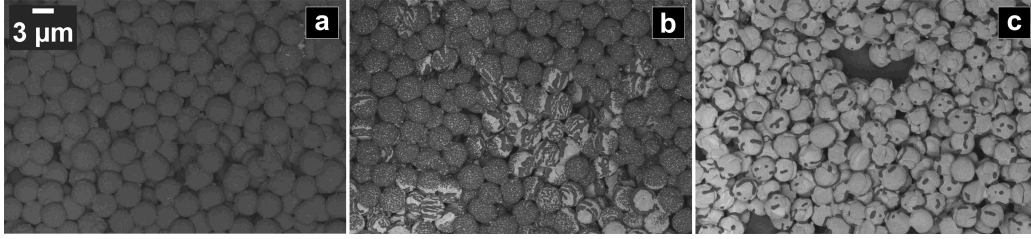


**Figure 6.5** – SEM images from ESB detector of  $\text{ZrO}_2\text{-Al}_2\text{O}_3$  microparticles (Zr-2-ALD) from ALD of alumina after temperature treatment at 1100 (a), 1300 (b), and 1500 °C (c) for 3 h (heating rate:  $5\text{ °C}\cdot\text{min}^{-1}$ ). Delamination of alumina becomes visible at 1300 °C in three differently pronounced states.

contrast to examples from the literature, the alumina network was separated from the zirconia spheres after heat treatment at 1500 °C in the present study (see Fig. 6.5(c)).

Moreover, the crystalline structure after thermal exposure up to 1500 °C (3 h) was investigated. Figure 6.6 presents the XRD patterns (a, b) and a comparison of thereby determined grain sizes (c) of bare (Zr-2) and alumina-coated zirconia microparticles from ALD (Zr-2-ALD) after thermal treatment. The zirconia cores have a tetragonal crystalline phase after calcination at 600 °C for 3 h. Interestingly, there were differences in martensitic phase transformation ratios after 800 °C. While bare zirconia microparticles nearly fully transformed to the monoclinic phase (a), alumina-covered particles still exhibited a significant tetragonal phase fraction (b). This result may be explained by the fact that the alumina coat could suppress the martensitic phase transformation due to inhibition of the volume expansion, which is needed for the  $t \rightarrow m$  phase transformation. [2] At 1000 °C and higher, both bare zirconia and alumina-coated zirconia particles exhibited the monoclinic crystalline phase up to 1500 °C. For bare  $\text{ZrO}_2$  particles after 1100 °C, a faint reflex at  $\sim 55^\circ$  appears, which originates from the sapphire substrate (a).

Additionally, the average grain sizes were calculated by using the Scherrer equation from XRD data up to 800 °C. At higher annealing temperatures the grain sizes became too large ( $> 80\text{ nm}$ ) for analysis by the Scherrer equation due to peak broadening of the XRD instrument. For details concerning the grain size analysis by the Scherrer equation see Section 4.2.2. To determine larger grains for higher temperatures, SEM images were used for graphical evaluation (see appendix, Fig. 8.5). For zirconia microparticles with an intact alumina coat and hence covered grains, cross sections were used to analyze the inner grain sizes. The results from pre-

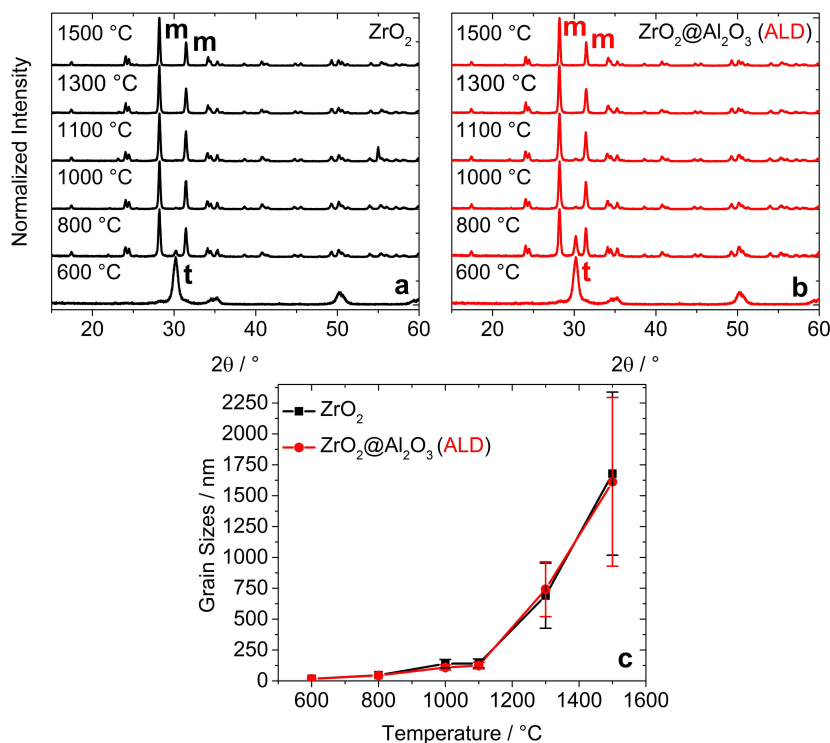


**Figure 6.6** – XRD data of bare  $ZrO_2$  (Zr-2, a) and  $ZrO_2-Al_2O_3$  microparticles (Zr-2-ALD, b) from ALD of alumina after temperature treatment at 600, 1000, 1100, 1300, and 1500 °C for 3 h (heating rate:  $5^\circ C \cdot min^{-1}$ ). Crystallite sizes (grain sizes) of bare  $ZrO_2$  (black) and  $ZrO_2-Al_2O_3$  (red) particles (c).

liminary analysis are depicted in Figure 6.6(c). From this data it can be seen that the grain sizes of both uncoated zirconia microparticles and alumina-coated zirconia microparticles from ALD show similar values over the entire temperature range, whereby their standard deviation regimes overlap. One drawback of the alumina layer from ALD is the delamination due to aggregation starting at 1300 °C. This process led to exposed and unprotected zirconia microparticles as shown in Figure 6.5. Thus, this observation makes the concept of alumina-coated zirconia microparticles unsuccessful for improvement of TBCs.

The results of this section indicate that the tetragonal phase of undoped zirconia microparticles could hardly be stabilized by an alumina shell from ALD. Furthermore, there is no difference in the grain growth behavior as the alumina shell separates from the zirconia cores at higher temperatures.

Therefore, the next section moves on to discuss the high-temperature stability of  $ZrO_2-Al_2O_3$  composite microparticles after PSM. In this case, the alumina depo-

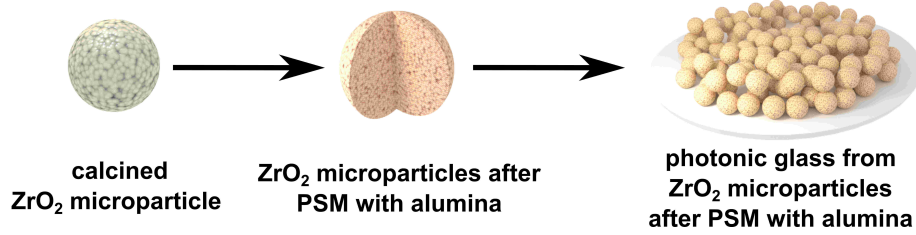


**Figure 6.7** – Preparation process of photonic glasses from  $\text{ZrO}_2$  microparticles after PSM with alumina. First, calcined ( $600\text{ }^\circ\text{C}$ , 3 h) bare zirconia microparticles were post-synthetically modified with alumina as explained in Section 8.2. Second, the obtained  $\text{ZrO}_2\text{-Al}_2\text{O}_3$  composite particles were deposited on sapphire substrates to yield photonic glasses.

sition occurred by sol-gel synthesis and hence, dispersed zirconia particles were treated with alumina in a post-synthetic process. In contrast to ALD of alumina, the particle assembly of photonic glasses on sapphire substrates followed after the alumina deposition.

### 6.1.3 Post-synthetic modification of $\text{ZrO}_2$ microparticles with alumina

As already mentioned before, PSM of  $\text{ZrO}_2$  microparticles with alumina was performed by using two different alumina precursors in a sol-gel synthesis (see Section 8.2 for experimental details). Here, the results for  $\text{ZrO}_2\text{-Al}_2\text{O}_3$  composite particles from aluminum chloride by using PVP as coupling agent are presented. The results of the PSM by using aluminum *i*-propoxide and those without the use of PVP as coupling agent will not be discussed in this dissertation as the results are very similar independent of the Al-precursor and the use of PVP.

The experimental preparation process is shown in Fig. 6.7. Here, calcined ( $600\text{ }^\circ\text{C}$ , 3 h)  $\text{ZrO}_2$  microparticles were modified by alumina in a post-synthetic process. Afterwards, the  $\text{ZrO}_2\text{-Al}_2\text{O}_3$  composite particles can be assembled to photonic glasses on sapphire substrates.

#### *Ex situ* heating experiments

SEM images from heating experiments of the  $\text{ZrO}_2$  (Zr-1) and  $\text{ZrO}_2\text{-Al}_2\text{O}_3$  composite particles (Zr-1-PSM) after heat treatment at  $1000$  and  $1200\text{ }^\circ\text{C}$  for 3 h with

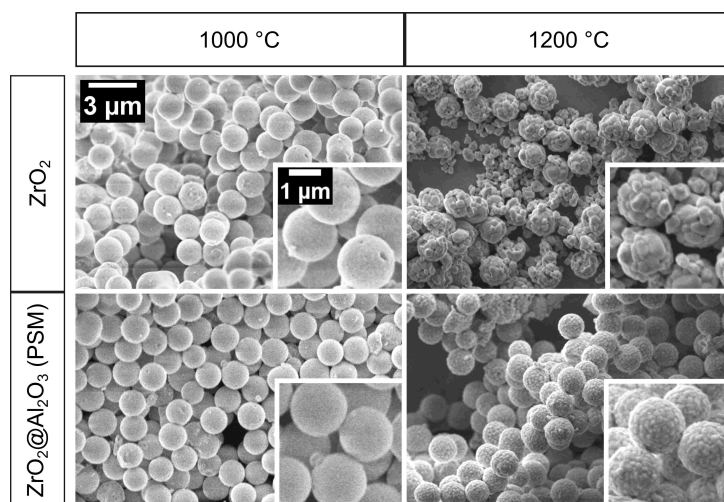


**Figure 6.8** – SEM images of bare  $ZrO_2$  (Zr-1) and  $ZrO_2-Al_2O_3$  composite microparticles (Zr-1-PSM) from sol-gel PSM with alumina after temperature treatment at 1000 and 1200 °C for 3 h (heating rate: 5 °C·min<sup>-1</sup>). SEM images with higher magnification (insets) reveal significant decreased grain growth after 1200 °C for  $ZrO_2-Al_2O_3$  composite particles compared to bare  $ZrO_2$  particles.

a heating rate of 5 °C·min<sup>-1</sup> and a cooling rate of  $\leq 5$  °C·min<sup>-1</sup> are shown in Figure 6.8.

The alumina-modified zirconia microparticles exhibit clearly an increased structural stability, while bare zirconia cores lose their integrity after 1200 °C. SEM images from Figure 6.8 can be compared with the XRD data from Figure 6.9, which show the crystalline structures and average grain sizes of bare  $ZrO_2$  (Zr-1; a, c) and  $ZrO_2-Al_2O_3$  composite (Zr-1-PSM; b, c) particles after calcination at 600 °C and annealing at temperatures up to 1200 °C. Noticeably at 1000 °C, the  $ZrO_2-Al_2O_3$  composite particles remain partially in the tetragonal phase, while bare zirconia cores already fully transformed to the monoclinic phase. After 1200 °C, both particle systems crystallized in the monoclinic phase. The investigation of grain sizes revealed that the grain growth of the alumina-modified zirconia particles is strongly inhibited yielding about half of the grain sizes compared to bare zirconia particles. This remarkable result is in good agreement with observations from the literature, where Srdic *et al.*[131] reported that the grain growth is effectively suppressed by the addition of alumina to nanosized powders of  $ZrO_2$  from chemical vapor deposition. Furthermore, Nazeri and Qadri[132] attributed the grain growth inhibition to constraint effects of alumina on zirconia grains. The obtained average grain size from SEM images by measuring surface grains of bare zirconia particles after

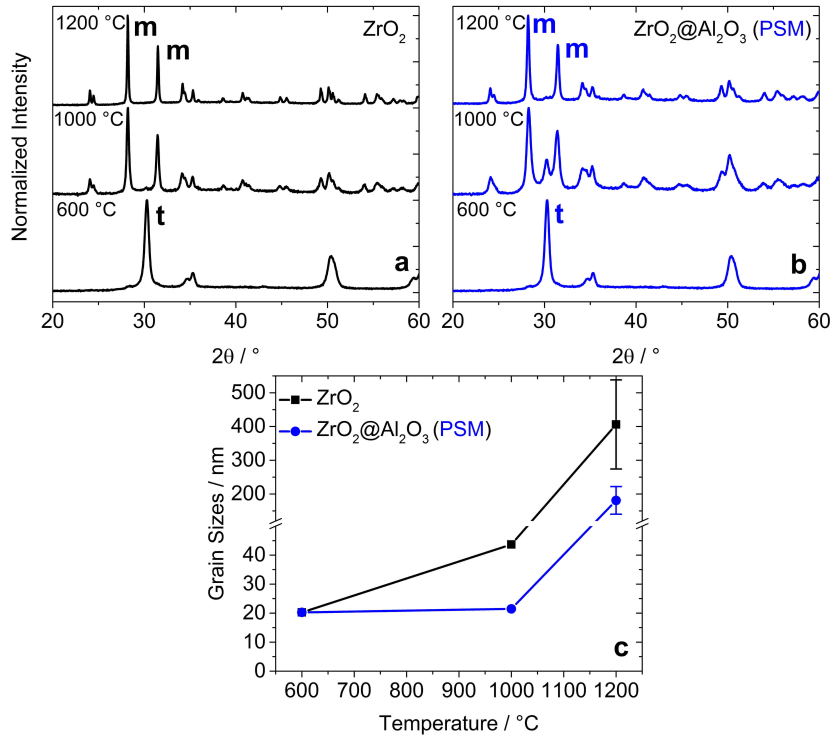


**Figure 6.9** – XRD data of bare ZrO<sub>2</sub> (Zr-1, a) and ZrO<sub>2</sub>–Al<sub>2</sub>O<sub>3</sub> composite microparticles (Zr-1-PSM, b) from sol-gel post-synthetic modification (PSM) with alumina after temperature treatment at 600, 1000, and 1200 °C for 3 h (heating rate: 5 °C·min<sup>-1</sup>). Crystallite sizes (grain sizes) of bare ZrO<sub>2</sub> (black) and ZrO<sub>2</sub>–Al<sub>2</sub>O<sub>3</sub> (blue) particles (c).

1200 °C thermal treatment was 406±132 nm, while 181±41 nm were determined for composite particles.

#### 6.1.4 Atomic layer deposition and post-synthetic modification of YSZ microparticles with alumina

After success of increasing the thermal stability and decreasing grain growth in undoped zirconia microparticles by sol-gel post-synthetic modification (PSM) with alumina, the core system was changed to YSZ (9.5 mol% Y) microparticles (YSZ-1, see Tab. 6.1) for further improvement of the thermal stability. Previous studies demonstrated that yttria doping decreases the grain growth by the solute-drag effect and therefore stabilizes the preferable tetragonal phase of zirconia.[2, 26, 27] These favorable properties can be combined with an alumina coating as an

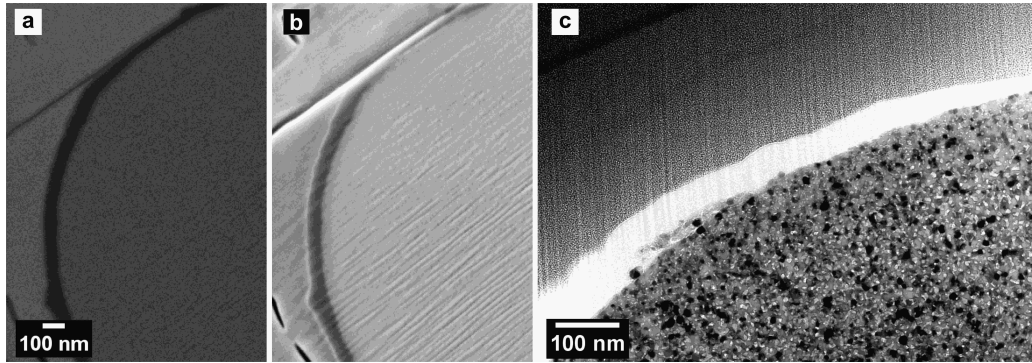


**Figure 6.10** – SEM images from ESB detector (a) and in-lens detector (b) of a FIB lamella from  $YSZ-Al_2O_3$  composite microparticle after coating with alumina by ALD. TEM image (c) of the  $YSZ-Al_2O_3$  composite microparticle showing small grains in the YSZ core after calcination at  $600\text{ }^\circ\text{C}$  (3 h).

oxygen barrier to prevent oxidation of the underlying bond-coat and superalloy in TBCs. Here, alumina-coating of YSZ microparticles using both, ALD and PSM, were investigated.

The alumina-coated YSZ microparticles from ALD were characterized by cross-sectional TEM and SEM from FIB preparation as shown in Fig. 6.10. Here, the SEM image (a) clearly shows that a homogeneous alumina coating was achieved by ALD, which is represented by different contrasts of YSZ and alumina in the energy selective backscattered (ESB) detector mode. Here, elements with higher atomic number (Zr) stronger scatter the incident electrons and therefore appear brighter in the image. Figure 6.10(b), obtained from YSZ-1-ALD with an in-lens detector, supports the finding of a  $\sim 47\text{ nm}$  intact alumina coat. The outer layer material is platinum from FIB lamella preparation to ensure an intact particle structure. Figure 6.10(c) provides a TEM image of the same alumina-coated YSZ microparticle lamella (YSZ-1-ALD), where the alumina layer appears bright in comparison due to the lowest atomic number yielding increased electron transmission. The YSZ core already exhibits a nano-grained structure after calcination at  $600\text{ }^\circ\text{C}$  for 3 h, clearly visible by different gray scales. Here, the different gray scales originate from different cut depths of the grains, the presence of porosity, and crystalline domain orientation. The investigation of grain sizes and crystalline phases will be discussed in the next section.

First, the high-temperature stability of photonic glasses built up from bare YSZ (YSZ-1), YSZ microparticles alumina-coated from ALD (YSZ-1-ALD), and YSZ

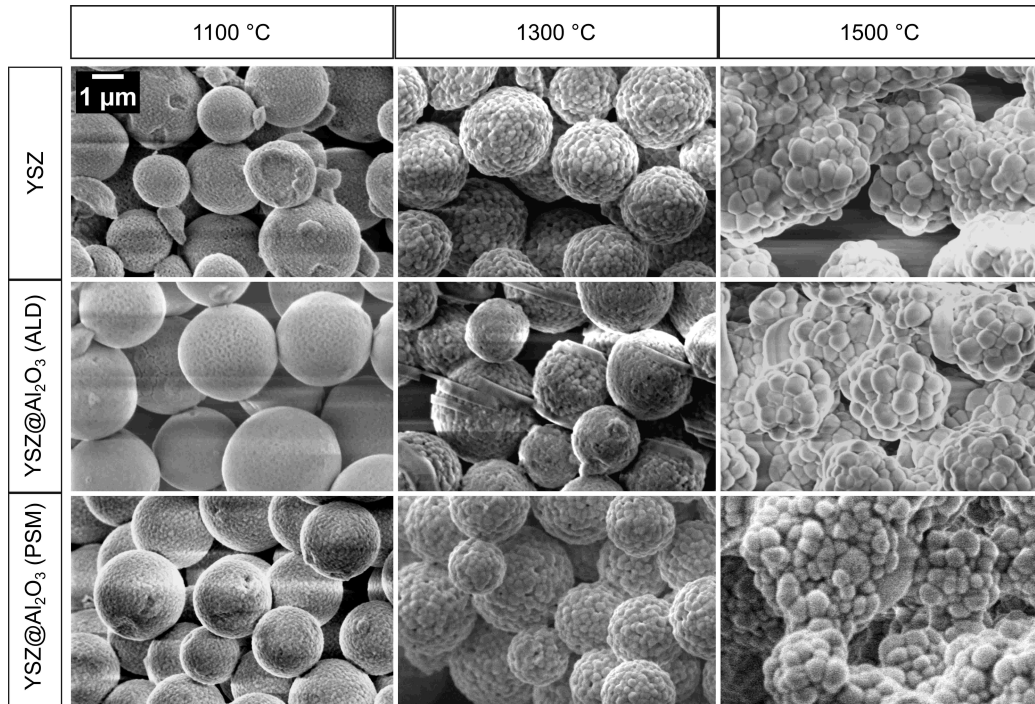


**Figure 6.11** – SEM images of bare YSZ (YSZ-1), alumina-coated YSZ microparticles from ALD (YSZ-1-ALD), and YSZ–Al<sub>2</sub>O<sub>3</sub> composite microparticles from PSM (YSZ-1-PSM) after heat treatment at 1100, 1300, and 1500 °C for 3 h (heating rate: 5 °C·min<sup>-1</sup>). No significant differences in grain growth were detected.

microparticles from PSM with alumina (YSZ-1-PSM) were investigated up to 1500 °C. SEM images of the YSZ, alumina-coated YSZ microparticles from ALD, and YSZ–Al<sub>2</sub>O<sub>3</sub> composite microparticles from PSM after thermal loading are provided in Figure 6.11.

A clear trend of increasing surface roughness and therefore increasing grain sizes with increasing temperature for all three samples was observed. From 1300 °C on, the grains are clearly visible in the SEM images, whereby the alumina from ALD separates from the YSZ core particles as already shown in Fig. 6.5. However, the degree of alumina and zirconia phase separation is stronger in the YSZ case compared to ZrO<sub>2</sub> particles. Here, predominantly uncovered YSZ particles and segregated alumina in between or on small areas of the core surfaces after thermal exposure at 1300 °C for 3 h were detected. In contrast to the preliminary analysis of undoped zirconia microparticles, the PSM of YSZ particles with alumina did also not lead to an improved high-temperature stability independent of the alumina precursor. A significant reduction of grain growth or a strong difference in phase

stability were not found. It should be mentioned that the YSZ core particles were larger than the before investigated  $ZrO_2$  particles and therefore, a positive influence on particle stability due to larger particle size and Y-doping was detected, which is already well-known.[2, 186]

Figure 6.12 shows a comparison of the crystalline structures of the YSZ (a), alumina-coated YSZ from ALD (b), and YSZ microparticles from PSM (c) after heating up to 1500 °C by XRD. The YSZ core particles are amorphous after sol-gel synthesis and first crystallize in tetragonal prime phase ( $t'$ ) after calcination at 800 °C for 3 h (a). The distorted crystalline structure can be attributed to the yttria-doping, as lattice constants change due to different sizes of  $Zr^{4+}$  and  $Y^{3+}$  ions. Thus, the  $\{110\}$  reflex at 35.3° shifts to 35.1° (a, inset). Since a mixed phase of  $t$  and  $t'$  phase is present after heating up to 1300 °C, the reflex can be found at 35.2°. After thermal treatment at 1500 °C, the monoclinic phase occurs additionally as small phase fractions for all three samples. These findings are consistent with that of Leib *et al.*,[2] who explained this observation by segregation of yttrium ions yielding formation of a Y-rich  $t'$  phase and a Y-lean  $t$  phase. After 1500 °C, small  $\{-111\}$  and  $\{111\}$  monoclinic peaks appear, while the monoclinic phase fraction is more pronounced for bare YSZ microparticles compared to  $YSZ-Al_2O_3$  particles from ALD and PSM. Thus, the alumina coating slightly suppresses the martensitic phase transformation. In contrast to earlier findings,[165] however, no evidence of crystalline alumina was detected except for a faint reflex at  $\sim 27^\circ$  after heat treatment at 1300 °C (b), which might originates from the sapphire substrate. A possible explanation for this is that the  $\sim 47$  nm alumina layer on  $\sim 2.6$   $\mu m$  YSZ microparticles only accounts for  $\sim 3.5\%$  of total weight fraction. Additionally, this assumption does not consider that the contact points between the particles are not covered with alumina. Furthermore, it is possible that the alumina deposition in lower layers was not as effective as on upper layers due to hindered accessibility over time during coating by ALD. These factors lead to a lower mass fraction of alumina than 3.5% and might explain the missing crystalline alumina signals in the XRD patterns after temperature treatment at  $\geq 1100$  °C (Fig. 6.6). Overall, the thin alumina coat exhibits only few lattice planes leading to broad signals with weak intensities due to a low mass fraction. Furthermore, alumina could be amorphous, which will not be detected by XRD.

The grain sizes from YSZ, alumina-coated YSZ from ALD, and  $YSZ-Al_2O_3$  microparticles from PSM are depicted in Figure 6.12(d). Average crystallite sizes

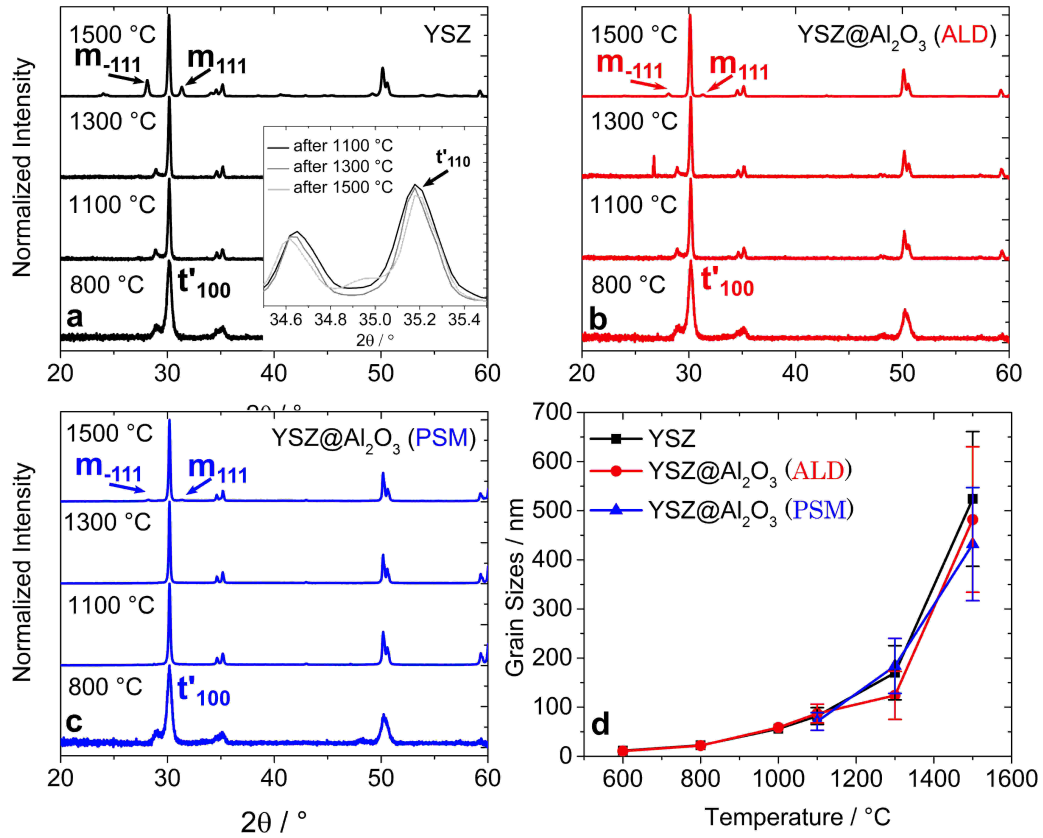


**Figure 6.12** – XRD data after temperature treatment up to 1500 °C (heating rate: 5 °C·min<sup>-1</sup>) of bare YSZ (YSZ-1, a), alumina-coated YSZ (YSZ-1-ALD) from ALD (b), and YSZ–Al<sub>2</sub>O<sub>3</sub> composite microparticles (YSZ-1-PSM) from PSM (c). Comparison of grain sizes (crystallite sizes) from bare YSZ (d, black), alumina-coated YSZ from ALD (d, red), and YSZ–Al<sub>2</sub>O<sub>3</sub> composite microparticles from PSM (d, blue) obtained by using the Scherrer equation (up to 1100 °C) and surface grains from SEM for higher temperatures. YSZ, alumina-coated YSZ from ALD, and YSZ–Al<sub>2</sub>O<sub>3</sub> composite microparticles from PSM showed similar grain growth behavior after thermal loading.

were determined from XRD data using the Scherrer equation up to 1100 °C. For higher temperatures, SEM images were used to determine the average grain size by analysis of the visible grains at the zirconia surface. Overall, the obtained grain sizes of YSZ, alumina-coated YSZ from ALD, and YSZ–Al<sub>2</sub>O<sub>3</sub> particles from PSM are smaller compared to undoped ZrO<sub>2</sub> particles from similar particle size, but exhibit among each other similar values up to 1500 °C. An overlap of the grain size standard deviations even for higher temperatures was observed leading to

the conclusion that there is hardly any additional grain growth inhibition of YSZ microparticles by alumina coating from ALD and PSM.

In summary, these results suggest that there is a correlation between PSM with alumina and increased temperature stability of undoped zirconia microparticles. Here, an improved structural stability, decreased grain sizes, and an inhibited martensitic phase transformation were obtained. These effects are hardly observed with such significance, when performing alumina encapsulation by ALD. Furthermore, alumina deposition on YSZ microparticles using both methods only led to slight inhibition of martensitic phase transformation at high-temperatures (1500 °C), whereby no significant differences in grain sizes were detected.

#### 6.1.5 EDX-mapping

After successful enhancement of the temperature stability (tetragonal phase stabilization and inhibition of grain growth) of undoped zirconia microparticles by PSM with alumina, the composite structure was investigated by EDX-mapping of as-synthesized (dried at 80 °C for 4 h) and heat-treated (1200 °C, 3 h) microparticle composites. For this purpose, FIB lamellae (thickness  $\leq 100$  nm) from  $ZrO_2-Al_2O_3$  composite particles were prepared and investigated by TEM. The results from EDX mappings of Zr, Al, and O are presented in Figure 6.13. High-angle annular dark-field scanning electron microscopy (HAADF-STEM) images are shown for comparison.

Surprisingly, the zirconium and aluminum element distributions do not show a typical core@shell structure. From EDX data in Figure 6.13 it is apparent that Al shows a homogeneous spatial distribution over the entire zirconia core after synthesis. This result is unexpected as not even a higher Al concentration at the zirconia surface was detected. As a consequence, it can be deduced that aluminum diffuses into the zirconia cores during sol-gel PSM yielding Al-doping rather than an alumina encapsulation. High resolution TEM investigation could not show structured Al at the grain boundaries of nanosized zirconia grains after calcination at 600 °C. Nevertheless, these results have to be interpreted with caution, as small scale structuring of Al on small zirconia grains cannot be disproved. To the best of my knowledge, post-synthetic doping of zirconia microparticles with alumina by sol-gel synthesis has never been reported. This remarkable improvement and new

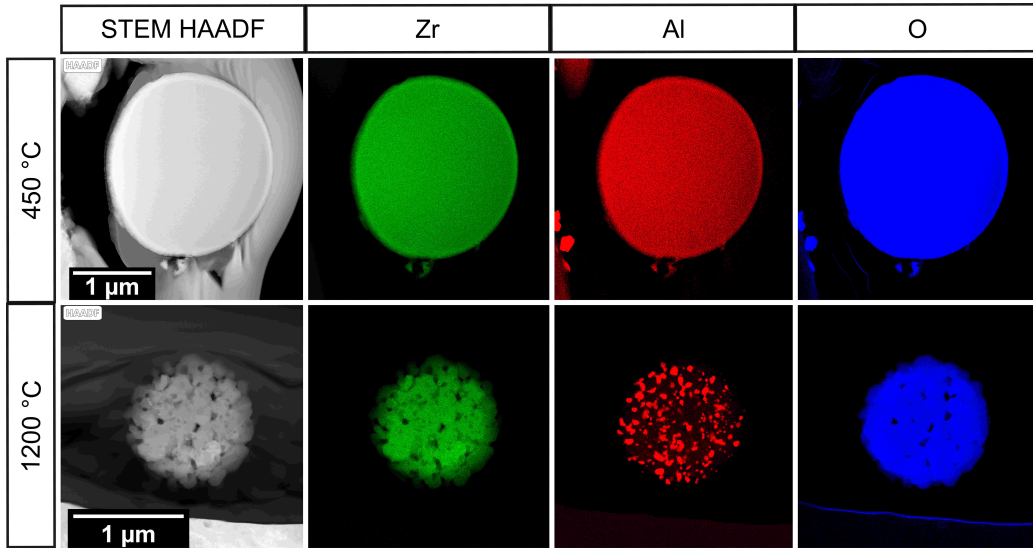


**Figure 6.13** – HAADF-STEM images and EDX-mapping data (Zr:green, Al:red, O:blue) of cross-sectional lamellae prepared from  $\text{ZrO}_2\text{-Al}_2\text{O}_3$  composite microparticles (Zr-1-PSM) after calcination at 450 and 1200 °C. The lamellae were prepared from  $\text{ZrO}_2\text{-Al}_2\text{O}_3$  composite microparticles using FIB technique. The apparent diameter of the FIB lamellae after heat treatment at 1200 °C is significantly smaller than the FIB lamellae after 450 °C, suggesting that the FIB cut through this particle was off-center.

possibility of doping open up a straightforward method for post-synthetic modification and stabilization of zirconia particles. Numerical results of the elemental composition (O, Al, Zr), representing integral values sampled over a specific area of the zirconia core (after 450 °C) are presented in Tab. 6.2 and reveal an Al mass fraction of  $\sim 2.8\%$ .

The apparent diameter of the FIB lamellae after heat treatment at 1200 °C is significantly smaller than the FIB lamellae after 450 °C, suggesting that the FIB cut through this particle was off-center. Volume and mass losses of such zirconia microparticles are nearly completed after heat treatment at 450 °C as shown by a previous study.[1] Interestingly, there were differences in spatial distribution of Al after heat treatment at 1200 °C for 3 h (see Fig. 6.13). Here, strong segregation of Al occurred yielding a separation of zirconia and alumina. In accordance with these results, previous studies have demonstrated that Al segregates in zirconia during the sintering process forming precipitations at the grain boundaries which efficiently suppress grain growth.[131, 133] These results are likely to be related to pinning of grain boundaries due to segregated dopant.[131] As a result of this, it can

**Table 6.2** – Elemental composition (O, Al, Zr) of zirconia cores of  $ZrO_2-Al_2O_3$  composite microparticles after calcination at 450 °C. The tabulated values were obtained from EDX mappings of a FIB-prepared lamella (from Fig. 6.13) by integrating the EDX signals over specific areas.

Element	Family	Atomic fraction (%)	Atomic error (%)	Mass fraction (%)	Mass error (%)
O	K	61.3	8.1	26.1	2.3
Al	K	4.5	1.1	2.8	0.6
Zr	K	34.2	6.2	71.1	10.8

be assumed that PSM by using alumina leads to significantly reduced grain growth and stabilizes the tetragonal phase in zirconia particles due to the solute-drag effect, similar to yttrium.

### 6.1.6 Optical properties

The next section of this work determines the optical properties of photonic glasses on sapphire substrates made of  $ZrO_2-Al_2O_3$  (Zr-2-ALD) and  $YSZ-Al_2O_3$  (YSZ-1-ALD) microparticles alumina-coated by ALD. Furthermore, both bare  $ZrO_2$  (Zr-2) and  $YSZ$  (YSZ-1) microparticles served as reference. Heat treatments up to 1500 °C were performed to characterize the change in reflectivity after thermal loading in the near infrared (NIR)/mid infrared (MIR) wavelength range, as broadband reflectors in this range are needed for desirable high-temperature applications such as TBCs.[187] Diffuse reflection spectra of  $ZrO_2$  (a),  $YSZ$  (b),  $ZrO_2-Al_2O_3$  from ALD (c), and  $YSZ-Al_2O_3$  from ALD (d) after heat treatment in the temperature range of 80 to 1500 °C are shown in Figure 6.14.

It is apparent from this figure that very few changes appear in reflection after thermal loading for both bare core particles ( $ZrO_2$  and  $YSZ$ ) and alumina-coated particles ( $ZrO_2-Al_2O_3$  and  $YSZ-Al_2O_3$ ) in the wavelength range from 1 to 5  $\mu m$ . The average diffuse reflection from an integrating sphere was  $\sim 50\%$  independent of the sample. For purpose of a complete alumina coating by ALD even in the lower layers of the PG, the layer thickness is limited to  $\sim 10 \mu m$ . To achieve a higher reflection, the layer thickness needs to be increased as already shown in the

## 6 Results and Discussion

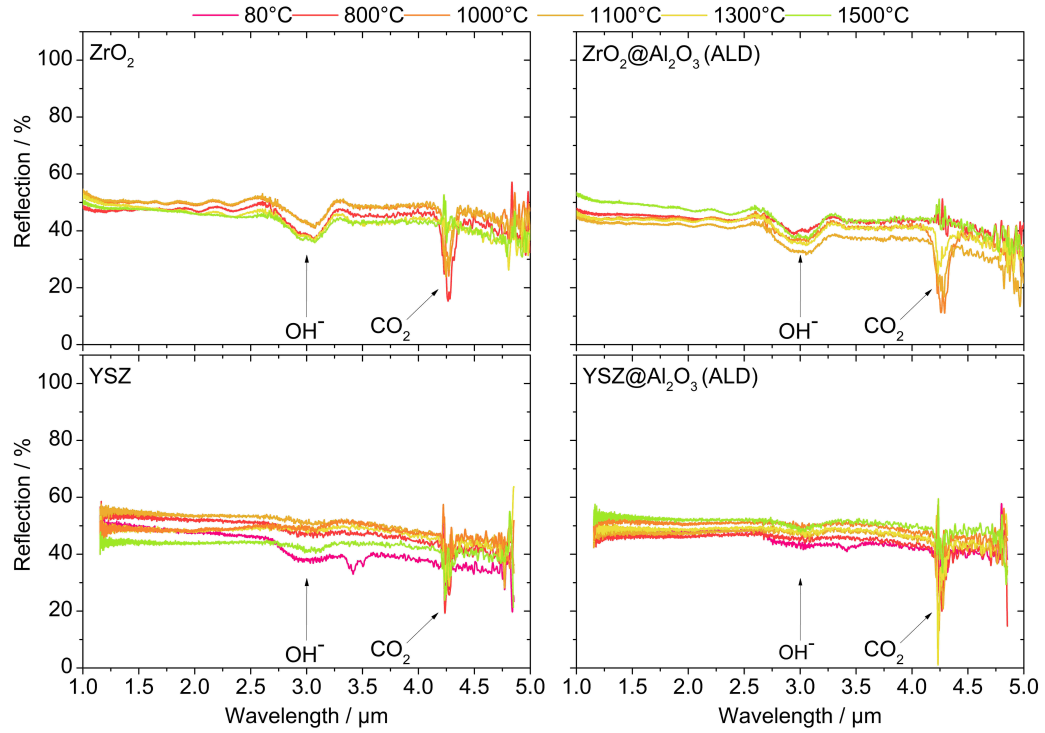


**Figure 6.14** – Diffuse reflection spectra of  $\text{ZrO}_2$  (Zr-2, a), YSZ (YSZ-1, b),  $\text{ZrO}_2\text{-Al}_2\text{O}_3$  from ALD (Zr-2-ALD, c), and YSZ- $\text{Al}_2\text{O}_3$  from ALD (YSZ-1-ALD, d) after heat treatment in the temperature range of 80 to 1500 °C.

literature.[2] In contrast to alumina-coated PGs from ALD, the layer thickness of PGs built up by  $\text{ZrO}_2\text{-Al}_2\text{O}_3$  and YSZ- $\text{Al}_2\text{O}_3$  composite particles from PSM with alumina would not be limited as the PG deposition process follows after PSM. Therefore, a higher overall reflection could be achieved. The reflection of such photonic glasses was not investigated in this study, but, as demonstrated in the SEM and XRD investigations, it is expected that the composite particles are even more stable under thermal loading.

Figure 6.14 reveals that bare  $\text{ZrO}_2$  and YSZ particles,  $\text{ZrO}_2\text{-Al}_2\text{O}_3$ , and YSZ- $\text{Al}_2\text{O}_3$  particles from ALD show a large dip in reflection between 2.5  $\mu\text{m}$  and 3.5  $\mu\text{m}$ . In this wavelength range, free hydroxide groups of the zirconia surface absorb the incident radiation. At  $\sim 4.2 \mu\text{m}$ , all four samples exhibit a narrow band absorption due to atmospheric  $\text{CO}_2$  in the chamber of the spectrometer.

### *6.1 ZrO<sub>2</sub>-Al<sub>2</sub>O<sub>3</sub> and YSZ-Al<sub>2</sub>O<sub>3</sub> composite microparticles*

In conclusion, the results of the optical characterization suggest that alumina encapsulation of zirconia by ALD does not influence the optical properties after thermal loading up to 1500 °C, which remained unchanged.

## 6.2 ZrO<sub>2</sub>@SiO<sub>2</sub> and YSZ@SiO<sub>2</sub> core@shell submicron particles

Parts of the following section have been published in RSC Advances 9 (2019), pp. 26902-26914. doi 10.1039/C9RA05078G.

Titel: Synthesis and thermal stability of ZrO<sub>2</sub>@SiO<sub>2</sub> core-shell submicron particles

Authors: Maik Finsel<sup>1</sup>, Maria Hemme<sup>1</sup>, Sebastian Döring<sup>1</sup>, Jil Rüter<sup>1</sup>, Gregor T Dahl<sup>1</sup>, Tobias Krekeler<sup>2</sup>, Andreas Kornowski<sup>1</sup>, Martin Ritter<sup>2</sup>, Horst Weller<sup>1</sup>, Tobias Vossmeier<sup>1</sup>

<sup>1</sup>*Institute of Physical Chemistry, University of Hamburg, Grindelallee 117, D-20146 Hamburg, Germany*

<sup>2</sup>*Electron Microscopy Unit, Hamburg University of Technology, Eißendorfer Straße 42, D-21073 Hamburg, Germany*

As first author, I was involved in writing the manuscript and developed the work plan to yield ZrO<sub>2</sub>@SiO<sub>2</sub> core@shell submicron particles. I synthesized most of the core@shell particles of this study and supervised the work of Maria Hemme, Sebastian Döring, and Jil Rüter who were doing their bachelor thesis (Maria Hemme) and advanced practical research placements (Sebastian Döring, Jil Rüter) in our research group. Data acquisition was carried out by me (SEM, TEM, XRD) and in collaboration with the co-authors Tobias Krekeler and Andreas Kornowski (TEM, EDX). Data evaluation was carried out by me (SEM, TEM, EDX, XRD, grain size determination) and in collaboration with the co-authors Tobias Krekeler, Andreas Kornowski, and Gregor Dahl (XRD, EDX, Rietveld). In addition to work covered in the manuscript, YSZ@SiO<sub>2</sub> core@shell submicron particles were also synthesized in this project to yield structural coloration. The optical properties and high-temperature stability of these YSZ@SiO<sub>2</sub> core@shell submicron particles are characterized and discussed in the last part of this section.

### 6.2.1 Synthesis of ZrO<sub>2</sub>@SiO<sub>2</sub> core@shell submicron particles

Fig. 6.15 shows the strategy, which was used for the sol-gel synthesis of ZrO<sub>2</sub>@SiO<sub>2</sub> core@shell particles. The main focus was to explore the synthesis and properties of

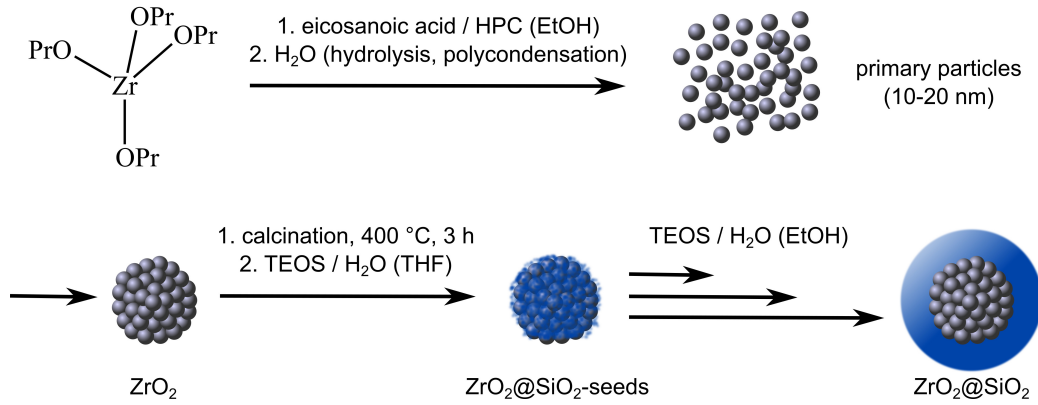


**Figure 6.15** – Sol-gel synthesis of  $ZrO_2@SiO_2$  core@shell particles: First, primary particles are formed by hydrolysis of zirconium *n*-propoxide and subsequent polycondensation. The primary particles aggregate and form  $ZrO_2$  submicron particles, which are calcined at 400 °C. Next,  $SiO_2$  seeds are deposited onto the particles by treatment with TEOS/ $H_2O$  in THF. After removing primary silica particles, closed  $SiO_2$  shells are deposited via a seeded growth process by successive addition of TEOS/ $H_2O$  in ethanol.

submicron core@shell particles with core sizes ranging from 100 to 400 nm. Such particles are of significant interest for photonic applications in the visible range of the light spectrum, such as structural colors[6] and the design of optical materials with adjustable refractive index.[7] Because grain coarsening and the  $t \rightarrow m$  transition (see Section 4.2) proceed in smaller submicron particles at lower temperatures than in larger micrometer-sized particles,[1] they are especially suited to study possible grain growth attenuation and phase stabilization via silica encapsulation.

Based on previous works,[62, 145, 146, 188, 189] our research group reported a facile sol-gel method for the synthesis of zirconia submicron particles with diameters ranging from 0.4 to 0.9  $\mu m$ . [1] In that approach, zirconia particles were formed by the hydrolysis of zirconium alkoxide precursors in the presence of carboxylic acid stabilizers. In order to further decrease the particle size for the present study, the previous protocol was modified by adjusting various parameters, including the stabilizer composition and the amount of water added, as detailed in Section 8.

As the addition of HPC seems to favor the stabilization of relatively small particles (see Section 4.3.1),[144] HPC was used (in addition to previously used eicosanoic acid) as stabilizer for the synthesis of  $ZrO_2$  particles with diameters below 0.4  $\mu m$ . This approach yielded spheroidal particles with a mean diameter of  $\sim 311$  nm (as-synthesized, dried at 80 °C for 4 h) and a reasonably narrow size distribution

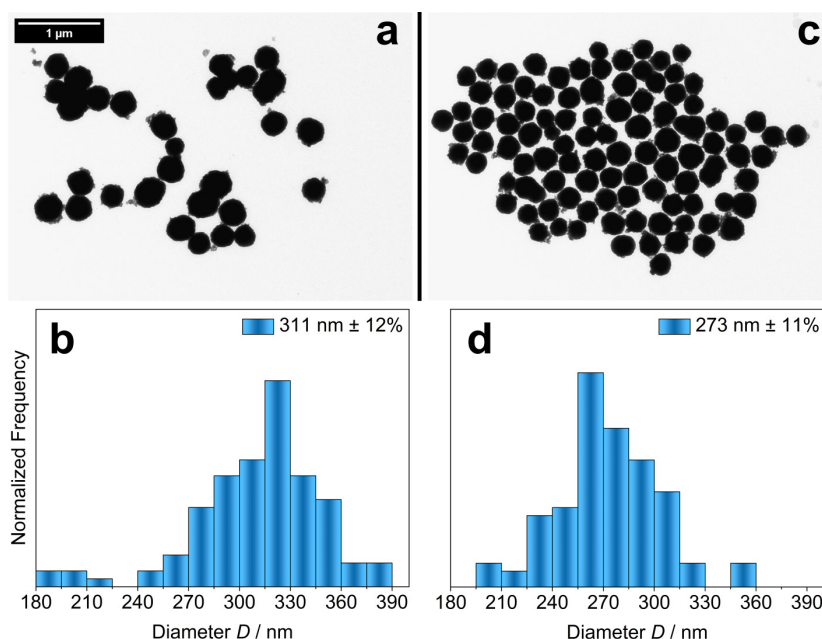


**Figure 6.16** – TEM images and sizing statistics of as-synthesized (a, b) and calcined (c, d) zirconia submicron particles. Average particle diameters and standard deviations were determined using *ImageJ* software by counting at least 100 particles.

(12% standard deviation) as shown in Fig. 6.16, where TEM images and size histograms of as-synthesized (a, b) and calcined (c, d) zirconia particles are presented. After synthesis, the purified particles were first dried at 80 °C for 4 hours and then calcined at 400 °C for 3 hours with a heating ramp of 5 °C·min<sup>-1</sup> and with a cooling rate of ≤5 °C·min<sup>-1</sup>. The calcined particles had a diameter of ~273 nm ± 11%.

Fig. 6.17(a) shows a representative TEM image of prepared zirconia cores. The TEM image captured at larger magnification (Fig. 6.17(a), inset) reveals a quite rough particle surface with occasionally attached ~10-30 nm sized granular structures. This morphology is attributed to the formation mechanism of the particles, in which primary particles with sizes in the 10-20 nm range are initially formed, which then aggregate to form the final particles, as indicated in Fig. 6.15.[62, 146, 186]

So far, only very few studies have been published regarding the synthesis of ZrO<sub>2</sub>@SiO<sub>2</sub> core@shell particles. As pointed out by Bai *et al.*[56] growing a homogeneous silica shell onto zirconia cores is challenging. They reported that pre-adsorption of PVP improved the colloidal stability of zirconia cores and enabled the deposition of homogeneous silica shells via hydrolysis of TEOS. However, a

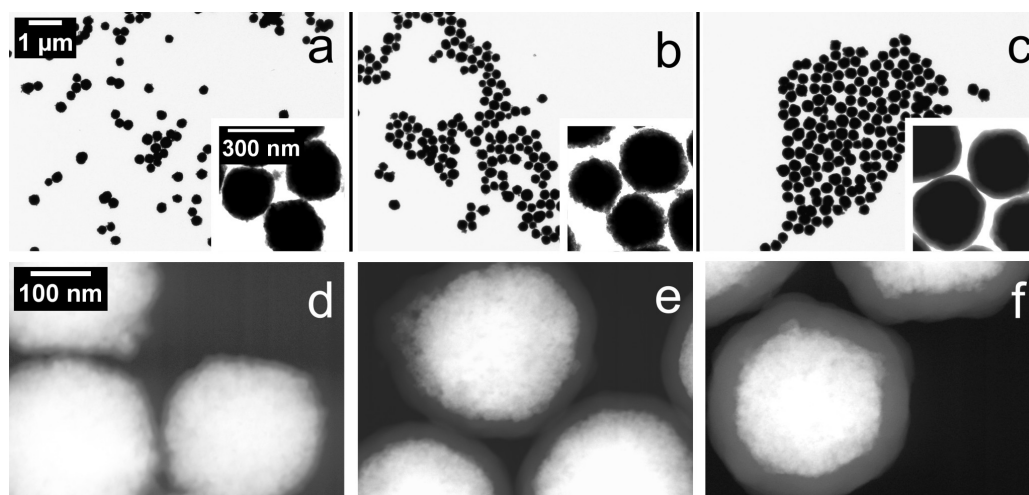


**Figure 6.17** – TEM images of calcined (400 °C, 3 h) zirconia core particles (a), pre-encapsulated and dried (80 °C, 4 h)  $\text{ZrO}_2@SiO_2$ -seeds particles (b), and dried (80 °C, 4 h)  $\text{ZrO}_2@SiO_2$  core@shell particles after deposition of a  $\sim 38$  nm thick silica shell (c). HAADF-STEM images of  $\text{ZrO}_2@SiO_2$  particles with initial shell thicknesses of  $\sim 26$  (d),  $\sim 38$  (e), and  $\sim 61$  nm (f). The particles shown in (d)-(f) were calcined at 450 °C for 3 h before TEM characterization.

polymeric adhesion layer may compromise the thermal stability of such core@shell particles. A different approach which does not require the need of a polymeric interfacial layer was reported by Yang *et al.*[7] In order to initiate the growth of homogeneous silica shells without inducing particle aggregation, they first adsorbed citric acid onto the particles' surface. This step decreased the negative zeta potential of the particles and, thus, enhanced the colloidal stability. Further, it was proposed that the adsorbed citric acid molecules served as a surface coupled catalyst for the hydrolysis of TEOS. As a result, they obtained non-aggregated  $\text{ZrO}_2@SiO_2$  particles with adjustable shell thicknesses. One drawback of using adsorbed citric acid is that it may impede high-temperature applications due to the organic interlayer between the core and the shell material.

Here, a facile seeded-growth approach for the growth of dense and homogeneous silica shells on zirconia cores without the need of any additional pre-adsorbed organic material was developed. In the first step, silica seeds were deposited onto the zirconia cores (pre-calcined at 400 °C for 3 h), as indicated in Fig. 6.15 and shown in Fig. 6.17(b). This was achieved by the hydrolysis of TEOS in THF in the presence of zirconia cores at 60 °C. The particles with silica seeds attached ( $\text{ZrO}_2@SiO_2$ -seeds particles) were then separated from non-bound silica clusters

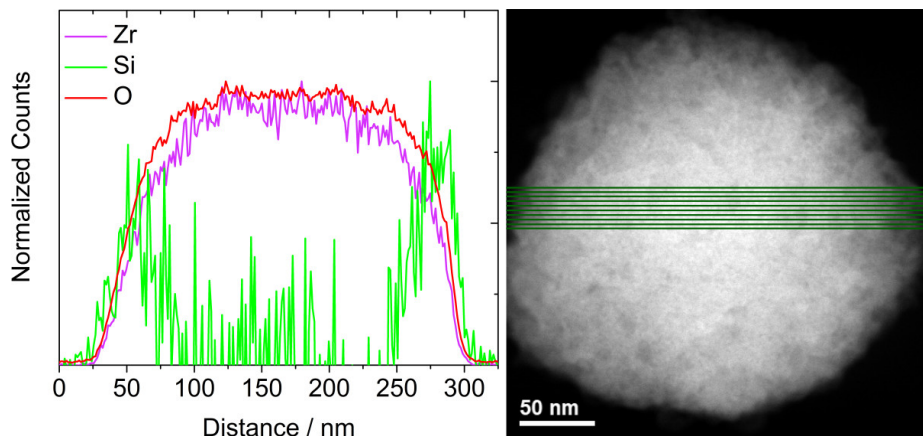


**Figure 6.18** – EDX line scan analysis of a pre-encapsulated  $\text{ZrO}_2@\text{SiO}_2$ -seeds particle. The silica sum line profile (10 lines, green) confirms successful deposition of silica on the particle’s surface (left). The green lines in the STEM image of the particle indicate the 10 line scan positions (right).

via centrifugation. After silica seed deposition and drying at  $80\text{ }^\circ\text{C}$  for 4 h, the TEM image in the inset in Fig. 6.17(b) indicates that the surface roughness of the particles was slightly more pronounced. However, in order to clearly prove the deposition of silica, the  $\text{ZrO}_2@\text{SiO}_2$ -seeds particles were characterized using EDX analysis. Fig. 6.18 shows an EDX line scan analysis across a single, pre-encapsulated zirconia particle. The Si signal clearly proves the successful deposition of silica at the particle’s surface.

In the second step, silica shells were grown on the seed-covered core particles. To this end, the seeded cores were redispersed in ethanol and, after addition of ammonium hydroxide solution, TEOS and water were added under mild heating ( $30\text{ }^\circ\text{C}$ ). In order to avoid secondary nucleation and growth of silica particles without zirconia cores, it was necessary to keep the TEOS concentration low. Therefore, TEOS and water were added gradually in portions and not at once. Finally, the obtained core@shell particles were separated from the remaining reaction mixture by centrifugation, resuspended in ethanol, and stored in suspension at room temperature until further use. In general, the thickness of the silica shells could be adjusted in the range from 10 to 180 nm by increasing the total amount of gradually added TEOS. However, for the present study, three samples of core@shell particles with different silica shell thicknesses were prepared. TEM images and sizing statistics of the silica encapsulated zirconia cores with three different shell thicknesses are presented in Fig. 6.19. After depositing the silica shells, the par-

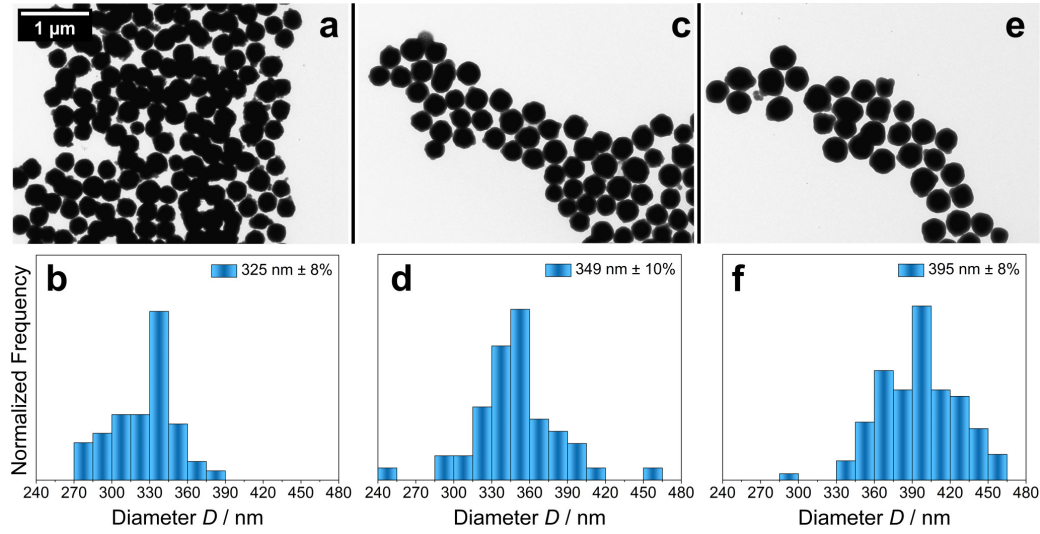


**Figure 6.19** – TEM images and sizing statistics of  $\text{ZrO}_2@\text{SiO}_2$  particles with different initial silica shell thicknesses (a,b:  $\sim 26$  nm; c,d:  $\sim 38$  nm; e,f:  $\sim 61$  nm). Average particle diameters and standard deviations were determined using *ImageJ* software by counting at least 100 particles.

ticles were isolated and dried at  $80^\circ\text{C}$  for 4 h, before their sizes were determined by TEM. With increasing shell thickness the average core@shell particle sizes were  $325\text{ nm} \pm 12\%$ ,  $349\text{ nm} \pm 10\%$ , and  $395\text{ nm} \pm 8\%$ . Subtracting the average core size (273 nm) from the average diameters of the  $\text{ZrO}_2@\text{SiO}_2$  particles returned silica shell thicknesses of  $\sim 26$ ,  $\sim 38$ , and  $\sim 61$  nm. Fig. 6.17, parts (c)-(f), show representative TEM and HAADF-STEM images of these  $\text{ZrO}_2@\text{SiO}_2$  particles after drying at  $80^\circ\text{C}$  for 4 h (c) and calcination at  $450^\circ\text{C}$  for 3 h (d)-(f). These images reveal a smooth, compact, and homogeneous shell covering the surface of the zirconia cores. With increasing shell thickness some narrowing of the particle size distribution was observed, as reported previously.[7, 56] Further, the HAADF-STEM images in Fig. 6.17 (d)-(f) reveal that calcining the  $\text{ZrO}_2@\text{SiO}_2$  particles at  $450^\circ\text{C}$  for 3 h decreased the initial silica shell thicknesses to  $\sim 10$ ,  $\sim 30$ , and  $\sim 50$  nm, respectively. This finding was attributed to the loss of residual water and organic components of the silica precursor, similar as reported previously for sol-gel derived zirconia microparticles.[1]

It is to emphasize that for successfully growing homogeneous silica shells it was necessary to first deposit the silica seed particles and then to separate the obtained seeded zirconia particles from the reaction mixture, before growing continuous silica shells. In a first set of experiments, continuous silica shells were tried to

grow directly onto the core particles by adding relatively high amounts of TEOS. These attempts only yielded SiO<sub>2</sub> particles loosely attached to the zirconia cores, similar as reported by Bai *et al.*[56] According to the model of LaMer,[190] too high TEOS concentrations lead to homonucleation and subsequent growth of pure silica particles, competing with silica shell growth. As a result, very heterogeneous samples were obtained, initially.

### 6.2.2 Thermal stability

#### Shape stability

In order to study the shape stability of ZrO<sub>2</sub>@SiO<sub>2</sub> core@shell particles upon heating they were calcined for three hours at 450, 800, 1000, and 1200 °C. Temperature profiles are provided in Section 8.3, Fig. 8.3. For each temperature, the heating rate was 5 °C·min<sup>-1</sup> and the target temperature was hold for 3 h. In the cooling process, the different ovens (see. Section 8.2) were programmed with a cooling rate of  $\leq 5$  °C·min<sup>-1</sup>. As reference sample, the bare core particles were heat-treated the same way.

SEM images presented in Fig. 6.20 show the bare ZrO<sub>2</sub> core particles, pre-encapsulated ZrO<sub>2</sub>@SiO<sub>2</sub>-seeds particles, as well as ZrO<sub>2</sub>@SiO<sub>2</sub> core@shell particles (initial shell thicknesses: ~26, ~38, and ~61 nm) after calcination. After 450 °C, the bare particles had a rough surface, most likely due to aggregation of primary particles during particle formation (see Fig. 6.15).[62, 146, 186] After calcination at 800 °C, however, significant grain coarsening was observed, leading to degradation of the original spheroidal particle shape. Upon calcination at 1000 °C, progressive grain growth destroyed the original shape of the bare particles. Finally, calcination at 1200 °C yielded larger faceted particles with irregular shape and a rather broad size distribution.

In striking contrast, the core@shell particles were stable and shape persistent independent of the silica shell thickness, even after calcination at 1000 °C. After heating to 450 °C, the shell surface appears rather smooth. Overall, this morphology did not change after increasing the temperature to 800 and 1000 °C. Finally, after calcination at 1200 °C also the core@shell particles disintegrated completely. The SEM images suggests that at such high-temperatures a molten mass of silica was formed which, upon cooling, solidified with enclosed fractured zirconia cores.

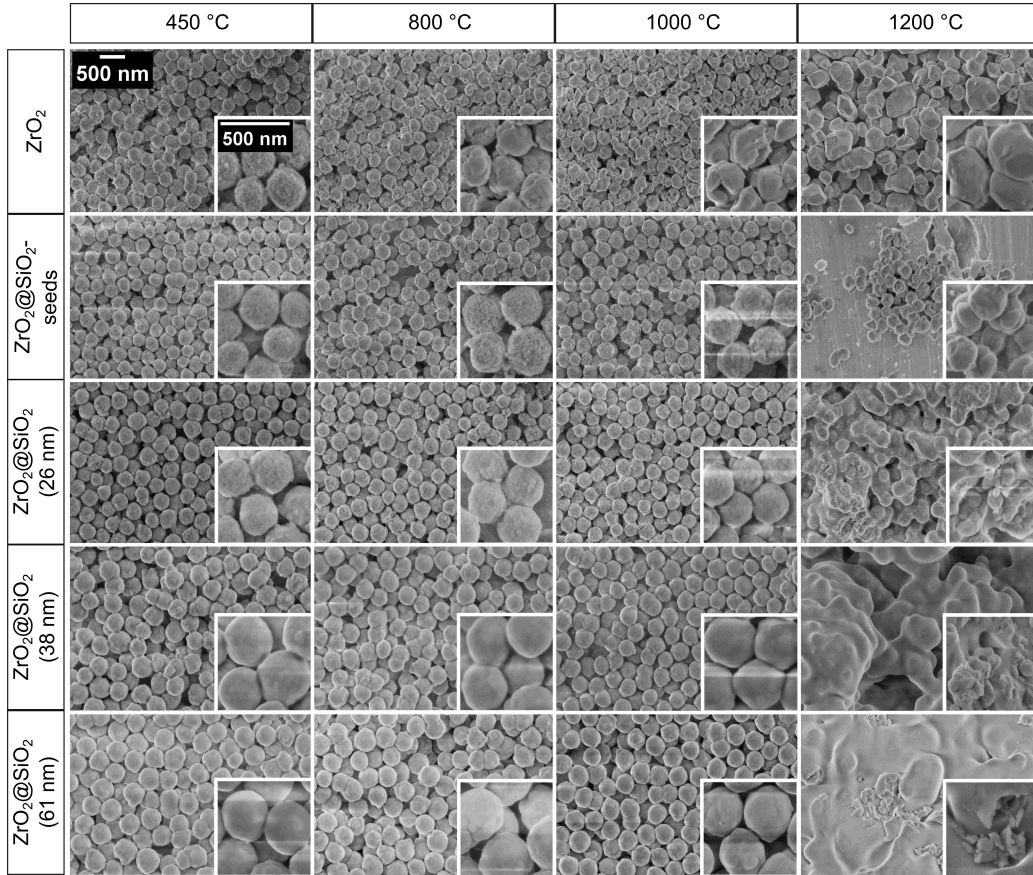


**Figure 6.20** – SEM images of bare  $ZrO_2$  cores, pre-encapsulated  $ZrO_2@SiO_2$ -seeds particles, and  $ZrO_2@SiO_2$  core@shell particles (initial shell thicknesses: 26, 38, and 61 nm) after calcination at 450, 800, 1000, and 1200 °C for 3 h (heating rate:  $5\text{ °C}\cdot\text{min}^{-1}$ ).

Interestingly, the spheroidal shape of the pre-encapsulated  $ZrO_2@SiO_2$ -seeds particles was also preserved after calcination at 1000 °C (see Fig. 6.20). However, in contrast to the  $ZrO_2@SiO_2$  core@shell particles, progression of grain coarsening with increasing temperature was clearly observable. After calcination at 1200 °C, the  $ZrO_2@SiO_2$ -seeds particles also lost their spheroidal shape, but the formed grains were obviously smaller than in case of the bare zirconia particles.

### Phase stability and grain growth

In accordance with previous studies,[1, 62, 63] the as-prepared zirconia particles are amorphous (see Fig. 6.21(a)). After calcining the bare core particles at 400 °C

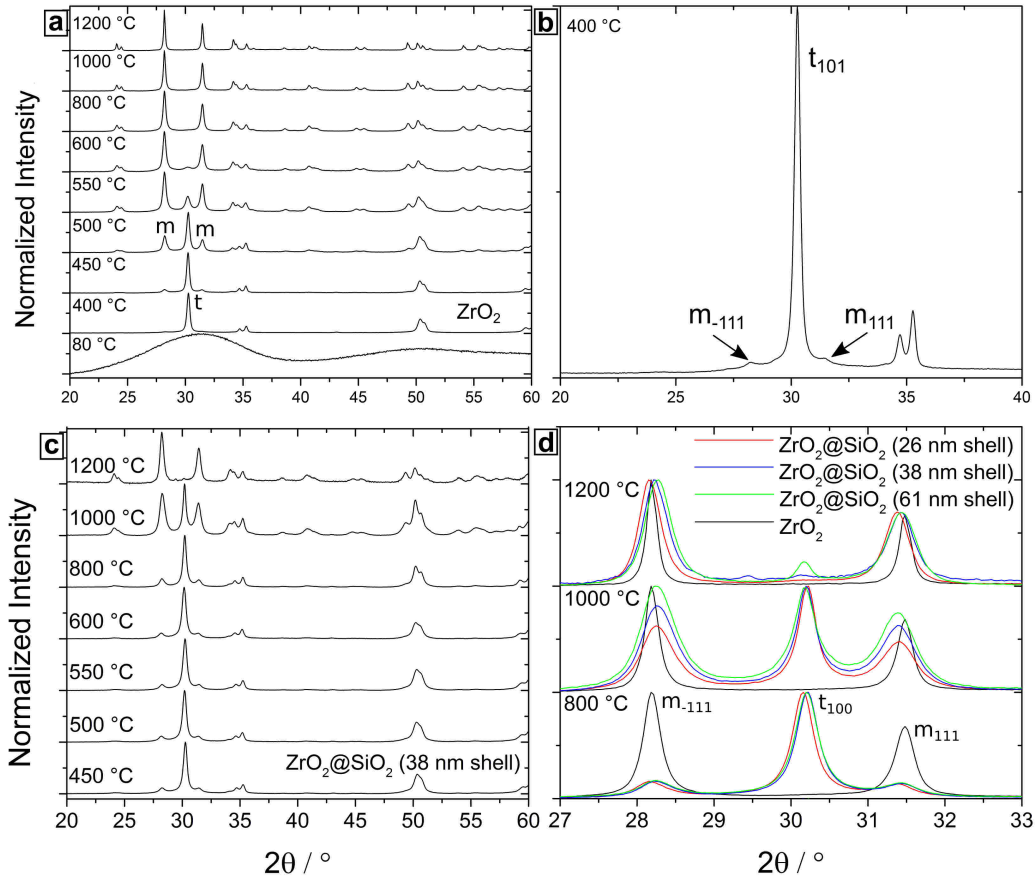


**Figure 6.21** – XRD data of bare  $\text{ZrO}_2$  submicron core particles (a), faint signals of monoclinic phase (-111 and 111 reflexes) for bare  $\text{ZrO}_2$  particles after 400 °C (b), XRD data of  $\text{ZrO}_2@SiO_2$  core@shell submicron particles with an initial shell thickness of 38 nm (c), and inset of XRD data from bare  $\text{ZrO}_2$  cores and the core@shell particles with 26, 38, and 61 nm thick silica shells (d). The samples were calcined for 3 h at different temperatures, as indicated (heating rate:  $5\text{ }^\circ\text{C}\cdot\text{min}^{-1}$ ). The bare zirconia cores transitioned almost completely to the monoclinic phase after heating above 600 °C, while the core@shell particles still exhibited significant tetragonal phase fractions (100 reflex) after heating to 1000 °C.

for 3 h, the amorphous phase mainly transitioned to the tetragonal phase. Only a very faint signal in the XRD data indicated the formation of the monoclinic phase (see Fig. 6.21(b)). However, after calcination at 450 °C a minor monoclinic fraction (<20 wt%, determined by Rietveld refinement) was detected. This early formation of the monoclinic phase is attributed to small isolated grains, which are loosely attached to the particles' surface (compare Fig. 6.17(a), inset). According to the literature, isolated tetragonal crystallites transition more rapidly to the monoclinic

phase than aggregated ones.[64] After calcination at higher temperatures, the bare zirconia particles gradually transformed to the monoclinic phase. Upon calcining at 600 °C only a very small residual tetragonal fraction is still observed and after heating to 800 °C the t→m transformation was complete.

The phase transitions presented in Fig. 6.21(a) are very similar to those reported earlier for somewhat larger submicron zirconia particles (diameter:  $\sim 0.75 \mu\text{m}$ , after calcination at 450 °C).[1] However, the particles started to transform to the monoclinic phase already at lower temperature. In general, tetragonal grain growth is less inhibited in smaller particles.[1, 191] Thus, in the case of presently studied smaller particles the critical tetragonal grain size, at which the phase transition occurs (see below), is already reached at a lower calcination temperature.

The XRD data shown in Fig. 6.21(c) reveal a striking influence of silica encapsulation on the phase stability. The data show the phase transitions of the  $ZrO_2@SiO_2$  core@shell particles with an initial shell thickness of  $\sim 38 \text{ nm}$ . While the bare zirconia cores had transformed almost completely to the monoclinic phase after calcination at 600 °C, the initial phase composition of the silica encapsulated cores ( $>80 \text{ wt\%}$  tetragonal,  $<20 \text{ wt\%}$  monoclinic, after 450 °C) changed only marginally after calcination at temperatures of up to 800 °C ( $\sim 70\%$  tetragonal,  $\sim 30\%$  monoclinic). The main phase transition to the monoclinic phase was observed after heating to 1000 °C. Finally, after calcination at 1200 °C, the t→m transformation was mostly completed ( $\geq 94\%$  monoclinic) and the core@shell structure of the particles was lost (see Fig. 6.20).

The  $ZrO_2@SiO_2$  particles with the initial shell thicknesses of  $\sim 26$  and  $\sim 61 \text{ nm}$  showed very similar phase transitions as those shown in Fig. 6.21(c). For comparison, Fig. 6.21(d) presents XRD data of core@shell particles with the three different shell thicknesses after calcination at 800, 1000, and 1200 °C. In all three samples the t→m transition occurred mainly when the samples were heated to 1000 °C. The data reveal only minor differences in phase stability.

In contrast, a clear difference in phase stability was observed for the pre-encapsulated  $ZrO_2@SiO_2$ -seeds particles. The XRD data shown in Fig. 6.22 clearly indicate that the initial treatment of the core particles with the silica precursor (TEOS) already led to some stabilization of the tetragonal phase. However, the effect was much less pronounced than in the case of the core@shell particles. A major fraction of the silica-seeded particles transformed already after calcination at 600 °C

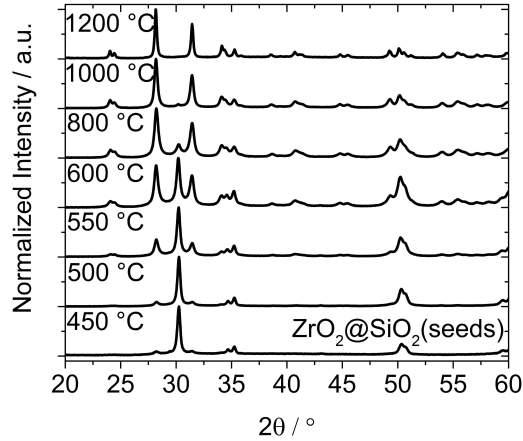


**Figure 6.22** – XRD data of pre-encapsulated  $\text{ZrO}_2@SiO_2$ -seeds particles. The samples were calcined for 3 h at different temperatures, as indicated (heating rate:  $5^\circ\text{C}\cdot\text{min}^{-1}$ ). The major fraction of the initial tetragonal phase had transitioned to the monoclinic phase after heating to 600 °C.

to the monoclinic phase and after calcination at 1000 °C the  $t \rightarrow m$  transformation was nearly finished.

It is to note that within the considered temperature range of up to 1200 °C our XRD data did not indicate the formation of zircon ( $\text{ZrSiO}_4$ ). This finding is in agreement with the study of Monte *et al.*,[65] who explored phase transitions in  $\text{ZrO}_2$ - $\text{SiO}_2$  binary oxides at similar temperatures. However, Aguilar *et al.*,[66] who also studied the crystallization of zirconia in  $\text{ZrO}_2$ - $\text{SiO}_2$  binary oxides, reported the formation of zircon after calcination at 1200 °C (and higher temperatures). In a silica rich mixture they also observed the formation of cristobalite after calcination at 1300 °C, which was absent in the present work.

In order to gain more insight into the microstructural changes after calcination, the grain sizes were determined after each thermal treatment (see Section 4.2.2 for details). As shown in Fig. 6.23 the tetragonal crystallite size of the bare zirconia cores was  $\sim 45$  nm after calcination at 450 °C. This size is similar to the critical grain size reported by Shukla and Seal[63] for submicron-sized (500 - 600 nm) zirconia particles (see Section 4.3.2 for details). Taking into account the aggregated structure of zirconia nanocrystals, Shukla and Seal[63] calculated a critical tetragonal grain size of 41 nm in aggregated zirconia particles, which is similar to the maximum tetragonal crystallite sizes observed in the current study (see Fig. 6.23).

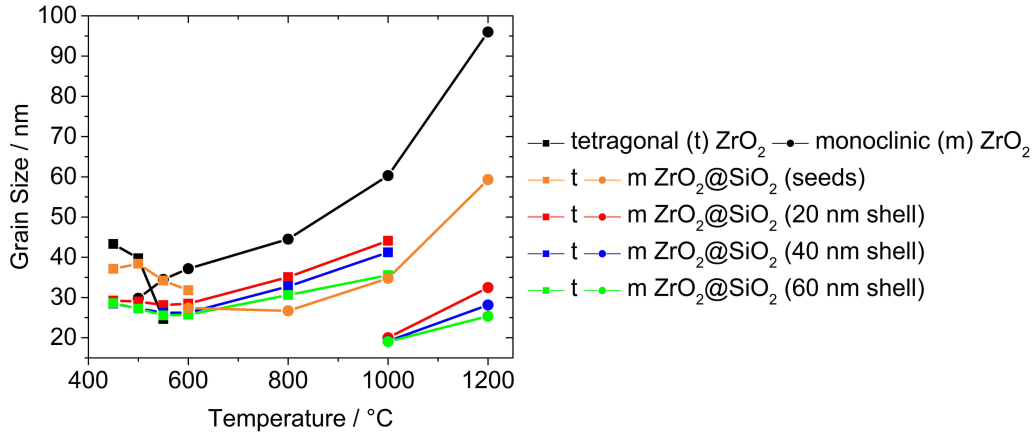


**Figure 6.23** – Crystallite sizes (grain sizes) of bare  $\text{ZrO}_2$  cores (black), pre-encapsulated  $\text{ZrO}_2@SiO_2$ -seeds particles (brown), and completely encapsulated  $\text{ZrO}_2@SiO_2$  core@shell particles (red, blue, green) after calcination at different temperatures (squares: tetragonal phase; circles: monoclinic phase). Crystallite sizes were determined from XRD data using the Scherrer equation. Due to instrumental broadening, crystallite sizes above  $\sim 80$  nm can only be considered as rough estimates of the actual crystallite size.

After calcination at  $500^\circ\text{C}$ , the apparent tetragonal crystallite size of the bare zirconia particles decreased to  $\sim 37$  nm. This finding is attributed to the predominant phase transition of larger tetragonal grains, leaving behind a population of somewhat smaller crystallites. The formed monoclinic crystallites had an average size of only  $\sim 30$  nm. This observation may suggest that the phase transition is associated with twinning of crystallites to relieve stresses, as reported previously.[192–195]

After calcination at  $550^\circ\text{C}$  some remaining smaller ( $\sim 22$  nm) tetragonal crystallites are still observed while the majority of larger grains had transitioned to the monoclinic phase with a crystallite size of  $\sim 35$  nm. Upon further increasing the calcination temperature, significant grain growth is observed leading to monoclinic crystallite sizes  $> 80$  nm after heating to  $1200^\circ\text{C}$ . The grain size of  $\sim 95$  nm after temperature treatment at  $1200^\circ\text{C}$  (see Fig. 6.23) must be considered with caution. Due to instrumental broadening, such large crystallite sizes ( $> 80$  nm) cannot be determined accurately with our XRD equipment.

In striking contrast to the bare zirconia particles, the grain growth of the encapsulated  $\text{ZrO}_2@SiO_2$  particles was strongly inhibited. After calcining at  $450^\circ\text{C}$ , the tetragonal grain size was  $\sim 29$  nm. After heating to  $500$  and  $550^\circ\text{C}$ , the grain size slightly decreased. This observation is attributed to the formation of smaller

## 6 Results and Discussion

tetragonal crystallites from residual amorphous zirconia, producing a smaller average grain size. Upon increasing the calcination temperature from 550 to 800 °C the tetragonal crystallites grew to sizes of  $\sim 30$ ,  $\sim 32$ , and  $\sim 34$  nm for particles with the initial shell thicknesses of  $\sim 61$ ,  $\sim 38$ , and  $\sim 26$  nm, respectively. At 1000 °C, the t $\rightarrow$ m transition occurred to slightly different extent (see Fig. 6.21) for the three samples, leaving behind differently sized tetragonal crystallites. However, as a general trend it was observed that, for each calcination temperature, the tetragonal crystallite size was smaller for thicker silica shell. Thus, the attenuation of grain growth became more effective with increasing shell thickness.

The monoclinic crystallites, which were formed after temperature treatment at 1000 °C, had a size of only  $\sim 20$  nm. Similar to the t $\rightarrow$ m transition of the bare zirconia cores, these crystallites were much smaller than the remaining tetragonal grains. As already mentioned, this observation is attributed to the relief of stress via twinning.[192–195] After sintering at 1200 °C, the monoclinic crystallites grew to sizes of 27 to 32 nm.

Compared to the bare zirconia cores and the fully encapsulated  $\text{ZrO}_2@\text{SiO}_2$  particles, the pre-encapsulated  $\text{ZrO}_2@\text{SiO}_2$ -seeds particles showed an intermediate progression in monoclinic grain growth after calcination at 1000 and 1200 °C, see Fig. 6.23. These findings are in general agreement with grain sizes and the shape stability observed in the SEM images of Fig. 6.20.

In summary, the deposition of silica shells on zirconia cores enabled a significant stabilization of the tetragonal phase. This is evidenced by a pronounced shift of the calcination temperature, from 500 to 1000 °C, at which the t $\rightarrow$ m transition is observed. In general agreement with previous studies, this stabilization is associated with a strong inhibition of the tetragonal grain growth.

In order to explain these findings it is useful to take into consideration the results of previous studies on  $\text{ZrO}_2\text{--SiO}_2$  binary oxides.[65, 66] These studies showed that already small amounts (1–10 mol%) of silica stabilize the tetragonal zirconia phase effectively. This stabilization has been attributed to constraint imposed on zirconia crystallites by the surrounding amorphous silica matrix as well as hindered mass transport through the silica matrix.[134] Thereby, crystallite growth is blocked and the tetragonal phase is stabilized by keeping the crystallite size below the critical grain size.[65, 196, 197] Additionally, it has been proposed that the high-melting, covalently bonded silica matrix with a low expansion coefficient impedes the

martensitic transition to the monoclinic phase as it requires a volume increase of 5%. [64]

Similar mechanisms are proposed to be responsible for the observed stabilization of the tetragonal phase of  $ZrO_2@SiO_2$  core@shell particles. In a previous study by our research group, [1] it was noted that initially formed tetragonal crystallites in submicron zirconia particles are significantly larger than those found in larger micrometer-sized particles. Thus, grain growth seems to be enhanced in particles with a larger surface-to-volume ratio. This finding indicates that crystallite growth is favored at the particle's surface, most likely because the crystallites are spatially less confined, mass transport at the surface is enhanced, and the overall surface energy decreases as the initially rough surface is smoothed due to consumption of material during grain growth. In line with this explanation and in general agreement with the constraint effect proposed for the phase stabilization in  $ZrO_2-SiO_2$  mixed oxides, the silica shell attenuates grain growth at the particle's surface because it enforces spatial confinement and inhibits mass transport. Thus, in order to grow the tetragonal crystallites, which are covered by a silica shell, to the critical grain size, the calcination temperature has to be increased significantly.

Another mechanism that may play a crucial role in the  $t \rightarrow m$  transition is related to chemisorption of oxygen as described more detailed in Section 4.3.2. Therefore, heating under inert gas or shielding the zirconia particle against oxygen would enhance its tetragonal phase stability. As the solubility of oxygen in amorphous silica is quite low, [198] and the high Si-O bond energy predicts a low concentration of oxygen vacancies and a low diffusion coefficient of oxygen in silica, [198–200] a silica shell is expected to provide an efficient diffusion barrier for oxygen. Thus, chemisorption of oxygen at oxygen vacancies of zirconia is impeded and the tetragonal phase is stabilized.

### EDX-mapping

In order to study thermally induced changes of the core@shell structure as well as the elemental distribution within the particles, cross-sectional lamellae of the  $ZrO_2@SiO_2$  particles (initial shell thickness:  $\sim 38$  nm) were prepared after heat treatment at 450, 800, and 1000 °C and characterized by EDX mapping. The EDX maps for Zr, Si, and O are presented in Fig. 6.24. The figure also shows the corresponding HAADF-STEM images.

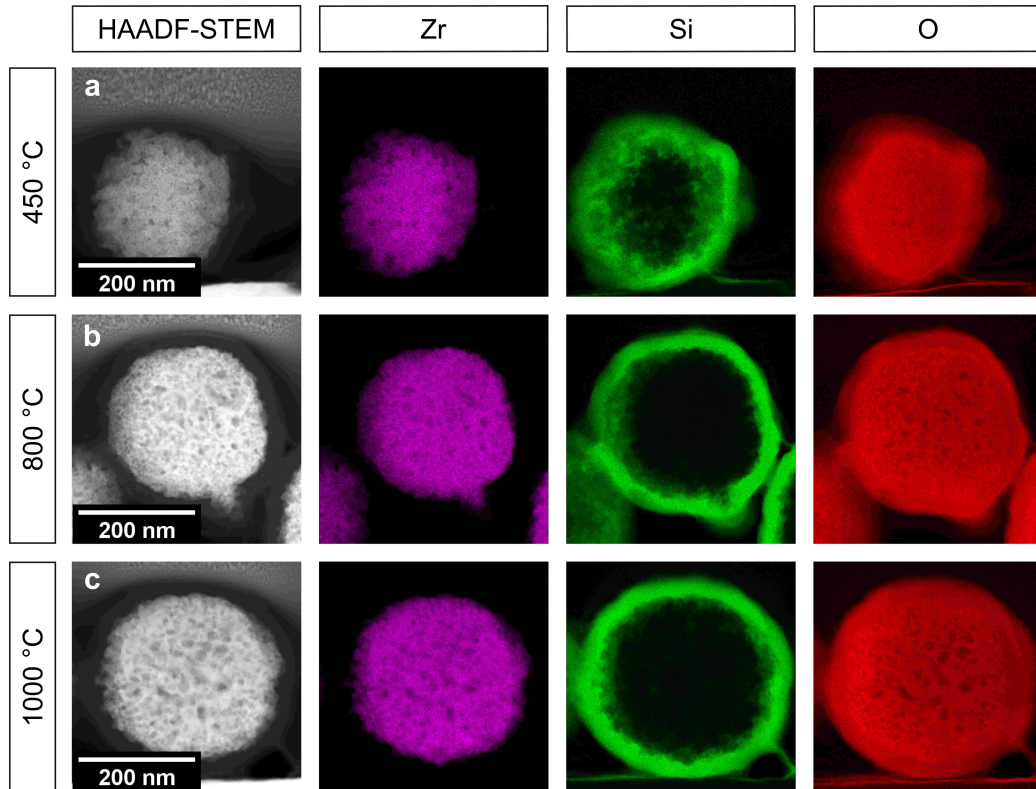


**Figure 6.24** – High-angle annular dark-field scanning transmission electron microscopy (HAADF-STEM) images and EDX-mapping data (Zr:magenta, Si:green, O:red) of cross-sectional lamellae prepared from  $\text{ZrO}_2@\text{SiO}_2$  core@shell particles after calcination at 450 °C (a), 800 °C (b), and 1000 °C (c). The lamellae were prepared from  $\text{ZrO}_2@\text{SiO}_2$  core@shell particles with an initial shell thickness of 38 nm using FIB technique.

Fig. 6.24(a) shows the HAADF-STEM image of a core@shell particle that was heat-treated at 450 °C. The apparent diameter of the zirconia core ( $\sim 240$  nm) is significantly smaller than the average core diameter of  $\sim 270$  nm, suggesting that the FIB cut through this particle was off-center. Thus, the images of this particle represent the projection of a cap of the particle through the FIB lamella (thickness  $< 100$  nm) and provide insight into the  $\text{ZrO}_2/\text{SiO}_2$  interfacial structure. First, the HAADF-STEM image and the Zr map clearly show that the  $\text{ZrO}_2$  core has a fine-grained structure with distinct surface roughness. Second, the Si map suggests a closed silica shell covering the  $\text{ZrO}_2$  core. On its inner side the amorphous silica shell adapts well to the rough  $\text{ZrO}_2$  surface and penetrates deep into pores. This finding confirms the good wettability of zirconia by silica. Third, the O map shows a quite homogenous distribution of oxygen. Only few oxygen deficient spots are

**Table 6.3** – Elemental composition (O, Si, Zr) of zirconia cores of  $ZrO_2@SiO_2$  particles (initial shell thickness: 38 nm) after calcination at different temperatures ( $T$ ), as indicated. The tabulated values were obtained from EDX mappings of FIB-prepared lamellae by integrating the EDX signals over specific areas, as indicated in Fig. 8.8 in the appendix.

$T$	Element	Family	Atomic fraction (%)	Atomic error (%)	Mass fraction (%)	Mass error (%)
450	O	K	71.4	9.0	31.6	2.7
450	Si	K	2.2	0.5	1.7	0.4
450	Zr	K	26.4	4.7	66.7	10.2
800	O	K	72.9	9.0	32.9	2.8
800	Si	K	1.6	0.4	1.2	0.3
800	Zr	K	25.6	4.5	65.8	10.1
1000	O	K	69.6	9.0	29.7	2.6
1000	Si	K	2.2	0.5	1.6	0.3
1000	Zr	K	28.3	5.1	68.7	10.6

observed, which match dark spots seen in the HAADF-STEM image, and indicate the presence of pores, which have not been filled (completely) by silica.

The particle that was calcined at 800 °C (Fig. 6.24(b)) had an apparent core size of  $\sim 270$  nm, which matches the average core diameter. Thus, this FIB lamella was most likely cut close to the center of the particle. The HAADF-STEM image and the Zr and O maps show that the porosity of the core increased significantly. Furthermore, the Si map shows a smooth densified silica shell with a thickness of 25-30 nm, in agreement with the HAADF-STEM images shown in Fig. 6.17(e). At the  $ZrO_2/SiO_2$  interface, the two materials appear quite sharply separated, though some silica still extends into cavities at the core's surface. Although the Si map indicates no silica at the center of the core, the numerical results of the integrated EDX signals reveal a Si fraction of 1-2 wt% (see Tab. 6.3).

This finding suggests that a small fraction of silicon may have diffused into the inner core region. The integrated EDX particle values sampled over specific areas of the zirconia cores are depicted in the appendix, Fig. 8.8 for each temperature.

## 6 Results and Discussion

The HAADF-STEM image and the elemental maps of the particle, which was calcined at 1000 °C (Fig. 6.24(c)), indicate slightly more pronounced coarsening of the porous core structure. In contrast, the silica shell as well as the ZrO<sub>2</sub>/SiO<sub>2</sub> interfacial region did not indicate any significant morphological changes. The EDX analysis at the center of the core suggests an unchanged Si fraction of 1-2 wt% (see Tab. 6.3).

In general, the EDX analysis of the core@shell particles supports the explanation for the observed attenuation of grain growth and phase stabilization. The zirconia cores are enclosed by a homogeneous, dense silica shell with a conformal ZrO<sub>2</sub>/SiO<sub>2</sub> interface, at which amorphous silica penetrates deep into the porous core structure. Thus, the silica shell is expected to effectively block mass transport at the core's surface[134] and to enforce the spatial confinement of crystallites. The closed silica shell can also block chemisorption of oxygen at oxygen vacancies and, thereby, suppress the t→m transition. In addition, a small fraction of Si was detected within the core after heat treatment at 450, 800, and 1000 °C. This finding may suggest that doping by Si may also contribute to the observed phase stabilization. In the literature, the possibility of Si-doping in zirconia has been discussed controversially. On the one hand, Kajihara *et al.*[134] and Ikuhara *et al.*[135] suggested that grain growth and mass transport in zirconia are inhibited by Si ions dissolved in the tetragonal zirconia lattice near grain boundaries and by Si segregation across grain boundaries. On the other hand, Guo *et al.*[136] and Gremillard *et al.*[137] found that silica forms vitreous pockets of glassy phase at the triple grain junctions.

The HAADF-STEM images shown in Fig. 6.24 do not provide information on the polycrystalline character of the zirconia cores. Therefore, the FIB lamellae were also characterized by bright field (BF) TEM. The obtained images are presented in Fig. 6.25. Here, the FIB-prepared cross-sectional lamellae of ZrO<sub>2</sub>@SiO<sub>2</sub> core@shell particles after calcination at 450, 800, and 1000 °C are shown. At larger magnifications, numerous lattice fringes are observed, clearly confirming the polycrystalline nature of the zirconia cores. However, in case of the particle calcined at 450 °C the TEM image also indicates amorphous material. After heating to 800 and 1000 °C the crystallinity increased significantly. Furthermore, the images confirm the formation of a conformal ZrO<sub>2</sub>/SiO<sub>2</sub> interface, as already discussed above.

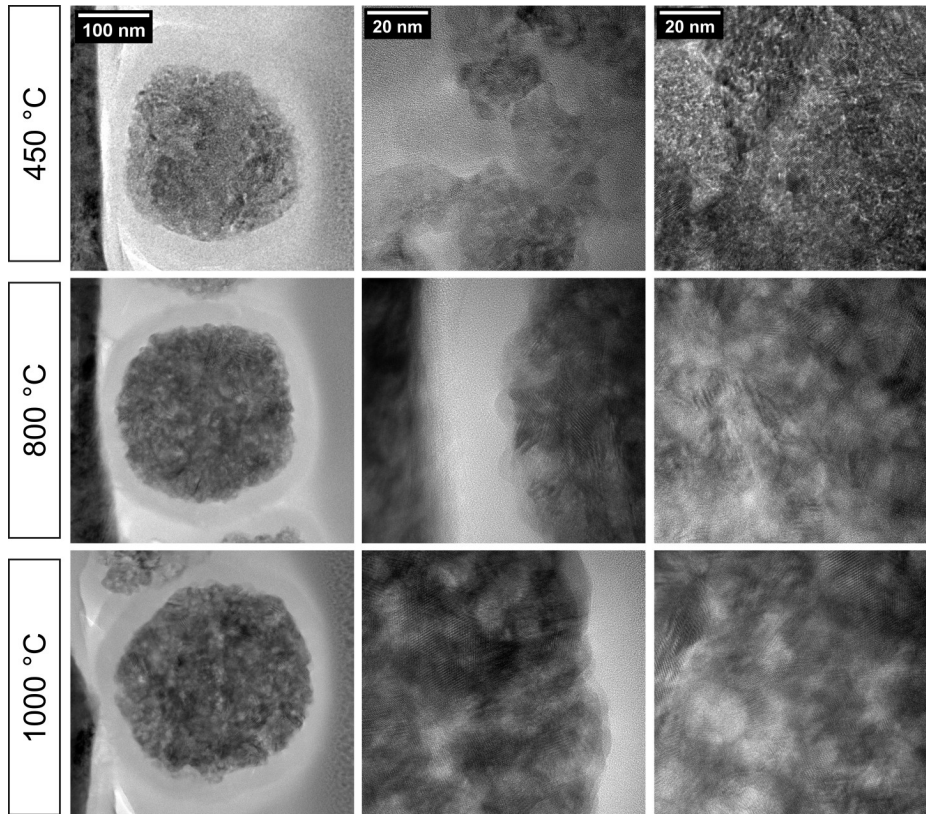


**Figure 6.25** – Bright field (BF) TEM images of cross-sectional FIB lamellae prepared from  $ZrO_2@SiO_2$  core@shell particles (initial shell thickness: 38 nm) after calcination at different temperatures, as indicated.

### 6.2.3 Optical properties

The last part of this dissertation focuses on the optical properties of  $YSZ@SiO_2$  core@shell particles in the visible range for possible applications as high-temperature stable structural colors and similar photonics such as wavelength selective filters.

For this purpose, smaller 5.5 mol% YSZ cores with a diameter of  $117 \text{ nm} \pm 10\%$  (see appendix for sizing statistics, Fig. 8.9) after calcination at  $480 \text{ }^\circ\text{C}$  for 3 h were used as shown by a TEM image in Fig. 6.26(a). Shang *et al.* reported that core@shell particles with a non-monotonous refractive index distribution in the size range of 100–200 nm are promising compositions for structural colors.[6] Furthermore, the high wavelength-sided edge of the band gap in a reflection spectrum of a PG is approximately twice as large as the motif diameter dependent on the effective

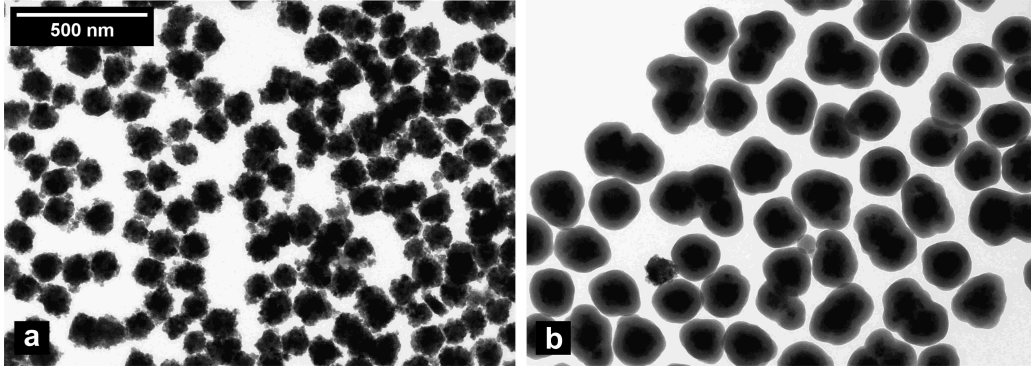


**Figure 6.26** – TEM image of YSZ submicron particles after calcination at 480 °C for 3 h (heating rate: 5 °C·min<sup>-1</sup>, a). TEM image of YSZ@SiO<sub>2</sub> core@shell submicron particles with a ~35 nm silica shell after drying at 80 °C for 4 h (b). Sizing statistics can be found in the appendix, Figures 8.9 and 8.10.

refractive index.[75] In consequence, the core@shell diameter needs to be smaller than the smallest visible wavelength to position the right reflection edge in the visible range of the light spectrum.

Calcined (480 °C, 3 h) YSZ submicron particles were encapsulated with five different silica shell thicknesses between 10 and 50 nm (see exemplary TEM image of 35 nm silica shell in Fig. 6.26(b)) by tuning the TEOS amount yielding core@shell diameters of 134 to 217 nm with standard deviations between 7 and 12% (see appendix for sizing statistics, Fig. 8.10). For investigation of the optical properties, the core@shell particles (dried at 80 °C for 4 h) were assembled to PGs on sapphire substrates as explained for microparticles in Section 8.2.1 and the reflection was measured in the visible range (see Fig. 6.27, a). Afterwards, the PGs were covered with a ~50 nm alumina coating by ALD (see appendix, Fig. 8.11) to fill the gaps between the particles with a high refractive index background (see Fig. 6.27, b).

As it can be seen from Figure 6.27 in the normalized reflection spectra, the YSZ@SiO<sub>2</sub> core@shell particles with 10–30 nm silica shells and air as matrix have the steepest reflection curves at the right reflection edge in the visible range. However, filling the matrix with alumina by ALD leads to improved reflection properties, whereby now the ~35 nm followed by the ~40 nm silica shell sample present the sharpest reflection edges. These differences in reflection depending on matrix material can be explained in part by the change of the effective refractive index and the diameter of the core@shell particles due to various silica shell thicknesses. A detailed analysis and characterization of the optical properties including a com-

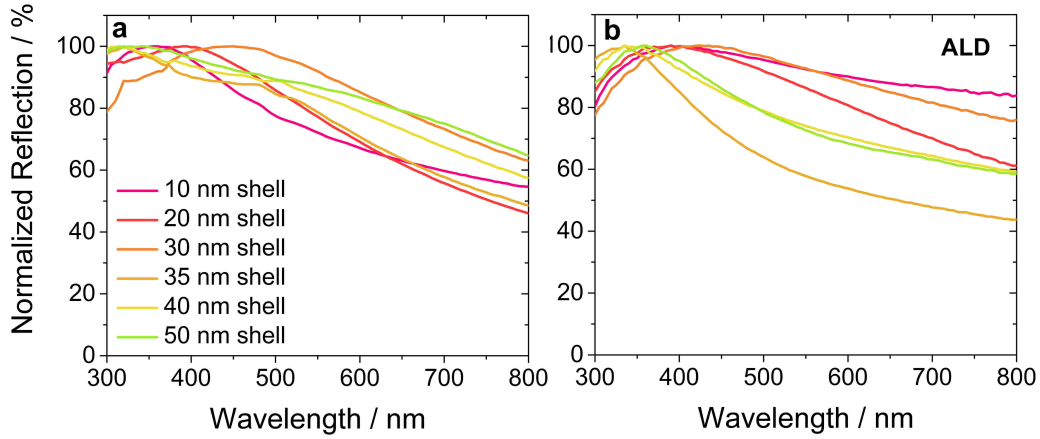


**Figure 6.27** – Normalized reflection spectra of  $YSZ@SiO_2$  core@shell particles as photonic glasses on sapphire substrates in the visible range with air (a) and alumina from ALD (b) as matrix between the particles. The YSZ core particles had a diameter of  $117\text{ nm} \pm 10\%$ , while the silica shell thickness varies from 10-50 nm.[201]

parison with data from simulation is currently a work in progress in collaboration with the group of Prof. Manfred Eich from the Institute of Optical and Electronic Materials at the Hamburg University of Technology.

Further analysis of the PGs from  $YSZ@SiO_2$  core@shell submicron particles in the dark room under diffuse illumination conditions demonstrated that both  $\sim 35$  and  $\sim 40$  nm showed a blue color in reflection compared to white reflection from core@shell particles with other silica shell thicknesses (see Fig. 6.28). White areas in the  $\sim 35$  and  $\sim 40$  nm sample result from multiple scattering as the layer thickness was partly too large.

For characterization of the high-temperature stability of such potential structural colors, heat treatments up to  $1000\text{ }^\circ\text{C}$  (3 h, heating and cooling rate:  $5\text{ }^\circ\text{C}\cdot\text{min}^{-1}$ ) were performed. For this purpose, the PGs on sapphire substrates from the most promising  $\sim 35$  nm silica shell assembly were investigated by reflection measurements, XRD, and SEM. Figure 6.29(a) represents the normalized reflection spectra of the PGs from  $\sim 35$  nm silica encapsulated YSZ submicron core@shell particles after ALD and heat treatments at 800 and  $1000\text{ }^\circ\text{C}$ . Here, it can clearly be seen that the slope of the right reflection edge gets flatter with increasing temperature. Photographs of the PGs after ALD (c) and temperature treatment at 800 (d) and  $1000\text{ }^\circ\text{C}$  (e) support this observation as the blue color faded with increasing temperature. Further analysis by XRD showed that the cubic phase of the calcined

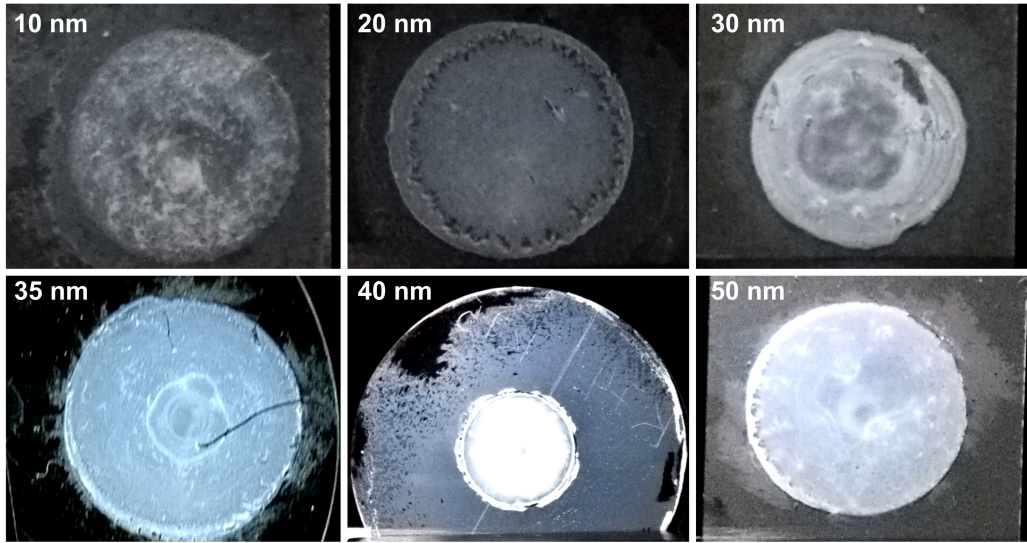


**Figure 6.28** – Photographs of photonic glasses on sapphire substrates made of YSZ@SiO<sub>2</sub> core@shell particles with alumina (from ALD) as matrix. Different silica shell thicknesses from YSZ@SiO<sub>2</sub> core@shell particles are indicated. Pictures were taken in the dark room under diffuse illumination conditions.

YSZ submicron particles remained unchanged even after thermal loading at 800 °C. After 1000 °C, additional peaks to the cubic phase can be found, which originate from the tetragonal prime and monoclinic phases. During the heating process, Y-rich phases form at the grain boundaries, while Y-lean areas arise inside the grains due to segregation (described in detail in Section 4.2.3). As a consequence, the Y-lean areas first transform to the tetragonal prime phase before transition to the monoclinic phase. Potential influences by the silica shell or the alumina coating on the YSZ submicron particles need further investigations. Additional peaks to the aforementioned crystalline phases from YSZ may arise from the sapphire substrate (s) or alumina coating, as indicated in Fig. 6.29(b). Moreover, the PGs from YSZ@SiO<sub>2</sub> core@shell submicron particles (~35 nm silica shell) were investigated by SEM to determine the particle and PG structure (see Fig. 6.29(f-g)). The SEM images after heat treatment at 800 (f) and 1000 °C (g) for 3 h (heating rate: 5 °C·min<sup>-1</sup>) reveal an intact spherical particle structure. The PG exhibits some holes, which originate from the deposition process. Interestingly, the gaps between the YSZ@SiO<sub>2</sub> particles are not completely filled by alumina from ALD as expected. Therefore, it can be presumed that further deposition of alumina on the PGs may improve the optical properties. Furthermore, using larger silica shells

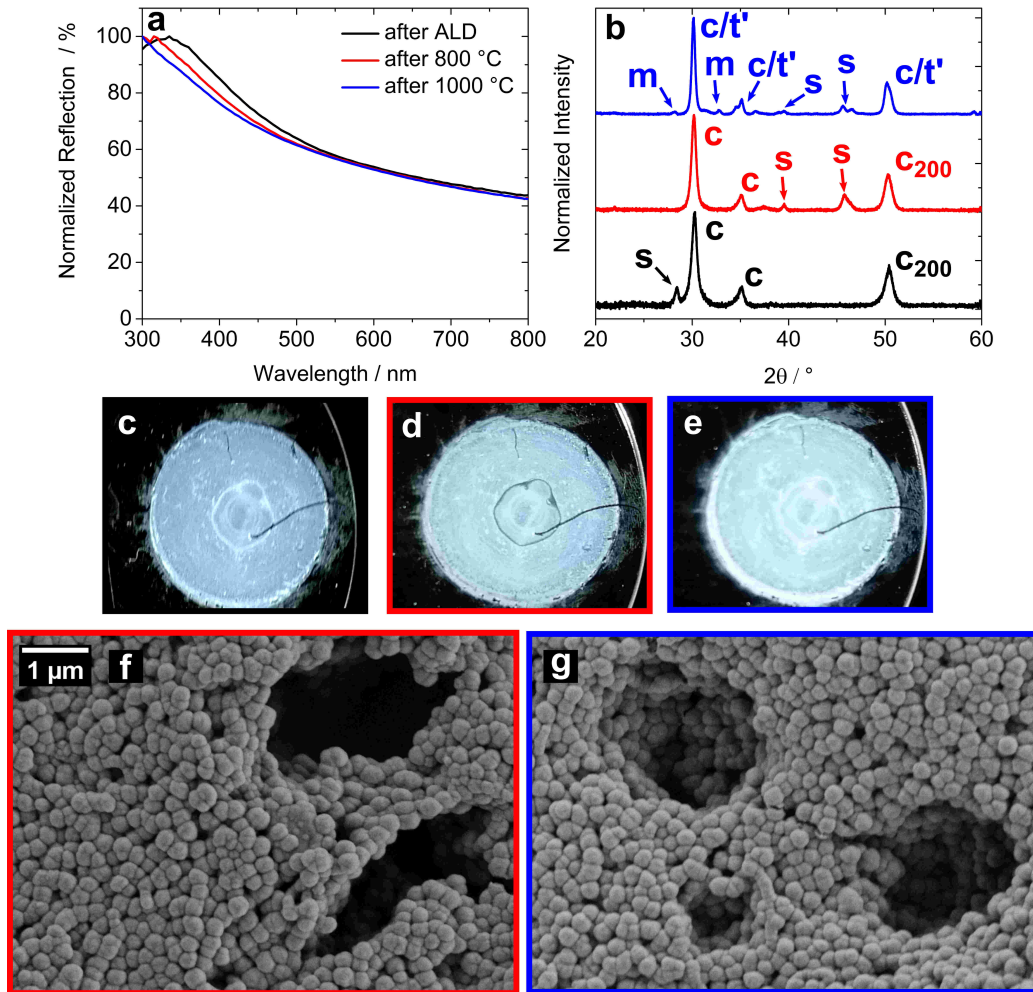


**Figure 6.29** – Normalized reflection spectra (a), [201] XRD data (b), [202] photographs (c-e), [201] and SEM images (f-g) of photonic glasses from  $YSZ@SiO_2$  core@shell submicron particles ( $\sim 35$  nm silica shell) after ALD (c) and heat treatments at 800 (d,f) and 1000 °C (e,g) for 3 h. [201]

(e.g., 40 nm or 50 nm) may improve the optical properties after heat treatment as a shrinkage of the shell was observed.

Further studies with more focus on the optical properties are suggested, which would go beyond the scope and focus of this work. It also requires improvements and modifications of particle dimensions and surfaces. Nevertheless, this study shows the potential for possible photonic high-temperature applications.

### 6.3 Sub-projects

In this section, the mechanical properties of zirconia microparticles, synthesized here, were characterized via microcompression experiments performed by the group of Prof. Wolfgang Peukert from the Institute of Particle Technology at the Friedrich-Alexander-University in Erlangen-Nürnberg. Data evaluation occurred in close collaboration and emerged as excellent complementary results to in-house particle characterizations. Furthermore, YSZ particles with a diameter of  $\sim 1 \mu\text{m}$  were synthesized for potential TPV application. Therefore, the obtained YSZ particles were deposited to monolayers on W/HfO<sub>2</sub> substrates. Afterwards, the optical properties were investigated in collaboration with the group of Prof. Manfred Eich from the Institute of Optical and Electronic Materials at the Hamburg University of Technology to evaluate the applicability as absorber/emitter for TPVs.

#### 6.3.1 Mechanical properties

Control and understanding of the mechanical properties of zirconia microparticles are essential not only for potential applications as TBC[1–3, 19–21] and emitter/absorber in TPV[13, 14] but also in high-performance liquid chromatography,[45, 189] where pressures up to 620 bar are reached and changes in the pore structure of the chromatographic supports are generally undesirable.[12] Furthermore, ceramics such as YSZ are used as new materials to substitute injured or damaged parts of the human body as bone tissue mimics and in dental applications.[15–18]

Thus, a major challenge remains the understanding and control of the mechanical properties of spherical zirconia microparticles. Besides the deposition process and its parameters for potential applications such as TBCs, the mechanical properties also depend on the particle composition, size, morphology, and doping. Therefore, improved TBCs require investigation of both thermal and mechanical stability to extend the cycle lifetime and improve the performance of turbine engines. The existing literature on the mechanical properties of (doped) zirconia is extensive and focuses particularly on compression experiments by using pillars and particles. Much uncertainty still exists about the relationship between the mechanical properties and the structure and composition of single particles.

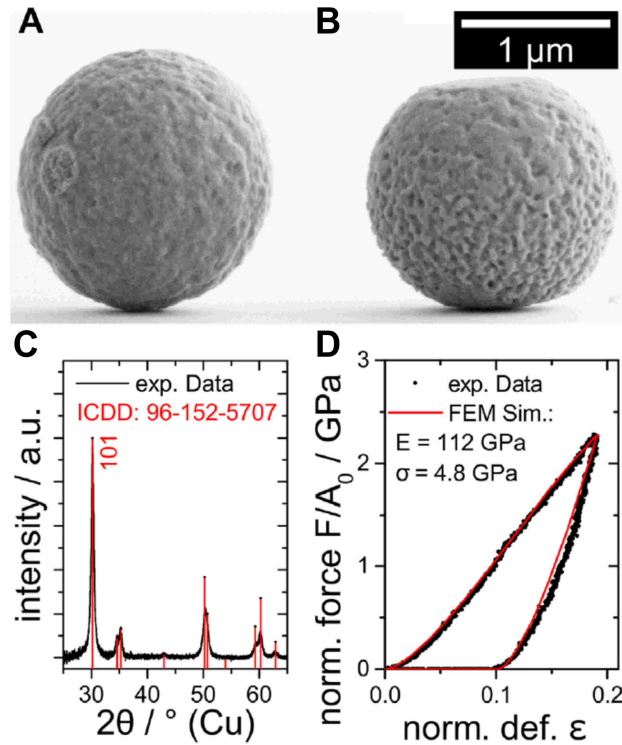


**Figure 6.30** – Side view SEM images of uncompressed (A) and compressed (B)  $\text{ZrO}_2$  particles. XRD pattern of the heat-treated  $\text{ZrO}_2$  powder sample including reference (C). Force-deformation data of the compressed  $\text{ZrO}_2$  particle (B) and fitted FEM simulation data (D). Figure and caption adapted from reference.[5]

In contrast to the thermally induced  $t \rightarrow m$  phase transition, the pressure-induced  $t \rightarrow m$  phase transition of pre-calcined ( $650\text{ }^\circ\text{C}$ , 3 h, heating rate:  $5\text{ }^\circ\text{C}\cdot\text{min}^{-1}$ , cooling rate:  $\leq 5\text{ }^\circ\text{C}\cdot\text{min}^{-1}$ )  $\text{ZrO}_2$  microparticles was investigated. Within the scope of a collaboration, mechanical properties of single undoped zirconia microparticles were characterized by *in situ* electron microscopy techniques and finite element simulations. Therefore, a SEM supported micromanipulator was used.[5, 203] This section gives a brief overview of the obtained results. Details can be found in our common publication of this sub-project.[5]

For this study,  $\text{ZrO}_2$  microparticles ( $D = 2.5\text{ }\mu\text{m}$  as-synthesized) were synthesized according to Leib *et al.*[1] Before investigation of the mechanical properties, the as-synthesized amorphous zirconia microparticles were calcined at  $650\text{ }^\circ\text{C}$  for 3 h, whereby the particles crystallized in the tetragonal phase (see Fig. 6.30(C)). Then, particle compression experiments were performed as shown in Figure 6.30(B, D).

## 6 Results and Discussion

Here, the calcined zirconia microparticles (see Fig. 6.30(A)) were deposited on silicon wafers and single particles were compressed (see Fig. 6.30(B)) by a diamond flat punch (plateau diameter = 4  $\mu\text{m}$ ). The obtained force-deformation (FD) curve and fitted finite element method (FEM) simulation curve are shown in Fig. 6.30(D). The FD curve exhibits a mixture of elastic and plastic deformation, whereby the plastic part can also be observed in the permanent deformation of the zirconia particle in Fig. 6.30(B). From FEM data, a Young's modulus of  $E_{\text{ZrO}_2}=112.0$  GPa, which is in good agreement with the literature values from porous tetragonal stabilized bulk zirconia,[204] and a yield stress of  $\sigma_{\text{ZrO}_2}=4.8$  GPa were obtained.

After microcompression, TEM lamellae ( $\sim 100$  nm) of the reference and compressed particles were prepared by using FIB technique for selected area electron diffraction (SAED) by TEM. Here, the SAED pattern of the uncompressed particle showed the tetragonal phase, while additional monoclinic peaks occurred for the compressed particle. Besides, we observed texturing of the formed monoclinic phase. The obtained radial intensity plots (A) and SAED positions (B) in the FIB lamella of a compressed zirconia microparticle are depicted in Fig. 6.31. From these data it can be seen that predominantly the center of the particle transforms to the monoclinic phase (see positions 3a, 3d, 2d, 1d, 1b, and 1a), where the SAED patterns clearly show  $\{-111\}$  and  $\{111\}$  peaks with only a small tetragonal  $\{101\}$  shoulder. Due to broad electron diffraction reflections from small grain sizes, the amount of monoclinic phase fraction could only be estimated to be 60–100%. Turning the focus to SAED positions close to the surface, e.g., positions 4b, 5d, and 4d, the monoclinic amount decreases yielding nearly pure tetragonal phase (position 5d). Furthermore, the FE simulation in Fig. 6.31(B) of the monoclinic to tetragonal ratio is in very good agreement with obtained experimental results. The FE simulation of the applied shear stress shows the spatial distribution of the stress-induced t $\rightarrow$ m transition.

The most striking result to emerge from the SAED data and FE simulation is that tetragonal crystallites transition to the monoclinic phase if their crystalline direction is parallel to the exposed shear stress, which needs to exceed 1.5 GPa.[5]

In summary, these results suggest that there is a correlation between local phase composition, crystallite orientation, and applied shear stress. Thus, the pressure-induced t $\rightarrow$ m phase transformation in zirconia microparticles is of interest for potential high-temperature applications with various pressure conditions.

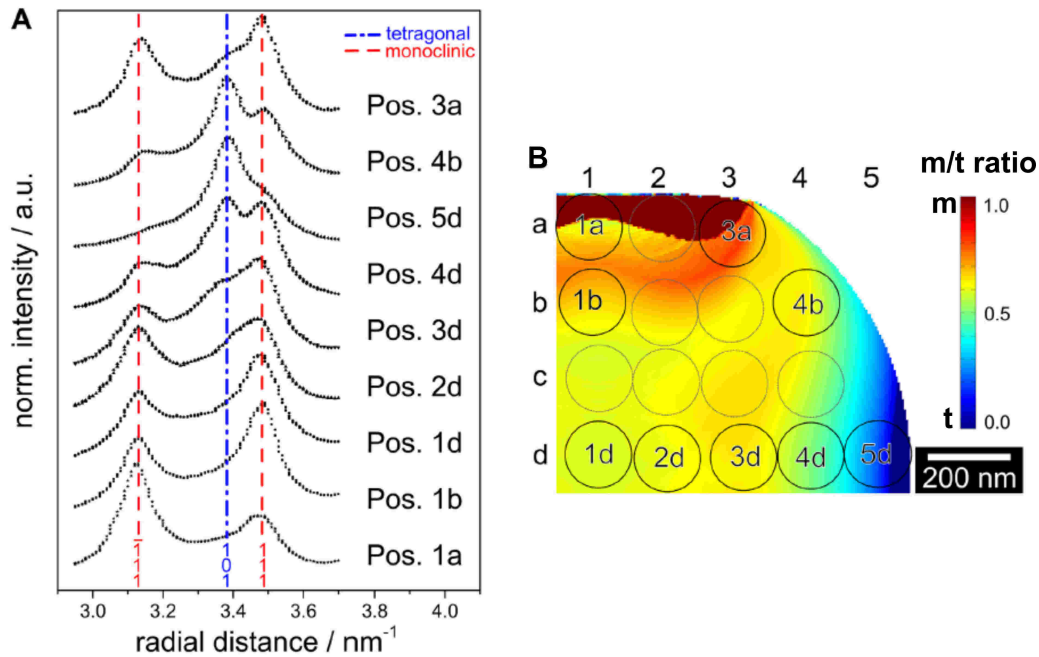


**Figure 6.31** – Comparison of the angular integrated radial intensity profiles of several aperture positions (A). Simulated amount of the tetragonal-to-monoclinic phase transformation in a 100 nm thick lamella (B). Circles denote the size and positions of the SAED aperture. Figure and caption adapted from reference.[5]

### 6.3.2 YSZ microparticles as absorber/emitter for TPVs

Besides potential TBC application,  $\text{ZrO}_2$  and YSZ gained attention as materials for high-temperature stable ( $> 1000^\circ\text{C}$ ) absorber/emitter in thermophotovoltaics (TPV).[205–207] Here, high absorption/emission at wavelengths  $< 2\ \mu\text{m}$  and low absorption/emission at longer wavelengths ( $> 2\ \mu\text{m}$ ) are desired to match the requirements of a TPV-cell. Heat emission due to high emissivities at longer wavelengths decreases the efficiency of a TPV-cell, as the energy of such low frequencies is not high enough to generate a photocurrent.[208]

Experiments by Dyachenko *et al.*[14] showed that a monolayer of  $\text{ZrO}_2$  submicron particles ( $D \sim 660\ \text{nm}$  after calcination at  $600^\circ\text{C}$  for 3 h) on a tungsten layer (100 nm thickness) coated with a hafnia layer (20 nm thickness) can be used as selective band edge absorber/emitter. Furthermore, the high-temperature stability was evaluated by annealing experiments up to  $1100^\circ\text{C}$  for 3 h (heating and cooling rate:  $10^\circ\text{C}\cdot\text{min}^{-1}$ ). In conclusion, they determined preserved optical properties after annealing at temperatures up to  $1000^\circ\text{C}$  under vacuum conditions, while

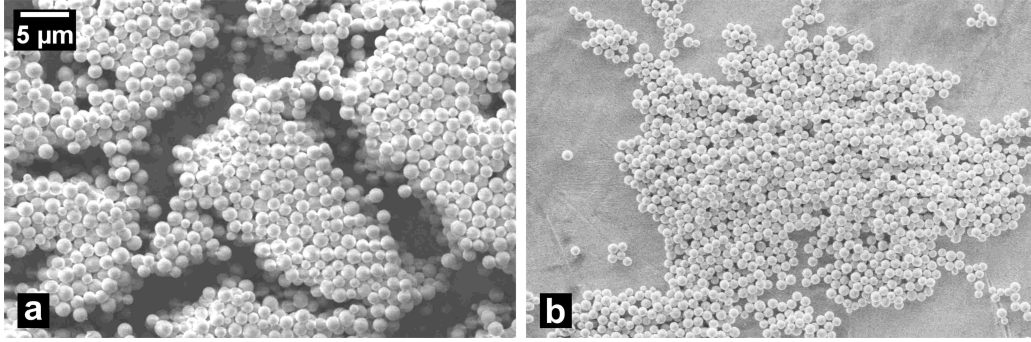


**Figure 6.32** – SEM images of as-synthesized ( $D \sim 1.33 \mu\text{m} \pm 17\%$ , a) and calcined ( $600^\circ\text{C}$ , 3 h,  $D \sim 930 \text{ nm} \pm 9\%$ , b) YSZ microparticles for potential application as absorber/emitter in TPV systems. Average particle diameters and standard deviations were determined using *ImageJ* software by counting at least 100 particles.

higher temperatures destroyed the tungsten substrate due to chemical reactions between the silicon substrate and the thin tungsten layer. The authors hypothesized that increasing the particle diameter to  $\sim 1 \mu\text{m}$  would improve the selectivity of the absorption/emission yielding a sharper band edge. Moreover, the high-temperature stability can be increased by using a bulk tungsten substrate and YSZ microspheres.[14]

For the purpose of improving the as mentioned TPV system, the sol-gel synthesis of YSZ microparticles from Section 6.1.1 ( $D = 2\text{--}5 \mu\text{m}$ ) was further modified to yield 7.5 mol% YSZ microparticles with a diameter of  $\sim 1 \mu\text{m}$  after calcination. Therefore, sol-gel synthesis parameters were adjusted, including the reduction of the stabilizer amount and an increase of the water concentration. Hence, an elevated hydrolysis rate yielded a shorter induction time and smaller particles. Furthermore, the extended stirring time was reduced from 4 min to 40 s in order to reduce the primary particle aggregation time (see Section 8.2 for details).

Figure 6.32 represents SEM images from the obtained as-synthesized (a) and calcined ( $600^\circ\text{C}$ , 3 h, heating and cooling rate:  $5^\circ\text{C}\cdot\text{min}^{-1}$ , b) YSZ microparticles. The as-synthesized YSZ microparticles exhibit a particle diameter of  $1.33 \mu\text{m}$  with a standard deviation of 17%. After calcination, particle shrinkage yielded a diameter of 930 nm (volume loss:  $\sim 51\%$ ) and a narrow standard deviation of 9%, which is close to the suggested particle dimension of the previous investigation.[14]

For the deposition of YSZ microparticle monolayers, sapphire substrates with a 200 nm tungsten layer and a 20 nm superficial hafnia coating were used. In contrast

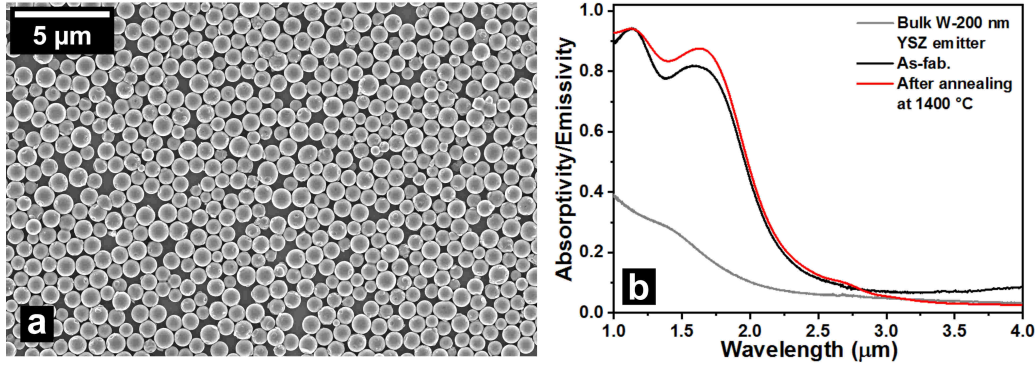


**Figure 6.33** – SEM image of the monolayer from calcined YSZ microparticles ( $D \sim 930$  nm) on the W/HfO<sub>2</sub> (200 nm W substrate with 20 nm HfO<sub>2</sub> coating) substrate (a). Absorptivity/Emissivity of bulk W-200 nm substrate, as-fabricated (as-fab.) YSZ microparticle monolayer on W/HfO<sub>2</sub> substrate, and YSZ microparticle monolayer on W/HfO<sub>2</sub> substrate after annealing at 1400 °C for 6 h (heating and cooling rate: 10 °C·min<sup>-1</sup>, b).[209]

to previous work,[14] where silicon substrates were utilized, sapphire substrates should exclude chemical reactions under heat treatment between the substrate and the tungsten layer. To achieve a YSZ monolayer, the calcined YSZ microparticles were suspended in ethanol by sonication yielding a concentration of 1 g·L<sup>-1</sup>. Afterwards, the YSZ particle suspension was dripped onto water until the water surface was fully covered by YSZ particles. Finally, the sapphire substrates with the W/HfO<sub>2</sub> layer were dipped under water and carefully lifted up yielding a YSZ microparticle monolayer (see Section 8.2.2 for details) as shown in Fig. 6.33(a). As it can be seen, there are some small gaps between the particles and the deposition method did not yield a highly ordered crystalline layer due to a bimodal size distribution. Nevertheless, the optical properties should not be dramatically influenced as they depend on resonances between neighboring particles as well as between single particles and the tungsten substrate.[14]

Figure 6.33(b) shows the absorptivity/emissivity of the YSZ particle monolayer on the W/HfO<sub>2</sub> substrate before and after annealing at 1400 °C (6 h, heating and cooling rate: 10 °C·min<sup>-1</sup>) in the wavelength range from 1 to 4 μm. The optical properties of a bulk 200 nm W substrate are shown for comparison. Monolayers from both as-deposited and heat-treated YSZ microparticles exhibit two absorption peaks at  $\sim 1.1$  μm and  $\sim 1.6$  μm as well as a sharp band gap edge at  $\sim 2$  μm. In the  $> 2.5$  μm wavelength range, a comparably low absorptivity for the as-deposited YSZ particle monolayer, the heat-treated YSZ monolayer, and the bulk reference

## 6 Results and Discussion

was obtained. In contrast to the previous investigation by Dyachenko *et al.*[14] of ZrO<sub>2</sub> particle monolayers on tungsten substrates, preserved optical properties were obtained even after heat treatment at 1400 °C for 6 h under vacuum. The reflection edge shifted to higher wavelengths as the particle diameter increased from  $D \sim 660$  nm to  $D \sim 930$  nm and a sharper reflection edge was obtained.

In summary, it was demonstrated that a monolayer of  $\sim 1 \mu\text{m}$  YSZ particles on W/HfO<sub>2</sub> substrates is a promising high-temperature stable absorber/emitter for TPV systems.

## 7 Outlook

For  $\text{ZrO}_2/\text{YSZ}-\text{Al}_2\text{O}_3$  composite microparticles with the perspective of TBC application, further research is required to determine the detailed mechanisms of tetragonal phase stabilization and grain growth inhibition by post-synthetic modification with alumina. The as-synthesized local Al distribution in the nanosized zirconia grains should be analyzed by using X-ray photoelectron spectroscopy (XPS) characterization of a FIB lamellae. Furthermore, the high-temperature stability of yttria and alumina co-doped zirconia microparticles should be evaluated as this study characterized only narrow yttria to alumina ratios (9.5 wt% Y, 1–2 wt% Al), which did not show an improved thermal stability compared to YSZ core particles. Moreover, the alumina encapsulation process of zirconia microparticles could be modified to yield dense and continuous alumina shells. For this purpose, future studies might try to combine the promising PSM from the present study with an ALD process to yield alumina modified and encapsulated zirconia microparticles. In contrast to the present study, a different ALD technique should be used to obtain a conformal coating of individual particles as shown in the literature for zirconia nanoparticles.[168, 170]

In future investigations, it might be possible to build a TBC prototype, where the commercial ceramic top-coat will be replaced by the most promising doped zirconia microparticles with regard to high-temperature stability. Here, the thermal stability of this particle system could be tested under application-oriented conditions.

For  $\text{ZrO}_2/\text{YSZ}@SiO_2$  core@shell submicron particles with perspective application as high-temperature stable structural colors, more work will be needed to further decrease the zirconia core particle size including narrow size distributions to match the best particle parameters for blue color in accordance with simulation data. An improved high-temperature stability and reduced grain growth for

## 7 Outlook

$\text{ZrO}_2@\text{SiO}_2$  core@shell submicron particles were already demonstrated in this dissertation, but the particle size of the zirconia core particles ( $\sim 270$  nm) was too large for coloration. Therefore, alternative synthesis approaches such as hydrothermal synthesis need to be considered as the sol-gel synthesis involves the aggregation of 10–20 nm primary particles yielding rough surfaces for particles  $\sim 100$  nm. Nevertheless, blue color was achieved in this study by fabricating photonic glasses of smaller  $\text{YSZ}@\text{SiO}_2$  core@shell submicron particles (YSZ core size:  $\sim 117$  nm; silica shell thickness:  $\sim 35$  nm) and by filling the gaps with alumina using ALD technique. High-temperature stability up to  $1000^\circ\text{C}$  (3 h) was demonstrated by XRD and SEM measurements, whereby the characterization of the optical properties revealed a decreasing slope of the reflection edge with increasing annealing temperature. For further improvements apart from zirconia particle size and distribution, the gaps in the PGs need to be filled more effectively than it was achieved in the present study by ALD. As a consequence from ALD results, future studies should try to infiltrate the PGs made of  $\text{YSZ}@\text{SiO}_2$  core@shell submicron particles with YSZ nanoparticles by drop-casting or spin-coating processes. Here, almost all gaps even in the bottom layers might be filled with the matrix material. In addition, YSZ represents a higher refractive index contrast to the silica shell compared to alumina. For improvement of high-temperature stability, the silica shell material should be changed to a more thermal stable material such as alumina.

Future studies on the current topic of structural colors from ceramic core@shell particles might also focus on inverse systems like  $\text{SiO}_2@\text{ZrO}_2$  core@shell submicron particles, where the core and the matrix have a lower refractive index compared to the shell material. One of the main advantages would be that the synthesis of monodisperse silica submicron particles is well-known, but the encapsulation of those particles with zirconia is still challenging. There is room for further progress in zirconia encapsulation by infiltration of photonic glasses made of silica particles. One major obstacle for this inverse core@shell particle system would be that the temperature stability is likely to be lower as the zirconia shell is unprotected against oxygen and unconfined, which might cause increased grain growth.

To develop a full picture of the thermal and mechanical stability of  $\text{ZrO}_2/\text{YSZ}-\text{Al}_2\text{O}_3$  composite particles and  $\text{ZrO}_2/\text{YSZ}@\text{SiO}_2$  core@shell submicron particles, additional studies will be needed. Therefore, microcompression experiments are suggested to determine the mechanical properties and t $\rightarrow$ m phase transition under pressure as they were already performed for  $\text{ZrO}_2$  microparticles in a fruitful col-

laboration with the research group of Prof. Peukert from Friedrich-Alexander University of Erlangen-Nürnberg. Furthermore, *in situ* XRD experiments in collaboration with the group of Prof. Martin Müller from the Helmholtz-Zentrum Geesthacht are needed to fully understand the effects of alumina modification and silica encapsulation on temperature stability of  $\text{ZrO}_2/\text{YSZ}$  particles.



## 8 Experimental Section

### 8.1 Materials

#### ZrO<sub>2</sub>

The following chemicals were used for synthesis of 2–5  $\mu\text{m}$  zirconia cores: Polyethersulfone (PES) filter (0.2  $\mu\text{m}$  pores) were purchased from Sartorius, anhydrous *n*-butanol (99.9%, dried over 0.4 nm molecular sieve), demineralized (demin.) water (ASC reagent), and eicosanoic acid (99.0%) were purchased from Sigma-Aldrich, and zirconium(IV) *n*-propoxide (70% in *n*-propanol) and zirconium(IV) *n*-butoxide (80% in *n*-butanol) were purchased from Alfa Aesar. Denatured ethanol (96%) from Grüssing, acetone (99.8%) from VWR, and *n*-butanol (99%) from Acros Organics were used for purification.

The following chemicals were used for synthesis of  $\sim 300$  nm zirconia cores: Anhydrous ethanol (99.5%) was purchased from Acros, demineralized water (ASC reagent), eicosanoic acid (99.0%), and hydroxypropyl cellulose (HPC, average  $M_w \sim 80.000$ ,  $M_n = 10.000$ , 99%) were purchased from Sigma-Aldrich and zirconium(IV) *n*-propoxide (70% in *n*-propanol) was purchased from Alfa Aesar. Denatured ethanol (96%) from Grüssing was used for purification.

#### YSZ

In addition to chemicals from undoped zirconia core synthesis, yttrium(III) *i*-propoxide (98%) purchased from abcr was used.

### **ZrO<sub>2</sub>/YSZ–Al<sub>2</sub>O<sub>3</sub>**

The following chemicals were used for PSM of zirconia and YSZ with alumina. Anhydrous tetrahydrofuran (THF, 99.8%) was purchased from Alfa Aesar, PES filter (0.2 μm pores) was purchased from Sartorius, and aluminium chloride (99.9%), anhydrous ethanol (99.9%), aluminum *i*-propoxide (99.9%), demineralized water (ASC reagent), and polyvinylpyrrolidone (PVP, average Mw~40.000) were purchased from Sigma-Aldrich. Demineralized water (Millipore Simplicity System, 18.2 MΩcm), acetone (99.8%) from VWR, and denatured ethanol (96%) from Grüssing were used for purification.

### **ZrO<sub>2</sub>@SiO<sub>2</sub> and YSZ@SiO<sub>2</sub>**

The following chemicals were used for silica shell synthesis. Anhydrous THF (≤99.7%) and ammonium hydroxide solution (28% NH<sub>3</sub> in H<sub>2</sub>O) were purchased from VWR, anhydrous ethanol (99.5%) was purchased from Acros, demineralized water (ASC reagent) and PVP (average Mw~40.000) were purchased from Sigma-Aldrich, and tetraethyl orthosilicate (TEOS, 99%) was purchased from Alfa Aesar. Demineralized water (Millipore Simplicity System, 18.2 MΩcm) and denatured ethanol (96%) from Grüssing were used for purification.

### **Assembly of photonic glasses**

Sapphire substrates (Al<sub>2</sub>O<sub>3</sub>, R-plane 1-102<0.5°, polished, Ra<0.5 nm) were purchased from Crystal GmbH and used for deposition of photonic glasses.

### **Atomic layer deposition of Al<sub>2</sub>O<sub>3</sub>**

Trimethylaluminum (TMA, 97%) and demin. water (ASC reagent) were purchased from Sigma-Aldrich and used for alumina (Al<sub>2</sub>O<sub>3</sub>) deposition.

## 8.2 Methods

### Synthesis of ZrO<sub>2</sub> cores

Spherical and monodisperse undoped zirconia microparticles were synthesized according to previous studies by Yan *et al.*[140] and Leib *et al.*,[1] slightly modified in this work to achieve as-synthesized particle diameters around  $\sim 2.6$  and  $\sim 5.4$   $\mu\text{m}$ . The whole procedure was conducted under nitrogen and with anhydrous solvents to preclude oxygen and to precisely control the water content during reaction.

For undoped zirconia microparticles with an as-synthesized diameter of  $\sim 2.6$   $\mu\text{m}$  (potential application as TBC), typically 584 mg (1.87 mmol) eicosanoic acid were dissolved under stirring (300 rpm) at 50 °C in 50 mL dry *n*-butanol (250 mL wide-mouth glass bottle), which was filtered through a PES syringe filter (0.2  $\mu\text{m}$  pores). Concurrently, 6.1 g (13.0 mmol) zirconium(IV) *n*-propoxide (70% in *n*-propanol) were sonicated (Badelin, Sonorex Super RK 106) for 5 min and then added under stirring (300 rpm) at 50 °C to the eicosanoic acid solution. Meanwhile, 0.8 mL water in 43 mL *n*-butanol (0.2  $\mu\text{m}$  PES filtered) were heated to 55 °C under stirring (300 rpm). After 30 min, the water solution in *n*-butanol was added under stirring (300 rpm) at 50 °C uniformly to the reaction solution over the course of 1 min. The reaction solution turned white after an induction time of 1.5 min. The obtained particle suspension was transferred onto an analogue tube roller (SRT6 Stuart, roller size length x diameter: 340 mm x 30 mm) and gently agitated for 30 min at room temperature and a rotation speed of 12 rpm. For purification, the reaction suspension was transferred into 100 mL ice-cooled *n*-butanol and then repetitively centrifuged (0 °C, 5 min, 250 x g) and washed with *n*-butanol, acetone, and ethanol (each solvent twice with  $\sim 35$  mL in the as mentioned order). The centrifugation speed was gradually reduced by 50 x g down to 50 x g. Finally, the zirconia particles were resuspended by sonication for 5 min in 5 mL ethanol.

For undoped zirconia microparticles with an as-synthesized diameter of  $\sim 5.4$   $\mu\text{m}$  (potential application as TBC), typically 503 mg (1.87 mmol) eicosanoic acid were dissolved under stirring (400 rpm) at 50 °C in 50 mL dry *n*-butanol (250 mL wide-mouth glass bottle), which was filtered through a PES syringe filter (0.2  $\mu\text{m}$  pores). Concurrently, 6.1 g (13.0 mmol) zirconium(IV) *n*-propoxide (70% in *n*-propanol) were sonicated (Badelin, Sonorex Super RK 106) for 5 min and then added under stirring (400 rpm) at 50 °C to the eicosanoic acid solution. Meanwhile, 0.7 mL

## 8 Experimental Section

water in 43 mL *n*-butanol (0.2  $\mu\text{m}$  PES filtered) were heated to 55  $^{\circ}\text{C}$  under stirring (400 rpm). After 30 min, the water solution in *n*-butanol was added under stirring (400 rpm) at 50  $^{\circ}\text{C}$  uniformly to the reaction solution over the course of 1 min. The reaction solution turned white after an induction time of 6.5 min. After 1 min extended stirring (400 rpm) at 50  $^{\circ}\text{C}$ , the obtained particle suspension was transferred onto an analogue tube roller (SRT6 Stuart, roller size length x diameter: 340 mm x 30 mm) and gently agitated for 105 min at room temperature and a rotation speed of 12 rpm. Finally, purification and resuspension of the obtained zirconia microparticles were performed analogously to the  $\sim 2.6 \mu\text{m}$  zirconia microparticles.

Monodisperse and spherical zirconia submicron particles were prepared according to previous studies from Widoniak *et al.*[62] and Leib *et al.*[1] Slight modifications of the protocols were necessary to obtain particles with diameters of  $\sim 300 \text{ nm}$  (before calcination). The reaction was carried out under nitrogen atmosphere using an EasyMax 402 Basic Plus Synthesis Workstation (Mettler Toledo). Anhydrous solvents were used to exclude oxygen and to control the water content precisely.

Synthesis of zirconia submicron particles (potential application as SC): 21 mg (0.067 mmol) eicosanoic acid and 30 mg HPC (average  $M_w \sim 80.000$ ,  $M_n = 10.000$ , 99%) were dissolved in 45 mL anhydrous ethanol using a 100 mL reactor vessel. Prior to use, ethanol was dried over 0.4 nm molecular sieves and filtered through a PES syringe filter (0.1  $\mu\text{m}$  pore size) to remove dust of the drying agent. The clear solution was heated to 60  $^{\circ}\text{C}$  under stirring (550 rpm). Meanwhile, 1.655 g (5.54 mmol) zirconium *n*-propoxide (70% in *n*-propanol) were sonicated for 10 min. After adding 200  $\mu\text{L}$  of demineralized water to the ethanolic solution of stabilizers, the undiluted zirconia precursor was added quickly (few seconds) by using a syringe (Vivomed, 2.00 x 120 mm). Within seconds, the solution turned white (induction time) and the suspension was stirred continuously (550 rpm) for 3 h. For purification, the obtained suspension was transferred into 50 mL ice-cooled ethanol and then centrifuged (-5  $^{\circ}\text{C}$ , 5 min, 6000 x g) to separate the particles from the supernatant. In three additional washing steps (each step  $\sim 35 \text{ mL}$  ethanol), the centrifugation speed was gradually reduced by 500 x g down to 4500 x g. Finally, the zirconia particles were resuspended by sonication for 5 min in 15 mL ethanol.

### Synthesis of YSZ cores

For 9.5 mol% (Y) YSZ microparticles with a diameter of  $\sim 4.3 \mu\text{m}$  before calcination (potential application as TBC), 655 mg (2.10 mmol) eicosanoic acid were dissolved in a 250 mL wide-mouth glass bottle under stirring (300 rpm) at  $50^\circ\text{C}$  in 45 mL dry *n*-butanol (0.2  $\mu\text{m}$  PES filtered). In the meantime, 6.13 g (15.0 mmol) zirconium(IV) *n*-butoxide (80% in *n*-butanol) and 389 mg yttrium(III) *i*-propoxid (1.39 mmol) were diluted in 10 mL dry *n*-propanol and sonicated for 20 min. The zirconia and yttria precursor mixture was quickly (few seconds) added to the eicosanoic acid solution under stirring (300 rpm) at  $50^\circ\text{C}$  by using a PES syringe filter (0.1  $\mu\text{m}$  pores). A freshly prepared solution of 0.75 mL water in 43 mL *n*-butanol was heated to  $55^\circ\text{C}$  under stirring (300 rpm) and added uniformly to the reaction solution over the course of 1 min. An extended stirring (300 rpm) of 4 min under the same conditions followed the induction time of 2 min. Afterwards, the obtained particle suspension was transferred onto an analogue tube roller (SRT6 Stuart, roller size length x diameter: 340 mm x 30 mm) for 120 min at  $50^\circ\text{C}$  and a rotation speed of 5 rpm. Finally, purification and resuspension of the obtained YSZ microparticles were performed analogously to the undoped zirconia microparticles.

For 7.5 mol% (Y) YSZ microparticles with a diameter of  $\sim 1.33 \mu\text{m}$  before calcination (potential application as TPV), 525 mg (1.68 mmol) eicosanoic acid were dissolved in a 250 mL wide-mouth glass bottle under stirring (250 rpm) at  $50^\circ\text{C}$  in 45 mL dry *n*-butanol (0.2  $\mu\text{m}$  PES filtered). In the meantime, 6.10 g (14.9 mmol) zirconium(IV) *n*-butoxide (80% in *n*-butanol) and 300 mg yttrium(III) *i*-propoxid (1.13 mmol) were diluted in 10 mL dry *n*-propanol and sonicated for 20 min. The zirconia and yttria precursor mixture was quickly (few seconds) added to the eicosanoic acid solution under stirring (250 rpm) at  $50^\circ\text{C}$  by using a PES syringe filter (0.1  $\mu\text{m}$  pores). A freshly prepared solution of 0.85 mL water in 43 mL *n*-butanol was heated up to  $55^\circ\text{C}$  under stirring (250 rpm) and added uniformly to the reaction solution over the course of 1 min. An extended stirring (250 rpm) of 40 s under the same conditions followed the induction time of 2 min and 20 s. Afterwards, the obtained particle suspension was transferred onto an analogue tube roller (SRT6 Stuart, roller size length x diameter: 340 mm x 30 mm) for 105 min at  $46^\circ\text{C}$  and a rotation speed of 12 rpm. Finally, purification and resuspension of the obtained YSZ microparticles were performed analogously to the undoped zirconia microparticles.

## 8 Experimental Section

For 5.5 mol% (Y) YSZ submicron particles with a diameter of  $\sim 117$  nm (potential application as SC), 14 mg (0.04 mmol) eicosanoic acid and 67 mg HPC were dissolved in 45 mL ethanol, which was filtered through a PES syringe filter (0.1  $\mu\text{m}$  pores). The clear solution was heated up to 55  $^{\circ}\text{C}$  under stirring (250 rpm). Meanwhile, 1.590 g (3.40 mmol) zirconium *n*-propoxide (70% in *n*-propanol) and 49 mg (0.18 mmol) yttrium *i*-propoxide in 5 mL *i*-propanol were sonicated for 15 min. After adding 220  $\mu\text{L}$  demin. water to the reaction solution, the precursors were quickly (few seconds) added by using a syringe (Vivomed, 2.00 x 120 mm). Within seconds, the solution turned white (induction time) and the suspension was stirred (250 rpm) further for 3 h. Purification and resuspension were similar to the synthesis of undoped  $\text{ZrO}_2$  submicron particles.

### Calcination of $\text{ZrO}_2$ and YSZ cores

All particles were dried at 80  $^{\circ}\text{C}$  for 4 h under ambient conditions (Heraeus Vacutherm VT from Thermo Scientific). Afterwards, the undoped zirconia and YSZ microparticles were calcined at 600  $^{\circ}\text{C}$ , the zirconia submicron particles at 400  $^{\circ}\text{C}$ , and the YSZ submicron particles at 480  $^{\circ}\text{C}$  for 3 h in a muffle oven (L9/SKM from Nabertherm GmbH). In each case, a heating rate of 5  $^{\circ}\text{C}\cdot\text{min}^{-1}$  and a cooling rate of  $\leq 5$   $^{\circ}\text{C}\cdot\text{min}^{-1}$  under ambient pressure and oxygen exposure were used. Calcination processes were performed prior to PSM with alumina or encapsulation with a silica shell, respectively, and further thermal treatments.

### Synthesis of $\text{ZrO}_2\text{-Al}_2\text{O}_3$ and YSZ- $\text{Al}_2\text{O}_3$ composite microparticles

Prior to PSM with alumina, 120 mg (20.4 mmol)  $\text{ZrO}_2$  or YSZ microparticles were suspended in 30 mL of an aqueous PVP solution (1 wt% PVP, average  $M_w \sim 80.000$ ,  $M_n = 10.000$ , 99%) under stirring (330 rpm) for 5 h by exclusion of light at room temperature. Purification was performed via centrifugation (0  $^{\circ}\text{C}$ , 2 min, 1000 x g) in water (twice) and ethanol (twice). For sol-gel PSM with alumina, 120 mg (20.4 mmol)  $\text{ZrO}_2$  or YSZ microparticles (with PVP at the particle surface), respectively, were suspended in 40 mL dry ethanol by sonication for 30 min. Afterwards, the suspension was heated up to 55  $^{\circ}\text{C}$  under stirring (400 rpm) followed by addition of 15 mg (0.15 mmol) aluminum *i*-propoxide in 10 mL dry ethanol. Then, the dispersion was stirred (400 rpm) further at 55  $^{\circ}\text{C}$  for 24 h. Purification

occurred via centrifugation (0 °C, 2 min, 1000 x g) in acetone (twice) and ethanol (twice). Finally, the obtained composite microparticles were resuspended in 2 mL ethanol.

Alternatively, the zirconia and YSZ microparticles were modified by using aluminum chloride as alumina precursor. For this purpose, 100 mg (0.820 mmol) ZrO<sub>2</sub> or YSZ microparticles, respectively, were suspended in 10 mL dry THF by sonication for 30 min. Meanwhile, 30 mg aluminum chloride (0.22 mmol) were dissolved in 10 mL dry THF under stirring (400 rpm) at 75 °C. The solvent THF was filtered through a PES syringe filter (0.2 µm pores) beforehand. After sufficient sonication, the particle suspension was added to the aluminum chloride solution under stirring (400 rpm) at 75 °C. The reaction mixture was further stirred (400 rpm) for 24 h under the same conditions. Purification and storage were performed analogously to the modification by aluminum *i*-propoxide.

### **Synthesis of ZrO<sub>2</sub>@SiO<sub>2</sub> and YSZ@SiO<sub>2</sub> core@shell submicron particles**

The encapsulation of calcined ZrO<sub>2</sub> and YSZ submicron particles with a silica shell was performed under nitrogen atmosphere using an EasyMax 402 Basic Plus Synthesis Workstation (Mettler Toledo) in two steps. First, in a modified Stöber pre-encapsulation step, 120 mg ZrO<sub>2</sub>/YSZ submicron particles were sonicated for 30 min in 55.5 mL THF. Afterwards, 500 µL demin. water were added under stirring (550 rpm) to the suspension, which was then heated to 60 °C. Then, 7.5 mL TEOS (33.5 mmol) were added and the suspension was stirred (550 rpm) for 19 h. For purification, the suspension was cooled down to 0 °C and centrifuged (0 °C, 5 min, 4000 x g) four times (each step washed with ~35 mL ethanol) to remove primary silica particles. The sedimented particles were then resuspended by sonication for 5 min in 120 mL ethanol.

In the second step (exemplary described for ZrO<sub>2</sub> cores), the suspension of pre-encapsulated ZrO<sub>2</sub>@SiO<sub>2</sub>-seeds particles was sonicated for 30 min, before adding 4.5 mL demin. water and 2.25 mL ammoniumhydroxide solution (15.8 mmol) under stirring (550 rpm) at room temperature. Afterwards, the reaction mixture was heated up to 30 °C and stirred (550 rpm) for 30 min, before addition of 0.3 mL TEOS (0.134 mmol) and 4.5 mL demin. water. After additional 75 min and 150 min, two further additions of, both, 0.102 mL TEOS (45.6 µmol) and 0.114 mL demin.

## 8 Experimental Section

water followed at the same conditions. Finally, 75 min after the last addition, the reaction was quenched by transferring the reaction suspension to 50 mL ice-cooled ethanol. The obtained core@shell particles were purified by repetitive centrifugation ( $-5\text{ }^{\circ}\text{C}$ , 4 min,  $4000\times g$ ), two times in ethanol and demineralized water, each. Finally, the particles were resuspended by sonication for 5 min in 10 mL ethanol. The above described procedure yielded  $\text{ZrO}_2@\text{SiO}_2$  core@shell particles with an average shell thickness of  $\sim 38$  nm. The silica shell thickness could be adjusted by varying the number of additions and the amounts of TEOS and water added to the reaction mixture. For different core particle sizes and amounts, TEOS and water volumes were adjusted according to the approximate particle surface area.

### 8.2.1 Assembly of photonic glasses

Photonic glasses made out of YSZ microparticles were deposited on sapphire substrates by using a polytetrafluorethylen (PTFE) ring ( $H = 8$  mm,  $T = 10$  mm) with an inner diameter of  $D = 10$  mm as shown in Figure 8.1.

Therefore, 500  $\mu\text{L}$  of a toluene-ethanol solution (ratio 1:4) were put into the PTFE ring, before 67  $\mu\text{L}$  of the calcined microparticle suspension in ethanol ( $c = 1\text{ g}\cdot\text{L}^{-1}$ ) were added to the solution by subsequent mixing of the dispersion. Thereafter, the microparticles uniformly sedimented to the sapphire surface, while the solvents slowly evaporated leaving a photonic glass behind.

Photonic glasses made out of undoped zirconia microparticles were deposited on sapphire substrates by using an equilateral PTFE rectangle ( $H = 8$  mm,  $T = 10$  mm, inner edge length = 20 mm). Here, the parameters from YSZ microparticles were adjusted to the larger deposition area.

The synthesized  $\text{YSZ}@\text{SiO}_2$  core@shell particles were also assembled on sapphire substrates as photonic glasses. For deposition, a PTFE ring with a height of 8 mm and an inner diameter of 10 mm was used. Typically, 500  $\mu\text{L}$  of  $\text{YSZ}@\text{SiO}_2$  particles in ethanol ( $c = 1\text{ g}\cdot\text{L}^{-1}$ ) were injected into the PTFE ring followed by mixing of the dispersion via repetitive mixing. The core@shell particles slowly segregated to the sapphire surface, whereby a photonic glass was formed.

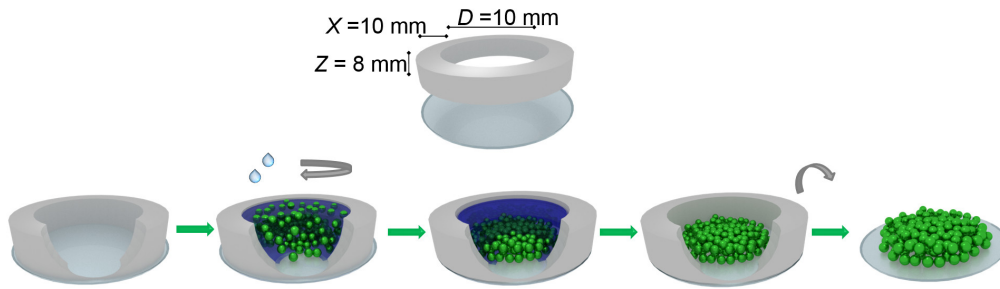


**Figure 8.1** – Deposition process of YSZ microparticles to photonic glasses on sapphire substrates. First, 500  $\mu\text{L}$  of a toluene-ethanol solution (ratio 1:4) were put into the PTFE ring, before 67  $\mu\text{L}$  of the calcined microparticle suspension in ethanol ( $c = 1 \text{ g}\cdot\text{L}^{-1}$ ) were added to the solution by subsequent mixing of the dispersion. After sedimentation of the particles and evaporation of the solvents, a photonic glass was formed. Figure adopted from reference.[178]

### 8.2.2 Deposition of a YSZ microparticle monolayer

The deposition process of YSZ microparticle monolayers on tungsten substrates was investigated and implemented in a collaboration with Yen Häntschi from the group of Prof. Gerold Schneider (Advanced Ceramics, Hamburg University of Technology).

For deposition of 7.5 mol% (Y) YSZ microparticle monolayers, sapphire substrates (5 x 5 mm) with a 200 nm tungsten layer and a 20 nm superficial hafnia coating were used. The substrates were oxygen-plasma cleaned before deposition process to generate a hydrophilic surface. To achieve a YSZ monolayer, the calcined (600  $^{\circ}\text{C}$ , 3 h, heating and cooling rate: 5  $^{\circ}\text{C}\cdot\text{min}^{-1}$ ) YSZ microparticles were suspended in ethanol and then homogenized by sonication for 15 min yielding a final concentration of 1  $\text{g}\cdot\text{L}^{-1}$ . Afterwards, the YSZ particle suspension was dripped carefully onto water in a crystallizing dish by using a pipette until the water surface was fully covered by YSZ particles. Finally, the sapphire substrates with W/HfO<sub>2</sub> layer were dipped under water and carefully lifted up in a  $\sim 45^{\circ}$  angle between the water surface and the top of the substrate yielding a YSZ microparticle monolayer.

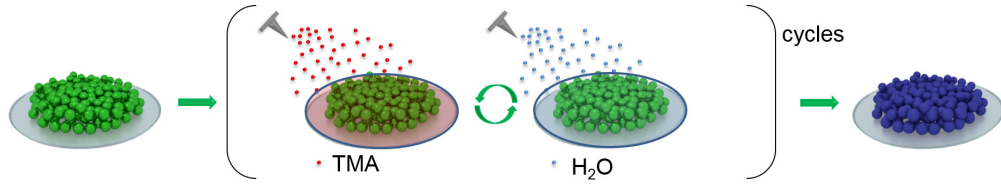


**Figure 8.2** – Schematic illustration of alumina ALD on photonic glasses (substrate: sapphire) from zirconia and YSZ microparticles. The particle assembly was alternately treated in several cycles with Trimethylaluminum (TMA) and water with a rinsing step (nitrogen) in between. Figure adapted from reference.[178]

### 8.2.3 Atomic layer deposition of alumina

Besides sol-gel PSM of the calcined zirconia and YSZ microparticles with alumina, deposition of alumina on assembled microparticles by ALD was conducted as schematically shown in Fig. 8.2.

Thus, the photonic glasses on sapphire substrates were put into an ALD reactor (Savannah™ 200 from Ultratech/Cambridge NanoTech). As alumina precursor, TMA and demin. water were used. In the ALD process, the two reactants were alternately sprayed into the reaction chamber, whereby it was flushed with nitrogen in between as illustrated in Fig. 8.2. The addition of the precursor occurred at 150 °C under constant nitrogen flow (30 sccm). After 300 cycles, an amorphous alumina shell with a layer thickness of  $\sim 47$  nm was obtained (see Section 8.3, Fig. 8.11).

The alumina shell thickness was determined by investigation of the refractive index due to spectral ellipsometry (SENPro™ from SENTECH Instruments GmbH) of a reference silicon sample, which was also placed in the reaction chamber. Additionally, the alumina shell thickness was investigated by cross-sectional TEM from FIB preparation of YSZ microparticles as lamellae.

The photonic glasses made out of YSZ@SiO<sub>2</sub> core@shell particles on sapphire substrates were also coated with  $\sim 50$  nm Al<sub>2</sub>O<sub>3</sub> by ALD (see Section 8.3, Fig. 8.7) to fill the air gaps between the particles as high refractive index background. This high refractive index material compared to silica ensures a non-monotonous refractive index distribution from zirconia core ( $\sim 2.2$ ) through silica shell ( $\sim 1.5$ ) into alumina matrix ( $\sim 1.8$ ) in the visible range. For an alumina thickness of  $\sim 50$  nm, 325 cycles were performed.

The results from ALD in this dissertation were obtained in collaboration with the group of Dr. Rolf Janßen from the Institute of Advanced Ceramics (TUHH) in Hamburg. The experimental implementation was conducted by Dr. Kalline Furlan.

#### 8.2.4 Microcompression of zirconia microparticles

The mechanical properties of zirconia microparticles were characterized by micro-compression experiments in collaboration with the group of Prof. Wolfgang Peukert from the Institute of Particle Technology at FAU in Erlangen-Nürnberg. The experimental implementation was performed by Jan Schwenger, Stefan Romeis, and Patrick Herre. Experimental details can be found in the referenced literature.[5]

## 8.3 Thermal loading

### ZrO<sub>2</sub>-Al<sub>2</sub>O<sub>3</sub> and YSZ-Al<sub>2</sub>O<sub>3</sub> composite microparticles

In order to identify the high-temperature stability, the assembled ZrO<sub>2</sub>-Al<sub>2</sub>O<sub>3</sub> and YSZ-Al<sub>2</sub>O<sub>3</sub> composite microparticles from PSM and ALD of alumina were first dried at 80 °C for 4 h (Heraeus Vacutherm VT from Thermo Scientific). Afterwards, the microparticles were calcined in the temperature range between 600 and 1500 °C for 3 h under ambient conditions. As reference, assembled undoped zirconia and YSZ microparticles were treated the same way. The heating rate was 5 °C·min<sup>-1</sup> followed by a cooling rate of ≤5 °C·min<sup>-1</sup> in each case as shown in Fig. 8.3. Heating experiments up to 1000 °C were conducted in a muffle oven (L9/SKM from Nabertherm GmbH), whereas temperature treatment above 1000 °C was performed in a tube furnace (SFT 16/180 from Carbolithe). To analyze changes in size and shape of the particles upon calcination, the samples were characterized by TEM (JEOL JEM-1011; Philips CM 300) and SEM (EVO MA 10; Leo Type 1550 Gemini, both Zeiss). Furthermore, cross-sectional lamellae of composite particles were prepared via FIB technique (FEI Helios NanoLab G3 UC) and characterized by TEM, HAADF-STEM, and EDX mapping (Thermo Scientific, Talos F200X). FIB preparation, HAADF-STEM, and EDX mappings were conducted in collaboration with the electron microscopy unit (BEEM) at the TUHH in Hamburg under the

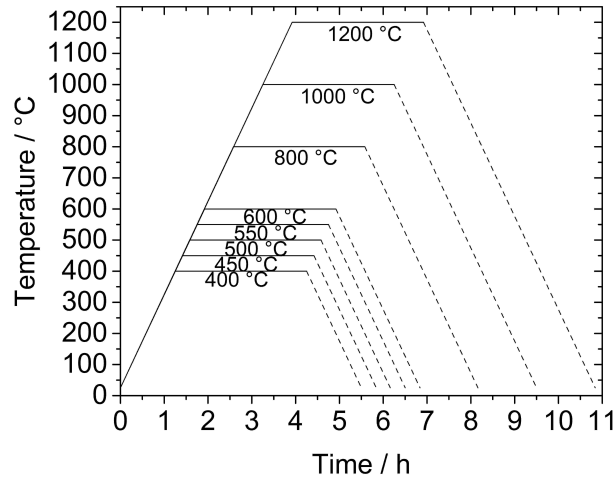


**Figure 8.3** – Temperature profiles used for calcination experiments. The heating rate was  $5\text{ }^{\circ}\text{C}\cdot\text{min}^{-1}$  and the highest temperature was kept constant for 3 h. The cooling rate was  $\leq 5\text{ }^{\circ}\text{C}\cdot\text{min}^{-1}$ .

leadership of Dr. Martin Ritter. Experimental implementation was performed by Tobias Krekeler. Additionally, the particles were characterized by *ex situ* XRD (Philips X’Pert PRO MPD). XRD measurements from photonic glasses on sapphire substrates were operated in collaboration with the group of Prof. Jörg Weißmüller from the Institute of Materials Physics and Technology at TUHH in Hamburg. Experimental implementation was performed by Rainer Behn (Bruker AXS, D8 Advance, Cu- $K_{\alpha}$  anode, Bragg-Brentano geometry, grazing incidence mode). Grain sizes were determined using the Scherrer equation and SEM images at higher temperatures using surface grains as shown in Section 8.3, Fig. 8.5. Optical properties of the obtained photonic glasses for potential TBC application were determined by NIR diffuse reflection spectra (FTIR, Vertex 70, Bruker) in collaboration with the group of Prof. Manfred Eich from the Institute of Optical and Electronic Materials at Hamburg University of Technology. Experimental implementation was performed by Dr. Guoliang Shang.

### YSZ microparticle monolayer

Investigation of the optical properties of YSZ microparticle monolayers on tungsten substrates occurred in collaboration with Dr. Manohar Chirumamilla from the group of Prof. Manfred Eich (Institute of Optical and Electronic Materials, Hamburg University of Technology). The annealing experiments were conducted

in a high-temperature vacuum furnace (RD-G WEBB) at  $2 \cdot 10^{-6}$  mbar. For heating and cooling rate,  $10 \text{ }^\circ\text{C} \cdot \text{min}^{-1}$  were used by holding the highest temperature of  $1400 \text{ }^\circ\text{C}$  for 6 h. Characterization of the optical properties was performed by using a Fourier transform infrared spectrometer (FTIR-Vertex 70, Bruker) in the range of 1 to  $4 \text{ } \mu\text{m}$ .

### ZrO<sub>2</sub>@SiO<sub>2</sub> and YSZ@SiO<sub>2</sub> core@shell submicron particles

After silica encapsulation, the obtained ZrO<sub>2</sub>@SiO<sub>2</sub> and YSZ@SiO<sub>2</sub> core@shell particles were dried at  $80 \text{ }^\circ\text{C}$  for 4 h in a vacuum oven (Heraeus Vacutherm VT, Thermo Scientific). Particle sizes, shell thicknesses, and size distributions were determined by TEM (JEOL JEM-1011; Philips CM 300). Afterwards, the obtained core@shell particles were calcined in the temperature range from  $450$  to  $1200 \text{ }^\circ\text{C}$  (ZrO<sub>2</sub>@SiO<sub>2</sub>). For comparison, the bare zirconia core particles and the pre-encapsulated ZrO<sub>2</sub>@SiO<sub>2</sub>-seeds particles were heat-treated the same way. The heat treatment up to  $1000 \text{ }^\circ\text{C}$  was done using the muffle oven (L9/SKM from Nabertherm GmbH), whereas the heat treatment at  $1200 \text{ }^\circ\text{C}$  was done using a tube furnace (SFT 16/100 from Carbolite). For all heat treatments the same heating ramp ( $5 \text{ }^\circ\text{C} \cdot \text{min}^{-1}$ ) and cooling rate ( $\leq 5 \text{ }^\circ\text{C} \cdot \text{min}^{-1}$ ) were used and the maximum temperature was held for 3 h (see Fig. 8.3). To analyze changes in size and shape of the particles upon calcination, the samples were characterized by TEM (JEOL JEM-1011; Phillips CM 300) and SEM (EVO MA 10; Leo Type 1550 Gemini, both Zeiss). Furthermore, cross-sectional lamellae of core@shell particles were prepared via FIB technique (FEI Helios NanoLab G3 UC) and characterized by TEM, HAADF-STEM, and EDX mapping (Thermo Scientific, Talos F200X). FIB preparation, HAADF-STEM, and EDX mappings were conducted in collaboration with the electron microscopy unit (BEEM) at the TUHH in Hamburg under the leadership of Dr. Martin Ritter. Experimental implementation was performed by Tobias Krekeler. Additionally, the particles were characterized by *ex situ* XRD (Philips X'Pert PRO MPD). For the analysis of phase compositions of ZrO<sub>2</sub>@SiO<sub>2</sub> core@shell submicron particles, the obtained diffractograms were background corrected and evaluated using the software Maud 2.76 and its built-in Rietveld refinement tool in collaboration with Gregor Dahl (Physical Chemistry, UHH).[210] For this purpose, an instrument calibration was conducted prior to the sample measurements in order to account for instrumental broadening. Crystallographic information for all zirconia phases originated from a work by Howard *et al.*[211]

## 8 *Experimental Section*

and were obtained from the ICSD online database (ICSD codes: 62993, 62994, 62995). Grain sizes were determined using the Scherrer equation as described in Section 4.2.2. Optical properties of the obtained photonic glassed for potential SC application were determined by visible reflection spectra (NIR-UV-VIS spectrometer with 150 mm integrating sphere accessories, Lambda 1050, Perkin Elmer) in collaboration with the group of Prof. Manfred Eich from the Institute of Optical and Electronic Materials at Hamburg University of Technology. Experimental implementation was performed by Dr. Guoliang Shang.

## Bibliography

- [1] E. W. Leib, U. Vainio, R. M. Pasquarelli, J. Kus, C. Czaschke, N. Walter, R. Janssen, M. Müller, A. Schreyer, H. Weller, and T. Vossmeier. “Synthesis and thermal stability of zirconia and yttria-stabilized zirconia microspheres”. In: *Journal of Colloid and Interface Science* 448 (2015), pp. 582–592. DOI: 10.1016/j.jcis.2015.02.049 (cit. on pp. 9, 13, 21, 22, 31, 33, 34, 36, 49, 50, 52, 66, 71, 75, 77, 79, 83, 92, 93, 105, 106).
- [2] E. W. Leib, R. M. Pasquarelli, J.J. do Rosário, P. N. Dyachenko, S. Döring, A. Puchert, A. Y. Petrov, M. Eich, G. A. Schneider, R. Janssen, H. Weller, and T. Vossmeier. “Yttria-stabilized zirconia microspheres: novel building blocks for high-temperature photonics”. In: *Journal of Materials Chemistry C* 4 (2016), pp. 62–74. DOI: 10.1039/c5tc03260a (cit. on pp. 9, 21, 22, 25, 35, 37, 38, 50, 56, 60, 63, 68, 92).
- [3] E. W. Leib, R. M. Pasquarelli, M. Blankenburg, M. Müller, A. Schreyer, R. Janssen, H. Weller, and T. Vossmeier. “High-temperature stable zirconia particles doped with yttrium, lanthanum, and gadolinium”. In: *Particle and Particle Systems Characterization* 33.9 (2016), pp. 645–655. DOI: 10.1002/ppsc.201600069 (cit. on pp. 9, 22, 37, 92).
- [4] Z. Du, X. M. Zeng, Q. Liu, C. A. Schuh, and C. L. Gan. “Superelasticity in micro-scale shape memory ceramic particles”. In: *Acta Materialia* 123 (2017), pp. 255–263. DOI: 10.1016/j.actamat.2016.10.047 (cit. on pp. 9, 21).
- [5] J. Schwenger, S. Romeis, P. Herre, T. Yokosawa, M. Finsel, E. W. Leib, H. Weller, T. Vossmeier, E. Spiecker, and W. Peukert. “Pressure induced local phase transformation in nanocrystalline tetragonal zirconia microparticles”. In: *Scripta Materialia* 163 (2019), pp. 86–90. DOI: 10.1016/j.scriptamat.2018.12.035 (cit. on pp. 9, 21, 27, 93–95, 113).
- [6] G. Shang, L. Maiwald, H. Renner, D. Jalas, M. Dosta, S. Heinrich, A. Petrov, and M. Eich. “Photonic glass for high contrast structural color”. In: *Scientific Reports* 8 (2018), pp. 1–9. DOI: 10.1038/s41598-018-26119-8 (cit. on pp. 9, 11, 12, 15, 21, 22, 71, 87).
- [7] X. Yang, N. Zhao, Q. Zhou, C. Cai, X. Zhang, and J. Xu. “Precise preparation of highly monodisperse  $\text{ZrO}_2\text{@SiO}_2$  core-shell nanoparticles with adjustable refractive indices”. In: *Journal of Materials Chemistry C* 1 (2013), pp. 3359–3366. DOI: 10.1039/c3tc30324a (cit. on pp. 9, 12, 41, 71, 73, 75).

## Bibliography

- [8] J. H. Shim, C.-C. Chao, H. Huang, and F. B. Prinz. “Atomic layer deposition of yttria-stabilized zirconia for solid oxide fuel cells”. In: *Chemistry of Materials* 19.15 (2007), pp. 3850–3854. DOI: 10.1021/cm070913t (cit. on pp. 9, 21).
- [9] D. Lu, J. Wang, L. Wang, D. Du, C. Timchalk, R. Barry, and Y. Lin. “A novel nanoparticle-based disposable electrochemical immunosensor for diagnosis of exposure to toxic organophosphorus agents”. In: *Advanced Functional Materials* 21.22 (2011), pp. 4371–4378. DOI: 10.1002/adfm.201100616 (cit. on pp. 9, 21).
- [10] W. Cao, O. K. Tan, W. Zhu, and B. Jiang. “Mechanical alloying and thermal decomposition of  $(\text{ZrO}_2)_{0.8}-(\alpha\text{-Fe}_2\text{O}_3)_{0.2}$  powder for gas sensing applications”. In: *Journal of Solid State Chemistry* 155.2 (2000), pp. 320–325. DOI: 10.1006/jssc.2000.8920 (cit. on pp. 9, 21).
- [11] C. S. Wright, R. I. Walton, D. Thompsett, J. Fisher, and S. E. Ashbrook. “One-step hydrothermal synthesis of nanocrystalline ceria-zirconia mixed oxides: The beneficial effect of sodium inclusion on redox properties”. In: *Advanced Materials* 19.24 (2007), pp. 4500–4504. DOI: 10.1002/adma.200602474 (cit. on pp. 9, 21, 38).
- [12] T. P. Weber, P. T. Jackson, and P. W. Carr. “Chromatographic evaluation of porous carbon-clad zirconia microparticles”. In: *Analytical Chemistry* 67 (1995), pp. 3042–3050. DOI: 10.1021/ac00113a045 (cit. on pp. 9, 21, 92).
- [13] P. N. Dyachenko, A. Y. Petrov, and M. Eich. “Perfect narrow-band absorber based on a monolayer of metallodielectric microspheres”. In: *Applied Physics Letters* 103.21 (2013), p. 211105. DOI: 10.1063/1.4832071 (cit. on pp. 9, 12, 22, 92).
- [14] P. N. Dyachenko, J. J. do Rosário, E. W. Leib, A. Y. Petrov, M. Störmer, H. Weller, T. Vossmeier, G. A. Schneider, and M. Eich. “Tungsten band edge absorber/emitter based on a monolayer of ceramic microspheres”. In: *Optics Express* 23.19 (2015), A1236–A1244. DOI: 10.1364/OE.23.0A1236 (cit. on pp. 9, 13, 92, 95–98).
- [15] M. C. C. S. Moraes, C. N. Elias, J. D. Filho, and L. G. de Oliveira. “Mechanical properties of alumina-zirconia composites for ceramic abutments”. In: *Materials Research* 7.4 (2004), pp. 643–649. DOI: 10.1590/S1516-14392004000400021 (cit. on pp. 9, 92).
- [16] H. Fischer, W. Rentzsch, and R. Marx. “Elimination of low-quality ceramic posts by proof testing”. In: *Dental Materials* 18.8 (2002), pp. 570–575. DOI: 10.1016/S0109-5641(01)00091-4 (cit. on pp. 9, 92).
- [17] O. Keith, R. P. Kusy, and J. Q. Whitley. “Zirconia brackets: An evaluation of morphology and coefficients of friction”. In: *American Journal of Orthodontics and Dentofacial Orthopedics* 106.6 (1994), pp. 605–614. DOI: 10.1016/S0889-5406(94)70085-0 (cit. on pp. 9, 92).

- [18] B. I. Ardlin. “Transformation-toughened zirconia for dental inlays, crowns and bridges: Chemical stability and effect of low-temperature aging on flexural strength and surface structure”. In: *Dental Materials* 18.8 (2002), pp. 590–595. DOI: 10.1016/S0109-5641(01)00095-1 (cit. on pp. 9, 92).
- [19] D. R. Clarke, M. Oechsner, and N. P. Padture. “Thermal-barrier coatings for more efficient gas-turbine engines”. In: *Materials Research Society Bulletin* 37.10 (2012), pp. 891–898. DOI: 10.1557/mrs.2012.232 (cit. on pp. 9, 22, 92).
- [20] A. Keyvani, M. Saremi, M. Heydarzadeh Sohi, and Z. Valefi. “A comparison on thermomechanical properties of plasma-sprayed conventional and nanostructured YSZ TBC coatings in thermal cycling”. In: *Journal of Alloys and Compounds* 541 (2012), pp. 488–494. DOI: 10.1016/j.jallcom.2012.06.062 (cit. on pp. 9, 22, 92).
- [21] P. N. Dyachenko, J. J. Do Rosário, E. W. Leib, A. Y. Petrov, R. Kubrin, G. A. Schneider, H. Weller, T. Vossmeier, and M. Eich. “Ceramic photonic glass for broadband omnidirectional reflection”. In: *American Chemical Society Photonics* 1.11 (2014), pp. 1127–1133. DOI: 10.1021/ph500224r (cit. on pp. 9, 20, 21, 92).
- [22] N. Vogel, S. Utech, G. T. England, T. Shirman, K. R. Phillips, N. Koay, I. B. Burgess, M. Kolle, D. A. Weitz, and J. Aizenberg. “Color from hierarchy: Diverse optical properties of micron-sized spherical colloidal assemblies”. In: *Proceedings of the National Academy of Sciences* 112.35 (2015), pp. 10845–10850. DOI: 10.1073/pnas.1506272112 (cit. on pp. 9, 22).
- [23] M. Harun-Ur-Rashid, A. B. Imran, T. Seki, M. Ishii, H. Nakamura, and Y. Takeoka. “Angle-independent structural color in colloidal amorphous arrays”. In: *ChemPhysChem* 11.3 (2010), pp. 579–583. DOI: 10.1002/cphc.200900869 (cit. on pp. 9, 21, 22).
- [24] J. G. Park, S. H. Kim, S. Magkiriadou, T. M. Choi, Y. S. Kim, and V. N. Manoharan. “Full-spectrum photonic pigments with non-iridescent structural colors through colloidal assembly”. In: *Angewandte Chemie - International Edition* 53.11 (2014), pp. 2899–2903. DOI: 10.1002/anie.201309306 (cit. on pp. 9, 12).
- [25] Y. Häntsch, G. Shang, A. Y. Petrov, M. Eich, and G. A. Schneider. “YSZ hollow sphere photonic glasses : tailoring optical properties for highly saturated non-iridescent structural coloration”. In: *Advanced Optical Materials* (2019), p. 1900428. DOI: 10.1002/adom.201900428 (cit. on p. 9).
- [26] C. Ren, Y. D. He, and D. R. Wang. “Cyclic oxidation behavior and thermal barrier effect of YSZ-(Al<sub>2</sub>O<sub>3</sub>/YAG) double-layer TBCs prepared by the composite sol-gel method”. In: *Surface and Coatings Technology* 206.6 (2011), pp. 1461–1468. DOI: 10.1016/j.surfcoat.2011.09.025 (cit. on pp. 9, 10, 60).

## Bibliography

- [27] I. W. Chen. “Mobility control of ceramic grain boundaries and interfaces”. In: *Materials Science and Engineering A* 166.1-2 (1993), pp. 51–58. DOI: 10.1016/0921-5093(93)90309-3 (cit. on pp. 9, 29, 60).
- [28] M. Matsumoto, N. Yamaguchi, and H. Matsubara. “Low thermal conductivity and high temperature stability of  $\text{ZrO}_2\text{-Y}_2\text{O}_3\text{-La}_2\text{O}_3$  coatings produced by electron beam PVD”. In: *Scripta Materialia* 50.6 (2004), pp. 867–871. DOI: 10.1016/j.scriptamat.2003.12.008 (cit. on p. 9).
- [29] N. P. Padture, M. Gell, and E. H. Jordan. “Thermal barrier coatings for gas-turbine engine applications”. In: *Science* 296.5566 (2002), pp. 280–284. DOI: 10.1126/science.1068609 (cit. on pp. 10, 28, 53).
- [30] A. Keyvani, M. Saremi, and M. H. Sohi. “Oxidation resistance of YSZ-alumina composites compared to normal YSZ TBC coatings at 1100 °C”. In: *Journal of Alloys and Compounds* 509.33 (2011), pp. 8370–8377. DOI: 10.1016/j.jallcom.2011.05.029 (cit. on p. 10).
- [31] J. Sun, B. Bhushan, and J. Tong. “Structural coloration in nature”. In: *Royal Society of Chemistry Advances* 3 (2013), pp. 14862–14889. DOI: 10.1039/c3ra41096j (cit. on pp. 11, 15, 20).
- [32] O. Sato, S. Kubo, and G. U. Zhong-Ze. “Structural color films with lotus effects, superhydrophilicity, and tunable stop-bands”. In: *Accounts of Chemical Research* 42.1 (2009), pp. 1–10. DOI: 10.1021/ar700197v (cit. on pp. 11, 16).
- [33] E. Shevtsova, C. Hansson, D. H. Janzen, and J. Kjaerandsen. “Stable structural color patterns displayed on transparent insect wings”. In: *Proceedings of the National Academy of Sciences* 108.2 (2011), pp. 668–673. DOI: 10.1073/pnas.1017393108 (cit. on pp. 11, 15).
- [34] A. Cesaratto, C. D’Andrea, A. Nevin, G. Valentini, F. Tassone, R. Alberti, T. Frizzi, and D. Comelli. “Analysis of cadmium-based pigments with time-resolved photoluminescence”. In: *Analytical Methods* 6.1 (2014), pp. 130–138. DOI: 10.1039/c3ay41585f (cit. on p. 11).
- [35] Wendusu, T. Yoshida, T. Masui, and N. Imanaka. “Novel environmentally friendly inorganic red pigments based on calcium bismuth oxides”. In: *Journal of Advanced Ceramics* 4.1 (2015), pp. 39–45. DOI: 10.1007/s40145-015-0129-1 (cit. on p. 11).
- [36] M. Jansen and H. P. Letschert. “Inorganic yellow-red pigments without toxic metals”. In: *Nature* 404 (2000), pp. 980–982. DOI: 10.1038/35010082 (cit. on p. 11).
- [37] J. Wang, Y. Zhang, S. Wang, Y. Song, and L. Jiang. “Bioinspired colloidal photonic crystals with controllable wettability”. In: *Accounts of Chemical Research* 44.6 (2011), pp. 405–415. DOI: 10.1021/ar1001236 (cit. on p. 12).

- [38] C. Xiao, R. V. Maligal-Ganesh, T. Li, Z. Qi, Z. Guo, K. T. Brashler, S. Goes, X. Li, T.W. Goh, R. E. Winans, and W. Huang. “High-temperature-stable and regenerable catalysts: Platinum nanoparticles in aligned mesoporous silica wells”. In: *ChemSusChem* 6.10 (2013), pp. 1915–1922. DOI: 10.1002/cssc.201300524 (cit. on p. 12).
- [39] K. A. Dahlberg and J. W. Schwank. “Synthesis of Ni@SiO<sub>2</sub> nanotube particles in a water-in-oil microemulsion template”. In: *Chemistry of Materials* 24.14 (2012), pp. 2635–2644. DOI: 10.1021/cm203779v (cit. on p. 12).
- [40] V. R. Calderone, J. Schütz-Widoniak, G. L. Bezemer, G. Bakker, C. Steurs, and A. P. Philipse. “Design of colloidal Pt catalysts encapsulated by silica nano membranes for enhanced stability in H<sub>2</sub>S streams”. In: *Catalysis Letters* 137.3-4 (2010), pp. 132–140. DOI: 10.1007/s10562-010-0359-3 (cit. on p. 12).
- [41] J. C. Park, J. U. Bang, J. Lee, C. H. Ko, and H. Song. “Ni@SiO<sub>2</sub> yolk-shell nanoreactor catalysts: High temperature stability and recyclability”. In: *Journal of Materials Chemistry* 20.7 (2010), pp. 1217–1388. DOI: 10.1039/b918446e (cit. on pp. 12, 39).
- [42] Q. Zhang, I. Lee, J. B. Joo, F. Zaera, and Y. Yin. “Core-shell nanostructured catalysts”. In: *Accounts of Chemical Research* 46.8 (2013), pp. 1816–1824. DOI: 10.1021/ar300230s (cit. on pp. 12, 39).
- [43] R. G. Chaudhuri and S. Paria. “Core/shell nanoparticles: Classes, properties, synthesis mechanisms, characterization, and applications”. In: *Chemical Reviews* 112.4 (2012), pp. 2373–2433. DOI: 10.1021/cr100449n (cit. on p. 12).
- [44] J. F. Li, Y. J. Zhang, S. Y. Ding, R. Panneerselvam, and Z. Q. Tian. “Core-shell nanoparticle-enhanced raman spectroscopy”. In: *Chemical Reviews* 117.7 (2017), pp. 5002–5069. DOI: 10.1021/acs.chemrev.6b00596 (cit. on p. 12).
- [45] A. Ahmed, K. Skinley, S. Herodotou, and H. Zhang. “Core-shell microspheres with porous nanostructured shells for liquid chromatography”. In: *Journal of Separation Science* 41.1 (2018), pp. 99–124. DOI: 10.1002/jssc.201700850 (cit. on pp. 12, 92).
- [46] R. Hayes, A. Ahmed, T. Edge, and H. Zhang. “Core-shell particles: Preparation, fundamentals and applications in high performance liquid chromatography”. In: *Journal of Chromatography A* 1357 (2014), pp. 36–52. DOI: 10.1016/j.chroma.2014.05.010 (cit. on p. 12).
- [47] M. Gumustas, P. Zalewski, S. A. Ozkan, and B. Uslu. “The history of the core-shell particles and applications in active pharmaceutical ingredients via liquid chromatography”. In: *Chromatographia* 82.1 (2019), pp. 17–48. DOI: 10.1007/s10337-018-3670-6 (cit. on p. 12).

## Bibliography

- [48] A. Bumb, S. K. Sarkar, N. Billington, M. W. Brechbiel, and K. C. Neuman. “Silica encapsulation of fluorescent nanodiamonds for colloidal stability and facile surface functionalization”. In: *Journal of the American Chemical Society* 135.21 (2013), pp. 7815–7818. DOI: 10.1021/ja4016815 (cit. on p. 12).
- [49] R. He, X. You, J. Shao, F. Gao, B. Pan, and D. Cui. “Core/shell fluorescent magnetic silica-coated composite nanoparticles for bioconjugation”. In: *Nanotechnology* 18.31 (2007), p. 315601. DOI: 10.1088/0957-4484/18/31/315601 (cit. on p. 12).
- [50] K. Y. Yoon, C. Kotsmar, D. R. Ingram, C. Huh, S. L. Bryant, T. E. Milner, and K. P. Johnston. “Stabilization of superparamagnetic iron oxide nanoclusters in concentrated brine with cross-linked polymer shells”. In: *Langmuir* 27.17 (2011), pp. 10962–10969. DOI: 10.1021/1a2006327 (cit. on p. 12).
- [51] F. Wang, X. Chen, Z. Zhao, S. Tang, X. Huang, C. Lin, C. Cai, and N. Zheng. “Synthesis of magnetic, fluorescent and mesoporous core-shell-structured nanoparticles for imaging, targeting and photodynamic therapy”. In: *Journal of Materials Chemistry* 21 (2011), pp. 11244–11252. DOI: 10.1039/c1jm10329f (cit. on p. 12).
- [52] Y. Kobayashi, H. Inose, T. Nakagawa, K. Gonda, M. Takeda, N. Ohuchi, and A. Kasuya. “Control of shell thickness in silica-coating of Au nanoparticles and their X-ray imaging properties”. In: *Journal of Colloid and Interface Science* 358.2 (2011), pp. 329–333. DOI: 10.1016/j.jcis.2011.01.058 (cit. on p. 12).
- [53] A. Petrov, H. Lehmann, M. Finsel, C. Klinke, H. Weller, and T. Vossmeier. “Synthesis and characterization of monodisperse metalodielectric SiO<sub>2</sub>@Pt@SiO<sub>2</sub> core-shell-shell particles”. In: *Langmuir* 32.3 (2016), pp. 848–857. DOI: 10.1021/acs.langmuir.5b03631 (cit. on pp. 12, 39).
- [54] L. Shi, Y. Zhang, B. Dong, T. Zhan, X. Liu, and J. Zi. “Amorphous photonic crystals with only short-range order”. In: *Advanced Materials* 25.37 (2013), pp. 5314–5320. DOI: 10.1002/adma.201301909 (cit. on pp. 12, 19, 20).
- [55] J. Ye, B. Van de Broek, R. De Palma, W. Libaers, K. Clays, W. Van Roy, G. Borghs, and G. Maes. “Surface morphology changes on silica-coated gold colloids”. In: *Colloids and Surfaces A: Physicochemical and Engineering Aspects* 322.1-3 (2008), pp. 225–233. DOI: 10.1016/j.colsurfa.2008.03.033 (cit. on p. 12).
- [56] A. Bai, H. Song, G. He, Q. Li, C. Yang, L. Tang, and Y. Yu. “Facile synthesis of core-shell structured ZrO<sub>2</sub>@SiO<sub>2</sub> via a modified Stöber method”. In: *Ceramics International* 42.6 (2016), pp. 7583–7592. DOI: 10.1016/j.ceramint.2016.01.166 (cit. on pp. 12, 72, 75, 76).

- [57] V. Srdic, B. Mojic, M. Nikolic, and S. Ognjanovic. “Recent progress on synthesis of ceramics core/shell nanostructures”. In: *Processing and Application of Ceramics 7.2* (2013), pp. 45–62. DOI: 10.2298/pac1302045s (cit. on pp. 12, 38–44).
- [58] W. Stöber, A. Fink, and E. Bohn. “Controlled growth of monodisperse silica spheres in the micron size range”. In: *Journal of Colloid and Interface Science* 26.1 (1968), pp. 62–69 (cit. on p. 12).
- [59] T. Ung, L. M. Liz-Marzán, and P. Mulvaney. “Optical properties of thin films of Au@SiO<sub>2</sub> particles”. In: *The Journal of Physical Chemistry B* 105.17 (2001), pp. 3441–3452. DOI: 10.1021/jp003500n (cit. on p. 12).
- [60] I. Lee, D. Kim, J. Kal, H. Baek, D. Kwak, D. Go, E. Kim, C. Kang, J. Chung, Y. Jang, S. Ji, J. Joo, and Y. Kang. “Quasi-amorphous colloidal structures for electrically tunable full-color photonic pixels with angle-independency”. In: *Advanced Materials* 22.44 (2010), pp. 4973–4977. DOI: 10.1002/adma.201001954 (cit. on p. 12).
- [61] H. Wang, X. Jiang, L. Qian, W. Chen, and M. Zhu. “Preparation of core-shell ZrO<sub>2</sub>@SiO<sub>2</sub> nanoparticles and its effect on properties of composites”. In: *Chinese Materials Conference: Advanced Functional Materials*. 2018, pp. 723–730. DOI: 10.1002/9781118998977 (cit. on p. 12).
- [62] J. Widoniak, S. Eiden-Assmann, and G. Maret. “Synthesis and characterisation of monodisperse zirconia particles”. In: *European Journal of Inorganic Chemistry* 2005.15 (2005), pp. 3149–3155. DOI: 10.1002/ejic.200401025 (cit. on pp. 13, 31, 36, 50, 52, 71, 72, 76, 77, 106).
- [63] S. Shukla and S. Seal. “Thermodynamic tetragonal phase stability in sol-gel derived nanodomains of pure zirconia”. In: *The Journal of Physical Chemistry B* 108.11 (2004), pp. 3395–3399. DOI: 10.1021/jp037532x (cit. on pp. 13, 23, 24, 36, 37, 52, 77, 80).
- [64] S. Shukla and S. Seal. “Mechanisms of room temperature metastable tetragonal phase stabilisation in zirconia”. In: *International Materials Reviews* 50.1 (2005), pp. 45–64. DOI: 10.1179/174328005x14267 (cit. on pp. 13, 22, 36, 37, 79, 83).
- [65] F. Monte, W. Larsen, and J. D. Mackenzie. “Stabilization of tetragonal ZrO<sub>2</sub> in ZrO<sub>2</sub>-SiO<sub>2</sub> binary oxides”. In: *Journal of the American Ceramic Society* 83.3 (2000), pp. 628–634. DOI: 10.1111/j.1151-2916.2000.tb01243.x (cit. on pp. 13, 80, 82).
- [66] D. H. Aguilar, L. C. Torres-Gonzalez, and L. M. Torres-Martinez. “A study of the crystallization of ZrO<sub>2</sub> in the sol-gel system: ZrO<sub>2</sub>-SiO<sub>2</sub>”. In: *Journal of Solid State Chemistry* 158.2 (2000), pp. 349–357. DOI: 10.1006/jssc.2001.9126 (cit. on pp. 13, 80, 82).

## Bibliography

- [67] L. Shi, H. Yin, R. Zhang, X. Liu, J. Zi, and D. Zhao. “Macroporous oxide structures with short-range order and bright structural coloration: A replication from parrot feather barbs”. In: *Journal of Materials Chemistry* 20 (2010), pp. 90–93. DOI: 10.1039/b915625a (cit. on pp. 15, 21).
- [68] S. Kinoshita and S. Yoshioka. “Structural colors in nature: The role of regularity and irregularity in the structure”. In: *ChemPhysChem* 6.8 (2005), pp. 1442–1459. DOI: 10.1002/cphc.200500007 (cit. on pp. 15, 16).
- [69] G. Tayeb, B. Gralak, and S. Enoch. “Structural colors in nature and butterfly-wing modeling”. In: *Optics and Photonics News* 14.2 (2003), pp. 38–43. DOI: 10.1364/opn.14.2.000038 (cit. on p. 15).
- [70] S. Yoshioka and S. Kinoshita. “Effect of macroscopic structure in iridescent color of the peacock feathers”. In: *Forma* 17 (2002), pp. 169–181 (cit. on pp. 15, 16).
- [71] Y. Chen, J. Gu, S. Zhu, T. Fan, D. Zhang, and Q. Guo. “Iridescent large-area ZrO<sub>2</sub> photonic crystals using butterfly as templates”. In: *Applied Physics Letters* 94.5 (2009), p. 053901. DOI: 10.1063/1.3078270 (cit. on pp. 15, 16).
- [72] J. D. Joannopoulos, P. R. Villeneuve, and S. H. Fan. “Photonic crystals: Putting a new twist on light”. In: *Nature* 386 (1997), pp. 143–149 (cit. on pp. 15, 19).
- [73] J. D. Joannopoulos, S. G. Johnson, J. N. Winn, and R. D. Meade. *Photonic crystals: Molding the flow of light*. 2008, pp. 1–5 (cit. on pp. 15–19).
- [74] M. Srinivasarao. “Nano-optics in the biological world: Beetles, butterflies, birds, and moths”. In: *Chemical Reviews* 99.7 (1999), pp. 1935–1962. DOI: 10.1021/cr970080y (cit. on p. 16).
- [75] G. Meltz, W. W. Morey, and W. H. Glenn. “Formation of Bragg gratings in optical fibers by a transverse holographic method”. In: *Optics Letters* 14.15 (1989), pp. 823–825. DOI: 10.1364/OL.14.000823 (cit. on pp. 17, 18, 88).
- [76] L. Rayleigh. “XVII. On the maintenance of vibrations by forces of double frequency, and on the propagation of waves through a medium endowed with a periodic structure”. In: *The London, Edinburgh, and Dublin Philosophical Magazine and Journal of Science* 24.147 (1887), pp. 145–159. DOI: 10.1080/14786448708628074 (cit. on p. 18).
- [77] E. Armstrong and C. O’Dwyer. “Artificial opal photonic crystals and inverse opal structures-fundamentals and applications from optics to energy storage”. In: *Journal of Materials Chemistry C* 3 (2015), pp. 6109–6143. DOI: 10.1039/c5tc01083g (cit. on pp. 19, 20).
- [78] C. López. “Materials aspects of photonic crystals”. In: *Advanced Materials* 15.20 (2003), pp. 1679–1704. DOI: 10.1002/adma.200300386 (cit. on p. 19).

- [79] V. L. Colvin. “From Opals to Optics: Colloidal Photonic Crystals”. In: *MRS Bulletin* 26.08 (2001), pp. 637–641. DOI: 10.1557/mrs2001.159 (cit. on p. 19).
- [80] K.-U. Fulda and B. Tiede. “Langmuir films of monodisperse 0.5  $\mu\text{m}$  spherical polymer particles with a hydrophobic core and a hydrophilic shell”. In: *Advanced Materials* 6.4 (1994), pp. 288–290. DOI: 10.1002/adma.19940060405 (cit. on p. 19).
- [81] A. Stein, B. E. Wilson, and S. G. Rudisill. “Design and functionality of colloidal-crystal-templated materials - Chemical applications of inverse opals”. In: *Chemical Society Reviews* 42 (2013), pp. 2763–2803. DOI: 10.1039/c2cs35317b (cit. on p. 19).
- [82] S. M. Yang and G. A. Ozin. “Opal chips: Vectorial growth of colloidal crystal patterns inside silicon wafers”. In: *Chemical Communications* 24 (2000), pp. 2507–2508. DOI: 10.1039/b008534k (cit. on p. 19).
- [83] M. Trau, D. A. Saville, and A. Aksay. “Field-induced layering of colloidal crystals”. In: *Science* 272.5262 (1996), pp. 706–709. DOI: 10.1126/science.272.5262.706 (cit. on p. 19).
- [84] A. T. Skjeltorp. “One- and two-dimensional crystallization of magnetic holes”. In: *Physical Review Letters* 51.25 (1983), pp. 2306–2309. DOI: 10.1103/PhysRevLett.51.2306 (cit. on p. 19).
- [85] K. Busch and S. John. “Photonic band gap formation in certain self-organizing systems”. In: *Physical Review E* 58.3 (1998), pp. 3896–3908. DOI: 10.1103/PhysRevE.58.3896 (cit. on p. 19).
- [86] Y. Takeoka. “Angle-independent structural coloured amorphous arrays”. In: *Journal of Materials Chemistry* 22 (2012), pp. 23299–23309. DOI: 10.1039/c2jm33643j (cit. on p. 20).
- [87] P. D. García, R. Sapienza, Á. Blanco, and C. López. “Photonic glass: A novel random material for light”. In: *Advanced Materials* 19.18 (2007), pp. 2597–2602. DOI: 10.1002/adma.200602426 (cit. on pp. 20, 21).
- [88] P. D. García, R. Sapienza, and C. López. “Photonic glasses: A step beyond white paint”. In: *Advanced Materials* 22.1 (2010), pp. 12–19. DOI: 10.1002/adma.200900827 (cit. on pp. 20, 21).
- [89] M. P. V. Albada and A. Lagendijk. “Observation of weak localization of light in a random medium”. In: *Physical Review Letters* 55 (1985), pp. 2692–2695. DOI: 10.1103/PhysRevLett.55.2692 (cit. on p. 20).
- [90] P. E. Wolf and G. Maret. “Weak localization and coherent backscattering of photons in disordered media”. In: *Physical Review Letters* 55 (1985), pp. 2696–2699. DOI: 10.1103/PhysRevLett.55.2696 (cit. on p. 20).

## Bibliography

- [91] P. W. Anderson. “Absence of diffusion in certain random lattices”. In: *Physical Review* 109.5 (1958), pp. 1492–1505. DOI: 10.1103/PhysRev.109.1492 (cit. on p. 20).
- [92] P. W. Anderson. “The question of classical localization: A theory of white paint?” In: *Philosophical Magazine B* 52.3 (1985), pp. 505–509. DOI: 10.1080/13642818508240619 (cit. on p. 20).
- [93] A. Z. Genack and N. Garcia. “Observation of photon localization in a three-dimensional disordered system”. In: *Physical Review Letters* 66.16 (1991), pp. 2064–2067. DOI: 10.1103/PhysRevLett.66.2064 (cit. on p. 20).
- [94] D. S. Wiersma, P. Bartolini, A. Lagendijk, and R. Righini. “Localization of light in a disordered medium”. In: *Nature* 390 (1997), pp. 671–673. DOI: 10.1038/37757 (cit. on p. 20).
- [95] R. Dalichaouch, J. P. Armstrong, S. Schultz, P. M. Platzman, and S. L. McCall. “Microwave localization by two-dimensional random scattering”. In: *Nature* 354 (1991), pp. 53–55. DOI: 10.1038/354053a0 (cit. on p. 20).
- [96] N. M. Lawandy, R. M. Balachandran, A. S. L. Gomes, and E. Sauvain. “Laser action in strongly scattering media”. In: *Nature* 368 (1994), pp. 436–438. DOI: 10.1038/368436a0 (cit. on p. 20).
- [97] J. J. Do Rosário, P. N. Dyachenko, R. Kubrin, R. M. Pasquarelli, A. Y. Petrov, M. Eich, and G. A. Schneider. “Facile deposition of YSZ-inverse photonic glass films”. In: *American Chemical Society Applied Materials and Interfaces* 6.15 (2014), pp. 12335–12345. DOI: 10.1021/am502110p (cit. on p. 21).
- [98] Y. Takeoka. “Stimuli-responsive opals: Colloidal crystals and colloidal amorphous arrays for use in functional structurally colored materials”. In: *Journal of Materials Chemistry C* 1.38 (2013), pp. 6059–6074. DOI: 10.1039/c3tc30885e (cit. on p. 21).
- [99] J. D. Forster, H. Noh, S. F. Liew, V. Saranathan, C. F. Schreck, L. Yang, J.-G. Park, R. O. Prum, S. G. J. Mochrie, C. S. O’Hern, H. Cao, and E. R. Dufresne. “Biomimetic isotropic nanostructures for structural coloration”. In: *Advanced Materials* 22.26-27 (2010), pp. 2939–2944. DOI: 10.1002/adma.200903693 (cit. on p. 21).
- [100] K. Chung, S. Yu, C. J. Heo, J. W. Shim, S. M. Yang, M. G. Han, H. S. Lee, Y. Jin, S. Y. Lee, N. Park, and J. H. Shin. “Flexible, angle-independent, structural color reflectors inspired by morpho butterfly wings”. In: *Advanced Materials* 24.18 (2012), pp. 2375–2379. DOI: 10.1002/adma.201200521 (cit. on p. 21).
- [101] T. Chraska, A. H. King, and C. C. Berndt. “On the size-dependent phase transformation in nanoparticulate zirconia”. In: *Materials Science and Engineering A* 286.1 (2000), pp. 169–178. DOI: 10.1016/S0921-5093(00)00625-0 (cit. on pp. 21, 23, 36).

- [102] T. Koch and P. Ziemann. “Zr-silicide formation during the epitaxial growth of Y-stabilized zirconia films on Si(100) and its avoidance by ion beam assisted deposition at a reduced temperature”. In: *Applied Surface Science* 99.1 (1996), pp. 51–57. DOI: 10.1016/0169-4332(95)00512-9 (cit. on p. 21).
- [103] D. Chen, L. Cao, F. Huang, P. Imperial, Y. B. Cheng, and R. A. Caruso. “Synthesis of monodisperse mesoporous titania beads with controllable diameter, high surface areas, and variable pore diameters (14–23 nm)”. In: *Journal of the American Chemical Society* 132.12 (2010), pp. 4438–4444. DOI: 10.1021/ja100040p (cit. on p. 21).
- [104] J. He, J. Chen, L. Ren, Y. Wang, C. Teng, M. Hong, J. Zhao, and B. Jiang. “Fabrication of monodisperse porous zirconia microspheres and their phosphorylation for friedel-crafts alkylation of indoles”. In: *American Chemical Society Applied Materials and Interfaces* 6.4 (2014), pp. 2718–2725. DOI: 10.1021/am405202d (cit. on p. 21).
- [105] R. H. J. Hannink, P. M. Kelly, and B. C. Muddle. “Transformation toughening in zirconia-containing ceramics”. In: *Journal of the American Ceramic Society* 83.3 (2000), pp. 461–487. DOI: 10.1111/j.1151-2916.2000.tb01221.x (cit. on p. 22).
- [106] A. Navrotsky. “Thermochemical insights into refractory ceramic materials based on oxides with large tetravalent cations”. In: *Journal of Materials Chemistry* 15 (2005), pp. 1883–1890. DOI: 10.1039/b417143h (cit. on pp. 22–24).
- [107] R. H. J. Hannink and M. V. Swain. “Progress in transformation toughening of ceramics”. In: *Annual Review of Materials Science* 24 (1994), pp. 359–408. DOI: 10.1146/annurev.ms.24.080194.002043 (cit. on p. 22).
- [108] V. G. Keramidas and W. B. White. “Raman scattering study of the crystallization and phase transformations of  $ZrO_2$ ”. In: *Journal of the American Ceramic Society* 57.1 (1974), pp. 22–24. DOI: 10.1111/j.1151-2916.1974.tb11355.x (cit. on pp. 23, 36).
- [109] R. Srinivasan, R. J. De Angelis, G. Ice, and B. H. Davis. “Identification of tetragonal and cubic structures of zirconia using synchrotron x-radiation source”. In: *Journal of Materials Research* 6.6 (1991), pp. 1287–1292. DOI: 10.1557/JMR.1991.1287 (cit. on pp. 23, 24, 36, 37, 52).
- [110] J. Livage, K. Doi, and C. Mazieres. “Nature and thermal evolution of amorphous hydrated zirconium oxide”. In: *Journal of the American Ceramic Society* 51.6 (1968), pp. 349–353. DOI: 10.1111/j.1151-2916.1968.tb15952.x (cit. on pp. 23, 36, 37).

## Bibliography

- [111] F. Zhang, P. J. Chupas, S. L. A. Lui, J. C. Hanson, W. A. Caliebe, P. L. Lee, and S. W. Chan. “In situ study of the crystallization from amorphous to cubic zirconium oxide: Rietveld and reverse Monte Carlo analyses”. In: *Chemistry of Materials* 19.13 (2007), pp. 3118–3126. DOI: 10.1021/cm061739w (cit. on pp. 23, 24, 36).
- [112] M. W. Pitcher, S. V. Ushakov, A. Navrotsky, B. F. Woodfield, G. Li, J. Boerio-Goates, and B. M. Tissue. “Energy crossovers in nanocrystalline zirconia”. In: *Journal of the American Ceramic Society* 88.1 (2005), pp. 160–167. DOI: 10.1111/j.1551-2916.2004.00031.x (cit. on p. 23).
- [113] N. L. Wu, T. F. Wu, and I. A. Rusakova. “Thermodynamic stability of tetragonal zirconia nanocrystallites”. In: *Journal of Materials Research* 16.3 (2001), pp. 666–669. DOI: 10.1557/JMR.2001.0114 (cit. on p. 23).
- [114] R. C. Garvie and M. F. Goss. “Intrinsic size dependence of the phase transformation temperature in zirconia microcrystals”. In: *Journal of Materials Science* 21.4 (1986), pp. 1253–1257. DOI: 10.1007/BF00553259 (cit. on p. 23).
- [115] R. C. Garvie, R. H. Hannink, and R. T. Pascoe. “Ceramic steel?” In: *Nature* 258 (1975), pp. 703–704. DOI: 10.1038/258703a0 (cit. on p. 24).
- [116] R. A. Miller, J. L. Smialek, and R. G. Garlick. “Phase stability in plasma-sprayed, partially stabilized zirconia-yttria”. In: *Science and technology of zirconia. Columbus, OH, American Ceramic Society, Inc., (Advances in Ceramics)* 3 (1981), pp. 241–253 (cit. on p. 24).
- [117] R. A. Miller, R. G. Garlick, and J. L. Smialek. “Phase distributions in plasma-sprayed zirconia-yttria”. In: *American Ceramic Society Bulletin* 62 (1983), pp. 1355–1358 (cit. on p. 24).
- [118] W. D. Kingery. “Plausible concepts necessary and sufficient for interpretation of ceramic grain-boundary phenomena: I, grain-boundary characteristics, structure, and electrostatic potential”. In: *Journal of The American Ceramic Society* 57.1 (1974), pp. 1–8. DOI: 10.1111/j.1151-2916.1974.tb11350.x (cit. on p. 25).
- [119] E. W. Leib. “Preparation of monodisperse zirconium dioxide microparticles for the fabrication of thermally stable photonic structures”. In: *Dissertation, Physical Chemistry, University of Hamburg* (2016) (cit. on pp. 25, 26).
- [120] M. N. Rahaman. *Ceramic processing and sintering*. CRC Press LLC, 2003, pp. 540–619 (cit. on p. 26).
- [121] I.-W. Chen. “Grain boundary kinetics in oxide ceramics with the cubic fluorite crystal structure and its derivatives”. In: *Interface Science* 8.2-3 (2000), pp. 147–156. DOI: 10.1023/A:1008742404071 (cit. on p. 26).

- [122] T. Miyoshi and H. Funakubo. “Effect of grain size on mechanical properties of full-dense Pb(Zr,Ti)O<sub>3</sub> ceramics”. In: *Japanese Journal of Applied Physics* 49.9S (2010), pp. 1–6. DOI: 10.1143/JJAP.49.09MD13 (cit. on p. 27).
- [123] J. I. Langford and A. J. C. Wilson. “Scherrer after sixty years: A survey and some new results in the determination of crystallite size”. In: *Journal of Applied Crystallography* 11 (1978), pp. 102–113. DOI: 10.1107/S0021889878012844 (cit. on p. 27).
- [124] S. Fabris, A. T. Paxton, and M. W. Finnis. “A stabilization mechanism of zirconia based on oxygen vacancies only”. In: *Acta Materialia* 50.20 (2002), pp. 5171–5178. DOI: 10.1016/S1359-6454(02)00385-3 (cit. on pp. 27–29).
- [125] S.-L. Hwang and I.-W. Chen. “Grain size control of tetragonal zirconia polycrystals using the space charge concept”. In: *Journal of the American Ceramic Society* 73.11 (1990), pp. 3269–3277. DOI: 10.1111/j.1151-2916.1990.tb06449.x (cit. on p. 28).
- [126] R. D. Shannon. “Revised effective ionic radii and systematic studies of interatomic distances in halides and chalcogenides”. In: *Acta Crystallographica A* 32 (1976), pp. 751–767. DOI: 10.1107/S0567739476001551 (cit. on p. 28).
- [127] A. Keyvani, M. Bahamirian, and A. Kobayashi. “Effect of sintering rate on the porous microstructural, mechanical and thermomechanical properties of YSZ and CSZ TBC coatings undergoing thermal cycling”. In: *Journal of Alloys and Compounds* 727 (2017), pp. 1057–1066. DOI: 10.1016/j.jallcom.2017.08.184 (cit. on p. 28).
- [128] R. A. Miller. “Current status of thermal barrier coatings - An overview”. In: *Surface and Coatings Technology* 30.1 (1987), pp. 1–11. DOI: 10.1016/0257-8972(87)90003-X (cit. on p. 28).
- [129] S. Ostanin and E. Salamatov. “Microscopic mechanism of stability in yttria-doped zirconia”. In: *Journal of Experimental and Theoretical Physics Letters* 74.11 (2001), pp. 552–555. DOI: 10.1134/1.1450289 (cit. on p. 28).
- [130] P. Li, I.-W. Chen, and J. E. Penner-Hahn. “X-ray-absorption studies of zirconia polymorphs. II. Effect of Y<sub>2</sub>O<sub>3</sub> dopant on ZrO<sub>2</sub> structure”. In: *Physical Review B* 48.14 (1993), pp. 10074–10081. DOI: 10.1103/PhysRevB.48.10074 (cit. on p. 29).
- [131] V. V. Srdić, M. Winterer, and H. Hahn. “Sintering behavior of nanocrystalline zirconia doped with alumina prepared by chemical vapor synthesis”. In: *Journal of the American Ceramic Society* 83.8 (2000), pp. 1853–1860. DOI: 10.1111/j.1151-2916.2000.tb01481.x (cit. on pp. 29, 59, 66).
- [132] A. Nazeri and S. B. Qadri. “Alumina-stabilized zirconia coatings for high-temperature protection of turbine blades”. In: *Surface and Coatings Technology* 86-87.Part 1 (1996), pp. 166–169. DOI: 10.1016/S0257-8972(96)03025-3 (cit. on pp. 29, 59).

## Bibliography

- [133] J. A. Allemann, B. Michel, H.-B. Märki, L. J. Gauckler, and E. M. Moser. “Grain growth of differently doped zirconia”. In: *Journal of the European Ceramic Society* 15.10 (1995), pp. 951–958. DOI: [https://doi.org/10.1016/0955-2219\(95\)00073-4](https://doi.org/10.1016/0955-2219(95)00073-4) (cit. on pp. 30, 66).
- [134] K. Kajihara, Y. Yoshizawa, and T. Sakuma. “The enhancement of superplastic flow in tetragonal zirconia polycrystals with SiO<sub>2</sub>-doping”. In: *Acta Metallurgica Et Materialia* 43.3 (1995), pp. 1235–1242. DOI: 10.1016/0956-7151(94)00320-H (cit. on pp. 30, 46, 82, 86).
- [135] Y. Ikuhara, P. Thavorniti, and T. Sakuma. “Solute segregation at grain boundaries in superplastic SiO<sub>2</sub>-doped TZP”. In: *Acta Materialia* 45.12 (1997), pp. 5275–5284. DOI: 10.1016/S1359-6454(97)00152-3 (cit. on pp. 30, 46, 86).
- [136] X. Guo, W. Sigle, J. U. Fleig, and J. Maier. “Role of space charge in the grain boundary blocking effect in doped zirconia”. In: *Solid State Ionics* 154-155 (2002), pp. 555–561. DOI: 10.1016/S0167-2738(02)00491-5 (cit. on pp. 30, 86).
- [137] L. Gremillard, T. Epicier, J. Chevalier, and G. Fantozzi. “Microstructural study of silica-doped zirconia ceramics”. In: *Acta Materialia* 48.18-19 (2000), pp. 4647–4652. DOI: 10.1016/S1359-6454(00)00252-4 (cit. on pp. 30, 86).
- [138] B. Fegley and E. A. Barringer. “Synthesis, characterization, and processing of monosized ceramic powders”. In: *Better Ceramics Through Chemistry I; Mat. Res. Soc. Symp. Proc.* 32 (1984), pp. 187–197 (cit. on p. 31).
- [139] B. Fegley, P. White, and H. K. Bowen. “Processing and characterization of ZrO<sub>2</sub> and Y-doped ZrO<sub>2</sub> powders”. In: *American Ceramic Society Bulletin* 64.8 (1985), pp. 1115–1120 (cit. on p. 31).
- [140] B. Yan, C. V. McNeff, P. W. Carr, and A. V. McCormick. “Synthesis and characterization of submicron-to-micron scale, monodisperse, spherical, and nonporous zirconia particles”. In: *Journal of the American Ceramic Society* 88.3 (2005), pp. 707–713. DOI: 10.1111/j.1551-2916.2005.00133.x (cit. on pp. 31, 35, 50, 105).
- [141] T. Halamus, P. Wojciechowski, and I. Bobowska. “Synthesis and characterization of (hydroxypropyl)cellulose/TiO<sub>2</sub> nanocomposite films”. In: *Polymers for Advanced Technologies* 19.7 (2008), pp. 807–811. DOI: 10.1002/pat.1038 (cit. on p. 32).
- [142] J. Y. Choi, C. H. Kim, and D. K. Kim. “Hydrothermal synthesis of spherical perovskite oxide powders using spherical gel powders”. In: *Journal of the American Ceramic Society* 81.5 (1998), pp. 1353–1356. DOI: 10.1111/j.1151-2916.1998.tb02490.x (cit. on p. 32).

- [143] T. Cai, Z. Hu, B. Ponder, J. St. John, and D. Moro. “Synthesis and study of and controlled release from nanoparticles and their networks based on functionalized hydroxypropylcellulose”. In: *Macromolecules* 36.17 (2003), pp. 6559–6564. DOI: 10.1021/ma030107h (cit. on p. 32).
- [144] S. Shukla, S. Seal, R. Vij, and S. Bandyopadhyay. “Effect of HPC and water concentration on the evolution of size, aggregation and crystallization of sol-gel nano zirconia”. In: *Journal of Nanoparticle Research* 4.6 (2002), pp. 553–559. DOI: 10.1023/A:1022886518620 (cit. on pp. 32, 71).
- [145] L. Lerot, F. Legrand, and P. De Bruycker. “Chemical control in precipitation of spherical zirconia particles”. In: *Journal of Materials Science* 26.9 (1991), pp. 2353–2358. DOI: 10.1007/BF01130181 (cit. on pp. 32, 33, 71).
- [146] T. Oghihara, N. Mizutani, and M. Kato. “Growth mechanism of monodispersed ZrO<sub>2</sub> particles”. In: *Journal of the American Ceramic Society* 72.3 (1989), pp. 421–426. DOI: 10.1111/j.1151-2916.1989.tb06146.x (cit. on pp. 32, 71, 72, 76).
- [147] O. Cantfort, B. Michaux, R. Pirard, J. P. Pirard, and a. J. Lecloux. “Synthesis and characterization of monodisperse spherical zirconia particles”. In: *Journal of Sol-Gel Science and Technology* 8.1-3 (1997), pp. 207–211. DOI: 10.1007/BF02436842 (cit. on p. 33).
- [148] J. Park, V. Privman, and E. Matijević. “Model of formation of monodispersed colloids”. In: *Journal of Physical Chemistry B* 105.47 (2001), pp. 11630–11635. DOI: 10.1021/jp011306a (cit. on p. 34).
- [149] R. Srinivasan, B. H. Davis, O. B. Cavin, and C. R. Hubbard. “Crystallization and phase transformation process in zirconia: An in situ high-temperature X-ray diffraction study”. In: *Journal of American Ceramic Society* 75.5 (1992), pp. 1217–1222. DOI: 10.1038/physci241048a0 (cit. on p. 36).
- [150] M. Dapiaggi, F. Maglia, I. Tredici, B. Maroni, G. Borghini, and U. A. Tamburini. “Complex thermal evolution of size-stabilized tetragonal zirconia”. In: *Journal of Physics and Chemistry of Solids* 71.8 (2010), pp. 1038–1041. DOI: 10.1016/j.jpics.2010.03.002 (cit. on p. 36).
- [151] D. E. Collins and K. J. Bowman. “Influence of atmosphere on crystallization of zirconia from a zirconium alkoxide”. In: *Journal of Materials Research* 13.5 (1998), pp. 1230–1237. DOI: 10.1557/JMR.1998.0175 (cit. on p. 37).
- [152] E.-M. Köck, M. Kogler, T. Götsch, L. Schlicker, M. F. Bekheet, A. Doran, A. Gurlo, B. Klötzer, B. Petermüller, D. Schildhammer, and S. Penner. “Surface chemistry of pure tetragonal ZrO<sub>2</sub> and gas-phase dependence of the tetragonal-to-monoclinic ZrO<sub>2</sub> transformation”. In: *Dalton Transactions* 46 (2017), pp. 4554–4570. DOI: 10.1039/c6dt04847a (cit. on p. 37).
- [153] C. Guiot, S. Grandjean, J.-P. Jolivet, and P. Batail. “Nano single crystals of yttria-stabilized zirconia”. In: *Crystal Growth and Design* 9.8 (2009), pp. 3548–3550. DOI: 10.1021/cg900292h (cit. on p. 38).

## Bibliography

- [154] Y. Chang, S. Dong, H. Wang, K. Du, Q. Zhu, and P. Luo. “Synthesis of monodisperse spherical nanometer  $ZrO_2$  ( $Y_2O_3$ ) powders via the coupling route of w/o emulsion with urea homogenous precipitation”. In: *Materials Research Bulletin* 47.3 (2012), pp. 527–531. DOI: 10.1016/j.materresbull.2011.12.055 (cit. on p. 38).
- [155] M. Hajizadeh-Oghaz, R. Shoja Razavi, and A. Ghasemi. “Synthesis and characterization of ceria–yttria co-stabilized zirconia (CYSZ) nanoparticles by sol–gel process for thermal barrier coatings (TBCs) applications”. In: *Journal of Sol-Gel Science and Technology* 74.3 (2015), pp. 603–612. DOI: 10.1007/s10971-015-3639-y (cit. on p. 38).
- [156] J. M. Luther, H. Zheng, B. Sadtler, and A. P. Alivisatos. “Synthesis of PbS nanorods and other ionic nanocrystals of complex morphology by sequential cation exchange reactions”. In: *Journal of American Chemical Society* 131.46 (2009), pp. 16851–16857. DOI: 10.1021/ja906503w (cit. on p. 38).
- [157] L. Spanhel, H. Weller, A. Fojtik, and A. Henglein. “Photochemistry of Semiconductor Colloids. 17. Strong luminescing CdS and CdS-Ag<sub>2</sub>S particles”. In: *Bericht der Bunsengesellschaft für physikalische Chemie* 91.2 (1987), pp. 88–94. DOI: 10.1002/bbpc.19870910204 (cit. on p. 39).
- [158] C. F. Hoener, K. A. Allan, A. J. Bard, A. Champion, M. A. Fox, T. E. Malouk, S. E. Webber, and J. M. White. “Demonstration of a shell-core structure in layered cadmium selenide-zinc selenide small particles by X-ray photoelectron and Auger spectroscopies”. In: *The Journal of Physical Chemistry* 96.9 (1992), pp. 3812–3817. DOI: 10.1021/j100188a045 (cit. on p. 39).
- [159] Z. Chen, Z. L. Wang, P. Zhan, J. H. Zhang, W. Y. Zhang, H. T. Wang, and N. B. Ming. “Preparation of metallodielectric composite particles with multishell structure”. In: *Langmuir* 20.8 (2007), pp. 3042–3046. DOI: 10.1021/la035326a (cit. on p. 39).
- [160] V. V. Shvartsman, F. Alawneh, P. Borisov, D. Kozodaev, and D. C. Lupascu. “Converse magnetoelectric effect in  $CoFe_2O_4$ – $BaTiO_3$  composites with a core-shell structure”. In: *Smart Materials and Structures* 20.7 (2011). DOI: 10.1088/0964-1726/20/7/075006 (cit. on p. 39).
- [161] K. Raidongia, A. Nag, A. Sundaresan, and C. N. R. Rao. “Multiferroic and magnetoelectric properties of core-shell  $CoFe_2O_4$ @  $BaTiO_3$  nanocomposites”. In: *Applied Physics Letters* 97.6 (2010), pp. 10–13. DOI: 10.1063/1.3478231 (cit. on p. 39).
- [162] R. A. Islam, V. Bedekar, N. Poudyal, J. P. Liu, and S. Priya. “Magnetoelectric properties of core-shell particulate nanocomposites”. In: *Journal of Applied Physics* 104.10 (2008). DOI: 10.1063/1.3013437 (cit. on p. 39).

- [163] V. Corral-Flores, D. Bueno-Baques, D. Carrillo-Flores, and J. A. Matutes-Aquino. “Enhanced magnetoelectric effect in core-shell particulate composites”. In: *Journal of Applied Physics* 99.8 (2006), pp. 1–4. DOI: 10.1063/1.2165147 (cit. on p. 39).
- [164] X. J. Wu and D. Xu. “Soft template synthesis of yolk/silica shell particles”. In: *Advanced Materials* 22.13 (2010), pp. 1516–1520. DOI: 10.1002/adma.200903879 (cit. on p. 39).
- [165] Y. Wang and W. J. Tseng. “A novel technique for synthesizing nanoshell hollow alumina particles”. In: *Journal of the American Ceramic Society* 92.S1 (2009), S32–S37. DOI: 10.1111/j.1551-2916.2008.02653.x (cit. on pp. 39, 42, 63).
- [166] Q. H. Powell, T. T. Kodas, and B. M. Anderson. “Coating of TiO<sub>2</sub> particles by chemical vapor deposition of SiO<sub>2</sub>”. In: *Chemical Vapor Deposition* 2.5 (1996), pp. 179–181. DOI: 10.1002/cvde.19960020505 (cit. on p. 40).
- [167] C. Janzen, J. Knipping, B. Rellinghaus, and P. Roth. “Formation of silica-embedded iron-oxide nanoparticles in low-pressure flames”. In: *Journal of Nanoparticle Research* 5.5-6 (2003), pp. 589–596. DOI: 10.1023/B:NANO.0000006109.37251.fd (cit. on p. 40).
- [168] J. A. McCormick, K. P. Rice, D. F. Paul, A. W. Weimer, and S. M. George. “Analysis of Al<sub>2</sub>O<sub>3</sub> atomic layer deposition on ZrO<sub>2</sub> nanoparticles in a rotary reactor”. In: *Chemical Vapor Deposition* 13.9 (2007), pp. 491–498. DOI: 10.1002/cvde.200606563 (cit. on pp. 40, 41, 99).
- [169] M. J. Weber, M. A. Verheijen, A. A. Bol, and W. M. M. Kessels. “Subnanometer dimensions control of core/shell nanoparticles prepared by atomic layer deposition”. In: *Nanotechnology* 26.9 (2015), p. 094002. DOI: 10.1088/0957-4484/26/9/094002 (cit. on pp. 40, 41).
- [170] L. F. Hakim, S. M. George, and A. W. Weimer. “Conformal nanocoating of zirconia nanoparticles by atomic layer deposition in a fluidized bed reactor”. In: *Nanotechnology* 16.7 (2005), S375–S381. DOI: 10.1088/0957-4484/16/7/010 (cit. on pp. 40, 41, 99).
- [171] A. W. Weimer. “Particle coating by atomic layer deposition (ALD)”. In: *International Congress for Particle Technology (PARTEC)* (2004), pp. 1–4 (cit. on p. 40).
- [172] V. Maurice, T. Georgelin, J.-M. Siaugue, and V. Cabuil. “Synthesis and characterization of functionalized core-shell  $\gamma$ -Fe<sub>2</sub>O<sub>3</sub>-SiO<sub>2</sub> nanoparticles”. In: *Journal of Magnetism and Magnetic Materials* 321.10 (2009), pp. 1408–1413. DOI: 10.1016/j.jmmm.2009.02.051 (cit. on p. 41).

## Bibliography

- [173] Z. Li, L. A. Fredin, P. Tewari, S. A. Dibenedetto, M. T. Lanagan, M. A. Ratner, and T. J. Marks. “In situ catalytic encapsulation of core-shell nanoparticles having variable shell thickness: Dielectric and energy storage properties of high-permittivity metal oxide nanocomposites”. In: *Chemistry of Materials* 22.18 (2010), pp. 5154–5164. DOI: 10.1021/cm1009493 (cit. on p. 42).
- [174] H. Jin, Z. Ji, Y. Li, M. Liu, J. Yuan, C. Xu, and S. Hou. “The preparation of a core/shell structure with alumina coated spherical silica powder”. In: *Colloids and Surfaces A: Physicochemical and Engineering Aspects* 441 (2014), pp. 170–177. DOI: 10.1016/j.colsurfa.2013.09.004 (cit. on p. 42).
- [175] F. Ye, J. Qin, M. S. Toprak, and M. Muhammed. “Multifunctional core-shell nanoparticles: Superparamagnetic, mesoporous, and thermosensitive”. In: *Journal of Nanoparticle Research* 13.11 (2011), pp. 6157–6167. DOI: 10.1007/s11051-011-0272-8 (cit. on p. 44).
- [176] X. Gao, K. M. K. Yu, K. Y. Tam, and S. C. Tsang. “Colloidal stable silica encapsulated nano-magnetic composite as a novel bio-catalyst carrier”. In: *Chemical Communications* 9.24 (2003), pp. 2998–2999. DOI: 10.1039/b310435d (cit. on p. 44).
- [177] S. O. Obare, N. R. Jana, and C. J. Murphy. “Preparation of polystyrene- and silica-coated gold nanorods and their use as templates for the synthesis of hollow nanotubes”. In: *Nano Letters* 1.11 (2001), pp. 601–603. DOI: 10.1021/nl0156134 (cit. on p. 44).
- [178] J. Rüter. “Synthesis and characterization of  $\text{ZrO}_2@Al_2O_3$  core-shell-microparticles for application as high-temperature stable thermal barrier coatings”. In: *Master thesis, Physical Chemistry, University of Hamburg* (2017) (cit. on pp. 49, 111, 112).
- [179] L. Sun, M. J. Annen, F. Lorenzano-Porras, P. W. Carr, and A. V. McCormick. “Synthesis of porous zirconia spheres for HPLC by polymerization-induced colloid aggregation (PICA)”. In: *Journal of Colloid and Interface Science* 163.2 (1994), pp. 464–473. DOI: 10.1006/jcis.1994.1125 (cit. on p. 49).
- [180] A. U. Limaye and J. J. Helble. “Morphological control of zirconia nanoparticles through combustion aerosol synthesis”. In: *Journal of the American Ceramic Society* 85.5 (2002), pp. 1127–1132. DOI: 10.1111/j.1151-2916.2002.tb00233.x (cit. on p. 49).
- [181] K. P. Furlan, R. M. Pasquarelli, T. Krekeler, M. Ritter, R. Zierold, K. Nielsch, G. A. Schneider, and R. Janssen. “Highly porous  $\alpha\text{-Al}_2\text{O}_3$  ceramics obtained by sintering atomic layer deposited inverse opals”. In: *Ceramics International* 43.14 (2017), pp. 11260–11264. DOI: 10.1016/j.ceramint.2017.05.176 (cit. on p. 55).

- [182] Z. Chen and N. Brandon. “Inkjet printing and nanoindentation of porous alumina multilayers”. In: *Ceramics International* 42.7 (2016), pp. 8316–8324. DOI: 10.1016/j.ceramint.2016.02.045 (cit. on p. 55).
- [183] S. Dutta, T. B. Kim, T. Krentz, R. P. Vinci, and H. M. Chan. “Sol-gel-derived single-crystal alumina coatings with vermicular structure”. In: *Journal of the American Ceramic Society* 94.2 (2011), pp. 340–343. DOI: 10.1111/j.1551-2916.2010.04307.x (cit. on p. 55).
- [184] S. Li, C.-A. Wang, and J. Zhou. “Effect of starch addition on microstructure and properties of highly porous alumina ceramics”. In: *Ceramics International* 39.8 (2013), pp. 8833–8839. DOI: 10.1016/j.ceramint.2013.04.072 (cit. on p. 55).
- [185] M. Barmala, A. Moheb, and R. Emadi. “Applying Taguchi method for optimization of the synthesis condition of nano-porous alumina membrane by slip casting method”. In: *Journal of Alloys and Compounds* 485.1-2 (2009), pp. 778–782. DOI: 10.1016/j.jallcom.2009.06.093 (cit. on p. 55).
- [186] K. Uchiyama, T. Ogihara, T. Ikemoto, N. Mizutani, and M. Kato. “Preparation of monodispersed Y-doped ZrO<sub>2</sub> powders”. In: *Journal of Materials Science* 22.12 (1987), pp. 4343–4347. DOI: 10.1007/BF01132027 (cit. on pp. 63, 72, 76).
- [187] D. R. Clarke and C. G. Levi. “Materials design for the next generation thermal barrier coatings”. In: *Annual Review of Materials Research* 33 (2003), pp. 383–417. DOI: 10.1146/annurev.matsci.33.011403.113718 (cit. on p. 67).
- [188] H. Kumazawa, Y. Hori, and E. Sada. “Synthesis of spherical zirconia fine particles by controlled hydrolysis of zirconium tetrabutoxide in 1-propanol”. In: *The Chemical Engineering Journal* 51.3 (1993), pp. 129–133. DOI: 10.1016/0300-9467(93)80023-H (cit. on p. 71).
- [189] B. Yan, C. V. McNeff, F. Chen, P. W. Carr, and A. V. McCormick. “Control of synthesis conditions to improve zirconia microspheres for ultrafast chromatography”. In: *Journal of the American Ceramic Society* 84.8 (2001), pp. 1721–1727. DOI: 10.1111/j.1551-2916.2001.tb00905.x (cit. on pp. 71, 92).
- [190] V. K. Lamer and R. H. Dinegar. “Theory, production and mechanism of formation of monodispersed hydrosols”. In: *Journal of the American Chemical Society* 72.11 (1950), pp. 4847–4854. DOI: 10.1021/ja01167a001 (cit. on p. 76).
- [191] S. Shukla, S. Seal, R. Vij, and S. Bandyopadhyay. “Reduced activation energy for grain growth in nanocrystalline yttria-stabilized zirconia”. In: *Nano Letters* 3.3 (2003), pp. 397–401. DOI: 10.1021/nl0259380 (cit. on p. 79).

## Bibliography

- [192] G. K. Bansal and A. H. Heuer. “On a martensitic phase transformation in zirconia ( $\text{ZrO}_2$ )—II. Crystallographic aspects”. In: *Acta Metallurgica* 22.4 (1974), pp. 409–417. DOI: 10.1016/0001-6160(74)90093-5 (cit. on pp. 81, 82).
- [193] V. P. Dravid, M. R. Notis, and C. E. Lyman. “Twinning and microcracking associated with monoclinic zirconia in the eutectic system zirconia–mullite”. In: *Journal of the American Ceramic Society* 71.4 (1988), pp. C-219–C-221. DOI: 10.1111/j.1151-2916.1988.tb05883.x (cit. on pp. 81, 82).
- [194] J. E. Bailey. “The monoclinic-tetragonal transformation and associated twinning in thin films of zirconia”. In: *Proceedings of the Royal Society of London. Series A. Mathematical and Physical Sciences* 279.1378 (1964), pp. 395–412. DOI: 10.1098/rspa.1964.0112 (cit. on pp. 81, 82).
- [195] Y. C. Wu and Y. T. Chiang. “The m-t transformation and twinning analysis of hot-pressed sintered 3YSZ ceramics”. In: *Journal of the American Ceramic Society* 94.7 (2011), pp. 2200–2212. DOI: 10.1111/j.1551-2916.2010.04347.x (cit. on pp. 81, 82).
- [196] T. Ono, M. Kagawa, and Y. Syono. “Ultrafine particles of the  $\text{ZrO}_2$ – $\text{SiO}_2$  system prepared by the spray-ICP technique”. In: *Journal of Materials Science* 20.7 (1985), pp. 2483–2487. DOI: 10.1007/BF00556078 (cit. on p. 82).
- [197] V. S. Nagarajan and K. J. Rao. “Crystallization studies of  $\text{ZrO}_2$ – $\text{SiO}_2$  composite gels”. In: *Journal of Materials Science* 24.6 (1989), pp. 2140–2146. DOI: 10.1007/BF02385434 (cit. on p. 82).
- [198] T. Bakos, S. N. Rashkeev, and S. T. Pantelides. “Reactions and diffusion of water and oxygen molecules in amorphous  $\text{SiO}_2$ ”. In: *Physical Review Letters* 88.5 (2002), p. 055508. DOI: 10.1103/PhysRevLett.88.055508 (cit. on p. 83).
- [199] R. H. Doremus. “Oxidation of silicon by water and oxygen and diffusion in fused silica”. In: *The Journal of Physical Chemistry* 80.16 (1976), pp. 1773–1775. DOI: 10.1021/j100557a006 (cit. on p. 83).
- [200] J. J. Perez-Bueno, R. Ramirez-Bon, Y. V. Vorobiev, F. Espinoza-Beltran, and J. Gonzalez-Hernandez. “Oxygen diffusion in silicon oxide films produced by different methods”. In: *Thin Solid Films* 379.1-2 (2000), pp. 57–63. DOI: 10.1016/S0040-6090(00)01568-6 (cit. on p. 83).
- [201] G. Shang. “Unpublished data”. In: *Institute of Optical and Electronic Materials, Hamburg University of Technology* (2019) (cit. on pp. 89, 91).
- [202] K. P. Furlan. “Unpublished data”. In: *Advanced Ceramics, Hamburg University of Technology* (2019) (cit. on p. 91).
- [203] S. Romeis, J. Paul, M. Ziener, and W. Peukert. “A novel apparatus for in situ compression of submicron structures and particles in a high resolution SEM”. In: *Review of Scientific Instruments* 83.9 (2012), p. 095105. DOI: 10.1063/1.4749256 (cit. on p. 93).

- [204] D. N. Boccaccini, H. L. Frandsen, S. Soprani, M. Cannio, T. Klemensø, V. Gil, and P. V. Hendriksen. “Influence of porosity on mechanical properties of tetragonal stabilized zirconia”. In: *Journal of the European Ceramic Society* 38.4 (2018), pp. 1720–1735 (cit. on p. 94).
- [205] L. G. Ferguson and F. Dogan. “Spectrally selective, matched emitters for thermophotovoltaic energy conversion processed by tape casting”. In: *Journal of Materials Science* 36.1 (2001), pp. 137–146. DOI: 10.1023/A:1004845205322 (cit. on p. 95).
- [206] A. Kohiyama, M. Shimizu, H. Kobayashi, F. Iguchi, and H. Yugami. “Spectrally controlled thermal radiation based on surface microstructures for high-efficiency solar thermophotovoltaic system”. In: *Energy Procedia* 57 (2014), pp. 517–523. DOI: 10.1016/j.egypro.2014.10.205 (cit. on p. 95).
- [207] J. J. Foley, C. Ungaro, K. Sun, M. C. Gupta, and S. K. Gray. “Design of emitter structures based on resonant perfect absorption for thermophotovoltaic applications”. In: *Optics Express* 23.24 (2015), A1373–A1387. DOI: 10.1364/oe.23.0a1373 (cit. on p. 95).
- [208] A. Lenert, Y. Nam, D. M. Bierman, and E. N. Wang. “Role of spectral non-idealities in the design of solar thermophotovoltaics”. In: *Optics Express* 22.S6 (2014), A1604–A1618. DOI: 10.1364/oe.22.0a1604 (cit. on p. 95).
- [209] M. Chirumamilla. “Unpublished data”. In: *Institute of Optical and Electronic Materials, Hamburg University of Technology* (2019) (cit. on p. 97).
- [210] L. Lutterotti and P. Scardi. “Simultaneous structure and size-strain refinement by the Rietveld method”. In: *Journal of Applied Crystallography* 23 (1990), pp. 246–252. DOI: 10.1107/S0021889890002382 (cit. on p. 115).
- [211] C. J. Howard, R. J. Hill, and B. E. Reichert. “Structures of ZrO<sub>2</sub> polymorphs at room temperature by high-resolution neutron powder diffraction”. In: *Acta Crystallographica Section B* B44 (1988), pp. 116–120. DOI: 10.1107/S0108768187010279 (cit. on p. 115).
- [212] <https://www.dguv.de/ifa/gestis/gestis-stoffdatenbank/index.jsp>, *Institut für Arbeitsschutz der Deutschen Gesetzlichen Unfallversicherung (IFA), GESTIS-Stoffdatenbank*. 2019 (cit. on pp. 145–147).



# Appendix

## Supplementary material

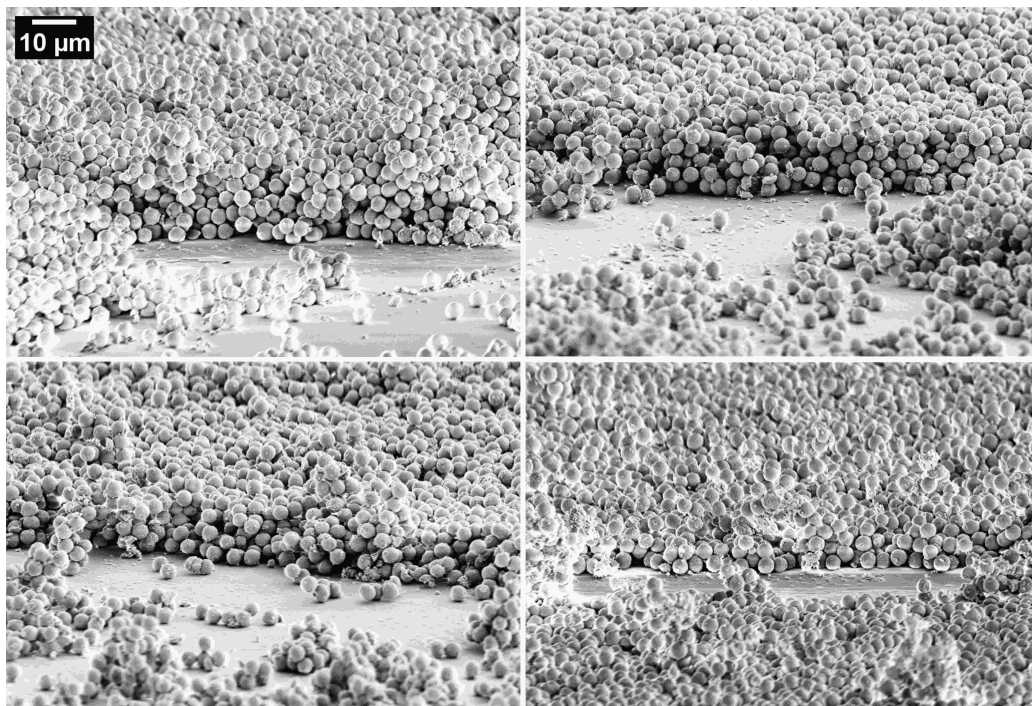


**Figure 8.4** – Exemplary SEM images of photonic glasses (edge) from zirconia microparticles (Zr-O2) used for determination of the layer thickness ( $\sim 10 \mu\text{m}$ ) by drawing at least 50 vertical lines in different images.

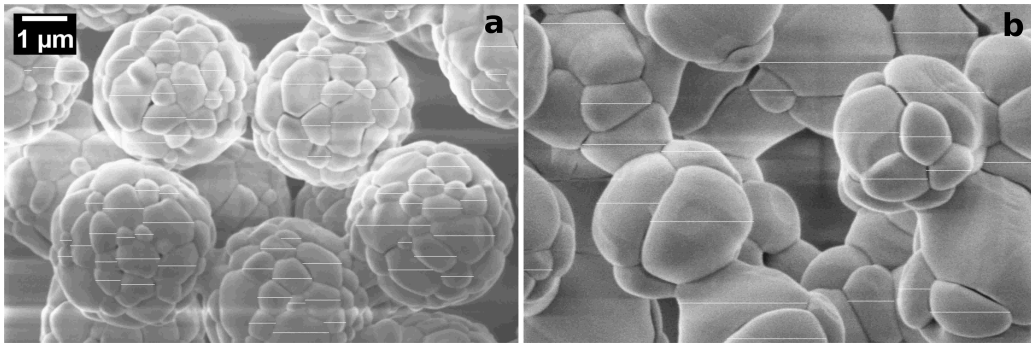


**Figure 8.5** – Exemplary SEM images of zirconia microparticles (Zr-02) after temperature treatment at 1300 °C (a) and 1500 °C (b) used for determination of the grain sizes by drawing at least 50 horizontal lines in different images. This method was used for analysis of grain sizes > 80 nm due to instrumental broadening of the XRD equipment.

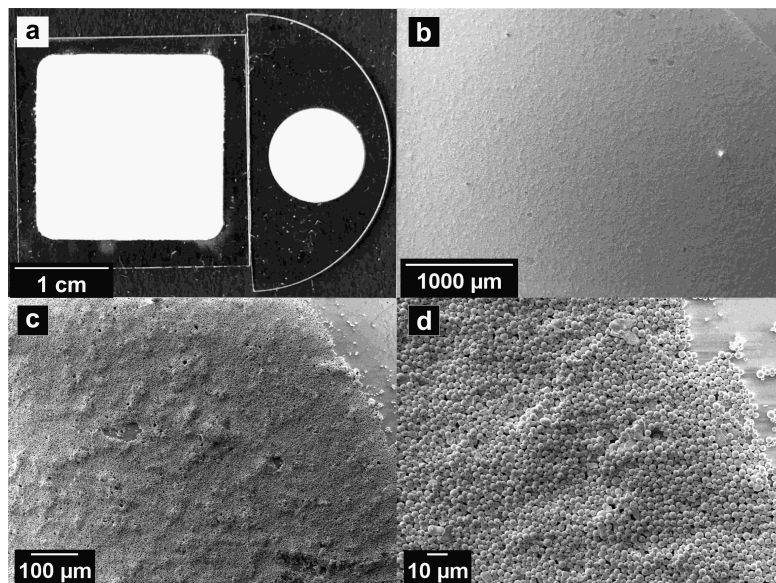


**Figure 8.6** – Overview photograph of photonic glasses from Zr-2 (a, left) and YSZ-1 (a, right) microparticles on sapphire substrates by using differently shaped PTFE templates. SEM images with different magnifications of photonic glasses from the YSZ-1 microparticles on sapphire substrates (b-d).

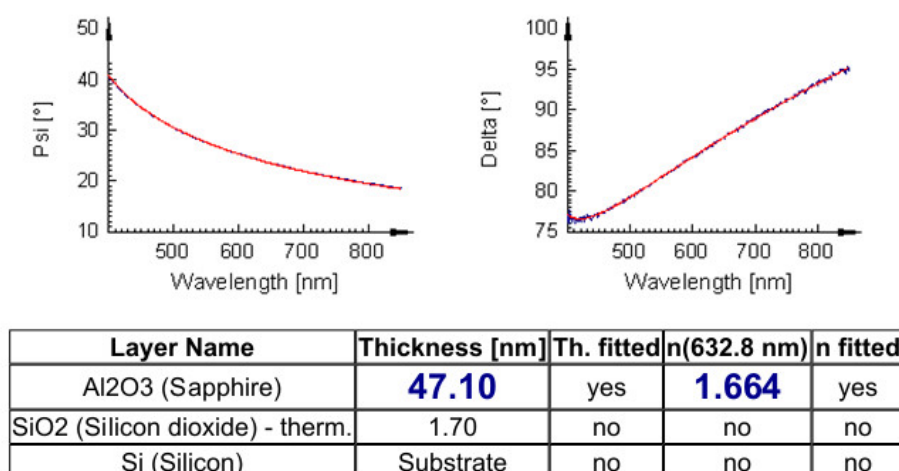


**Figure 8.7** – Alumina coating thickness determination from ALD for  $\text{ZrO}_2$  (Zr-02) and YSZ (YSZ-01) microparticles by measuring the refractive index due to spectral ellipsometry of a reference silicon sample which was also placed in the reaction chamber.

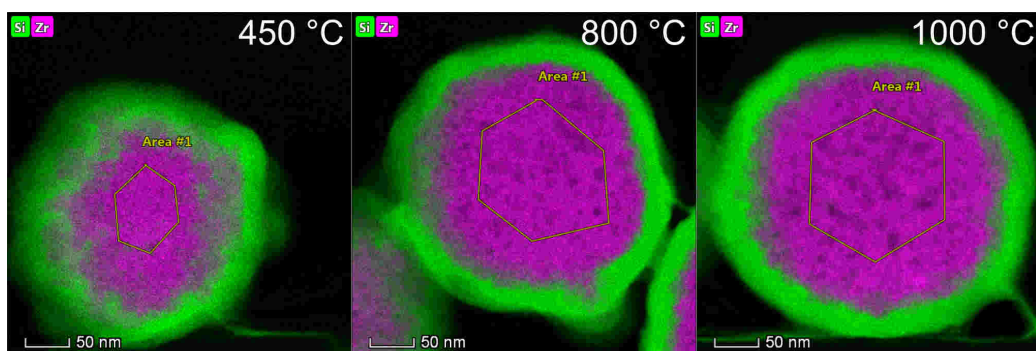


**Figure 8.8** – EDX mappings of FIB lamellae of  $\text{ZrO}_2@SiO_2$  core@shell particles (initial shell thickness: 38 nm; Zr: magenta; Si: green). The FIB lamellae were prepared from core@shell particles calcined at 450, 800, and 1000 °C, as indicated.

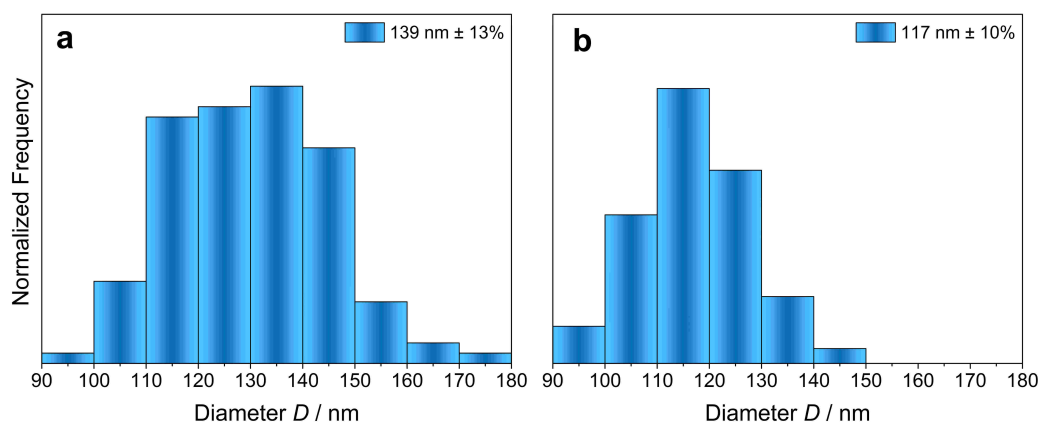


**Figure 8.9** – Sizing statistics of as-synthesized (a) and calcined (570 °C, 3 h, b) YSZ submicron particles. Average particle diameters and standard deviations were determined using *ImageJ* software by counting at least 100 particles.

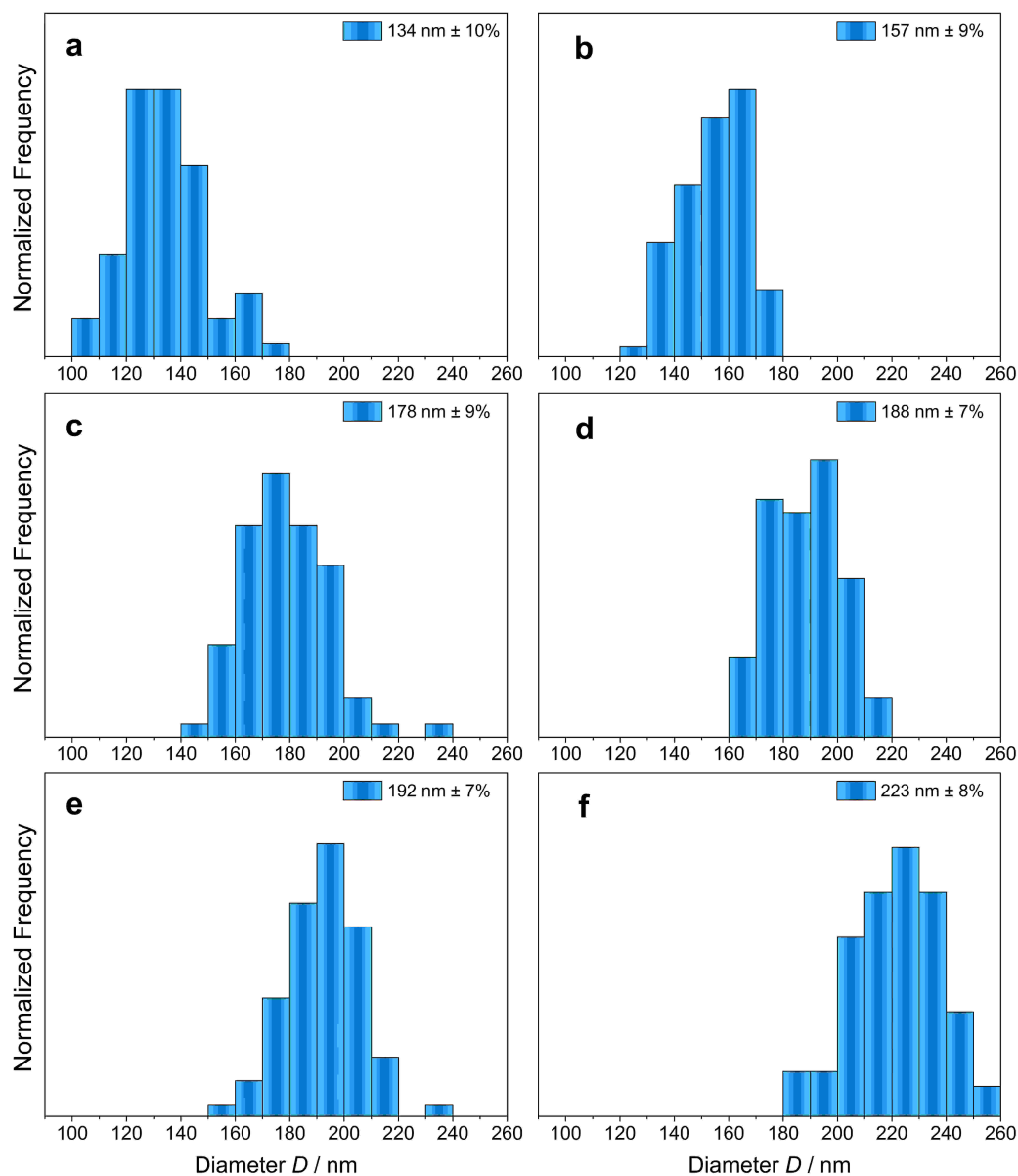
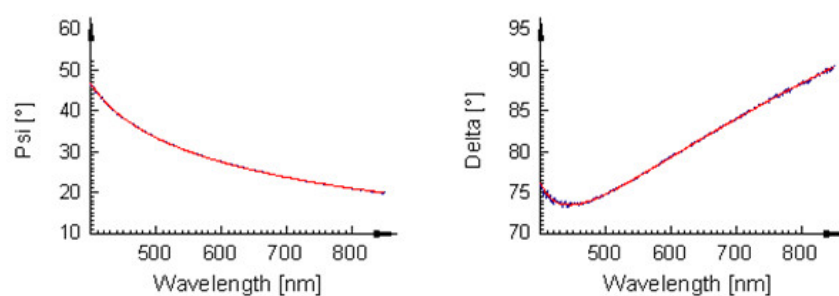


**Figure 8.10** – Sizing statistics of as-synthesized (dried at 80 °C, 4 h)  $\text{ZrO}_2@SiO_2$  core@shell submicron particles with initial shell thicknesses of  $\sim 10$  nm (a),  $\sim 20$  nm (b),  $\sim 30$  nm (c),  $\sim 35$  nm (d),  $\sim 40$  nm (e), and  $\sim 50$  nm (f). Average particle diameters and standard deviations were determined using *ImageJ* software by counting at least 100 particles.



Layer Name	Thickness [nm]	Th. fitted	n(632.8 nm)	n fitted
Al <sub>2</sub> O <sub>3</sub> (Sapphire)	<b>51.47</b>	yes	<b>1.679</b>	yes
SiO <sub>2</sub> (Silicon dioxide) - therm.	2.72	no	no	no
Si (Silicon)	Substrate	no	no	no

**Figure 8.11** – Alumina shell thickness determination from ALD for YSZ@SiO<sub>2</sub> core@shell submicron particles by measuring the refractive index due to spectral ellipsometry of a reference silicon sample which was also placed in the reaction chamber.

## Safety

List of chemicals used and their CAS number, GHS symbols, hazard -, and precautionary statements.[212]

Chemical	CAS Number	GHS Symbols	Hazard Statements	Precautionary Statements
acetone	67-64-1		H225, H319, H336, EUH066	P210, P240, P305+P351+P338, P403+P233
ammonium hydroxide solution (28%)	1336-21-6		H290, H314, H335, H400	P260, P273, P280, P301+P330+P331, P303+P361+P353, P305+P351+P338
aluminum chloride	7446-70-0		H314	EUH014
aluminum <i>i</i> -propoxide	555-31-7		H228	P210
<i>n</i> -butanol	71-36-3		H226, H302, H318, H315, H335, H336	P210, P280, P302+P352, P304+P340, P305+P351+P338
eicosanoic acid	506-30-9	-	-	-
ethanol	506-30-9		H225, H319	P210, P240, P305+P351+P338, P403+P233

*continues on next page*

## Appendix

List of chemicals used and their CAS number, GHS symbols, hazard -, and precautionary statements.[212]

Chemical	CAS Number	GHS Symbols	Hazard Statements	Precautionary Statements
hydroxypropyl cellulose	9004-64-2	-	-	-
polyninyl-pyrrolidone	9003-39-8	-	-	-
tetraethyl orthosilicate	78-10-4		H226, H332, H319, H335	P210, P261, P280, P303+P361+P353, P304+P340+P312, P370+P378, P403+P235
tetrahydrofuran	109-99-9		H225, H302, H319, H335, H351, EUH019	P210, P233, P280, P370+P378, P501
toluene	108-88-3		H225, H361d, H304, H373, H315, H336	P210, P302+P352, P301+P310+P330, P308+P313, P240, P314, P403+P233
trimethylaluminum	75-24-1		H250, H260, H314, EUH014	P210, P280, P231+P232, P305+P351+P338, P370+P378, P422
yttrium(III) <i>i</i> -propoxide	2172-12-5		H228, H315, H319, H335	P210, P261, P305+P351+P338

*continues on next page*

List of chemicals used and their CAS number, GHS symbols, hazard -, and precautionary statements.[212]

Chemical	CAS Number	GHS Symbols	Hazard Statements	Precautionary Statements
zirconium <i>n</i> -propoxide	23519-77-9		H226, H318, H336	P231, P422, P301+P310, P305+P351+P338, P403+P233
zirconium(IV) -oxide	1314-23-4	-	-	-

## List of all H, EUH, and P Statements

**Table 8.2** – All H, EUH, and P Statements.

<b>Identifier</b>	<b>Statement</b>
H200	Unstable explosives.
H201	Explosive; mass explosion hazard.
H202	Explosive, severe projection hazard.
H203	Explosive; fire, blast or projection hazard.
H204	Fire or projection hazard.
H205	May mass explode in fire.
H220	Extremely flammable gas.
H221	Flammable gas.
H222	Extremely flammable aerosol.
H223	Flammable aerosol.
H224	Extremely flammable liquid and vapour.
H225	Highly flammable liquid and vapour.
H226	Flammable liquid and vapour.
H228	Flammable solid.
H240	Heating may cause an explosion.
H241	Heating may cause a fire or explosion.
H242	Heating may cause a fire.
H250	Catches fire spontaneously if exposed to air.
H251	Self-heating: may catch fire.
H252	Self-heating in large quantities; may catch fire.
H260	In contact with water releases flammable gases which may ignite spontaneously.
H261	In contact with water releases flammable gases.
H270	May cause or intensify fire; oxidiser.
H271	May cause fire or explosion; strong oxidiser.

*continues on next page*

---

<b>Identifier</b>	<b>Statement</b>
H272	May intensify fire; oxidiser.
H280	Contains gas under pressure; may explode if heated.
H281	Contains refrigerated gas; may cause cryogenic burns or injury.
H290	May be corrosive to metals.
H300	Fatal if swallowed.
H301	Toxic if swallowed.
H302	Harmful if swallowed.
H304	May be fatal if swallowed and enters airways.
H310	Fatal in contact with skin.
H311	Toxic in contact with skin.
H312	Harmful in contact with skin.
H314	Causes severe skin burns and eye damage.
H315	Causes skin irritation.
H317	May cause an allergic skin reaction.
H318	Causes serious eye damage.
H319	Causes serious eye irritation.
H330	Fatal if inhaled.
H331	Toxic if inhaled.
H332	Harmful if inhaled.
H334	May cause allergy or asthma symptoms or breathing difficulties if inhaled.
H335	May cause respiratory irritation.
H336	May cause drowsiness or dizziness.
H340	May cause genetic defects. <i>(state route of exposure if it is conclusively proven that no other routes of exposure cause the hazard)</i>

---

*continues on next page*

Identifier	Statement
H341	Suspected of causing genetic defects. <i>⟨state route of exposure if it is conclusively proven that no other routes of exposure cause the hazard⟩</i>
H350	May cause cancer. <i>⟨state route of exposure if it is conclusively proven that no other routes of exposure cause the hazard⟩</i>
H351	Suspected of causing cancer. <i>⟨state route of exposure if it is conclusively proven that no other routes of exposure cause the hazard⟩</i>
H360	May damage fertility or the unborn child. <i>⟨state specific effect if known⟩ ⟨state route of exposure if it is conclusively proven that no other routes of exposure cause the hazard⟩</i>
H361	Suspected of damaging fertility or the unborn child. <i>⟨state specific effect if known⟩ ⟨state route of exposure if it is conclusively proven that no other routes of exposure cause the hazard⟩</i>
H362	May cause harm to breast-fed children.
H370	Causes damage to organs <i>⟨or state all organs affected, if known⟩</i> . <i>⟨state route of exposure if it is conclusively proven that no other routes of exposure cause the hazard⟩</i>
H371	May cause damage to organs <i>⟨or state all organs affected, if known⟩</i> . <i>⟨state route of exposure if it is conclusively proven that no other routes of exposure cause the hazard⟩</i>
H372	Causes damage to organs <i>⟨or state all organs affected, if known⟩</i> through prolonged or repeated exposure. <i>⟨state route of exposure if it is conclusively proven that no other routes of exposure cause the hazard⟩</i>
H373	May cause damage to organs <i>⟨or state all organs affected, if known⟩</i> through prolonged or repeated exposure. <i>⟨state route of exposure if it is conclusively proven that no other routes of exposure cause the hazard⟩</i>

*continues on next page*

<b>Identifier</b>	<b>Statement</b>
H400	Very toxic to aquatic life.
H410	Very toxic to aquatic life with long lasting effects.
H411	Toxic to aquatic life with long lasting effects.
H412	Harmful to aquatic life with long lasting effects.
H413	May cause long lasting harmful effects to aquatic life.
H350i	May cause cancer by inhalation.
H360F	May damage fertility.
H360D	May damage the unborn child.
H361f	Suspected of damaging fertility.
H361d	Suspected of damaging the unborn child.
H360FD	May damage fertility. May damage the unborn child.
H361fd	Suspected of damaging fertility. Suspected of damaging the unborn child.
H360Fd	May damage fertility. Suspected of damaging the unborn child.
H360Df	May damage the unborn child. Suspected of damaging fertility.
EUH001	Explosive when dry.
EUH006	Explosive with or without contact with air.
EUH014	Reacts violently with water.
EUH018	In use may form flammable/explosive vapour-air mixture.
EUH019	May form explosive peroxides.
EUH044	Risk of explosion if heated under confinement.
EUH029	Contact with water liberates toxic gas.
EUH031	Contact with acids liberates toxic gas.
EUH032	Contact with acids liberates very toxic gas.
EUH066	Repeated exposure may cause skin dryness or cracking.
EUH070	Toxic by eye contact.

*continues on next page*

Appendix

---

<b>Identifier</b>	<b>Statement</b>
EUH071	Corrosive to the respiratory tract.
EUH059	Hazardous to the ozone layer.
EUH201	Contains lead. Should not be used on surfaces liable to be chewed or sucked by children.
EUH201A	Warning! contains lead.
EUH202	Cyanoacrylate. Danger. Bonds skin and eyes in seconds. Keep out of the reach of children.
EUH203	Contains chromium (VI). May produce an allergic reaction.
EUH204	Contains isocyanates. May produce an allergic reaction.
EUH205	Contains epoxy constituents. May produce an allergic reaction.
EUH206	Warning! Do not use together with other products. May release dangerous gases (chlorine).
EUH207	Warning! Contains cadmium. Dangerous fumes are formed during use. See information supplied by the manufacturer. Comply with the safety instructions.
EUH208	Contains <i>&lt;name of sensitising substance&gt;</i> . May produce an allergic reaction.
EUH209	Can become highly flammable in use.
EUH209A	Can become flammable in use.
EUH210	Safety data sheet available on request.
EUH401	To avoid risks to human health and the environment, comply with the instructions for use.
P101	If medical advice is needed, have product container or label at hand.
P102	Keep out of reach of children.
P103	Read label before use.
P201	Obtain special instructions before use.

---

*continues on next page*

Identifier	Statement
P202	Do not handle until all safety precautions have been read and understood.
P210	Keep away from heat/sparks/open flames/hot surfaces. — No smoking.
P211	Do not spray on an open flame or other ignition source.
P220	Keep/Store away from clothing/.../combustible materials.
P221	Take any precaution to avoid mixing with combustibles ...
P222	Do not allow contact with air.
P223	Keep away from any possible contact with water, because of violent reaction and possible flash fire.
P230	Keep wetted with ...
P231	Handle under inert gas.
P232	Protect from moisture.
P233	Keep container tightly closed.
P234	Keep only in original container.
P235	Keep cool.
P240	Ground/bond container and receiving equipment.
P241	Use explosion-proof electrical/ventilating/lighting/... equipment.
P242	Use only non-sparking tools.
P243	Take precautionary measures against static discharge.
P244	Keep reduction valves free from grease and oil.
P250	Do not subject to grinding/shock/.../friction.
P251	Pressurized container: Do not pierce or burn, even after use.
P260	Do not breathe dust/fume/gas/mist/vapours/spray.
P261	Avoid breathing dust/fume/gas/mist/vapours/spray.

*continues on next page*

Appendix

---

<b>Identifier</b>	<b>Statement</b>
P262	Do not get in eyes, on skin, or on clothing.
P263	Avoid contact during pregnancy/while nursing.
P264	Wash ... thoroughly after handling.
P270	Do not eat, drink or smoke when using this product.
P271	Use only outdoors or in a well-ventilated area.
P272	Contaminated work clothing should not be allowed out of the workplace.
P273	Avoid release to the environment.
P280	Wear protective gloves/protective clothing/eye protection/face protection.
P281	Use personal protective equipment as required.
P282	Wear cold insulating gloves/face shield/eye protection.
P283	Wear fire/flame resistant/retardant clothing.
P284	Wear respiratory protection.
P285	In case of inadequate ventilation wear respiratory protection.
P231 + P232	Handle under inert gas. Protect from moisture.
P235 + P410	Keep cool. Protect from sunlight.
P301	IF SWALLOWED:
P302	IF ON SKIN:
P303	IF ON SKIN (or hair):
P304	IF INHALED:
P305	IF IN EYES:
P306	IF ON CLOTHING:
P307	IF exposed:
P308	IF exposed or concerned:
P309	IF exposed or if you feel unwell:
P310	Immediately call a POISON CENTER or doctor/physician.

---

*continues on next page*

---

<b>Identifier</b>	<b>Statement</b>
P311	Call a POISON CENTER or doctor/physician.
P312	Call a POISON CENTER or doctor/physician if you feel unwell.
P313	Get medical advice/attention.
P314	Get medical advice/attention if you feel unwell.
P315	Get immediate medical advice/attention.
P320	Specific treatment is urgent (see . . . on this label).
P321	Specific treatment (see . . . on this label).
P322	Specific measures (see . . . on this label).
P330	Rinse mouth.
P331	Do NOT induce vomiting.
P332	If skin irritation occurs:
P333	If skin irritation or rash occurs:
P334	Immerse in cool water/wrap in wet bandages.
P335	Brush off loose particles from skin.
P336	Thaw frosted parts with lukewarm water. Do not rub affected area.
P337	If eye irritation persists:
P338	Remove contact lenses, if present and easy to do. Continue rinsing.
P340	Remove victim to fresh air and keep at rest in a position comfortable for breathing.
P341	If breathing is difficult, remove victim to fresh air and keep at rest in a position comfortable for breathing.
P342	If experiencing respiratory symptoms:
P350	Gently wash with plenty of soap and water.
P351	Rinse cautiously with water for several minutes.
P352	Wash with plenty of soap and water.
P353	Rinse skin with water/shower.

---

*continues on next page*

Appendix

---

<b>Identifier</b>	<b>Statement</b>
P360	Rinse immediately contaminated clothing and skin with plenty of water before removing clothes.
P361	Remove/Take off immediately all contaminated clothing.
P362	Take off contaminated clothing and wash before reuse.
P363	Wash contaminated clothing before reuse.
P370	In case of fire:
P371	In case of major fire and large quantities:
P372	Explosion risk in case of fire.
P373	DO NOT fight fire when fire reaches explosives.
P374	Fight fire with normal precautions from a reasonable distance.
P375	Fight fire remotely due to the risk of explosion.
P376	Stop leak if safe to do so.
P377	Leaking gas fire: Do not extinguish, unless leak can be stopped safely.
P378	Use . . . for extinction.
P380	Evacuate area.
P381	Eliminate all ignition sources if safe to do so.
P390	Absorb spillage to prevent material damage.
P391	Collect spillage.
P301 + P310	IF SWALLOWED: Immediately call a POISON CENTER or doctor/physician.
P301 + P312	IF SWALLOWED: Call a POISON CENTER or doctor/physician if you feel unwell.
P301 + P330 + P331	IF SWALLOWED: rinse mouth. Do NOT induce vomiting.
P302 + P334	IF ON SKIN: Immerse in cool water/wrap in wet bandages.
P302 + P350	IF ON SKIN: Gently wash with plenty of soap and water.

---

*continues on next page*

Identifier	Statement
P302 + P352	IF ON SKIN: Wash with plenty of soap and water.
P303 + P361 + P353	IF ON SKIN (or hair): Remove/Take off immediately all contaminated clothing. Rinse skin with water/shower.
P304 + P340	IF INHALED: Remove victim to fresh air and keep at rest in a position comfortable for breathing.
P304 + P341	IF INHALED: If breathing is difficult, remove victim to fresh air and keep at rest in a position comfortable for breathing.
P305 + P351 + P338	IF IN EYES: Rinse cautiously with water for several minutes. Remove contact lenses, if present and easy to do. Continue rinsing.
P306 + P360	IF ON CLOTHING: Rinse immediately contaminated clothing and skin with plenty of water before removing clothes.
P307 + P311	IF exposed: Call a POISON CENTER or doctor/physician.
P308 + P313	IF exposed or concerned: Get medical advice/attention.
P309 + P311	IF exposed or if you feel unwell: Call a POISON CENTER or doctor/physician.
P332 + P313	If skin irritation occurs: Get medical advice/attention.
P333 + P313	If skin irritation or rash occurs: Get medical advice/attention.
P335 + P334	Brush off loose particles from skin. Immerse in cool water/wrap in wet bandages.
P337 + P313	If eye irritation persists: Get medical advice/attention.
P342 + P311	If experiencing respiratory symptoms: Call a POISON CENTER or doctor/physician.
P370 + P376	In case of fire: Stop leak if safe to do so.
P370 + P378	In case of fire: Use ... for extinction.
P370 + P380	In case of fire: Evacuate area.

*continues on next page*

Appendix

Identifier	Statement
P370 + P380 + P375	In case of fire: Evacuate area. Fight fire remotely due to the risk of explosion.
P371 + P380 + P375	In case of major fire and large quantities: Evacuate area. Fight fire remotely due to the risk of explosion.
P401	Store . . .
P402	Store in a dry place.
P403	Store in a well-ventilated place.
P404	Store in a closed container.
P405	Store locked up.
P406	Store in corrosive resistant/. . . container with a resistant inner liner.
P407	Maintain air gap between stacks/pallets.
P410	Protect from sunlight.
P411	Store at temperatures not exceeding °C/°F.
P412	Store at temperatures not exceeding 50 °C/122 °F.
P413	Store bulk masses greater than kg/lbs at temperatures not exceeding °C/°F.
P420	Store away from other materials.
P422	Store contents under . . .
P402 + P404	Store in a dry place. Store in a closed container.
P403 + P233	Store in a well-ventilated place. Keep container tightly closed.
P403 + P235	Store in a well-ventilated place. Keep cool.
P410 + P403	Protect from sunlight. Store in a well-ventilated place.
P410 + P412	Protect from sunlight. Do not expose to temperatures exceeding 50 °C/122 °F.
P411 + P235	Store at temperatures not exceeding °C/°F. Keep cool.
P501	Dispose of contents/container to . . .

## Danksagung

Zuerst möchte ich Horst Weller und Tobias Vossmeier für die freundliche Aufnahme in den Arbeitskreis Weller danken, wo ich in den letzten Jahren sehr viel gelernt habe und immer Spaß an dem spannenden Projekt meiner Promotion hatte.

Tobias Vossmeier und Alf Mews danke ich ganz herzlich für die Übernahme der Erst- und Zweitgutachten. Außerdem danke ich Horst Weller, Simone Mascotto und Gabriel Bester, die sich bereit erklärt haben, die Prüfungskommission meiner Disputation zu bilden.

Besonders bedanken möchte ich mich bei Tobias Vossmeier für die Bereitstellung einer spannenden und abwechslungsreichen Arbeit, eine stets „offene Tür“ für Probleme, anregende Diskussionen und die Durchsicht dieser Arbeit. Tobias hat mir stets das Gefühl der Wertschätzung entgegengebracht, mich motiviert neues zu lernen und stets das Beste rauszuholen.

Des Weiteren danke ich allen Kooperationspartnern und Koautoren innerhalb des SFB 986 für den wissenschaftlichen Austausch, bei dem jeder etwas von seinem Fachgebiet dazu beitragen hat, gemeinsam erfolgreich an wissenschaftlichen Fragestellungen zu arbeiten. Besonders bedanken möchte ich mich in diesem Zusammenhang bei Kaline Furlan für zahlreiche ALD-Beschichtungen meiner photonischen Gläser und Unterstützung bei TGA-DSC und XRD-Messungen. Die Zusammenarbeit mit Kaline habe ich besonders genossen, da sich unsere Überlegungen immer gut ergänzten und wir so zielstrebig zu vielen schönen Ergebnissen gekommen sind. Außerdem möchte ich Guoliang Shang und Manohar Chirumamilla für die Simulationen der optischen Eigenschaften und Berechnung der Partikelparameter danken, die grundlegend für die Planungen meiner Synthesen waren. Außerdem möchte ich mich bei Guoliang und Manohar für die optischen Messungen bedanken. Des Weiteren möchte ich Yen Häntsch aus dem SFB 986 für die schöne Zusammenarbeit und die gemeinsame Assemblierung von Monolagen danken. Tobias Krekeler danke ich für zahlreiche TEM- und EDX-Messungen. Abschließend möchte ich Malte Blankenburg für die zahlreichen Messungen am Desy danken, bei denen er viele Stunden mit mir an der Beamline und später bei der Auswertung verbracht hat. Ich hatte auch vor allem bei den monatlichen Meetings und den gemeinsamen Summer Schools im Rahmen des MGK sehr viel Spaß und möchte mich dafür

## *Appendix*

bei allen Mitgliedern bedanken, besonders bei Alette Winter, Ulrike Herzog und Sophia Jördens für die Organisation.

In diesem Zusammenhang möchte ich mich auch bei der Deutschen Forschungsgemeinschaft für die Finanzierung des erfolgreichen SFB 986 und bei Elisabeth Leib für die sehr gute Vorarbeit auf dem Gebiet meiner Promotion bedanken.

Stefan Romeis, Jan Schwenger und Patrick Herre danke ich für die sehr fruchtbare Kooperation zur Charakterisierung der mechanischen Eigenschaften und habe mich sehr gefreut, mir persönlich ein Bild davon in Erlangen machen zu können.

Ich danke dem gesamten AK Weller für die schönen letzten Jahre, eine sehr angenehme Atmosphäre, wissenschaftliche und nicht-wissenschaftliche Diskussionen, Bier-Abende, Feiern, Dart und Kickerrunden auch außerhalb der Uni. Besonders bedanken möchte ich mich dabei bei den C6 und A1-Mitgliedern Gregor Dahl, Clemens Schröter und Michael Kampferbeck. Unsere gemeinsamen Meetings, Tagungen, Konferenzen und Diskussionen haben mir immer sehr viel Spaß gemacht und eure Anregungen haben mir stets weiter geholfen. In sehr guter Erinnerung sind mir die gemeinsamen Konferenzen mit Gregor in Dubai und Boston geblieben, danke dafür. Ein großes Dankeschön möchte ich auch an Jil Rüter richten, die nicht nur mit Praktika und ihrer Masterarbeit einen wesentlichen Anteil an den Ergebnissen meiner Promotion hat, sondern auch danach sich stets die vielen Gedanken zu meiner Arbeit anhören musste und mich auch in schwierigen Phasen aufzumuntern wusste. Des Weiteren danke ich meinen übrigen aktuellen und ehemaligen Bürokollegen Hendrik Schlicke, Svenja Kunze, Mazlum Yesilmen und Sophia Bittinger für die wunderbare Atmosphäre und gute Laune im Büro. Außerdem möchte ich Daniel Jostes, Rieke Koll, Lasse Haberkorn, Felix Thiel, Bendix Ketelsen, Hauke Hartmann, Sebastian Willruth, Hauke Heller und allen anderen aktuellen und vor allem ehemaligen AK Mitgliedern für die vielen netten Gespräche im Sozialraum und die gemeinsame Zeit danken.

Kathrin Hoppe danke ich für die Organisation der Praktika. Außerdem danke ich den Sekretärinnen Beate Kreutzer, Marion Manin, Sigrid Zeckert, Martina Krasa und dem Studienbüro Chemie für die zuverlässige Hilfe bei organisatorischen Anliegen während meiner Promotion. Andreas Kornowski, Stefan Wernen, Robert Schön und Almut Barck danke ich für die zahlreichen und teilweise sehr aufwendigen TEM, SEM und XRD-Messungen in den letzten Jahren. Andreas möchte ich dabei noch für die hilfreichen Diskussionen meiner TEM-Ergebnisse danken.

Außerdem möchte ich meinen Praktikanten Maria Hemme, Sebastian Döring, Jil Rüter, Julian Petry, Martin Sosniok, Delil Yesilmen, Sara Grundewald und Ken Hölscher für die erfolgreiche und motivierende Zusammenarbeit und schönen Ergebnisse danken. Ihr habt mir sehr viel praktische Arbeit abgenommen, wodurch die große Anzahl an verschiedenen Untersuchungen erst möglich war.

Für das Korrekturlesen meiner Arbeit danke ich Tobias Vossmeier, Gregor Dahl, Jil Rüter, Alexey Petrov, Phillip Witthöft, Coralie Finsel und Lars Gäbel.

Außerdem möchte ich mich bei Tim Arne Wilhelm bedanken, der mich davon überzeugt hat, der Sechsten Herren von St. Pauli auch nach der Zeit als aktiver Spieler als Co-Trainer erhalten zu bleiben. Fußball ist eine sehr willkommene Abwechslung bei so einer besonders familiären Mannschaft und Willy hatte immer auch ein offenes Ohr für meine Arbeit neben taktischen Diskussion für das nächste Spiel bei unseren täglichen Telefonaten.

Schließlich danke ich meinen Freunden für ihre ständige Unterstützung während meines gesamten Studiums. Besonders hervorheben möchte ich dabei Jörn Lindemann, Sebastian Bartels, Phillip Witthöft, Katharina Meldal, Johanna Weise, Ann-Katrin Schwarz, Philipp Bahlke, Jessica Redmann, Ann-Katrin Sassnau und alle, die vergessen habe. Vielen Dank für die Abwechslung und den Ausgleich, sei es bei legendären PS4-Abenden oder im Stadion, zur Promotion.

Abschließend möchte ich mich bei meiner gesamten Familie für die besonders liebevolle Unterstützung in den letzten 8 Jahren bedanken. Ein besonderer Dank geht an Brigitte und Klaus Seeger, die mich ermutigt haben, ein Chemiestudium anzufangen und dafür gesorgt haben, dass ich mich voll auf das Studium konzentrieren konnte. Ein großes Dankeschön geht an Coralie Finsel, die immer dafür gesorgt hat, dass ich außerhalb der Uni auch mal von der Arbeit abschalten kann und mir stets den Rücken freigehalten hat, wenn es mal etwas stressiger wurde. Außerdem hat Cora stets die richtigen Worte gefunden, um mich auch in schwierigen Phasen wieder aufzubauen und stets eine positive Einstellung an den Tag zu legen. Abschließend möchte ich mich natürlich bei meinen Eltern Gisela Finsel und Dieter Finsel und meiner Schwester Julia Finsel für die großartige Unterstützung und viel Verständnis bedanken, auch wenn ich mal nicht so viel Zeit hatte. Ohne euch alle wäre meine Arbeit so nicht möglich gewesen. DANKE!

## Curriculum Vitae

### Personal details

Name: Maik Finsel  
E-mail: maik.finsel@gmail.com  
Date of birth: 30. Dezember 1989  
Place of birth: Winsen/Luhe

### Education

11.2015 - 08.2019 SFB 986 member in working group of Prof. Dr. Horst Weller  
Physical Chemistry, MIN-Faculty  
*University of Hamburg, Germany*

10.2013 - 10.2015 M.Sc. Chemistry  
*University of Hamburg, Germany*

09.2014 - 11.2014 Erasmus program  
*University of Southern Denmark, Odense, Denmark*

11.2010 - 09.2013 B.Sc. Chemistry  
*University of Hamburg, Germany*

06.2009 Allgemeine Hochschulreife  
*Gymnasium Salzhausen, Germany*

## Conferences

### 2019

**Tailor-made Multiscale Materials Systems (SFB 986 Workshop)** (Hamburg, Germany)

June 19<sup>th</sup> - 21<sup>th</sup>, 2019

Maik Finsel, Maria Hemme, Sebastian Döring, Jil Rüter, Gregor T Dahl, Tobias Krekeler, Andreas Kornowski, Martin Ritter, Horst Weller, Tobias Vossmeier

Synthesis and thermal stability of ceramic core-shell particles (**poster**)

### 2018

**MRS** (Boston, USA)

November 25<sup>th</sup> - 30<sup>th</sup>, 2018

Maik Finsel, Jil Rüter, Maria Hemme, Kaline P. Furlan, Guoliang Shang, Rolf Janßen, Alexander Yu. Petrov, Manfred Eich, Horst Weller, Tobias Vossmeier

Synthesis and Characterization of  $\text{ZrO}_2@\text{SiO}_2/\text{Al}_2\text{O}_3$  Core-Shell Particles for Application as Structural Colors and Thermal Barrier Coatings (**poster**)

**Summer School, Graduate School** (Bad Bevensen, Germany)

July 9<sup>th</sup> - 13<sup>th</sup>, 2018

Modern Methods of Material Characterization

*Appendix*

**2017**

**Nano and Materials Science** (Dubai, UAE)

October 16<sup>th</sup> - 18<sup>th</sup>, 2017

Maik Finsel, Gregor Dahl, Sebastian Döring, Quynh Yen Nguyen, Guoliang Shang, Alexander Yu. Petrov, Manfred Eich, Gerold A. Schneider, Horst Weller, Tobias Vossmeier

Synthesis and Optical Properties of Monodisperse ZrO<sub>2</sub>@SiO<sub>2</sub> Core-Shell Particles for Application as Structural Colors (**talk**)

**International Congress Engineering of Advanced Materials** (Erlangen, Germany)

October 10<sup>th</sup> - 12<sup>th</sup>, 2017

M. Finsel, G. Dahl, M. Hemme, and T. Vossmeier

Synthesis and Thermal Stability of Monodisperse ZrO<sub>2</sub>@SiO<sub>2</sub> Core-Shell Submicron Particles (**poster**)

**International Symposium of GRK 1896** (Erlangen, Germany)

October 9<sup>th</sup>, 2017

M. Finsel, G. Dahl, M. Hemme, and T. Vossmeier

Synthesis and Thermal Stability of Monodisperse ZrO<sub>2</sub>@SiO<sub>2</sub> Core-Shell Submicron Particles (**poster**)

**Summer School, Graduate School** (Bad Bevensen, Germany)

July 3<sup>th</sup> - 7<sup>th</sup>, 2017

Concept, Design and Presentation of Academic Posters / Optimizing Strategies for Publishing Research in English

**2017**

**3<sup>rd</sup> International Conference and Expo on Ceramics and Composite Materials** (Madrid, Spain)

June 26<sup>th</sup> - 27<sup>th</sup>, 2017

Maik Finsel, Gregor Dahl, Maria Hemme, Horst Weller, Tobias Vossmeier

Synthesis and Thermal Stability of Monodisperse ZrO<sub>2</sub>@SiO<sub>2</sub> Core-Shell Submicron Particles (**talk** and **moderator**)

**2016**

**Summer School, Graduate School** (Travemünde, Germany)

June 6<sup>th</sup> - 10<sup>th</sup>, 2016

Characterization Methods for Multi-Scale Materials

*Appendix*

# Eidesstattliche Erklärung

Hiermit erkläre ich, dass die vorliegende Arbeit von mir selbstständig verfasst wurde und ich keine anderen als die angegebenen Quellen und Hilfsmittel benutzt habe. Ich versichere, dass die vorliegende Arbeit von mir nicht in einem anderen Prüfungsverfahren eingereicht und ebenso keine weiteren Promotionsversuche unternommen wurden.

---

Ort, Datum

---

Maik Finsel